Upscaling Approaches for Nonlinear Processes in Lithium-Ion Batteries

Vasilena Taralova

Vom Fachbereich Mathematik der
Technischen Universität Kaiserslautern
zur Verleihung des akademischen Grades
Doktor der Naturwissenschaften
(Doctor rerum naturalium, Dr. rer. nat.)
genehmigte Dissertation

Datum der Disputation:
11. Mai 2015

1. Gutachter: Prof. Dr. Oleg Iliev
2. Gutachter: Prof. Dr. Yalchin Efendiev

D386

Acknowledgements

First, I would like to thank my supervisor Professor Oleg Iliev for his professional guidance and support during my research. I would also like to express my gratitude to Professor Yalchin Efendiev and Professor Raytcho Lazarov for their hospitality during my stay at Texas A&M University and for the fruitful discussions and valuable comments which helped me gain insight into the subject of this thesis. I would like to gratefully acknowledge Dr. Jochen Zausch and Professor Arnulf Latz for the many valuable discussions we had on Lithium-ion batteries and for the patience with which they answered all my questions. I would also like to thank Dr. Donald Brown for the productive collaboration.
I would like to thank Dr. Markus Lindner and Dr. Christian Wieser from Adam Opel AG with whom I had the opportunity to work and learn about the practical aspects and industrial applications of Li-ion batteries.
I would also like to thank my colleagues from the department Flow and Material Simulation at Fraunhofer ITWM for the pleasant and fruitful working environment. I gratefully acknowledge the financial support by Fraunhofer ITWM.
Furthermore, I thank my PhD committee for putting their time and effort into reviewing this thesis.
Last, but not least, I would like to thank my husband Maxim Taralov, my parents and family for their love and continuous support during my PhD.

Contents

List of Symbols

c^e - concentration of Lithium ions in the electrolyte

c^s - concentration of Lithium ions in the active particles

ϕ^e - potential in the electrolyte

ϕ^s - potential in the solid

T - temperature

D^e - interdiffusion coefficient in the electrolyte; strictly posivite

D^s - interdiffusion coefficient in the active particles; strictly posivite

t_+ - transference number of Lithium ions

κ^e - electric (ionic) conductivity in the electrolyte; strictly positive

κ^s - electric (electronic) conductivity in the solid; strictly positive

$\mathbf{N}$ - ionic flux

$\mathbf{j}$ - electrical current

F - Faraday constant

R - Universal gas constant

η_s - overpotential

U_0 - half cell open circuit potential

$c_{s,max}$ - maximum concentration of ions in the active particle

k - reaction rate

soc - state of charge, i.e. $\frac{c_s}{c_{s,max}}$

Chapter 1

Introduction

1.1 Motivation

Lithium-ion batteries are one of the most widely used types of rechargeable batteries in present days and they can be found in all kinds of portable electronics, such as laptops, cell phones, digital cameras, tablets, cordless electrical tools and many more. Another application of Li-ion batteries, which has become very sought-after in the last decades, is in electrical vehicles. Li-ion batteries are preferred due to their advantages over other types of rechargeable batteries, such as their high energy density, no memory effect, a big number of charge/discharge cycles and their light weight. Mathematical modeling of Li-ion batteries aims to help the design of better batteries in terms of lifetime and capacity. Laboratory experiments for testing different battery cell configurations are expensive and time consuming. On the other hand, numerical simulations provide a fast and cheap tool for analysing the battery cell performance for various types of electrode geometries, as well as applied currents and material parameters.

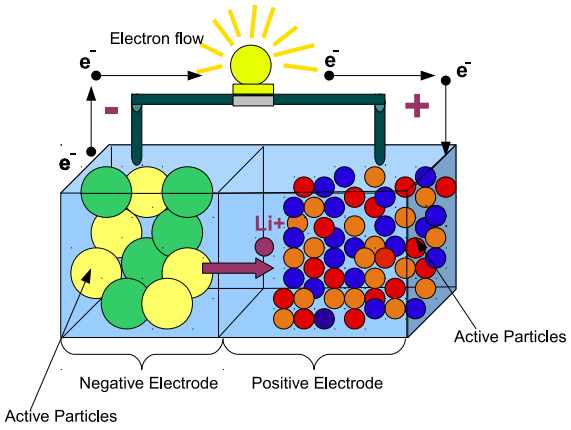

Figure 1.1: A single battery cell

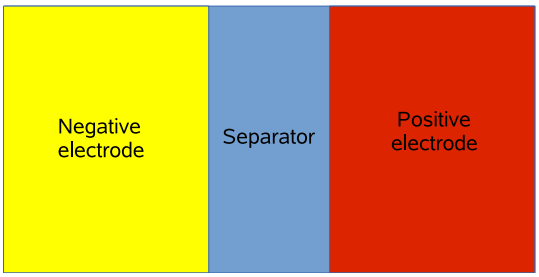

Figure 1.2: A schematic battery cell

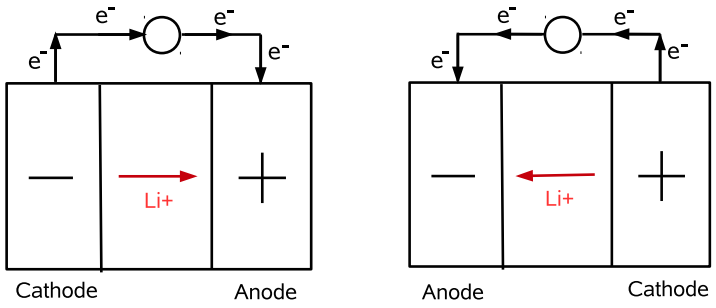

a. Discharging b. Charging

Figure 1.3: Discharging and charging of a battery cell

A typical Li-ion battery consists of many electrically connected electrochemical cells like the one shown in Figure 1.1. The thickness of a typical single planar cell is about several hundreds of micrometers. Each cell has two electrodes – negative and positive, as well as a separator between them as shown in Figure 1.2. Both electrodes have porous structure which is composed of two distinct phases – solid active material and liquid electrolyte. The active material consists of many connected solid particles having a typical size of 1 to 10 μm. The voids between the active particles are filled with liquid electrolyte. The electrodes have porous structure because this leads to a bigger surface area of the active material, which in turn results in a bigger power density and capacity of the battery cell. Positively charged lithium ions travel in the electrolyte and are being transported from one electrode to the other. The lithium ions are then stored in the active particles of the porous electrodes. The process of insertion of lithium ions into the active material is called intercalation and the reverse process – deintercalation. On the other hand, electrons can move only in the active material and not in the electrolyte. When the battery is being charged or discharged the electrons are forced to flow through a closed external circuit in order to migrate from one electrode to the other. The diffusion of lithium ions is a transport of species due to concentration gradients and the migration of electrons is due to electric fields. The electrode in a battery cell is referred to as either a cathode or an anode. The definition of anode and cathode depends on the direction of the current. In general, we call current any movement of charged particles, but the common convention is that the direction of the current coincides with the flow of the positive charge, i.e., where a positive charge would move. Therefore, current flows in the same direction as positive

charge carriers and in the opposite direction of negative charge carriers. The anode is defined as the electrode where current flows in from outside. By analogy, the cathode is defined as the electrode where current flows out. However, in rechargeable batteries the flow of Li+ reverses its direction between charge and discharge. Consequently, depending on the direction of the current each electrode becomes either the anode or the cathode as shown in Figure 1.3. We use the following naming convention for the battery electrodes: we call "cathode" the electrode, from which Li+ move away during charging and during discharging it receives Li+. By analogy, we call "anode" the electrode, which pushes away Li+ during discharging and accepts Li+ during charging. This means that we call anode always the negative electrode and cathode – always the positive electrode.
Lithium-ion batteries are also multiscale systems with processes occuring at different lengthscales. In the current work we are interested in capturing electrochemical phenomena on the scale of a single battery cell. Therefore, we call the ***macroscale*** the lengthscale of the whole electrode and the ***microscale*** is the scale where we can distinguish the complex porous structure of the battery electrodes. In this thesis we consider the microscale Li-ion battery model [48] developed by Latz, Zausch and Iliev. The model is isothermal and can be viewed as a special case (by taking the temperature to be constant) of the later derived non-isothermal model proposed by Latz and Zausch [47]. For a more detailed description of a Li-ion battery and the electrochemical processes involved, as well as for numerical simulations on the microscale, we refer to [70] and [71]. The model is based on nonlinear diffusion equations for the transport of Lithium ions and charges in the electrolyte and in the solid active particles. The coupling of the two phases is due to electrochemical reactions that occur on the solid-electrolyte interface. The interface kinetics is modelled by the highly nonlinear Butler-Volmer interface conditions. Due to the porous structure of the electrodes, direct numerical simulations (with the standard Finite Element Method, for example) lead to a very big number of degrees of freedom and ill-conditioned problems. This makes the numerical solving very complicated and computationally expensive. Therefore our aim is to capture effectively the macroscopic properties of the electrodes by applying different upscaling techniques which lead to a significant decrease in the number of unknowns, making the problem much easier to handle numerically. In the current work we focus on two upscaling techniques for partial differential equations - the Asymptotic Homogenization Method and the Multiscale Finite Element Method (abbreviated as MsFEM). The two methods are very different in nature. Therefore, before deciding which method to choose, one has to weigh their advantages and disadvantages depending on the results they want to achieve. The homogenization method is restricted only to periodic media and respectively periodically oscillating coefficients and solutions, whereas the MsFEM deals with oscillatory coefficients and solutions which do not need to be periodic. The idea behind the homogenization method is to average in a special way the differential operator and to derive upscaled macroscopic partial differential equations which describe the macroscopic behaviour of the medium. Another important feature of the homogenization is the derivation of explicit analytical formulas for effective medium coefficients. The MsFEM follows the Finite Element Method (FEM) framework but with specially constructed multiscale basis functions which capture the local properties of the differential operator. The construction of the multiscale basis functions requires solving local boundary value problems and then storing their solutions. The MsFEM

is very suitable for parallel implementations because the multiscale basis functions are constructed independently of one another.

1.2 Goals of the thesis

Most of the macroscale Li-ion battery models that are available are empirical. Such model, for example, is the famous and widely used volume averaged 1D+1D model proposed by Doyle, Fuller and Newman [22]. The goal of the thesis is to derive effective macroscale battery models analytically, starting from the microscopic description of the electrochemical processes in the battery. This rigorous approach allows deriving upscaled models, which are consistent with the underlying microscale features of the problem. Furthermore, our aim is to develop fast and efficient upscaling algorithms for Lithium-ion battery models, which accurately capture the macroscopic properties of the battery electrodes. We develop upscaling approaches for both regular periodic and random structure of the electrode particles. In the first case we apply the asymptotic homogenization method and in the second case – a modified MsFEM for perforated domains with nonlinear Neumann boundary conditions on the holes. The two upscaling techniques, that we consider in the context of Li-ion batteries, allow for flexibility because they can be applied in different scenarios depending on the research purposes and the quantities of interest to be observed. The common idea behind the application of the two methods to the Li-ion battery model [48] is to consider each medium – the electrolyte and the solid phase, as two separate perforated domains, coupled by the nonlinear Butler-Volmer interface conditions. Furthermore, as we will see in the thesis, not all quantities of interest are scale-separable which demands leaving some of the equations on the microscale and coupling them with the upscaled equations on the macroscale. Thus arises the necessity to establish upscaling algorithms adapted to coupled macro-micro problems in perforated domains with nonlinear Neumann boundary conditions on the perforations' boundary. An example for a battery cell with periodic arrangement of the particles can be found in [59] and a random distribution of the solid particles is given in [21] and [1].

1.3 State of the art and main contributions of the thesis

There are only few available works dealing with upscaling of Lithium-ion battery models starting from microscale theories. This area is still under active ongoing research.
The first part of the thesis is devoted to the ***asymptotic homogenization*** of the considered microscale Li-ion battery model [48]. Some of the pioneering and most significant works in the field of the theory of the asymptotic homogenization method are the books [8], [63], [44], [38], [17], and [58], where convergence results are proven and a vast range of problems is considered.
Another approach to prove convergence in the asymptotic homogenization method is the so-called ***two-scale convergence method***, which was introduced by Nguetseng [54] and

later developed by Allaire [3]. The method is based on deriving a two-scale homogenized problem, which is a combination of the standard homogenized problem from the asymptotic homogenization method and cell equations. Furthermore, a two-scale convergence is defined and a new method for proving the convergence of the homogenization process is given.
The periodic unfolding method was introduced by Cioranescu, Damlamian and Griso [16]. It is a fixed domain method which increases the space dimension of the problem, but, on the other hand, leads to significant simplifications in the proofs and simplifies the homogenization process by turning it to a weak, or even strong convergence problem in L^p spaces. The periodic unfolding method is well studied for different classes of problems including problems in perforated domains [18]. In [19] the method is applied to an elliptic problem in perforated domains with nonlinear boundary conditions on the holes. Weak convergence results are proven in the context of the unfolding method and under the assumption that the nonlinear boundary condition is a continuously differentiable and monotonously non-decreasing function. The asymptotic homogenization method in domains with holes is studied also in [20] and [4].
In [32] is considered a nonlinear reaction-diffusion model in the context of metabolic processes in cells. The setup of this problem is similar to what we have in the microscale Li-ion battery model. The solution domain is a porous medium consisting of two components which are separated by an interface. One of the components of the porous medium is a connected domain and the other one is a disconnected domain composed of periodically arranged inclusions. The model equations describe the transport of different substances in the two subdomains as well as their exchange at the interface. The concentrations of these substances are discontinuous functions across the interface but the normal fluxes are continuous and are given by a nonlinear function of the concentrations on both sides of the interface. This is exactly the case in our Li-ion battery model where the highly nonlinear Butler-Volmer interface conditions are imposed on the solid-electrolyte interface. In [32] the nonlinear interface transmission function is scaled explicitly with the small parameter ε, so that the total flux across the interface does not blow up in the asymptotic limit. On the other hand, we show that the nonlinear interface exchange current densities in the Li-ion battery model depend implicitly on ε and we must not scale them additionally. An effective homogenized model is derived in [32] with the help of the two-scale convergence method. Furthermore, using the unfolding operator, a convergence result is proven under the assumption of Lipschitz continuity of the nonlinear transmission function.
A homogenization approach for non-periodic media is ***the numerical homogenization method*** which is considered, for example, in [27], [28] and [26]. The method is based on local Laplacian formulations and its idea is to replace the oscillatory medium coefficient $k_\varepsilon(x)$ with grid-block effective constant coefficients $\tilde{k}$ which are tensors. By definition the coefficient $\tilde{k}$ is a discrete quantity relying on the discretization of the medium and is computed by solving local boundary value problems and averaging the flux in each grid block. In particular $\tilde{k}$ depends on the location and geometry of the grid block in which it is computed.
We suppose periodic structure of the battery electrodes and we apply the homogenization theory to derive upscaled macroscopic equations starting from the microscopic model [48]. We follow and extend the homogenization framework developed by Ciucci and Lai [45]. They upscale the microscopic battery model derived in [46]. This microscale model is

also based on diffusion equations for the transport of ions and charges in the liquid and solid phase as well as their coupling via the Butler-Volmer interface conditions. A very important step in the homogenization of the problem is the upscaling of the Butler-Volmer reaction model. The interface conditions can be correctly homogenized only if we accurately determine their asymptotic order. In [45] it is stated that the interface exchange current densities are of the order of the small parameter, but no clarification is provided as why this is the case. One of our main contributions is that in the present work we derive asymptotically the order of the current densities and we numerically verify the proposed homogenized model. We note that in [45] no numerical evidence is provided to validate the derived upscaled model. Another substantial difference between our approach and the one proposed in [45] is that our homogenization procedure takes into account the microscale boundary conditions and properly upscales them.

We show numerical results for two types of periodicity cells. The first one consists of a single cut-off spherical particle and the second one – of random ellipsoid particles. In the first case we run a series of numerical simulations varying the particles' size in order to demonstrate convergence with respect to the small parameter. In the second scenario we show numerical experiments for both low and very high applied currents. We observe a very good agreement between the solution of the homogenized model and that of the microscale one in both test cases.

Another paper where the homogenization theory is applied to derive macroscopic battery model starting from a microscopic one is [62]. However, in [62] there are no numerical or theoretical results showing that the derived homogenized model is a good approximation of the microscale one. The obtained upscaled model is based on the homogenization of all model equations, including that for the diffusion of Lithium ions in the active particles, which is not scale-separable under general assumptions. Therefore this approach is restricted only to the special cases when the battery operates at low discharge/charge rates and when the electrode particles are very small so that the diffusion of Lithium within the particles is fast. These assumptions ensure uniform deposition of Lithium ions in the electrode particles, which guarantees scale separation for the concentration of Li+ in the solid, thus allowing for its successful homogenization. Following [45], in this work we derive coupled macro-micro model with microscale equation for the diffusion of Lithium ions in the electrode particles. This makes our approach very general because it does not depend on the diffusion in the electrode particles as well as on the applied current.

One of the most popular electrochemical models for Li-ion batteries, on the lengthscale of the whole electrode, is the 1D+1D model proposed by Doyle et al. [22]. This model, however, is derived directly on the macroscale and is restricted only to spherical active particles. Fitting of the parameters is required if the model is to be applied for non-spherical particles, but this approach is not rigorous and does not guarantee meaningful and consistent with the microscale behaviour results. On the other hand, our upscaling technique allows for randomly shaped and arranged particles in a single period. This is the case because the homogenization method results in rigorously and systematically derived analytical expressions for the effective transport coefficients, which incorporate the underlying microscopic features of the electrodes and are independent of the parameter set.

The focus of the second part of the thesis is on the upscaling of the microscale Li-ion

battery model [48] via the ***Multiscale Finite Element Method***. The foundations of the method were laid in the early 80's by Babuška et al. in [41], [39] and [40], where they consider a special class of one and two-dimensional problems with rough coefficients and construct finite element basis functions adapted to the properties of the considered differential operators. Later, in the mid 90's, the method was generalized and established by Hou, Wu and Cai in the papers [68] and [69]. In [25] the method is studied extensively and many applications are given. The method is based on the Finite Element Method framewrok with specially constructed multiscale basis functions which capture the local properties of the differential operator and thus allow for significant reduction of the degrees of freedom. In the ***MsFEM with oversampling*** one solves the local problems (for computing the multiscale basis) on domains which are larger than the coarse mesh finite elements in order to capture the differential operator properties on the boundary of the macro elements. This results in a nonconforming finite element method with convergence results proven in [75]. One could also use oscillatory boundary conditions on the edges of the macro elements [25]. This is also done to capture the behaviour of the solution on the edges of the macro elements and the resulting FEM is conforming since the boundary conditions for adjacent elements are the same. In [10] a MsFEM for high-contrast elliptic interface problems is introduced and studied.

Another multiscale method is the ***heterogeneous multiscale method*** studied, for example, in [23], [24], [35], [34], [55], [37] and [36]. The heterogeneous multiscale method is a framework for coupling and solving models at different scales. The method is based on some incomplete macroscale model where the missing numerical data is computed with the help of the given microscale model. There is a freedom in the choice of a macroscale solver and it is adapted to the specifics of the considered problem. The coupling between the macroscale and the microscale solver is data-based. This means that the macroscale state of the system provides the environment and consequently the constraints for the microscale solver, which in turn transfers back numerical data (such as fluxes, forces, etc.) to the macrosystem.

In our work we consider the MsFEM in the context of Li-ion batteries which leads to the adaptation of the method to problems in perforated domains with nonlinear Neumann boundary conditions on the perforations' boundary. To the best of our knowledge, there is no previous work done in this direction so far. The only available paper is [12] and it regards MsFEM in perforated domains but with zero Dirichlet boundary conditions on the boundary of the holes. The foundations for the perforated MsFEM with zero Dirichlet data are laid in the paper [11] which is devoted to MsFEM with nonconforming Crouzeix-Raviart type of finite elements. However, the case with Neumann data on the perforations' boundary, which we consider in the thesis, requires a completely different numerical approach than that discussed in [12].

The application of the developed in [12] Crouzeix-Raviart MsFEM to a class of stationary diffusion and advection-diffusion problems in perforated domains is considered in [57]. The designed in [12] framework is extended by introducing bubble functions and considering non-homogeneous boundary conditions on the exterior boundary of the solution domain. Extensive numerical results are shown in order to demonstrate the efficiency of the proposed numerical approach in contrast to the standard MsFEM.

The ***main contributions of the thesis*** are summarized as follows:

- Derivation of an upscaled Li-ion battery model via the homogenization theory
  - Application and analysis of the asymptotic homogenization method in perforated domains in the context of Li-ion battery models
  - Rigorous derivation of the asymptotic order of the interface exchange current densities
  - Rigorous upscaling of the microscale Neumann boundary conditions
  - Detailed numerical investigation of the derived upscaled model with self-implemented C++ code
- Developing a Multiscale Finite Element Method for perforated domains with Neumann data on the boundary of the perforations
  - Construction of a new type of multiscale finite element basis functions in perforated domains with Neumann data on the boundary of the perforations
  - Application and analysis of the MsFEM in perforated domains for zero and nonzero Neumann, as well as for nonlinear Neumann boundary conditions on the boundary of the holes
  - Numerical study of the convergence of the proposed method with self-implemented C++ code
- Application of the MsFEM in perforated domains to a simplified 2D Li-ion battery problem
  - Application and analysis of the proposed MsFEM for perforated domains in the context of Li-ion battery models
  - Numerical investigation of the convergence of the proposed algorithm with self-implemented C++ code

1.4 Structure of the thesis

The thesis is organized as follows.
We start with the microscale Li-ion battery model [48] in Chapter 2. We describe the solution domain, we give the electrolyte phase and solid phase diffusion equations, as well as the highly nonlinear Butler-Volmer interface conditions and an appropriate set of boundary conditions.
In Chapter 3 we introduce and explain the asymptotic homogenization method and we apply the method to a linear elliptic model problem in order to illustrate it. No new results are present in the chapter. It has solely an educational role and serves to outline the main ingredients of the homogenization method, which we later apply to the microscale Li-ion battery model [48]. We also give some basic definitions and facts from functional analysis and Sobolev spaces, which we need to state main convergence results in the homogenization method and later in the MsFEM. In the end of the chapter we give a simple numerical example.

In Chapter 4 we present the asymptotic homogenization method for perforated domains, which is the basis for the homogenization of our two-phase Li-ion battery problem. We address the important issue with the conservation of the total flux across the perforations' boundary with the consequence of it being the scaling with ε (the dimensionless so-called small parameter in the homogenization theory) of the Neumann data on the holes. We also consider the case when the Neumann boundary condition on the perforations' boundary is a periodically oscillating function and we show extensive numerical results for different test cases. We do not have any new contributions in this chapter. Its purpose is to illustrate with a simple model problem the concept of the homogenization method in perforated domains, because it serves as the foundation for the asymptotic homogenization of the considered microscale Li-ion battery model [48].
Chapter 5 is devoted to the upscaling of the microscale electrochemical Li-ion battery model [48] via the homogenization theory, which is a main contribution of the thesis. Since the concentration of Lithium ions in the solid phase is not a scale-separable function, we cannot upscale this quantity and we leave the equation for the concentration in the active material on the microscale. All other quantities – the concentration of Li+ in the electrolyte, the potential in the electrolyte and the potential in the solid, are scale-separable and therefore we homogenize the electrolyte phase equations as well as the potential equation in the solid. We couple the macroscale homogenized equations and the microscale equation for the concentration of Li+ in the solid with the nonlinear Butler-Volmer interface conditions. We rigorously prove the asymptotic order of the interface exchange current densities, which is crucial for the correct upscaling of the battery model and is also an original result. We homogenize accordingly the Neumann boundary conditions in the microscale model to derive effective ones. The numerical solving of the coupled macro-micro upscaled problem is also addressed. We discuss in detail the numerical methods that we use and we show comprehensive numerical results for two different types of solid phase geometries. Finally, we briefly discuss the advantages of the proposed homogenized coupled macro-micro model and we finish the chapter with a short summary.
In Chapter 6 we introduce the Multiscale Finite Element Method. The chapter has only an educational role and we need it for completeness and clarity of the exposition. First we briefly explain the method and then we discuss scale separation in the context of the MsFEM, as well as the choice of coarse grid size. We also comment on the choice of boundary conditions for the local problems that we solve in order to construct the multiscale basis functions. Lastly, we state the main convergence result and we show a simple numerical example in order to illustrate the method.
Chapter 7 is dedicated to the MsFEM in perforated domains with Neumann boundary conditions on the holes. In this chapter we construct a new type of multiscale basis functions and we extend the classical MsFEM to problems in perforated domains with Neumann data on the boundary of the perforations. This is an original result of the thesis. We analyse the suggested numerical algorithm by applying it to different test problems and we show numerically its convergence.
In Chapter 8 we consider a simplified 2D Li-ion battery model, which we solve with the help of the MsFEM in perforated domains with nonlinear Neumann boundary condition on the perforations. This time-dependent nonlinear problem is an extension of the constructed in Chapter 7 MsFEM for perforated domains with Neumann boundary condition on the

holes. The results presented in this chapter are original. We consider a two-phase problem, where the coupling between the electrolyte and the solid phase is due to nonlinear interface conditions similar to the Butler-Volmer conditions that we have in the microscale model [48]. In this simplified probelm, by analogy with the real microscale Li-ion battery model [48], we assume that only the electrolyte phase quantity is scale-separable. Therefore, we apply the MsFEM to solve the electrolyte phase equation and we couple it to a microscale solid phase problem via the nonlinear interface conditions. We solve the coupled macro-micro problem semi-implicit in time. Finally, we show numerical convergence of the proposed algorithm.
We conclude with a summary of the thesis in Chapter 9.

Chapter 2

Mathematical Model

2.1 Introduction

In this chapter we present the microscale Li-ion battery model [48] whose upscaling is the main focus of the thesis. We start with a description of the solution domain in Section 2.2, which consists of two phases - electrolyte and solid. Then, in Section 2.3 and Section 2.4, we give the transport equations for Lithium ions and charges in each of the two phases. The highly nonlinear interface conditions that couple the electrolyte and the solid phase are introduced in Section 2.5, and in Section 2.6 we close the model equations with a set of boundary conditions.

2.2 Solution domain

With $\Omega \in \mathbb{R}^3$ we denote the domain of the whole battery cell which consists of two electrodes- anode and cathode, and pure electrolyte between them as shown in Figure 2.1. With $\partial\Omega$ we denote the boundary of Ω. The electrolyte domain is denoted with Ω_e (given in blue in Figure 2.2), and Ω_a (given in yellow in Figure 2.2) and Ω_c (given in red in Figure 2.2) are the domains of the anode and cathode active particles, respectively, with boundaries $\partial\Omega_a$ and $\partial\Omega_c$. In Figure 2.2 the rectangle ABCD is the domain of the anode and the rectangle EFGH is the cathode domain. Each electrode consists both of electrolyte and active material. Let us denote with Ω^e_{anode} the electrolyte domain in the anode (given in blue), and with $\Omega^e_{cathode}$ - the electrolyte in the cathode (given in blue). It is then clear that the electrolyte domain Ω_e consists of three subdomains - Ω^e_{anode}, $\Omega^e_{cathode}$ and $\Omega^e_{separator}$, i.e., $\Omega_e = \Omega^e_{anode} \cup \Omega^e_{separator} \cup \Omega^e_{cathode}$, where $\Omega^e_{separator}$ is the layer of pure electrolyte between the two electrodes and it plays the role of a separator. In Figure 2.2 the domain $\Omega^e_{separator}$ is the rectangle BEHC. Furthermore, $\Omega_{anode} = \Omega^e_{anode} \cup \Omega_a$ and $\Omega_{cathode} = \Omega^e_{cathode} \cup \Omega_c$. Finally, with $\Omega_{electrode}$ we denote either the anode electrode domain Ω_{anode} or the cathode one - $\Omega_{cathode}$. With Ω_s, where the subscript "s" stands for solid particles, we denote the union of the anode and cathode particles, i.e., $\Omega_s = \Omega_a \cup \Omega_c$. Then it is clear that $\Omega = \Omega_e \cup \Omega_s$.

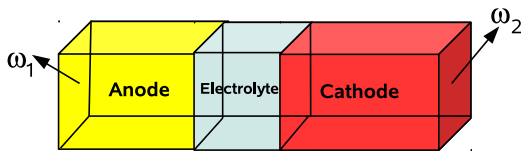

Figure 2.1: Schematic 3D solution domain

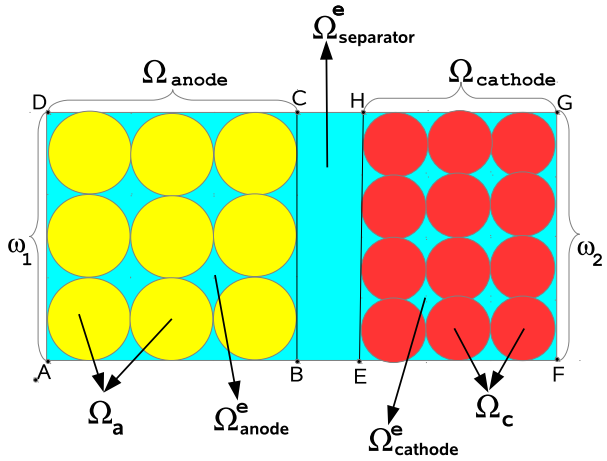

Figure 2.2: Cross section of the 3D solution domain

2.3 Equations in the electrolyte

The electrolyte phase equations couple the concentration c^e of Lithium ions and the electrochemical potential ϕ^e:

$$\frac{\partial c^e}{\partial t} - \nabla \cdot (k^e_{11}(c^e)\nabla c^e + k^e_{12}\nabla \phi^e) = 0, \quad x \in \Omega_e \tag{2.3.1a}$$

$$-\nabla \cdot (k^e_{21}(c^e)\nabla c^e + k^e_{22}\nabla \phi^e) = 0, \quad x \in \Omega_e \tag{2.3.1b}$$

The coefficients in the equations have the following form

$$\begin{aligned} k^e_{11}(c^e) &= D^e + \frac{RT}{F^2}\frac{(t_+)^2\kappa^e}{c^e}, & k^e_{12} &= \kappa^e \frac{t_+}{F} \\ k^e_{21}(c^e) &= \frac{RT}{F}\frac{\kappa^e t_+}{c^e}, & k^e_{22} &= \kappa^e \end{aligned} \tag{2.3.2}$$

where D^e is the interdiffusion coefficient, κ^e is the electric (ionic) conductivity in the electrolyte, F is the Faraday constant, R is the universal gas constant, T is the temperature (which we take to be constant) and t_+ is the transference number of Lithium ions.

2.4 Equations in the solid particles

The equations describing the transport of Lithium ions and charges in the solid particles (active material) are given as follows

$$\frac{\partial c^s}{\partial t} - \nabla \cdot (D^s \nabla c^s) = 0, \quad x \in \Omega_s \tag{2.4.1a}$$

$$-\nabla \cdot (\kappa^s \nabla \phi^s) = 0, \quad x \in \Omega_s \tag{2.4.1b}$$

where c^s is the concentration of Lithium ions in the solid particles and ϕ^s is the electrical potential in the solid. We make no distinction between anode and cathode active particles since the equations describing the electrochemical processes in both types of particles are identical, except for the values of the ion diffusion coefficient D^s and the electronic conductivity κ^s which are different in the two electrodes:

$$D^s = \begin{cases} D^s_{anode}, & x \in \Omega_a, \\ \\ D^s_{cathode}, & x \in \Omega_c \end{cases} \tag{2.4.2}$$

and

$$\kappa^s = \begin{cases} \kappa^s_{anode}, & x \in \Omega_a, \\ \\ \kappa^s_{cathode}, & x \in \Omega_c \end{cases} \tag{2.4.3}$$

2.5 Interface conditions

The flux of lithium ions $\mathbf{N}$ and the electric current density $\mathbf{J}$ in the electrolyte and in the active (solid) particles are respectively

$$\mathbf{N}^e = -\left(k^e_{11}(c^e)\nabla c^e + k^e_{12}\nabla \phi^e\right) \tag{2.5.1a}$$

$$\mathbf{J}^e = -\left(k^e_{21}(c^e)\nabla c^e + k^e_{22}\nabla \phi^e\right) \tag{2.5.1b}$$

$$\mathbf{N}^s = -D^s \nabla c^s \tag{2.5.1c}$$

$$\mathbf{J}^s = -\kappa^s \nabla \phi^s \tag{2.5.1d}$$

These fluxes are continuous across the interface γ between the solid particles and the electrolyte

$$\mathbf{N}^s \cdot \mathbf{n_s} = \mathbf{N}^e \cdot \mathbf{n_s} = \mathcal{N}(c^e, c^s, \phi^e, \phi^s), \quad x \in \gamma \tag{2.5.2a}$$

$$\mathbf{J}^s \cdot \mathbf{n_s} = \mathbf{J}^e \cdot \mathbf{n_s} = \mathcal{J}(c^e, c^s, \phi^e, \phi^s), \quad x \in \gamma, \tag{2.5.2b}$$

whereas the concentration of Lithium ions and the potential are discontinuous functions across the solid-electrolyte interface. The unit normal vector $\mathbf{n_s}$ points in direction from the solid particles to the electrolyte and γ is the interface boundary between the solid particles and the electrolyte in the electrode domain $\Omega_{electrode}$. The interface exchange

current densities $\mathcal{N}$ and $\mathcal{J}$ are highly nonlinear functions given by the Butler-Volmer reaction model

$$\mathcal{N} = \frac{k}{F}\sqrt{c^e c^s \left(c^s_{max} - c^s\right)}\left[\exp\left(\frac{F\eta}{2RT}\right) - \exp\left(\frac{-F\eta}{2RT}\right)\right] \tag{2.5.3}$$

$$\mathcal{J} = F\mathcal{N}. \tag{2.5.4}$$

In the latter $\eta = \phi^s - \phi^e - U_0(c^s)$, where $U_0(c^s)$ is the open circuit potential.

2.6 Boundary conditions

With ω_1 and ω_2 we denote the outer anode and cathode boundary walls as shown in Figure 2.1. On the anode particles boundary $\omega_1 \cap \partial\Omega_a$ we impose constant potential

$$\phi^s(x) = E_1^s = const, \tag{2.6.1}$$

and on the cathode particles boundary $\omega_2 \cap \partial\Omega_c$ we impose constant current

$$-\left(\kappa^s \nabla\phi^s\right) \cdot \mathbf{n} = E_2^s = const. \tag{2.6.2}$$

We also assume that no Lithium ions and electrons leave the battery

$$\nabla c^s \cdot \mathbf{n} = 0, \quad x \in \{\omega_1 \cap \partial\Omega_a\} \cup \{\omega_2 \cap \partial\Omega_c\} \tag{2.6.3}$$

with the rest of the battery cell walls being insulated

$$\mathbf{N}^e \cdot \mathbf{n} = \mathbf{J}^e \cdot \mathbf{n} = 0, \quad x \in \partial\Omega \tag{2.6.4a}$$

$$\mathbf{N}^s \cdot \mathbf{n} = \mathbf{J}^s \cdot \mathbf{n} = 0, \quad x \in \partial\Omega \backslash \{\omega_1 \cup \omega_2\}. \tag{2.6.4b}$$

Chapter 3

Asymptotic Homogenization Method

3.1 Introduction

In this Chapter we present and discuss in detail the asymptotic homogenization method. The method was introduced in the 70's and some of the most prominent works on the topic are [8], [63], [44], [17], [3] and [58]. This chapter does not contain original results and its role is to give an introduction to the homogenization method, which is the first upscaling technique that we apply to the microscale Li-ion battery model [48]. In Section 3.2 we briefly explain the foundations of the method. In the next Section 3.3 we give some basic definitions and theorems from functional analysis, which we need in order to present the method in details in Section 3.4 and to state the main convergence result in Section 3.5. Finally, we illustrate the method with a numerical example in Section 3.6.

3.2 Setup of the method

The asymptotic homogenization method deals with partial differential equations with periodically oscillating coefficients. This type of equations model various physical problems arising in media with periodic structure. In this kind of physical problems there are present two natural spatial lengthscales. One of the scales measures the variations within a single period (this is the so-called "fast" scale) and the other one quantifies the variations within the whole domain of interest (the so-called "slow" scale). The aim of the method is to derive macroscale "homogenized" equations which adequately describe the macroscopic behaviour of the oscillatory solution. In turn this leads to a significant decrease in the computational effort needed to solve the considered problem. In these problems the size l of a single period of the microstructure is small compared to the size L of a sample of the medium. We start from the microscopic description of the problem and we seek a macroscopic, or averaged, description. Roughly speaking, the idea of the method is to take advantage of the periodicity by capturing the microscale oscillatory behaviour in a single "magnified" period and then to incorporate this microscale cell information into effective homogenized coefficients. This is done by solving a boundary value problem in a representative period.
First we give a brief schematic overview of the method and then, in the next section, we

explain the asymptotic homogenization method by applying it to a simple model problem. Let us consider the following equation

$$\mathcal{L}u = f, \quad x \in \Omega \tag{3.2.1}$$

where $\mathcal{L}$ is some partial differential operator with periodically oscillating coefficient with period l, and u and f are functions of x. We want to investigate the behaviour of the partial differential equation as $\varepsilon = \dfrac{l}{L} \to 0$, i.e., as the size l of the periodicities goes to zero which is equivalent to their number becoming infinitely large. Therefore an asymptotic analysis is required as $\varepsilon \to 0$. It is important to note that the homogenization method is applicable only to scale-separable problems, where the magnitude of the oscillations is of the order of the small parameter ε. We illustrate the idea of scale separation with an one-dimensional example shown in Figure 3.2 and we give schematical description of the homogenization method in Figure 3.1.

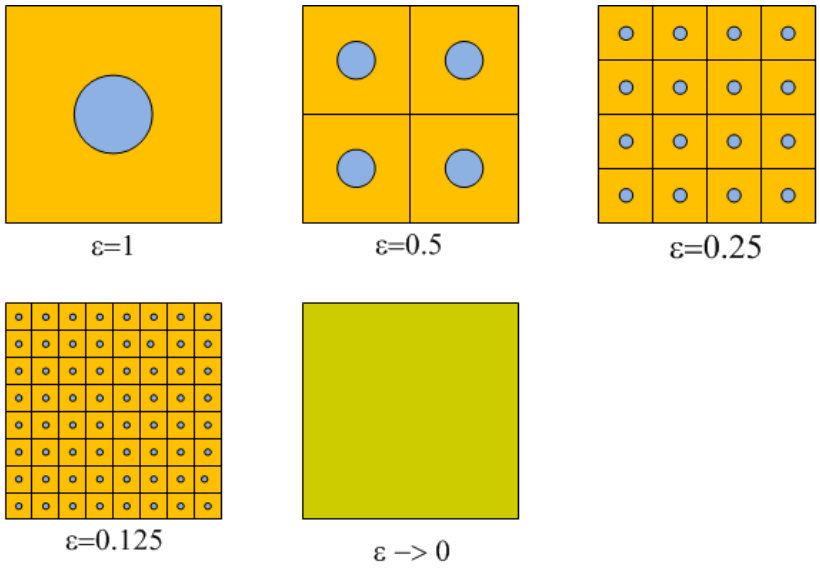

Figure 3.1: Illustration of the homogenization process

We obtain a family of partial differential operators $\mathcal{L}_\varepsilon$ with coefficients oscillating with period εL, and a family of solutions u_ε, which satisfy

$$\mathcal{L}_\varepsilon u_\varepsilon = f, \quad x \in \Omega \tag{3.2.2}$$

complemented by appropriate boundary conditions. Assuming that the sequence u_ε converges, in some sense, to a limit u^h, we look for a so-called homogenized operator $\mathcal{L}^h$ such that u^h is a solution of

$$\mathcal{L}^h u^h = f, \quad x \in \Omega \tag{3.2.3}$$

We use a two-scale asymptotic expansion of the solution u_ε in order to find the precise form of the homogenized operator $\mathcal{L}^h$. Hence we postulate the following ansatz for u_ε (see

Figure 3.2)

$$u_\varepsilon(x) = u_0\left(x, \frac{x}{\varepsilon}\right) + \varepsilon u_1\left(x, \frac{x}{\varepsilon}\right) + \varepsilon^2 u_2\left(x, \frac{x}{\varepsilon}\right) + \dots \tag{3.2.4}$$

where we denote

$$y = \frac{x}{\varepsilon} \tag{3.2.5}$$

and each term $u_i(x, y)$ is periodic in y. Inserting the asymptotic expansion (3.2.4) in (3.2.2) and identifying equal powers of ε leads to a cascade of equations for each term u_i. Averaging with respect to y the equation for u_0 gives the homogenized equation

$$\mathcal{L}^h u_0 = f \tag{3.2.6}$$

The precise form of the operator $\mathcal{L}^h$ is computed with the help of a so-called auxiliary cell problem. There exist analytical formulas for the computation of the effective coefficients of the homogenized problem (3.2.6). These upscaled coefficients describe the macroscopic properties of the underlying medium and their construction involves the solution of a boundary value problem in a single periodicity cell, which is the above mentioned cell problem.

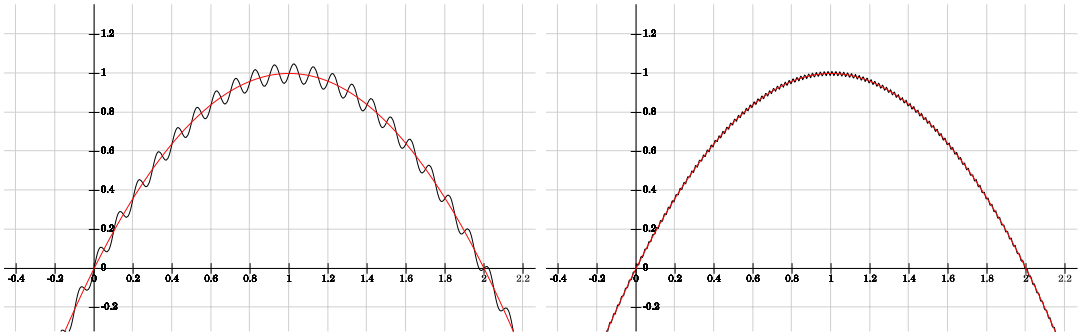

(a) $\varepsilon = 0.05$ (b) $\varepsilon = 0.01$

Figure 3.2: Example for scale separation of the function $u_\varepsilon(x) = u_0(x) + \varepsilon u_1\left(x, \frac{x}{\varepsilon}\right)$ (in black on the pictures) with $u_0(x) = x(2 - x)$ (in red) and $u_1\left(x, \frac{x}{\varepsilon}\right) = \varepsilon \sin\left(\pi \frac{x}{\varepsilon}\right)$

3.3 Some basic notions and definitions

First, we give some basic definitions, propositions and theorems that we will use. We follow the book of Cioranescu and Donato ([17]). For more details on distributions and weak derivatives, as well as Banach spaces, Sobolev spaces, etc., see [29] and [61].

Definition 1. We consider partial differential equations of the form

$$Lu = f,$$

where L is a linear differential operator of the form

$$Lu = -\sum_{i,j=1}^{n} \frac{\partial}{\partial x_i}\left(a_{ij}(x)\frac{\partial u}{\partial x_j}\right) + \sum_{i=1}^{n} \frac{\partial}{\partial x_i}\left(b_i u\right) + cu$$

which acts on functions $u : \Omega \longrightarrow \mathbb{R}$, where Ω is an open set in $\mathbb{R}^n$. We assume the given coefficients functions $a_{ij}(x)$, $b_i(x)$, $c(x) : \Omega \longrightarrow \mathbb{R}$ satisfy $a_{ij}, b_i, c \in L^\infty(\Omega)$. We say that the operator L is ***elliptic*** if the matrix $\mathcal{A} = (a_{ij})_{i,j=1}^{n}$ is positive definite, i.e., if

$$\eta \mathcal{A} \eta^T > 0, \quad \forall \eta \in \mathbb{R}^n, \quad and \quad \eta \neq \vec{0}$$

which is equivalent to

$$\sum_{i,j=1}^{n} a_{ij}(x)\eta_i\eta_j > 0, \quad \forall \eta = (\eta_1, \eta_2, \ldots, \eta_n) \in \mathbb{R}^n, \quad and \quad \eta \neq \vec{0}$$

Definition 2. The operator L from Definition 1 is ***uniformly elliptic*** on Ω if there exists a constant $\theta > 0$ such that

$$\sum_{i,j=1}^{n} a_{ij}(x)\eta_i\eta_j \geq \theta \left|\eta\right|^2$$

for x almost everywhere in Ω and for all $\eta \in \mathbb{R}^n$.

Definition 3. Let $p \in \mathbb{R}$ with $1 \leq p < +\infty$. Let Ω be an open set in $\mathbb{R}^n$. We define the following Lebesgue spaces

$$L^p(\Omega) = \left\{ f | f : \Omega \longrightarrow \mathbb{R}, f \quad is \quad measurable \quad such \quad that \int_\Omega |f(x)|^p \, dx < +\infty \right\}$$

$$L^\infty(\Omega) = \{ f | f : \Omega \longrightarrow \mathbb{R}, f \quad is \quad measurable \quad such \quad that \quad there \quad exists \quad C \in \mathbb{R}, \\ C \geq 0 \quad with \quad |f(x)| \leq C \quad almost \quad everywhere \quad on \quad \Omega \}$$

Proposition 1. *Let $p \in \mathbb{R}$ with $1 \leq p \leq +\infty$. The set $L^p(\Omega)$ is a Banach space for the norm*

$$\|f\|_{L^p(\Omega)} = \begin{cases} \left(\int_\Omega |f(x)|^p \, dx \right)^{\frac{1}{p}} & if \quad p < +\infty, \\ \\ inf \left\{ C, |f(x)| \leq C \quad almost \quad everywhere \quad on \quad \Omega \right\}, if \quad p = +\infty \end{cases}$$

If $p = 2$, the space $L^2(\Omega)$ is a Hilbert space for the scalar product

$$(f, g)_{L^2(\Omega)} = \int_\Omega f(x) g(x) \, dx$$

Definition 4. (***Weak convergence***) Let X be a Banach space equipped with the norm $\|\cdot\|_X$. A sequence $\{x_n\}$ in X is said to ***converge weakly*** to $x \in X$ if and only if

$$\langle \varphi, x_n \rangle_{X',X} \longrightarrow \langle \varphi, x \rangle_{X',X}, \quad as \quad n \to \infty, \quad \forall \varphi \in X'$$

where X' is the set of all linear and continuous maps $\varphi : X \longrightarrow \mathbb{R}$ and is called the dual space of X. Furthermore, if $\varphi \in X'$, the image $\varphi(x) \in \mathbb{R}$ of $x \in X$ is denoted by $\langle \varphi, x \rangle_{X',X}$. The weak convergence is denoted by

$$x_n \rightharpoonup x \quad weakly \quad in \quad X$$

Definition 5. (***Strong convergence***) Let X be a Banach space equipped with the norm $\|\cdot\|_X$. A sequence $\{x_n\}$ in X is said to ***converge strongly*** to $x \in X$ if and only if

$$\|x_n - x\|_X \longrightarrow 0 \quad as \quad n \to \infty$$

Definition 6. Let $1 \leq p \leq +\infty$. The Sobolev space $W^{1,p}(\Omega)$ is defined by

$$W^{1,p}(\Omega) = \left\{ u | u \in L^p(\Omega), \frac{\partial u}{\partial x_i} \in L^p(\Omega), \quad i = 1, 2, \ldots, n \right\},$$

where the derivatives $\dfrac{\partial u}{\partial x_i}$ are weak derivatives and are taken in the sense of distributions.

Definition 7. For $p = 2$, we denote $W^{1,2}(\Omega) = H^1(\Omega)$, i.e.,

$$H^1(\Omega) = \left\{ u | u \in L^2(\Omega), \frac{\partial u}{\partial x_i} \in L^2(\Omega), \quad i = 1, 2, \ldots, n \right\}$$

Proposition 2. *The space $W^{1,p}(\Omega)$ is a Banach space for the norm*

$$\|u\|_{W^{1,p}(\Omega)} = \|u\|_{L^p(\Omega)} + \sum_{i=1}^{n} \left\| \frac{\partial u}{\partial x_i} \right\|_{L^p(\Omega)}$$

For $1 \leq p < +\infty$. This norm is equivalent to the following one

$$\|u\|_{W^{1,p}(\Omega)} = \left(\|u\|^p_{L^p(\Omega)} + \sum_{i=1}^{n} \left\| \frac{\partial u}{\partial x_i} \right\|^p_{L^p(\Omega)} \right)^{\frac{1}{p}}$$

Definition 8. Let $\alpha, \beta \in \mathbb{R}$, such that $0 < \alpha < \beta$. We denote by $\mathcal{M}(\alpha, \beta, \Omega)$ the set of the $n \times n$ matrices $\mathcal{A} = (a_{ij}(x))_{1 \leq i,j \leq n} \in (L^\infty(\Omega))^{n \times n}$ such that

$$(i) \quad \eta \mathcal{A} \eta^T \geq \alpha |\eta|^2$$

$$(ii) \quad |\mathcal{A}\eta| \leq \beta |\eta|$$

for any $\eta \in \mathbb{R}^n$ and almost everywhere on Ω. Condition (i) is equivalent to the classical uniform ellipticity condition given in Definition 2 for the operator L from Definition 1

$$L = -\sum_{i,j=1}^{n} \frac{\partial}{\partial x_i} \left(a_{ij}(x) \frac{\partial}{\partial x_j} \right)$$

If a matrix $\mathcal{A}$ satisfies the uniform ellipticity inequality, we will say that the matrix $\mathcal{A}$ is elliptic.

Definition 9. (***Well-posedness***) Let $\mathcal{P}$ be a boundary value problem and $\mathcal{U}$ and $\mathcal{F}$ be two Banach spaces. We say that $\mathcal{P}$ is well-posed with respect to $\mathcal{U}$ and $\mathcal{F}$ if
(1) for any element $f \in \mathcal{F}$ there exists a solution $u \in \mathcal{U}$ of $\mathcal{P}$,
(2) the solution is unique,
(3) the mapping $f \in \mathcal{F} \longmapsto u \in \mathcal{U}$ is continuous.

Definition 10. In this work we will refer to $Y = [0, L] \times [0, L] \times \ldots \times [0, L] \subset \mathbb{R}^n$ as ***the reference period***, where $L \in \mathbb{R}$ and $L > 0$. Let $f(x) : \mathbb{R}^n \longrightarrow \mathbb{R}$ be a function defined almost everywhere on $\mathbb{R}^n$. We will say that the function f is Y***- periodic*** if and only if

$$f(x + kL\mathbf{e_i}) = f(x) \quad a.e. \quad on \quad \mathbb{R}^n, \quad \forall k \in \mathbb{Z}, \quad \forall i \in \{1, 2, \ldots, n\}$$

where $\{\mathbf{e_1}, \mathbf{e_2}, \ldots, \mathbf{e_n}\}$ is the canonical basis of $\mathbb{R}^n$.

Definition 11. Let $C^\infty_{per}(Y)$ be the subset of $C^\infty(\mathbb{R}^n)$ of Y-periodic functions. We denote by $H^1_{per}(Y)$ the closure of $C^\infty_{per}(Y)$ for the H^1-norm.

Definition 12. We denote

$$W_{per}(Y) = \left\{ v \in H^1_{per}(Y) : \int_Y v(x)\, dx = 0 \right\}$$

Definition 13. Let Ω be a bounded open set in $\mathbb{R}^n$ and f a function in $L^1(\Omega)$. The ***mean value*** of f over Ω is the real number $\mathcal{M}_\Omega(f)$ and is given by

$$\mathcal{M}_\Omega(f) = \frac{1}{|\Omega|} \int_\Omega f(y)\, dy$$

3.4 Application of the method to a model problem

We want to investigate the asymptotic behaviour of the following family of linear elliptic partial differential equations with periodically oscillating coefficient $a_\varepsilon(x)$ when $\varepsilon \to 0$

$$-\nabla \cdot (a_\varepsilon(x) \nabla u_\varepsilon) = f(x), \quad x \in \Omega \subset \mathbb{R}^2 \tag{3.4.1a}$$

$$u_\varepsilon(x) = 0, \quad x \in \partial\Omega \tag{3.4.1b}$$

where the period of the oscillations of $a_\varepsilon(x)$ is εL, i.e.,

$$a_\varepsilon(x + k(\varepsilon L)\mathbf{e_i}) = a_\varepsilon(x), \quad \forall k \in \mathbb{Z}, \quad i = \{1, 2\} \tag{3.4.2}$$

with $\mathbf{e_i}$ being the canonical basis of $\mathbb{R}^2$. We assume that $f(x)$ is a given function such that $f \in H^{-1}(\Omega)$. We define the matrix $\mathcal{A}_\varepsilon = \left(a^\varepsilon_{ij}(x)\right)^2_{i,j=1}$ by

$$\mathcal{A}_\varepsilon = \begin{pmatrix} a_\varepsilon(x) & 0 \\ 0 & a_\varepsilon(x) \end{pmatrix} \tag{3.4.3}$$

with $a_{11}^{\varepsilon} = a_{22}^{\varepsilon} = a_{\varepsilon}(x)$ and $a_{12}^{\varepsilon} = a_{21}^{\varepsilon} = 0$. Let the matrix $\mathcal{A}_{\varepsilon}$ satisfies the conditions from Definition 8, i.e., $\mathcal{A}_{\varepsilon} \in M(\alpha, \beta, \Omega)$. Therefore conditions (i) and (ii) from Definition 8 are equivalent to

$$0 < \alpha \leq a_{\varepsilon}(x) \leq \beta, \quad \forall x \in \Omega \tag{3.4.4}$$

We assume that we have a regular periodic microstructure of the domain Ω with $\varepsilon L = l << L$ being the size of the periodicities. The medium varies rapidly on the small scale l and slowly on the large scale L. Here x is the so called global (slow) variable and $y = \dfrac{x}{\varepsilon}$ is its respective local (fast) variable. Let us denote with Y_i^{ε} the microscopic periodicity cells. Then after the change of variables $y = \dfrac{x}{\varepsilon}$, each microscopic periodicity cell Y_i^{ε} with characteristic length l transforms into the upscaled periodicity cell Y_i with characteristic length L. Then we translate each cell Y_i into the reference periodicty cell $Y = [0, L] \times [0, L]$ via the translation τ_i:

$$\tau_i : y' = y + \xi_i \tag{3.4.5}$$

where for fixed i the vector ξ_i is a constant, fixed one $\forall y \in Y_i$. It is clear that the characteristic length of the reference periodicity cell Y is also L.
From now on, unless specified otherwise, when we write the change of variables $y = \dfrac{x}{\varepsilon}$ we will mean both scaling and translation to the reference period, without explicitly writing or mentioning the translation.
According to Definition 10, we have that $a_{\varepsilon}(x) = a\left(\dfrac{x}{\varepsilon}\right) = a(y)$ is Y-periodic function in y.
We look for the solution of (3.4.1) in the form of the following two-scale asymptotic expansion:

$$u_{\varepsilon}(x) = u_0\left(x, \frac{x}{\varepsilon}\right) + \varepsilon u_1\left(x, \frac{x}{\varepsilon}\right) + \varepsilon^2 u_2\left(x, \frac{x}{\varepsilon}\right) + O(\varepsilon^3) \tag{3.4.6}$$

which is equivalent to

$$u_{\varepsilon}(x) = u_0\left(x, y\right) + \varepsilon u_1\left(x, y\right) + \varepsilon^2 u_2\left(x, y\right) + O(\varepsilon^3) \tag{3.4.7}$$

where all the terms u_0, u_1 and u_2 are Y-periodic functions in the y variable. The leading term u_0 accounts for the averaged macroscopic behaviour of the solution u_{ε}, whereas the first and second terms - εu_1 and $\varepsilon^2 u_2$ account for the periodic microscale oscillations in the solution. We want the two-scale asymptotic expansipon of $u_{\varepsilon}(x)$ to be a solution of the partial differential equation (3.4.1a). This means that if we plug (3.4.6) in (3.4.1a) we will obtain an equality which must be satisfied for all $x \in \Omega$. Thus, after substituting u_{ε} with its asymptotic expansion and after taking into account that the differentiation operator becomes

$$\nabla = \nabla_x + \frac{1}{\varepsilon}\nabla_y, \tag{3.4.8}$$

we obtain

$$-\left(\nabla_x+\frac{1}{\varepsilon}\nabla_y\right)\cdot\left(a(y)\left(\nabla_x+\frac{1}{\varepsilon}\nabla_y\right)\left(u_0(x,y)+\varepsilon u_1(x,y)+\varepsilon^2u_2(x,y)\right)\right)=f(x)$$

$$\Longleftrightarrow$$

$$-\left(\nabla_x+\frac{1}{\varepsilon}\nabla_y\right)\cdot\left(a(y)\left(\frac{1}{\varepsilon}\nabla_yu_0+\nabla_xu_0+\nabla_yu_1+\varepsilon\nabla_xu_1+\varepsilon\nabla_yu_2+\varepsilon^2\nabla_xu_2\right)\right)=f(x) \tag{3.4.9}$$

which is equivalent to

$$\begin{aligned}&-\frac{1}{\varepsilon^2}\nabla_y\cdot(a(y)\nabla_yu_0)-\frac{1}{\varepsilon}\nabla_y\cdot(a(y)\nabla_xu_0+a(y)\nabla_yu_1)-\\&-\nabla_y\cdot(a(y)\nabla_xu_1+a(y)\nabla_yu_2)-\varepsilon\nabla_y\cdot(a(y)\nabla_xu_2)-\frac{1}{\varepsilon}\nabla_x\cdot(a(y)\nabla_yu_0)-\\&-\nabla_x\cdot(a(y)\nabla_xu_0+a(y)\nabla_yu_1)-\varepsilon\nabla_x\cdot(a(y)\nabla_xu_1+a(y)\nabla_yu_2)+O(\varepsilon^2)=f(x)\end{aligned} \tag{3.4.10}$$

Finally we obtain

$$\begin{aligned}&-\frac{1}{\varepsilon^2}\nabla_y\cdot(a(y)\nabla_yu_0)-\\&-\frac{1}{\varepsilon}\left[\nabla_y\cdot(a(y)\nabla_xu_0+a(y)\nabla_yu_1)+\nabla_x\cdot(a(y)\nabla_yu_0)\right]-\\&-\varepsilon^0\left[\nabla_y\cdot(a(y)\nabla_xu_1+a(y)\nabla_yu_2)+\nabla_x\cdot(a(y)\nabla_xu_0+a(y)\nabla_yu_1)\right]+\\&+O(\varepsilon)=f(x)\end{aligned} \tag{3.4.11}$$

Since the latter equality must be true for each $x\in\Omega$, we equal like powers of ε. This way we obtain the following equations for $u_0(x,y)$, $u_1(x,y)$ and $u_2(x,y)$, respectively:

$$\varepsilon^{-2}:-\nabla_y\cdot(a(y)\nabla_yu_0)=0 \tag{3.4.12a}$$

$$\varepsilon^{-1}:-\left[\nabla_y\cdot(a(y)\nabla_xu_0+a(y)\nabla_yu_1)+\nabla_x\cdot(a(y)\nabla_yu_0)\right]=0 \tag{3.4.12b}$$

$$\varepsilon^{0}:-\left[\nabla_y\cdot(a(y)\nabla_xu_1+a(y)\nabla_yu_2)+\nabla_x\cdot(a(y)\nabla_xu_0+a(y)\nabla_yu_1)\right]=f(x) \tag{3.4.12c}$$

3.4.1 Order ε^{-2}

We arrive at the following equation for the zero order term $u_0(x,y)$ of the asymptotic expansion (3.4.6):

$$-\nabla_y\cdot(a(y)\nabla_yu_0)=0,\quad (x,y)\in[\Omega\times Y] \tag{3.4.13}$$

We want to solve equation (3.4.13) with respect to the y variable, assuming that $x \in \Omega$ is a given parameter. In order to obtain the weak form of the considered problem, we first have to multiply equation (3.4.13) by a test function and then to integrate over the solution domain Y

$$-\int_Y \nabla_y \cdot (a(y)\nabla_y u_0)\, v(y)\, dy = 0 \tag{3.4.14}$$

which is equivalent to

$$\int_Y \nabla_y \cdot (v(y)a(y)\nabla_y u_0)\; dy - \int_Y a(y)\nabla_y u_0 \cdot \nabla_y v\, dy = 0, \quad \forall v \in H^1_{per}(Y) \tag{3.4.15}$$

Now we apply the divergence theorem and we obtain

$$\underbrace{\int_{\partial Y} v(y)a(y)\nabla_y u_0 \cdot \mathbf{n}\, ds}_{=0} - \int_Y a(y)\nabla_y u_0 \cdot \nabla_y v\, dy = 0, \quad \forall v(y) \in H^1_{per}(Y) \Longleftrightarrow$$

$$-\int_Y a(y)\nabla_y u_0 \cdot \nabla_y v\, dy = 0, \quad \forall v(y) \in H^1_{per}(Y) \tag{3.4.16}$$

In the latter equality we have that $\int_{\partial Y} v(y)a(y)\nabla_y u_0 \cdot \mathbf{n}\, ds = 0$ due to symmetry (we assume that the reference periodicity cell is symmetric as shown in Figure 3.3) and periodicity (we have periodic microstructure, i.e., all the functions $v(y)$, $a(y)$ and $u_0(x, y)$ are Y-periodic with respect to the y variable which means that these functions take equal values on the opposite sides (faces) of the periodicity cell Y and the outward unit normal vectors $\mathbf{n}$ are collinear but pointing in opposite directions). Finally, the weak formulation of equation (3.4.13) reads: find $u_0 \in H^1_{per}(Y)$ such that the following integral equality is valid for all functions $v \in H^1_{per}(Y)$

$$\int_Y a(y)\nabla_y u_0 \cdot \nabla_y v\, dy = 0 \tag{3.4.17}$$

Since (3.4.17) is true for each Y-periodic test function in $H^1_{per}(Y)$, we can take as a test function $v(y) = u_0(x, y)$ (assuming x is a given parameter) and thus we obtain

$$\int_Y a(y)\nabla_y u_0 \cdot \nabla_y u_0\, dy = 0 \Longleftrightarrow \tag{3.4.18}$$

$$0 \leq \int_Y a(y) \sum_{i=1}^{2} \left(\frac{\partial u_0}{\partial y_i}\right)^2 dy = 0 \tag{3.4.19}$$

We have that $a(y) = a_\varepsilon(x)$ and due to (3.4.4) we obtain that

$$0 < \alpha \leq a(y) \leq \beta, \quad \forall y \in Y \tag{3.4.20}$$

which means that $a(y) > 0, \forall y \in Y$. Therefore (3.4.19) is true if and only if

$$\left(\frac{\partial u_0}{\partial y_i}\right)^2 = 0, \quad \forall i = 1,2 \Longleftrightarrow \frac{\partial u_0}{\partial y_i} = 0, \quad \forall i = 1,2 \Longleftrightarrow u_0 = u_0(x) \tag{3.4.21}$$

Thus we obtained that u_0 is a function of x only and does not depend on the y variable.

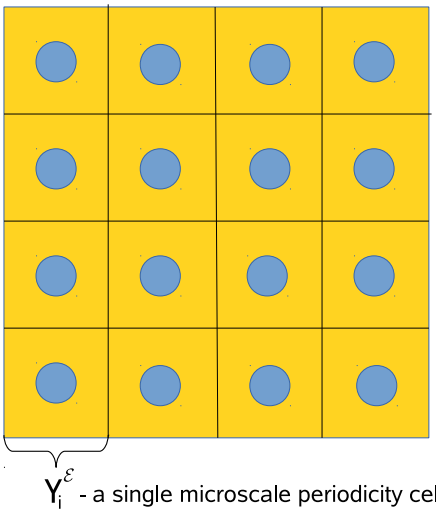

Figure 3.3: Periodic media

3.4.2 Order ε^{-1}: Cell problems

We have the following equation for the function $u_1(x, y)$:

$$-\left[\nabla_y \cdot (a(y)\nabla_x u_0 + a(y)\nabla_y u_1) + \nabla_x \cdot (a(y)\nabla_y u_0)\right] = 0, \quad (x, y) \in [\Omega \times Y] \tag{3.4.22}$$

where $\nabla_y u_0(x) = 0$ and therefore the latter equation becomes

$$\nabla_y \cdot (a(y)\nabla_x u_0 + a(y)\nabla_y u_1) = 0 \tag{3.4.23}$$

which is equivalent to

$$\nabla_y \cdot (a(y)\nabla_y u_1) = -\nabla_y \cdot (a(y)\nabla_x u_0), \quad (x, y) \in [\Omega \times Y] \tag{3.4.24}$$

Now we seek the solution u_1 in the following scale-separable form

$$u_1(x, y) = \nabla_x u_0 \cdot \varphi(y), \tag{3.4.25}$$

where $\varphi(y) = (\varphi_1(y), \varphi_2(y))$ is a vector function. The functions $\varphi_i(y) : \mathbb{R}^2 \longrightarrow \mathbb{R}$ are Y-periodic since the function $u_1(x, y)$ is an Y-periodic function. The representation (3.4.25) is equivalent to

$$u_1(x, y) = \sum_{i=1}^{2} \frac{\partial u_0}{\partial x_i}(x)\varphi_i(y) \tag{3.4.26}$$

Now we substitute u_1 with its equal form (3.4.26) in the partial differential equation (3.4.24) and we get

$$\nabla_y \cdot \left(a(y) \sum_{i=1}^{2} \frac{\partial u_0}{\partial x_i}(x) \nabla_y \varphi_i \right) = -\nabla_y \cdot (a(y) \nabla_x u_0) \Longleftrightarrow \tag{3.4.27}$$

(3.4.28)

$$\nabla_y \cdot \left(a(y) \sum_{i=1}^{2} \frac{\partial u_0}{\partial x_i}(x) \nabla_y \varphi_i \right) = -\nabla_y \cdot \left(a(y) \sum_{i=1}^{2} \frac{\partial u_0}{\partial x_i} \vec{\mathbf{e_i}} \right) \tag{3.4.29}$$

where $\vec{\mathbf{e_1}} = (1,0)$ and $\vec{\mathbf{e_2}} = (0,1)$. The latter is equvalent to

$$\sum_{i=1}^{2} \frac{\partial u_0}{\partial x_i}(x) \left(\nabla_y \cdot (a(y) \nabla_y \varphi_i) \right) + \sum_{i=1}^{2} \frac{\partial u_0}{\partial x_i}(x) \left(\nabla_y \cdot (a(y) \vec{\mathbf{e_i}}) \right) = 0 \Longleftrightarrow \tag{3.4.30}$$

$$\sum_{i=1}^{2} \frac{\partial u_0}{\partial x_i}(x) \left[\nabla_y \cdot (a(y) \nabla_y \varphi_i) + \nabla_y \cdot (a(y) \vec{\mathbf{e_i}}) \right] = 0 \tag{3.4.31}$$

Since we want (3.4.31) to be satisfied for all $x \in \Omega$, this will be true if and only if each of the terms multiplied by $\dfrac{\partial u_0}{\partial x_i}(x)$ in the sum in the left-hand side of (3.4.31) is equal to zero, i.e.,

$$\nabla_y \cdot (a(y) \nabla_y \varphi_i) + \nabla_y \cdot (a(y) \vec{\mathbf{e_i}}) = 0 \tag{3.4.32}$$

for $i = 1, 2$. This is equivalent to

$$\nabla_y \cdot (a(y) \nabla_y \varphi_i) = -\frac{\partial a}{\partial y_i}(y) \tag{3.4.33}$$

for $i = 1, 2$.
Thus, we obtained that $u_1(x, y) = \nabla_x u_0 \cdot \varphi$ is a solution of (3.4.24) if and only if the Y-periodic functions $\varphi_i(y)$, $i = 1, 2$, satisfy the following ***auxiliary cell problems***

$$-\nabla_y \cdot (a(y) \nabla_y \varphi_i) = \frac{\partial a}{\partial y_i}(y), \quad y \in Y \tag{3.4.34}$$

We apply periodic boundary conditions on ∂Y (see Figure 3.4)

$$\varphi_i(y)|_{AD} = \varphi_i(y)|_{BC}$$
$$\varphi_i(y)|_{AB} = \varphi_i(y)|_{CD}$$

and in order to fix the solution we require that

$$\int_Y \varphi_i(y)\, dy = 0$$

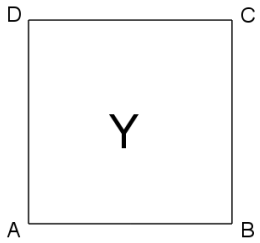

Figure 3.4: Solution domain of the auxiliary cell problems in 2D

3.4.3 Order ε^0: Homogenized problem

From (3.4.12c) we obtain the following equation for the function $u_2(x, y)$, from which we will derive the homogenized equation for $u_0(x)$:

$$-\nabla_y \cdot (a(y)\nabla_x u_1 + a(y)\nabla_y u_2) - \nabla_x \cdot (a(y)\nabla_x u_0 + a(y)\nabla_y u_1) = f(x) \tag{3.4.35}$$

for $(x, y) \in [\Omega \times Y]$. Now we average the latter equation over the reference periodicity cell, i.e., we integrate both sides of the equation over the domain of the reference period Y and we divide by the measure of Y

$$\begin{aligned}
&-\frac{1}{|Y|}\int_Y \nabla_y \cdot (a(y)\nabla_x u_1 + a(y)\nabla_y u_2)\, dy - \\
&-\frac{1}{|Y|}\int_Y \nabla_x \cdot (a(y)\nabla_x u_0 + a(y)\nabla_y u_1)\, dy = f(x) \Longleftrightarrow \\
&\\
&-\frac{1}{|Y|}\underbrace{\int_{\partial Y} (a(y)\nabla_x u_1 + a(y)\nabla_y u_2) \cdot \mathbf{n}\, ds}_{=0} - \\
&-\frac{1}{|Y|}\int_Y \nabla_x \cdot (a(y)\nabla_x u_0 + a(y)\nabla_y u_1)\, dy = f(x) \Longleftrightarrow
\end{aligned}$$

where the integral over ∂Y is zero due to symmetry and periodicity and $\frac{1}{|Y|}\int_Y f(x)\, dy = \frac{f(x)}{|Y|}\int_Y 1\, dy = \frac{f(x)}{|Y|}|Y| = f(x)$. Thus we get

$$-\frac{1}{|Y|}\int_Y \nabla_x \cdot (a(y)\nabla_x u_0 + a(y)\nabla_y u_1)\, dy = f(x) \tag{3.4.36}$$

We substitute $u_1(x,y) = \sum_{i=1}^{2} \frac{\partial u_0}{\partial x_i}(x)\varphi_i(y)$ and $\nabla_x u_0 = \sum_{i=1}^{2} \frac{\partial u_0}{\partial x_i}\vec{\mathbf{e}}_i$ in (3.4.36), and we obtain

$$-\frac{1}{|Y|}\int\limits_Y \nabla_x \cdot \left(a(y)\nabla_x u_0 + a(y)\sum_{i=1}^{2} \frac{\partial u_0}{\partial x_i}(x)\nabla_y \varphi_i \right) dy = f(x) \Longleftrightarrow$$

$$-\frac{1}{|Y|}\nabla_x \cdot \left(\int\limits_Y \left(a(y)\nabla_x u_0 + a(y)\sum_{i=1}^{2} \frac{\partial u_0}{\partial x_i}(x)\nabla_y \varphi_i \right) dy \right) = f(x) \Longleftrightarrow$$

$$-\frac{1}{|Y|}\nabla_x \cdot \left(\left(\int\limits_Y a(y)\, dy \right) \nabla_x u_0 + \sum_{i=1}^{2} \frac{\partial u_0}{\partial x_i}(x) \left(\int\limits_Y a(y)\nabla_y \varphi_i \, dy \right) \right) = f(x) \Longleftrightarrow$$

$$-\frac{1}{|Y|}\nabla_x \cdot \left(\left(\int\limits_Y a(y)\, dy \right) \sum_{i=1}^{2} \frac{\partial u_0}{\partial x_i}\vec{\mathbf{e}}_i + \sum_{i=1}^{2} \frac{\partial u_0}{\partial x_i}(x) \left(\int\limits_Y a(y)\nabla_y \varphi_i \, dy \right) \right) = f(x) \Longleftrightarrow$$

$$-\frac{1}{|Y|}\nabla_x \cdot \left(\sum_{i=1}^{2} \frac{\partial u_0}{\partial x_i} \left(\int\limits_Y a(y)\, dy \right) \vec{\mathbf{e}}_i + \sum_{i=1}^{2} \frac{\partial u_0}{\partial x_i} \left(\int\limits_Y a(y)\nabla_y \varphi_i \, dy \right) \right) = f(x) \Longleftrightarrow$$

$$-\frac{1}{|Y|}\nabla_x \cdot \left(\sum_{i=1}^{2} \frac{\partial u_0}{\partial x_i} \left(\int\limits_Y a(y)\vec{\mathbf{e}}_i \, dy + \int\limits_Y a(y)\nabla_y \varphi_i \, dy \right) \right) = f(x) \Longleftrightarrow$$

$$-\nabla_x \cdot \left(\sum_{i=1}^{2} \frac{\partial u_0}{\partial x_i} \left(\frac{1}{|Y|}\int\limits_Y a(y) \left(\vec{\mathbf{e}}_i + \nabla_y \varphi_i \right) dy \right) \right) = f(x) \tag{3.4.37}$$

where

$$\vec{\mathbf{e}}_1 + \nabla_y \varphi_1 = \left(1 + \frac{\partial \varphi_1}{\partial y_1}, \frac{\partial \varphi_1}{\partial y_2} \right)$$
$$\vec{\mathbf{e}}_2 + \nabla_y \varphi_2 = \left(\frac{\partial \varphi_2}{\partial y_1}, 1 + \frac{\partial \varphi_2}{\partial y_2} \right)$$

and if $\nu(y) = (\nu_1(y), \nu_2(y), \ldots, \nu_n(y)) \in \mathbb{R}^n$ is a vector, then

$$\int\limits_Y \nu(y)\, dy = \left(\int\limits_Y \nu_1(y)\, dy, \int\limits_Y \nu_2(y)\, dy, \ldots, \int\limits_Y \nu_n(y)\, dy \right)$$

Finally, taking into account that

$$\sum_{i=1}^{2} \frac{\partial u_0}{\partial x_i} \left(\frac{1}{|Y|} \int\limits_Y a(y) \left(\vec{\mathbf{e}}_i + \nabla_y \varphi_i \right) \, dy \right) =$$

$$= \begin{pmatrix} \frac{1}{|Y|} \int\limits_Y a(y) \left(1 + \frac{\partial \varphi_1}{\partial y_1} \right) dy & \frac{1}{|Y|} \int\limits_Y a(y) \frac{\partial \varphi_2}{\partial y_1} \, dy \\ \\ \frac{1}{|Y|} \int\limits_Y a(y) \frac{\partial \varphi_1}{\partial y_2} \, dy & \frac{1}{|Y|} \int\limits_Y a(y) \left(1 + \frac{\partial \varphi_2}{\partial y_2} \right) dy \end{pmatrix} \begin{pmatrix} \frac{\partial u_0}{\partial x_1} \\ \\ \frac{\partial u_0}{\partial x_2} \end{pmatrix} \tag{3.4.38}$$

we obtain the following homogenized problem

$$-\nabla_x \cdot \left(a^H \nabla_x u_0 \right) = f(x), \quad x \in \Omega, \tag{3.4.39a}$$

$$u_0(x) = 0, \quad x \in \partial\Omega \tag{3.4.39b}$$

where the homogenized effective coefficient a^H is the following tensor

$$\left(a^H \right)_{i,j=1}^{2} = \frac{1}{|Y|} \int\limits_Y a(y) \left(\delta_{ij} + \frac{\partial \varphi_j}{\partial y_i}(y) \right) dy \tag{3.4.40}$$

and its elements are constants. We denote

$$\mathcal{A}^H = \begin{pmatrix} a_{11}^H & a_{12}^H \\ \\ a_{21}^H & a_{22}^H \end{pmatrix} \tag{3.4.41}$$

The effective tensor a^H describes the macroscopic properties of the underlying periodic medium. Solving numerically the microscale problem (3.4.1) for small ε is computationally expensive because it requires very high resolution and consequently a big number of degrees of freedom. Solving the homogenized problem (3.4.39) and the cell problem (3.4.34), on the other hand, is a standard problem and demands significantly less degrees of freedom.

3.5 Main convergence result

Now we consider a generalized version of the model problem (3.4.1), namely we have the following boundary value problem

$$-\nabla \cdot \left(\mathcal{A}_\varepsilon(x) \nabla u_\varepsilon \right) = f(x), \quad x \in \Omega \subset \mathbb{R}^n \tag{3.5.1a}$$

$$u_\varepsilon(x) = 0, \quad x \in \partial\Omega \tag{3.5.1b}$$

where the coefficient matrix $\mathcal{A}_\varepsilon$ is given by

$$\mathcal{A}_\varepsilon(x) = \left(a_{ij}^\varepsilon(x) \right)_{1 \le i,j \le n} \in M(\alpha, \beta, \Omega) \tag{3.5.2}$$

with

$$\mathcal{A}_\varepsilon(x) = \mathcal{A}\left(\frac{x}{\varepsilon}\right) = \mathcal{A}(y) = (a_{ij}(y))_{1\leq i,j\leq n} \in M(\alpha,\beta,Y) \tag{3.5.3}$$

and

$$a_{ij}^\varepsilon(x) = a_{ij}\left(\frac{x}{\varepsilon}\right) = a_{ij}(y) \tag{3.5.4}$$

where $a_{ij}(y)$ (for $i,j = 1,2,\ldots,n$) are Y-periodic functions. Furthermore, $\alpha,\beta \in \mathbb{R}$, such that $0 < \alpha < \beta < \infty$, and $M(\alpha,\beta,\Omega)$ (respectively $M(\alpha,\beta,Y)$) are given by Definition 8. We assume that problem (3.5.1) is well-posed according to Definition 9. Then, the respective limit problem is

$$-\nabla_x \cdot \left(\mathcal{A}^H \nabla_x u_0\right) = f(x), \quad x \in \Omega \subset \mathbb{R}^n, \tag{3.5.5a}$$

$$u_0(x) = 0, \quad x \in \partial\Omega \tag{3.5.5b}$$

where the homogenized effective tensor $\mathcal{A}^H$ is given by

$$\left(a^H\right)_{i,j=1}^n = \frac{1}{|Y|}\int_Y a(y)\left(\delta_{ij} + \frac{\partial\varphi_j}{\partial y_i}(y)\right)dy \tag{3.5.6}$$

where the Y-periodic functions $\varphi_i(y)$, $i = 1,2,\ldots,n$, are solution to the following cell problems

$$-\nabla_y \cdot (a(y)\nabla_y\varphi_i) = \frac{\partial a}{\partial y_i}(y), \quad y \in Y \tag{3.5.7}$$

and $\mathcal{M}_Y(\varphi_i) = 0$. Then, the following Theorems 1 and 2, which are taken from [17], give the main convergence results in the asymptotic homogenization theory:

Theorem 1. *Let $f \in H^{-1}(\Omega)$ and u_ε be the solution of problem (3.5.1) with $\mathcal{A}_\varepsilon$ defined by (3.5.2)-(3.5.4). Then,*

$$(i) \quad u_\varepsilon \rightharpoonup u_0 \quad \textit{weakly} \quad \textit{in} \quad H_0^1(\Omega)$$

$$(ii) \quad \mathcal{A}_\varepsilon \nabla u_\varepsilon \rightharpoonup \mathcal{A}^H \nabla u^0 \quad \textit{weakly} \quad \textit{in} \quad \left(L^2(\Omega)\right)^n$$

where u^0 is the unique solution in $H_0^1(\Omega)$ of the homogenized problem (3.5.5). The matrix $\mathcal{A}^H$ given by (3.5.6) is constant and elliptic.

Theorem 2. *Let $f \in H^{-1}(\Omega)$ and u_ε be the solution of (3.5.1) with $\mathcal{A}_\varepsilon$ defined by (3.5.2)-(3.5.4). Then, u_ε admits the following asymptotic expansion*

$$u_\varepsilon = u_0 + \varepsilon\sum_{k=1}^n \varphi_k\left(\frac{x}{\varepsilon}\right)\frac{\partial u_0}{\partial x_k} + \varepsilon^2\sum_{k,l=1}^n \zeta^{kl}\left(\frac{x}{\varepsilon}\right)\frac{\partial^2 u_0}{\partial x_k \partial x_l} + \ldots$$

where u_0 is solution of (3.5.5), *$\varphi_k \in W_{per}(Y)$ is the solution of the auxiliary cell problem* (3.5.7) *and ζ^{kl} by*

$$\left|\begin{array}{l} -\nabla\cdot\left(a(y)\nabla\zeta^{kl}\right) = -a_{kl}^H - \displaystyle\sum_{i,j=1}^{n}\frac{\partial(a_{ij}\delta_{ki}\varphi_l)}{\partial y_i} - \sum_{j=1}^{n} a_{kj}\frac{\partial(\varphi_l - y_l)}{\partial y_j} \quad in \quad Y, \\ \\ \zeta^{kl}(y) \quad is \quad Y-periodic, \\ \\ \displaystyle\int_Y \zeta^{kl}(y)\,dy = 0 \end{array}\right.$$

Moreover, if $f \in C^\infty(\bar{\Omega})$, $\partial\Omega$ is of class C^∞ and, furthermore, $\varphi_k, \zeta_{kl} \in W^{1,\infty}(Y)$, $\forall k,l = 1,\ldots,n$, then there exists a constant C independent of ε, such that

$$\left\| u_\varepsilon - \left(u_0 + \varepsilon\sum_{k=1}^{n}\varphi_k\left(\frac{x}{\varepsilon}\right)\frac{\partial u_0}{\partial x_k} + \varepsilon^2\sum_{k,l=1}^{n}\zeta^{kl}\left(\frac{x}{\varepsilon}\right)\frac{\partial^2 u_0}{\partial x_k\partial x_l}\right)\right\|_{H^1(\Omega)} \le C\sqrt{\varepsilon}$$

Remark: In the latter Theorem 2 the error estimate can be written also as

$$\left\| u_\varepsilon - \left(u_0 + \varepsilon u_1 + \varepsilon^2 u_2\right)\right\|_{H^1(\Omega)} \le C\sqrt{\varepsilon}$$

where $u_1(x,y) = \displaystyle\sum_{k=1}^{n}\varphi_k(y)\frac{\partial u_0}{\partial x_k}(x)$ and $u_2(x,y) = \displaystyle\sum_{k,l=1}^{n}\zeta^{kl}(y)\frac{\partial^2 u_0}{\partial x_k\partial x_l}(x)$.
The following theorem is taken from [58] and it gives a weak convergence result in H_0^1 as well as strong convergence in L^2.

Theorem 3. *Let u_ε be the weak solution of* (3.5.1) *with $f = f(x) \in L^2(\Omega)$, $\Omega \in \mathbb{R}^n$ bounded and $\mathcal{A}_\varepsilon$ defined by* (3.5.2)-(3.5.4). *Furthermore, let u_0 be the weak solution of the homogenized problem* (3.5.5) *with $\mathcal{A}^H$ given by* (3.5.6). *Then*

$$u_\varepsilon \rightharpoonup u_0 \quad weakly \quad in \quad H_0^1(\Omega) \tag{3.5.8}$$

and

$$\|u_\varepsilon - u_0\|_{L^2(\Omega)} \longrightarrow 0, \quad when \quad \varepsilon \to 0 \tag{3.5.9}$$

3.6 Numerical example

We solve problem (3.4.1) and the respective homogenized problem (3.4.39) in the unit square domain $\Omega = [0,1]\times[0,1] \subset \mathbb{R}^2$. Then, it is clear that the characteristic length of the solution domain is $L = 1$ and the reference periodicity cell is $Y = [0,1]\times[0,1]$. We take $a_\varepsilon(x) = \cos(32\pi x_1)\cos(32\pi x_2) + 1.1 > 0$ and $f(x) = 16$. The coefficient $a_\varepsilon(x)$ is a periodic function because $\cos x$ is a periodic function with period 2π. The arguments of the function $a_\varepsilon(x)$ satisfy

$$\left|\begin{array}{l} 0 \le x_1 \le 1 \\ 0 \le x_2 \le 1 \end{array}\right. \Rightarrow \left|\begin{array}{l} 0 \le 32\pi x_1 \le 32\pi \\ 0 \le 32\pi x_2 \le 32\pi \end{array}\right.$$

and consequently we have 16 periods in each direction - x_1 and x_2. This means that the small parameter is $\varepsilon = \frac{1}{16}$ and is also equal to the characteristic length l of the period of the microstructure. Therefore the period of the coefficient $a_\varepsilon(x)$ is $\varepsilon L = \frac{1}{16}$. We have that

$$-1 \leq \cos(32\pi x_1)\cos(32\pi x_2) \leq 1 \Longleftrightarrow$$

$$0 < 0.1 \leq \cos(32\pi x_1)\cos(32\pi x_2) + 1.1 \leq 2.1 \Longleftrightarrow$$

$$0 < 0.1 \leq a_\varepsilon(x) \leq 2.1$$

which means that there exist $\alpha = 0.1 > 0$ and $\beta = 2.1 > 0$, such that $0 < \alpha < \beta$ and $0 < \alpha < a_\varepsilon(x) < \beta$, and hence the conditions from Definition 8 are satisfied and the differential operator in (3.4.1) is uniformly elliptic.
Here we will not discuss the numerical solving of the problem. We give a detailed description of the numerical methods that we use throughout this work in Chapter 5. We only note that we apply the Finite Element Method (see [9], [13], [60] for reference) in order to solve numerically the homogenized problem (3.4.39) as well as the microscale one – (3.4.1). In Table 3.6.1 and 3.6.2 with "Elements" we denote the number of finite elements that we use for the discretization of problems (3.4.39) and (3.4.1), and with "Nodes" – the number of degrees of freedom. For the subsequent simulations we use linear Lagrange triangular finite elements and we triangulate the solution domain with the program Triangle [67].
First, in Figure 3.5 we show the solutions of the auxiliary cell problems (3.4.34). In Figure 3.6, 3.7 and 3.8(a) is given the solution to the microscale problem (3.4.1) for different number of degrees of freedom. As we can see from Table 3.6.2 when we decrease four times the number of finite elements, which is equivalent to decreasing the diameter of the mesh twice, the solution converges to a limit one with maximum value of 1.217. On the other hand, by looking at the data in Table 3.6.1 and Table 3.6.2, we observe that in the homogenized problem only 2113 degrees of freedom are enough to achieve the same accuracy as that of the microscale solution in the case of 525313 nodes (see also Figure 3.8). Also, the computational time needed for solving the homogenized problem is 513 times less than the one needed for the microscale problem. We show the solution to the homogenized problem for different number of degrees of freedom in Figure 3.9 and Figure 3.8(b).

Table 3.6.1: Homogenized solution

Elements	Nodes	Maximum value of the solution	Run time [s]
256	145	1.224	0.221309
1024	545	1.218	0.233244
4096	2113	1.217	0.269582

Table 3.6.2: Microscale solution

Elements	Nodes	Maximum value of the solution	Run time [s]
4096	2113	1.072	0.070222
16384	8321	1.175	0.287618
65536	33025	1.207	1.55162
262144	131585	1.215	12.0219
1048576	525313	1.217	138.517

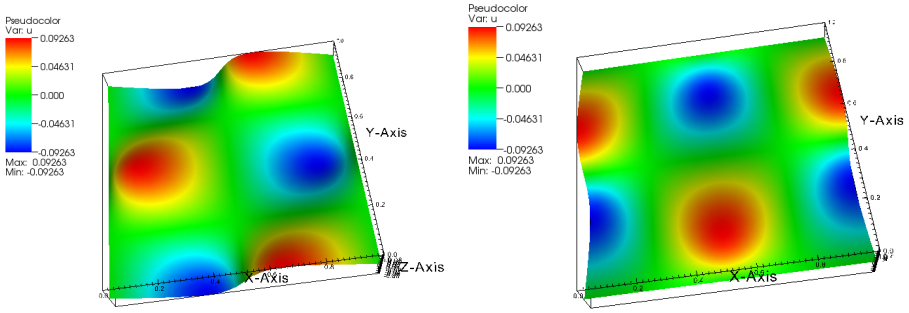

Figure 3.5: Solutions of the cell problems

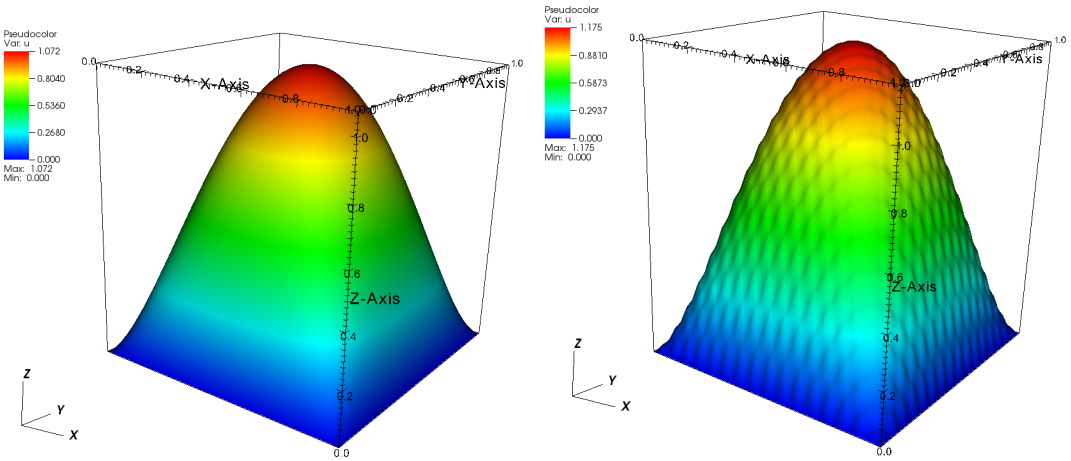

(a) 4096 finite elements (b) 16384 finite elements

Figure 3.6: Reference microscale solution

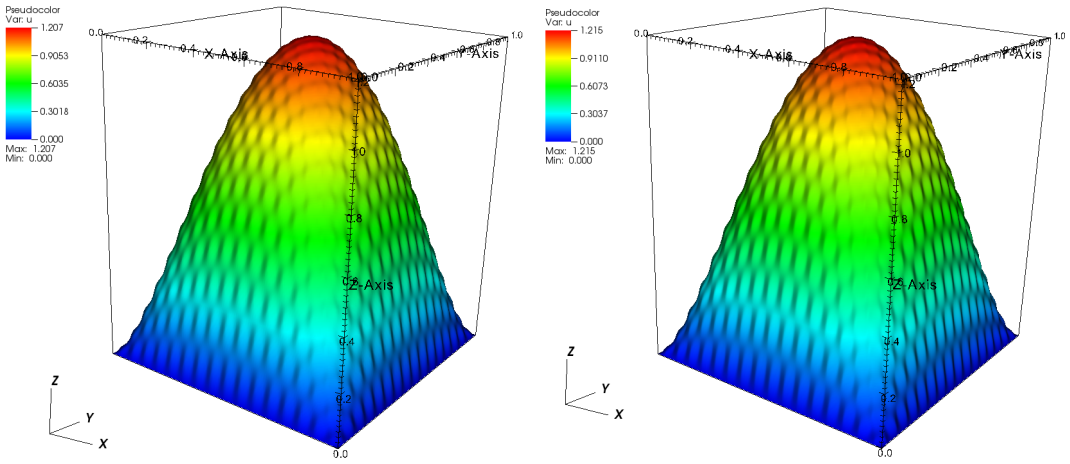

(a) 65536 finite elements (b) 262144 finite elements

Figure 3.7: Reference microscale solution

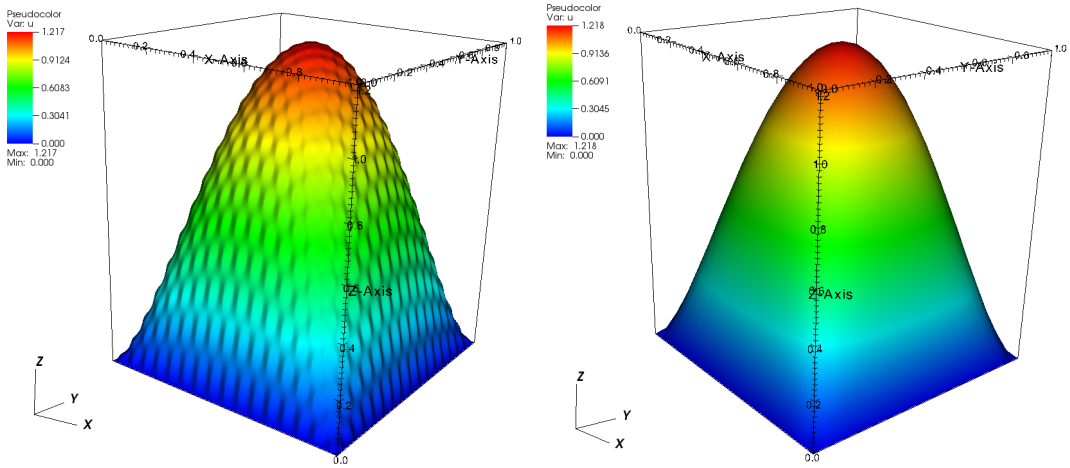

(a) Microscale solution with 1048576 finite elements and 525313 degrees of freedom (b) Homogenized solution with 1024 finite elements and 545 degrees of freedom

Figure 3.8: Reference microscale solution and homogenized solution

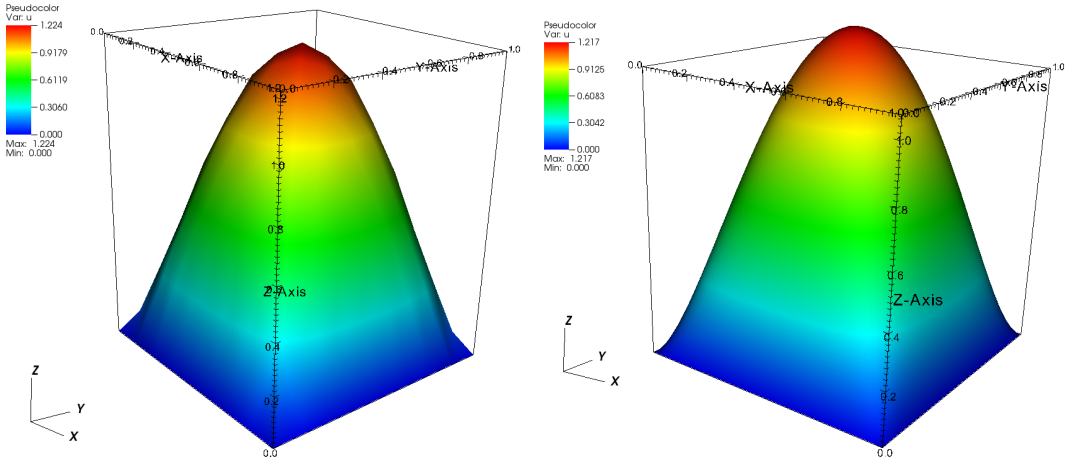

(a) 256 finite elements and 145 DOF (b) 4096 finite elements and 2113 DOF

Figure 3.9: Homogenized solution

Chapter 4

Asymptotic Homogenization Method in Perforated Domains

4.1 Motivation and introduction

The homogenization of the isothermal Lithium-ion battery model, which we consider in Chapter 5, is based on the asymptotic homogenization method in perforated domains due to the porous nature of the battery electrodes. Therefore, in this chapter we briefly introduce the homogenization method in domains with holes in the case of Neumann boundary conditions on the boundary of the perforations. This type of problems may arise in the mathematical modeling of different natural phenomena, such as flow in porous media ([5], [6]). Although in this chapter we do not present new results, it is essential for understanding the homogenization of the more complex Li-ion battery model from Chapter 2. A convergence of the microscale solution to the homogenized one as $\varepsilon \to 0$, in the case of nonzero Neumann data on the holes, is proved in [15] in the context of the periodic unfolding method [16]. In the case of nonisolated holes and zero Neumann on the perforations, a convergence result is proved in [4] and [2]. For isolated holes and zero Neumann, there is a convergence result available in [20]. A class of elliptic problems in perforated domains with nonlinear conditions on the boundary of the holes is considered in [19] and the periodic unfolding method for Robin problems in perforated domains is studied in [18].
For clarity and simplicity of the exposition we consider only two-dimensional boundary value problems. We start with the setup of the problem in Section 4.2. In Section 4.3 we discuss the important issue with the conservation of the total flux across the boundary of the holes and the consequent asymptotic scaling of the Neumann boundary condition on the perforations. The homogenization procedure is given in detail in Section 4.4, where we pay special attention to the homogenization of the Neumann boundary conditions on the perforations' boundary. In Section 4.5 we consider the specific case when the Neumann data on the holes is a periodically oscillating function. We conclude with numerical examples in Section 4.6. We show numerical results for different oscillating coefficients, as well as right-hand sides, Neumann boundary conditions on the holes, and various values of the small parameter ε.

4.2 Setup of the problem

We want to investigate the asymptotic behaviour of the following boundary value problem when $\varepsilon \to 0$

$$-\nabla \cdot (k_\varepsilon(x)\nabla u_\varepsilon) = f(x), \quad x \in \Omega_\varepsilon \subset \mathbb{R}^2, \tag{4.2.1a}$$

$$-k_\varepsilon(x)\nabla u_\varepsilon \cdot \mathbf{n} = \varepsilon g(x), \quad x \in \partial B_\varepsilon, \tag{4.2.1b}$$

$$u_\varepsilon(x) = 0, \quad x \in \partial\Omega \tag{4.2.1c}$$

where the domain $\Omega_\varepsilon = \Omega \backslash B_\varepsilon$ is perforated with $\Omega = [0,1] \times [0,1] \subset \mathbb{R}^2$ and B_ε being the domain of the perforations (see Figure 4.1(a)). It is then clear that $\Omega = \Omega_\varepsilon \cup B_\varepsilon$. We assume that the perforations are periodically arranged and that $\partial B_\varepsilon \cap \partial\Omega = \emptyset$, where $\partial\Omega$ is the boundary of Ω and ∂B_ε is the boundary of the perforations. With $\mathbf{n}$ we denote the unit normal vector to the perforations boundary ∂B_ε pointing in direction from Ω_ε into B_ε. We also have that $k_\varepsilon(x)$ is a periodically oscillating coefficient with period ε, where ε is the size of the periodic microstructures. Therefore if we denote the fast microscopic variable with $y = \dfrac{x}{\varepsilon}$, we have that

$$k_\varepsilon(x) = k\left(\frac{x}{\varepsilon}\right) = k(y) \tag{4.2.2}$$

where $k(y)$ is Y-periodic function.

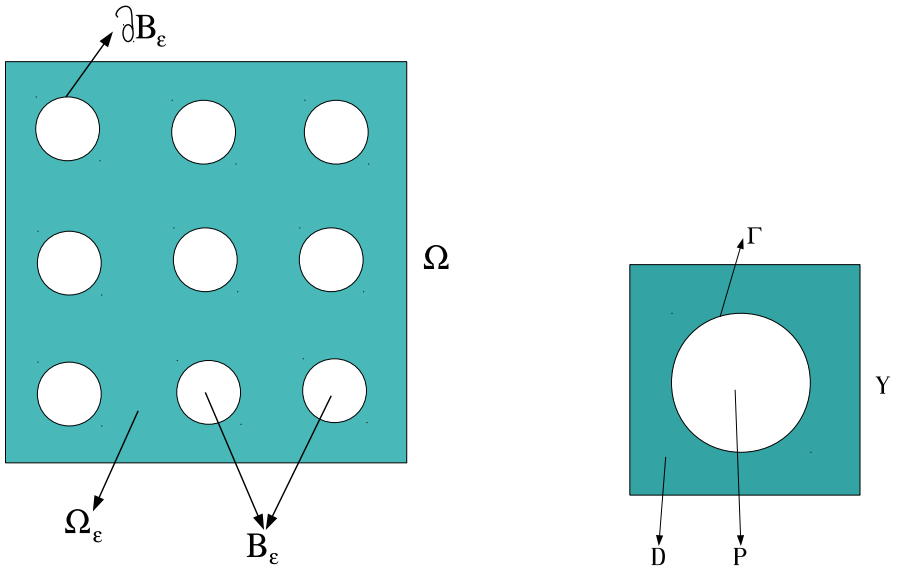

(a) Perforated solution domain

(b) Perforated reference periodicity cell

Figure 4.1: Solution domain and reference period

We denote with M the number of all microscale periodicity cells in the domain Ω_ε. Let Y_i^ε be a single microscale periodicity cell ($i = 1, 2, \ldots, M$), where $Y_i^\varepsilon = D_i^\varepsilon \cup P_i^\varepsilon \cup \Gamma_i^\varepsilon$ with D_i^ε

being the nonepmty domain in the microscopic periodicity cell, P_i^ε is the perforation and Γ_i^ε is the perforation boundary. It is clear that $\Omega = \bigcup_{i=1}^{M} Y_i^\varepsilon$. As before, we scale each microscale periodicity cell: $Y_i^\varepsilon \xrightarrow{y=\frac{x}{\varepsilon}} Y_i$ and then we translate it to the unit reference periodicity cell: $Y_i \xrightarrow{y'=y+\xi_i} Y$, where the reference period is $Y = [0,1] \times [0,1]$. We also recall that ξ_i is a constant vector for each upscaled cell Y_i (i.e. for each $y \in Y_i$, the translation vector ξ_i is fixed). Then we have that $Y = D \cup P \cup \Gamma$ where D is the nonepmty domain in the reference periodicity cell, P is the perforation and Γ is the perforation boundary (see Figure 4.1(b)).
For very small ε the number of perforations becomes very big, whereas the size of the perforations becomes very small compared to that of the whole computational domain Ω. This leads to an ill-conditioned problem and consequently expensive and complicated numerical simulations. Obviously ε approaching 0 is equivalent to the holes becoming infinitesimally small and consequently the domain Ω_ε converging to a homogeneous one. Therefore, our goal is to perform an asymptotic analysis for $\varepsilon \to 0$ and to derive a limit homogenized equation defined for all x in the unperforated domain Ω, which correctly captures the macroscopic behaviour of the solution u_ε to (4.2.1).

4.3 Conservation of the flux

The total flux across the whole perforations boundary is

$$
\begin{aligned}
I &= \int_{\partial B_\varepsilon} -k_\varepsilon(x)\nabla u_\varepsilon \cdot \mathbf{n}\, ds_x = \int_{\partial B_\varepsilon} \varepsilon g(x)\, ds_x = \\
&= \sum_{i=1}^{M} \int_{\Gamma_i^\varepsilon} \varepsilon g(x)\, ds_x = \sum_{i=1}^{M} \left(\varepsilon \int_{\Gamma_i^\varepsilon} g(x)\, ds_x \right) = \\
&= \sum_{i=1}^{M} \left(\varepsilon \int_{\Gamma_i} \varepsilon g_1(y)\, ds_y \right) = \sum_{i=1}^{M} \left(\varepsilon^2 \int_{\Gamma} g_2(y')\, ds_{y'} \right) = \\
&= \varepsilon^2 \sum_{i=1}^{M} \left(\int_{\Gamma} g_2(y')\, ds_{y'} \right) = \varepsilon^2 O\left(\frac{1}{\varepsilon^2}\right) \int_{\Gamma} g_2(y')\, ds_{y'} = \\
&= O(1) \int_{\Gamma} g_2(y')\, ds_{y'}
\end{aligned}
\tag{4.3.1}
$$

where we do the subsequent changes of variables: $y = \dfrac{x}{\varepsilon}$ and $y' = y + \xi^i$. Since M is the number of all microscopic periodicity cells, and we have a domain in $\mathbb{R}^2$, it follows that

$M \sim O\left(\frac{1}{\varepsilon^2}\right)$. Thus, from (4.3.1) we obtain that

$$I = O(1) \int_{\Gamma} g_2(y')\, ds_{y'} \tag{4.3.2}$$

which means that the total flux across the boundary of the perforations is $O(1)$ and does not depend on the small parameter ε. Therefore I does not blow-up or go to zero when $\varepsilon \to 0$. If in (4.2.1b) we had instead

$$-k_\varepsilon(x)\nabla u_\varepsilon \cdot \mathbf{n} = g(x), \quad x \in \partial B_\varepsilon \tag{4.3.3}$$

then the total flux would be

$$I = \frac{1}{\varepsilon} \int_{\Gamma} g_2(y')\, ds_{y'} \tag{4.3.4}$$

and $\lim\limits_{\varepsilon \to 0} I = \infty$ which is physically incorrect (see [5], [6]). We want the total flux I to be preserved in the asymptotics so that u_ε converges to some limit (homogenized) solution u_0 when $\varepsilon \to 0$.

4.4 Homogenization

First we introduce the characteristic function

$$\chi_\varepsilon(x) = \begin{cases} 1, & x \in \bar{\Omega}_\varepsilon, \\ 0, & x \in B_\varepsilon \end{cases} \tag{4.4.1}$$

where $\chi_\varepsilon(x) = \chi\left(\frac{x}{\varepsilon}\right) = \chi(y)$ is a periodically oscillating function with period ε and $\chi(y)$ is Y-periodic function, given by

$$\chi(y) = \begin{cases} 1, & y \in D \cup \Gamma, \\ 0, & y \in P \end{cases} \tag{4.4.2}$$

Since we want to derive an upscaled partial differential equation defined in the whole unperforated domain $\Omega = \Omega_\varepsilon \cup B_\varepsilon$, we start the homogenization procedure by defining problem (4.2.1) for all $x \in \Omega$. We do this with the help of the above defined characteristic function and we arrive at the following problem

$$-\nabla \cdot \left(\tilde{k}_\varepsilon(x)\nabla u_\varepsilon\right) = \chi_\varepsilon(x) f(x), \quad x \in \Omega, \tag{4.4.3a}$$

$$-\tilde{k}_\varepsilon(x)\nabla u_\varepsilon \cdot \mathbf{n} = \varepsilon g(x), \quad x \in \partial B_\varepsilon, \tag{4.4.3b}$$

$$u_\varepsilon(x) = 0, \quad x \in \partial\Omega \tag{4.4.3c}$$

where the coefficient

$$\tilde{k}_\varepsilon(x) = \chi_\varepsilon(x) k_\varepsilon(x) = \chi(y) k(y) = \tilde{k}(y) \tag{4.4.4}$$

is periodically oscillating with period ε, and $\tilde{k}(y)$ is Y-periodic. Now we want to homogenize problem (4.4.3).

4.4.1 Homogenization of the Neumann boundary conditions on the perforations' boundary

We start the homogenization procedure with the upscaling of the Neumann boundary condition (4.4.3b) imposed on the perforations boundary ∂B_ε

$$-\tilde{k}_\varepsilon(x)\nabla u_\varepsilon \cdot \mathbf{n} = \varepsilon g(x), \quad x \in \partial B_\varepsilon \tag{4.4.5}$$

which is equivalent to

$$-k_\varepsilon(x)\nabla u_\varepsilon \cdot \mathbf{n} = \varepsilon g(x), \quad x \in \partial B_\varepsilon \tag{4.4.6}$$

since $\chi_\varepsilon(x) = 1$ for $x \in \partial B_\varepsilon$.
As already discussed in the previous chapter, we have the following asymptotic expansion ansatz for the solution u_ε

$$u_\varepsilon(x) = u_0(x) + \varepsilon u_1\left(x, \frac{x}{\varepsilon}\right) + \varepsilon^2 u_2\left(x, \frac{x}{\varepsilon}\right) \tag{4.4.7}$$

with $y = \dfrac{x}{\varepsilon}$ and $\nabla = \nabla_x + \dfrac{1}{\varepsilon}\nabla_y$. Consequently for the flux on the boundary of the perforations we obtain

$$\begin{aligned}
-k_\varepsilon(x)\nabla u_\varepsilon \cdot \mathbf{n} &= -k(y)\left(\nabla_x + \frac{1}{\varepsilon}\nabla_y\right)\left(u_0(x) + \varepsilon u_1(x,y) + \varepsilon^2 u_2(x,y)\right) = \\
&= -k(y)\left(\nabla_x u_0 + \nabla_y u_1\right)\cdot \mathbf{n} - \\
&\quad -\varepsilon k(y)\left(\nabla_x u_1 + \nabla_y u_2\right)\cdot \mathbf{n} - \\
&\quad -\varepsilon^2 k(y)\nabla_x u_2 \cdot \mathbf{n}
\end{aligned} \tag{4.4.8}$$

and since $-k_\varepsilon(x)\nabla u_\varepsilon \cdot \mathbf{n} = \varepsilon g(x)$, we have that

$$\begin{aligned}
\varepsilon g(x) = &- k(y)\left(\nabla_x u_0 + \nabla_y u_1\right)\cdot \mathbf{n} - \\
&- \varepsilon k(y)\left(\nabla_x u_1 + \nabla_y u_2\right)\cdot \mathbf{n} - \\
&- \varepsilon^2 k(y)\nabla_x u_2 \cdot \mathbf{n}
\end{aligned} \tag{4.4.9}$$

Now, after we match equal powers of ε in (4.4.9), we obtain

$$\varepsilon^{-1}: \quad -k(y)\left(\nabla_x u_0 + \nabla_y u_1\right)\cdot \mathbf{n} = 0, \quad (x,y) \in [\Omega \times \Gamma] \tag{4.4.10a}$$

$$\varepsilon^{0}: \quad -k(y)\left(\nabla_x u_1 + \nabla_y u_2\right)\cdot \mathbf{n} = g(x), \quad (x,y) \in [\Omega \times \Gamma] \tag{4.4.10b}$$

4.4.2 Auxiliary cell problems

By analogy with the model problem from Chapter 3, after we group like powers of ε, from the ε^{-1} order we obtain the following PDE for the function $u_1(x, y)$:

$$\nabla_y \cdot \left(\tilde{k}(y) \nabla_x u_0 + \tilde{k}(y) \nabla_y u_1 \right) = 0, \quad (x, y) \in [\Omega \times Y] \tag{4.4.11}$$

which is equivalent to

$$\nabla_y \cdot \left(k(y) \nabla_x u_0 + k(y) \nabla_y u_1 \right) = 0, \quad (x, y) \in [\Omega \times D] \tag{4.4.12}$$

since

$$\tilde{k}(y) = \chi(y) k(y) = \begin{cases} k(y), & y \in D, \\ \\ 0, & y \in P = Y \backslash D \end{cases}$$

Equation (4.4.12) is equipped also with the Neumann boundary condition (4.4.10a)

$$-k(y) \left(\nabla_x u_0 + \nabla_y u_1 \right) \cdot \mathbf{n} = 0, \quad (x, y) \in [\Omega \times \Gamma] \tag{4.4.13}$$

We look for the solution u_1 to (4.4.12) in the following form

$$u_1(x, y) = \sum_{i=1}^{2} \frac{\partial u_0}{\partial x_i}(x) \phi_i(y) \tag{4.4.14}$$

where $\phi_i(y)$ for $i = 1, 2$ is a solution of the same partial differential equation as in the model cell problems (3.4.34)

$$-\nabla_y \cdot \left(k(y) \nabla_y \phi_i \right) = \frac{\partial k(y)}{\partial y_i}, \quad y \in D \tag{4.4.15}$$

Now we substitute $\nabla_x u_0$ with $\displaystyle\sum_{i=1}^{2} \frac{\partial u_0}{\partial x_i} \vec{\mathbf{e}}_1$ (where $\vec{\mathbf{e}}_1 = (1, 0)$ and $\vec{\mathbf{e}}_2 = (0, 1)$) and $u_1(x, y)$ with (4.4.14) in the Neumann boundary condition (4.4.13), and we get

$$k(y) \left(\sum_{i=1}^{2} \frac{\partial u_0}{\partial x_i}(x) \vec{\mathbf{e}}_i + \sum_{i=1}^{2} \frac{\partial u_0}{\partial x_i}(x) \nabla_y \phi_i \right) \cdot \mathbf{n} = 0 \tag{4.4.16}$$

which is equivalent to

$$\sum_{i=1}^{2} \frac{\partial u_0}{\partial x_i}(x) k(y) \left(\vec{\mathbf{e}}_i + \nabla_y \phi_i \right) \cdot \mathbf{n} = 0 \tag{4.4.17}$$

The latter equality must be satisfied for all $x \in \Omega$, which is fulfilled if and olny if

$$\left| \begin{array}{l} k(y) \left(\vec{\mathbf{e}}_1 + \nabla_y \phi_1 \right) \cdot \mathbf{n} = 0 \\ \\ k(y) \left(\vec{\mathbf{e}}_2 + \nabla_y \phi_2 \right) \cdot \mathbf{n} = 0 \end{array} \right. \tag{4.4.18}$$

and since $k(y) \neq 0$, it follows that

$$\left| \begin{array}{l} (\vec{\mathbf{e}}_1 + \nabla_y \phi_1) \cdot \mathbf{n} = 0 \\ \\ (\vec{\mathbf{e}}_2 + \nabla_y \phi_2) \cdot \mathbf{n} = 0 \end{array} \right. \tag{4.4.19}$$

which is equivalent to

$$\left| \begin{array}{l} \nabla_y \phi_1 \cdot \mathbf{n} = -\vec{\mathbf{e}}_1 \cdot \mathbf{n} \\ \\ \nabla_y \phi_2 \cdot \mathbf{n} = -\vec{\mathbf{e}}_2 \cdot \mathbf{n} \end{array} \right. \tag{4.4.20}$$

Finally, we arrive at the following auxiliary cell problem

$$-\nabla_y \cdot (k(y) \nabla_y \phi_i) = \frac{\partial k(y)}{\partial y_i}, \quad y \in D \tag{4.4.21a}$$

$$-\nabla_y \phi_i \cdot \mathbf{n} = \vec{\mathbf{e}}_i \cdot \mathbf{n}, \quad y \in \Gamma \tag{4.4.21b}$$

We also have that $\phi_i(y)$ is Y-periodic function and in order for (4.4.21) to have an unique solution, we impose the following condition

$$\int_D \phi_i(y)\, dy = 0 \tag{4.4.22}$$

4.4.3 Homogenized problem

By analogy with the homogenization of the model problem from Chapter 3, we obtain the following equation for the zero order term $u_0(x)$

$$-\nabla_y \cdot \left(\tilde{k}(y) \nabla_x u_1 + \tilde{k}(y) \nabla_y u_2 \right) - \nabla_x \cdot \left(\tilde{k}(y) \nabla_x u_0 + \tilde{k}(y) \nabla_y u_1 \right) = \chi(y) f(x) \tag{4.4.23}$$

where $(x, y) \in [\Omega \times Y]$. Now, just as we did in Chapter 3, we average the latter equation over the reference periodicity cell

$$\begin{aligned} &-\frac{1}{|Y|} \int_Y \nabla_y \cdot \left(\tilde{k}(y) \nabla_x u_1 + \tilde{k}(y) \nabla_y u_2 \right) dy - \\ &-\frac{1}{|Y|} \int_Y \nabla_x \cdot \left(\tilde{k}(y) \nabla_x u_0 + \tilde{k}(y) \nabla_y u_1 \right) dy = \frac{1}{|Y|} \int_Y \chi(y) f(x)\, dy \end{aligned} \tag{4.4.24}$$

Taking into account that for any vector function $\nu = (\nu_1(x,y), \nu_2(x,y))$ the following is valid

$$\int\limits_Y \nabla_y \cdot \left(\tilde{k}(y)\nu\right)\, dy = \int\limits_Y \left[\frac{\partial}{\partial y_1}\left(\tilde{k}(y)\nu_1(x,y)\right) + \frac{\partial}{\partial y_2}\left(\tilde{k}(y)\nu_2(x,y)\right)\right] dy =$$

$$= \int\limits_D \left[\frac{\partial}{\partial y_1}\left(k(y)\nu_1(x,y)\right) + \frac{\partial}{\partial y_2}\left(k(y)\nu_2(x,y)\right)\right] dy +$$

$$+ \int\limits_P \left[\underbrace{\frac{\partial}{\partial y_1}\left(0.\nu_1(x,y)\right)}_{=0} + \underbrace{\frac{\partial}{\partial y_2}\left(0.\nu_2(x,y)\right)}_{=0}\right] dy =$$

$$= \int\limits_D \left[\frac{\partial}{\partial y_1}\left(k(y)\nu_1(x,y)\right) + \frac{\partial}{\partial y_2}\left(k(y)\nu_2(x,y)\right)\right] dy + \underbrace{\int\limits_P 0\, dy}_{=0} =$$

$$= \int\limits_D \nabla_y \cdot \left(k(y)\nu\right)\, dy$$

equation (4.4.24) becomes

$$\begin{aligned} &-\frac{1}{|Y|}\int\limits_D \nabla_y \cdot \left(k(y)\nabla_x u_1 + k(y)\nabla_y u_2\right)\, dy - \\ &-\frac{1}{|Y|}\int\limits_D \nabla_x \cdot \left(k(y)\nabla_x u_0 + k(y)\nabla_y u_1\right)\, dy = f(x)\frac{1}{|Y|}\int\limits_D 1\, dy \end{aligned} \tag{4.4.25}$$

For the first integral in the sum on the left-hand side of (4.4.25) we apply the divergence theorem and we get

$$-\frac{1}{|Y|}\int\limits_{\partial D} \left(k(y)\nabla_x u_1 + k(y)\nabla_y u_2\right) \cdot \mathbf{n}\, ds_y -$$

$$-\frac{1}{|Y|}\int\limits_D \nabla_x \cdot \left(k(y)\nabla_x u_0 + k(y)\nabla_y u_1\right)\, dy = \frac{|D|}{|Y|} f(x) \tag{4.4.26}$$

Since $\partial D = \partial Y \cup \Gamma$, the latter is equivalent to

$$-\frac{1}{|Y|}\underbrace{\int\limits_{\partial Y}(k(y)\nabla_x u_1 + k(y)\nabla_y u_2)\cdot \mathbf{n}\, ds_y}_{=0} - \frac{1}{|Y|}\int\limits_{\Gamma}\underbrace{(k(y)\nabla_x u_1 + k(y)\nabla_y u_2)\cdot \mathbf{n}}_{=-g(x)}\, ds_y$$

$$-\frac{1}{|Y|}\int\limits_{D}\nabla_x\cdot(k(y)\nabla_x u_0 + k(y)\nabla_y u_1)\, dy = \frac{|D|}{|Y|}f(x) \tag{4.4.27}$$

where the integral over ∂Y vanishes due to the Y-periodicity of the functions $k(y)$, $u_1(x,y)$, $u_2(x,y)$, and the symmetry of the boundary ∂Y of the reference period Y. Thus (4.4.27) becomes

$$\frac{1}{|Y|}\int\limits_{\Gamma} g(x)\, ds_y - \frac{1}{|Y|}\int\limits_{D}\nabla_x\cdot(k(y)\nabla_x u_0 + k(y)\nabla_y u_1)\, dy = \frac{|D|}{|Y|}f(x) \tag{4.4.28}$$

which is equivalent to

$$-\frac{1}{|Y|}\int\limits_{D}\nabla_x\cdot(k(y)\nabla_x u_0 + k(y)\nabla_y u_1)\, dy = \frac{|D|}{|Y|}f(x) - \frac{|\Gamma|}{|Y|}g(x) \tag{4.4.29}$$

Now we perform analogous to (3.4.37) calculations and we arrive at the following homogenized problem

$$-\nabla_x\cdot(k^*\nabla_x u_0) = \frac{|D|}{|Y|}f(x) - \frac{|\Gamma|}{|Y|}g(x), \quad x\in\Omega, \tag{4.4.30a}$$

$$u_0(x) = 0, \quad x\in\partial\Omega \tag{4.4.30b}$$

where the effective diffusion coefficient k^* is a tensor and has the following form

$$k^*_{ij} = \frac{1}{|Y|}\int\limits_{D} k(y)\left(\delta_{ij} + \frac{\partial\phi_j}{\partial y_i}(y)\right) dy \tag{4.4.31}$$

for $i,j = 1,2$.

Remark: The initial microscale Neumann boundary condition (4.2.1b) imposed on the boundary of the perforations ∂B_ε comes in an averaged form as a right-hand side term in the homogenized problem (4.4.30).

4.5 The case when $g(x)$ is a periodically oscillating function

Let us consider the case when $g(x)$ is a periodically oscillating function with the same period as the coefficient $k_\varepsilon(x)$. In the homogenization process we want to get rid of all

rapidly oscillating functions since they make the problem ill-posed and computationally expensive. Therefore we have to take care also of the periodically oscillating function $g_\varepsilon(x)$. Hence we transfer its oscillations to the reference period Y by making the change of variables $y = \dfrac{x}{\varepsilon}$ and we denote

$$g_\varepsilon(x) = G\left(\frac{x}{\varepsilon}\right) = G(y) \tag{4.5.1}$$

where the period of $g_\varepsilon(x)$ is ε, and the function $G(y)$ is Y-periodic. Then we modify accordingly the ε^0 order Neumann boundary condition (4.4.10b)

$$\varepsilon^0: \quad -k(y)\left(\nabla_x u_1 + \nabla_y u_2\right)\cdot \mathbf{n} = G(y), \quad (x,y) \in [\Omega \times \Gamma] \tag{4.5.2}$$

and the homogenized equation (4.4.28) becomes

$$\frac{1}{|Y|}\int\limits_{\Gamma} G(y)\, ds_y - \frac{1}{|Y|}\int\limits_{D} \nabla_x \cdot \left(k(y)\nabla_x u_0 + k(y)\nabla_y u_1\right)\, dy = \frac{|D|}{|Y|} f(x) \tag{4.5.3}$$

which is equivalent to

$$-\frac{1}{|Y|}\int\limits_{D} \nabla_x \cdot \left(k(y)\nabla_x u_0 + k(y)\nabla_y u_1\right)\, dy = \frac{|D|}{|Y|} f(x) - \frac{1}{|Y|}\int\limits_{\Gamma} G(y)\, ds_y \tag{4.5.4}$$

Thus, the final homogenized problem, in the case of a periodically oscillating function $g_\varepsilon(x)$, is

$$-\nabla_x \cdot \left(k^* \nabla_x u_0\right) = \frac{|D|}{|Y|} f(x) - \frac{1}{|Y|}\int\limits_{\Gamma} G(y)\, ds_y, \quad x \in \Omega, \tag{4.5.5a}$$

$$u_0(x) = 0, \quad x \in \partial\Omega \tag{4.5.5b}$$

4.6 Numerical examples

We consider test cases with 8 and 16 perforations per row in the unit square domain Ω as shown in Figure 4.3. This means that we have a total of $8^2 = 64$ or $16^2 = 256$ perforations, respectively, and consequently $\varepsilon = \dfrac{1}{8} = 0.125$ or $\varepsilon = \dfrac{1}{16} = 0.0625$. We take different values for the coefficient $k_\varepsilon(x)$ and the right-hand side $f(x)$, and we also consider different functions $g(x)$ for the Neumann boundary conditions on the perforations boundary. We compare the homogenized solution with the reference microscale one. We run experiments with varying number of degrees of freedom both for the homogenized problem and for the microscale one. The reference periodicity cell Y is given in Figure 4.2. In Examples 1 to 4 we show numerical results for $g(x)$ being nonperiodic function and in Example 5 we take $g_\varepsilon(x)$ to be a periodically oscillating function. From the numerical examples we see that even for relatively big values of ε, the homogenized solution is a very good approximation of the microscale one.

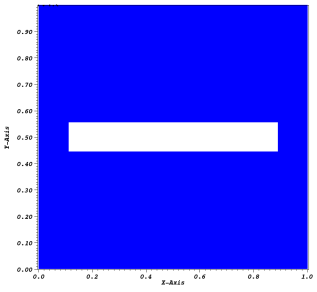

Figure 4.2: Solution domain for the cell problems

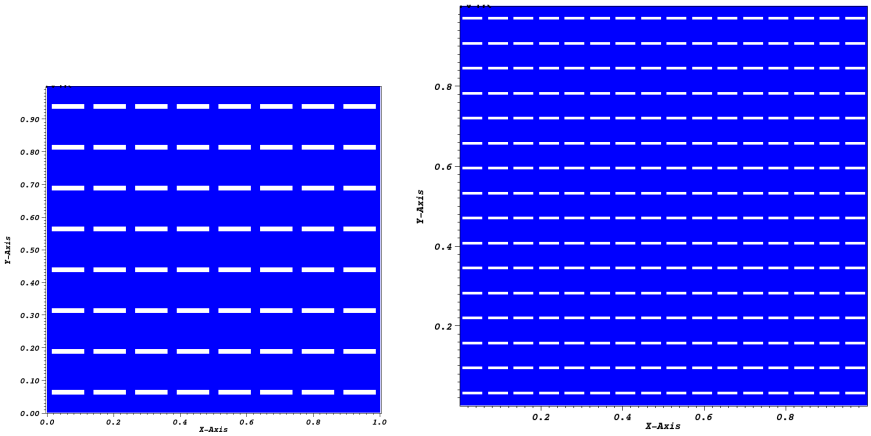

(a) $\varepsilon = \frac{1}{8}$ (b) $\varepsilon = \frac{1}{16}$

Figure 4.3: Solution domains for the microscale problems

In Tables 4.6.1, 4.6.2 and 4.6.3 we give the exact form and values of all the functions and parameters that we use in Example 1, 2 and 3, respectively. As we can see from Figures 4.4, 4.5, 4.6, 4.7, 4.8 and 4.9, when we increase the number of unknowns in the microscale simulation, the microscale solution, indeed, converges to the homogenized limit one. Moreover, the degrees of freedom in the homogenized problem are significantly less than those needed for the microscale problem in order to achieve the same accuracy.
In Tables 4.6.4, 4.6.5, 4.6.6 and 4.6.7 are given the parameters that we use in Examples 4 and 5. In Figure 4.10 and 4.11 we show the homogenized and microscale solution for different number of degrees of freedom and we observe that we need only 846 DOF for the homogenized problem in order to obtain the same approximate solution as that of the microscale problem with 147918 DOF. In Figures 4.13 and 4.12 we show the homogenized solution calculated with different number of unknowns and we see that when we increase the degrees of freedom, the solution changes very little. Therefore, even with only 178 DOF in the homogenized problem we obtain a very good approximation of the microscale one obtained with 147918 DOF. The same conclusions also apply to the results that we observe in Figure 4.14, as well as to Example 5 and Figures 4.15, 4.16, 4.17, 4.18 and 4.19, where $g_\varepsilon(x)$ is a periodically oscillating function with the same period as $k_\varepsilon(x)$.

4.6.1 Example 1

Table 4.6.1:

ε	$k_\varepsilon(x)$	$f(x)$	$g(x)$	DOF microscale	DOF homogenized
$\frac{1}{8} = 0.125$	3	16	1	74729	8107
				147918	

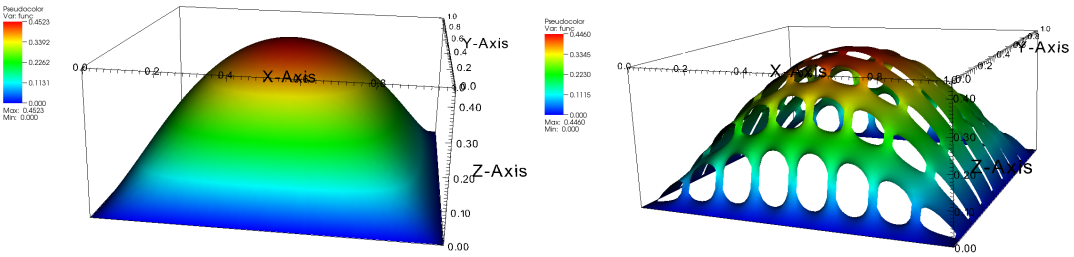

(a) Homogenized solution with 8107 DOF and maximum value of 0.4523

(b) Microscale solution with 74729 DOF and maximum value of 0.4460

Figure 4.4: Comparison between the homogenized and the microscale solution

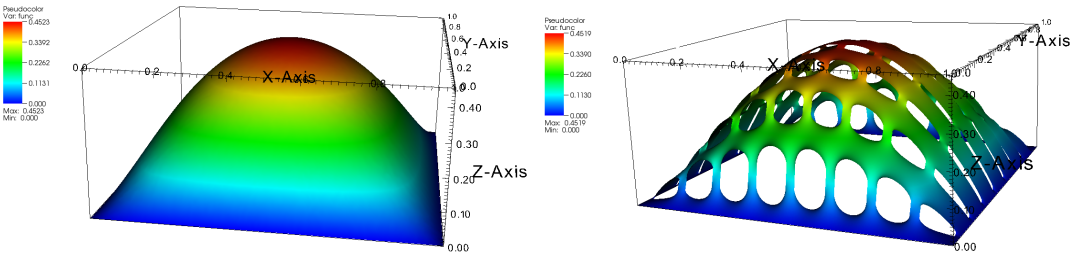

(a) Homogenized solution with 8107 DOF and maximum value of 0.4523

(b) Microscale solution with 147918 DOF and maximum value of 0.4519

Figure 4.5: Comparison between the homogenized and the microscale solution

4.6.2 Example 2

Table 4.6.2:

ε	$k_\varepsilon(x)$	$f(x)$	$g(x)$	DOF microscale	DOF homogenized
$\frac{1}{8} = 0.125$	3	16	0	74729	8107
				147918	

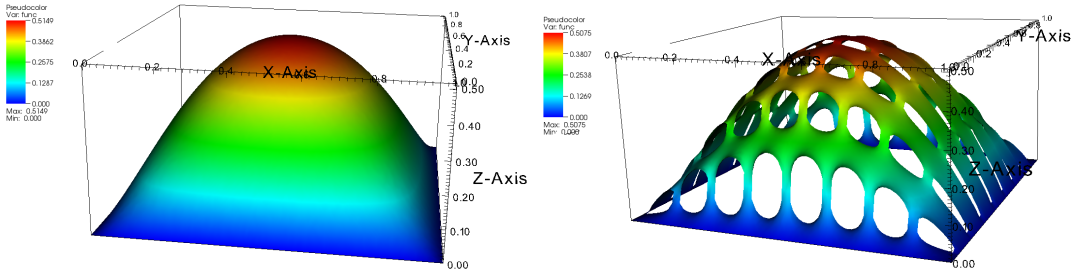

(a) Homogenized solution with 8107 DOF and maximum value of 0.5149

(b) Microscale solution with 74729 DOF and maximum value of 0.5075

Figure 4.6: Comparison between the homogenized and the microscale solution

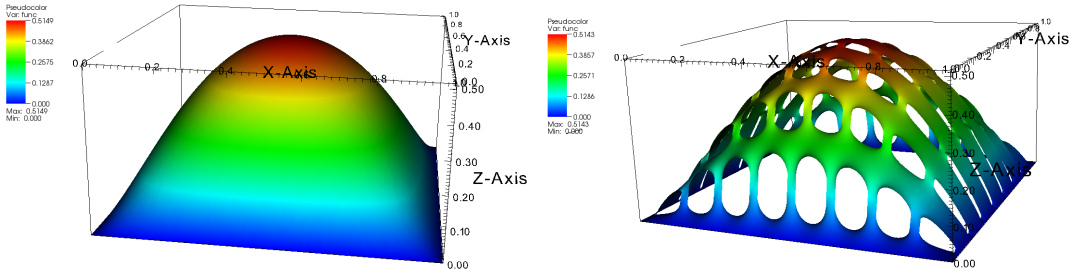

(a) Homogenized solution with 8107 DOF and maximum value of 0.5149

(b) Microscale solution with 147918 DOF and maximum value of 0.5143

Figure 4.7: Comparison between the homogenized and the microscale solution

4.6.3 Example 3

Table 4.6.3:

ε	$k_\varepsilon(x)$	$f(x)$	$g(x)$	DOF microscale	DOF homogenized
$\frac{1}{8} = 0.125$	$\cos(32\pi x_1)\cos(32\pi x_2) + 1.1$	16	1	74729	8107
				147918	

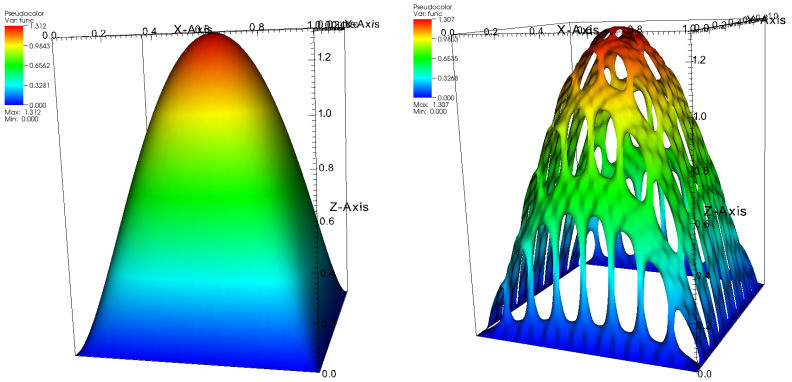

(a) Homogenized solution with 74729 8107 DOF and maximum value of 1.312

(b) Microscale solution with 74729 DOF and maximum value of 1.307 1.312

Figure 4.8: Comparison between the homogenized and the microscale solution

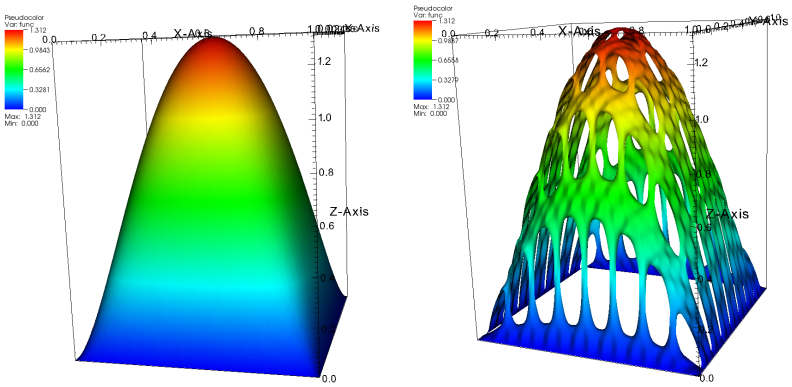

(a) Homogenized solution with 147918 8107 DOF and maximum value of 1.312

(b) Microscale solution with 147918 DOF and maximum value of 1.312 1.312

Figure 4.9: Comparison between the homogenized and the microscale solution

4.6.4 Example 4

$$\varepsilon = \frac{1}{8} = 0.125$$

Table 4.6.4:

ε	$k_\varepsilon(x)$	$f(x)$	$g(x)$	DOF microscale	DOF homogenized
$\frac{1}{8} = 0.125$	$\cos(32\pi x_1)\cos(32\pi x_2) + 1.1$	16	$x_1^2 + 3x_1x_2$	74729	178
				147918	846
					4080
					8107

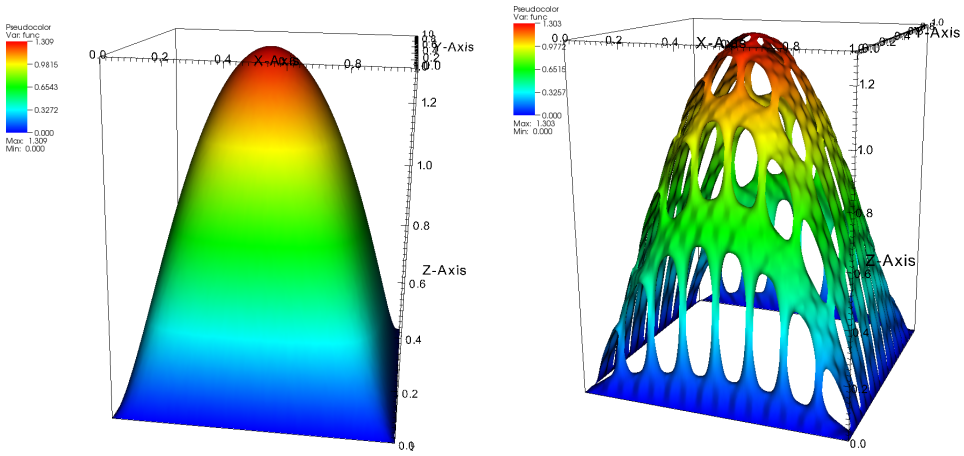

(a) Homogenized solution with 8107 DOF and maximum value of 1.309

(b) Microscale solution with 74729 DOF and maximum value of 1.303

Figure 4.10: Comparison between the homogenized and the microscale solution

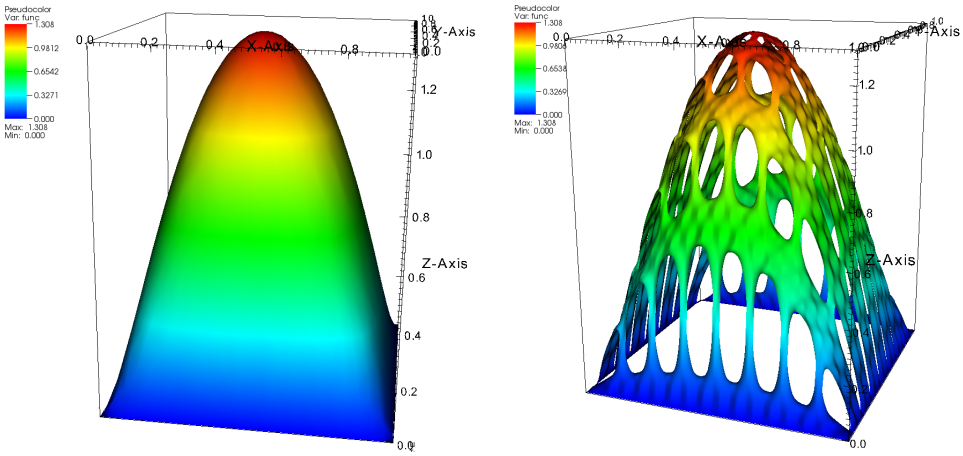

(a) Homogenized solution with 846 DOF and maximum value of 1.308

(b) Microscale solution with 147918 DOF and maximum value of 1.308

Figure 4.11: Comparison between the homogenized and the microscale solution

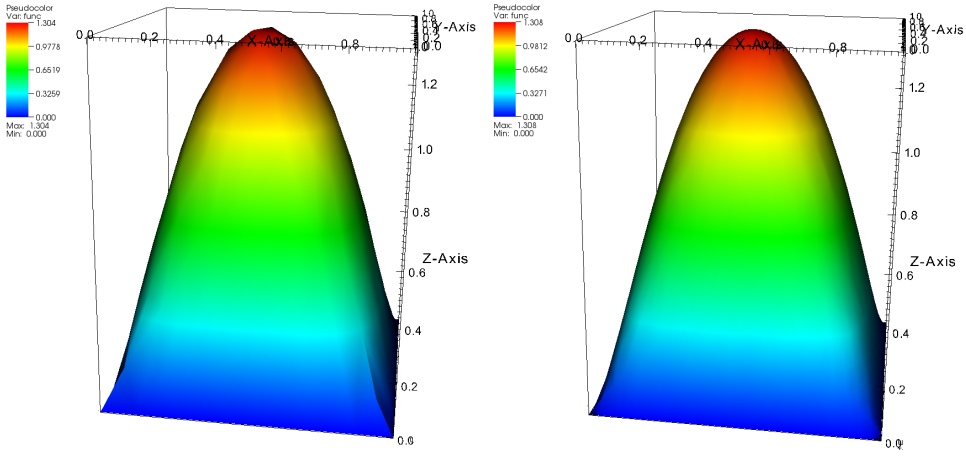

(a) Homogenized solution with 178 DOF and maximum value of 1.304

(b) Homogenized solution with 846 DOF and maximum value of 1.308

Figure 4.12: Homogenized solution calculated with different number of degrees of freedom

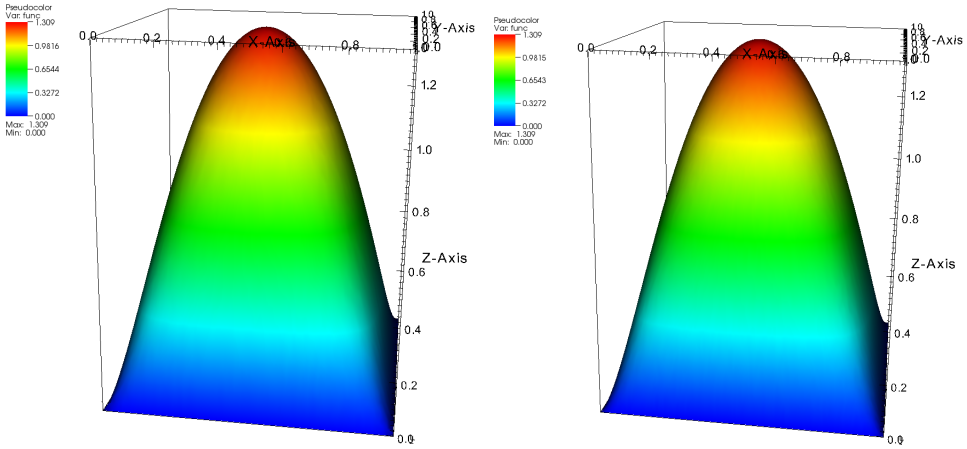

(a) Homogenized solution with 4080 DOF and maximum value of 1.309

(b) Homogenized solution with 8107 DOF and maximum value of 1.309

Figure 4.13: Homogenized solution calculated with different number of degrees of freedom

$$\varepsilon = \frac{1}{16} = 0.0625$$

Table 4.6.5:

ε	$k_\varepsilon(x)$	$f(x)$	$g(x)$	DOF microscale	DOF homogenized
$\frac{1}{16} = 0.0625$	$\cos(32\pi x_1)\cos(32\pi x_2) + 1.1$	16	$x_1^2 + 3x_1x_2$	147918	846

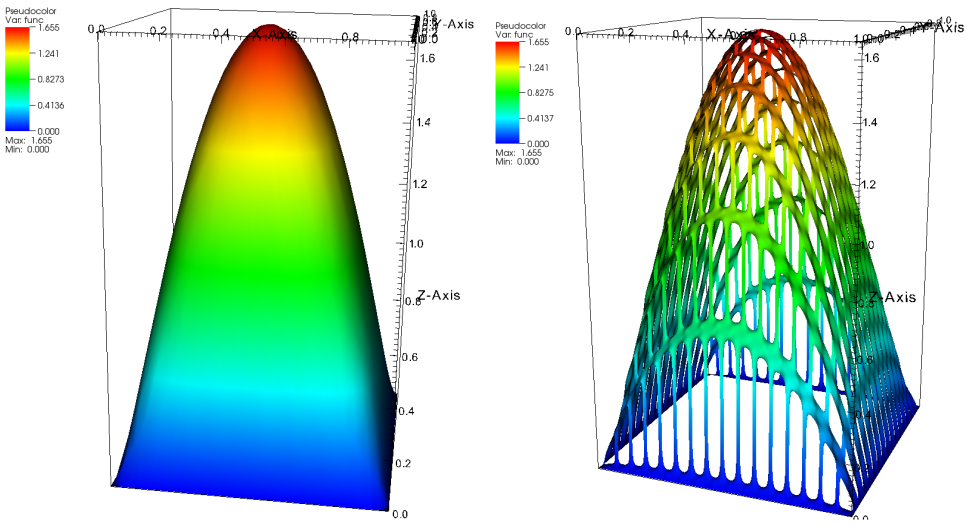

(a) Homogenized solution with 846 DOF and maximum value of 1.655

(b) Microscale solution with 147918 DOF and maximum value of 1.655

Figure 4.14: Comparison between the homogenized and the microscale solution

4.6.5 Example 5

$$\varepsilon = \frac{1}{8} = 0.125$$

Table 4.6.6:

ε	$k_\varepsilon(x)$	$f(x)$	$g_\varepsilon(x)$	DOF microscale	DOF homogenized
$\frac{1}{8} = 0.125$	$\cos(32\pi x_1)\cos(32\pi x_2) + 1.1$	16	$\cos(32\pi x_1)$	147918	846
				367891	

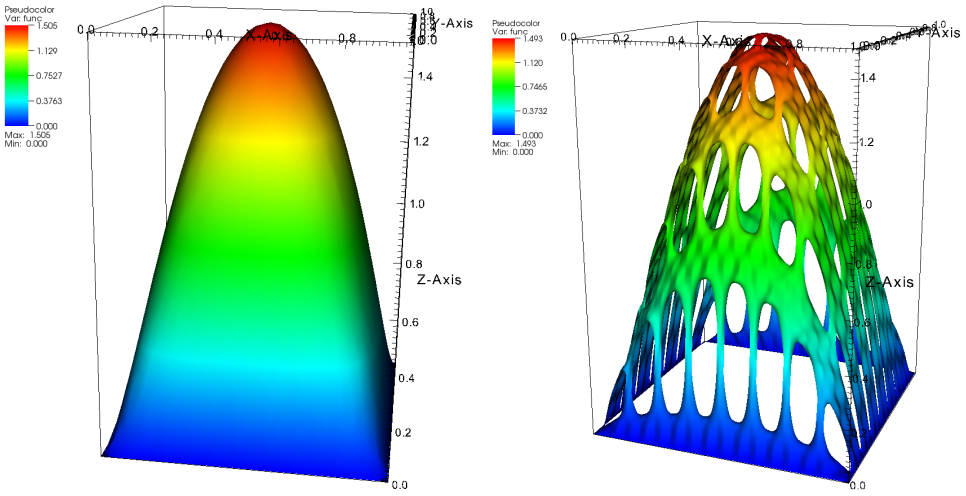

(a) Homogenized solution with 846 DOF and maximum value of 1.505

(b) Microscale solution with 147918 DOF and maximum value of 1.493

Figure 4.15: Comparison between the homogenized and the microscale solution

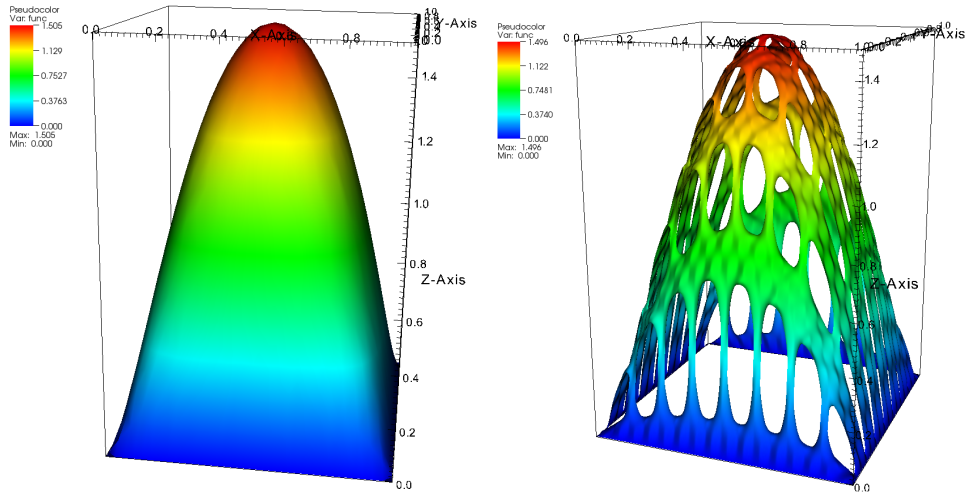

(a) Homogenized solution with 846 DOF and maximum value of 1.505

(b) Microscale solution with 367891 DOF and maximum value of 1.496

Figure 4.16: Comparison between the homogenized and the microscale solution

$$\varepsilon = \frac{1}{16} = 0.0625$$

Table 4.6.7:

ε	$k_\varepsilon(x)$	$f(x)$	$g_\varepsilon(x)$	DOF microscale	DOF homogenized
$\frac{1}{16} = 0.0625$	$\cos(32\pi x_1)\cos(32\pi x_2) + 1.1$	16	$\cos(32\pi x_1)$	150465	846
				372417	
				742563	

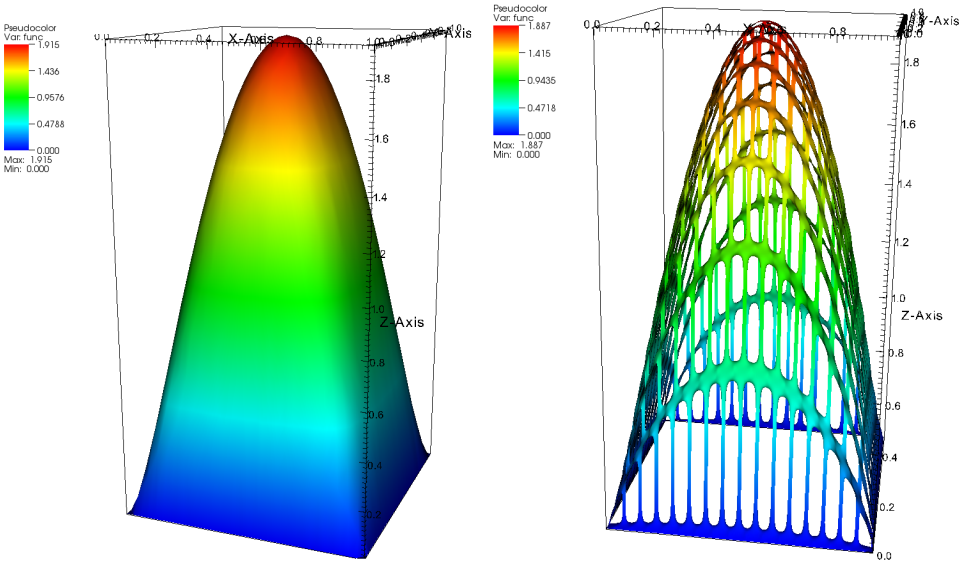

(a) Homogenized solution with 846 DOF and maximum value of 1.915

(b) Microscale solution with 150465 DOF and maximum value of 1.887

Figure 4.17: Comparison between the homogenized and the microscale solution

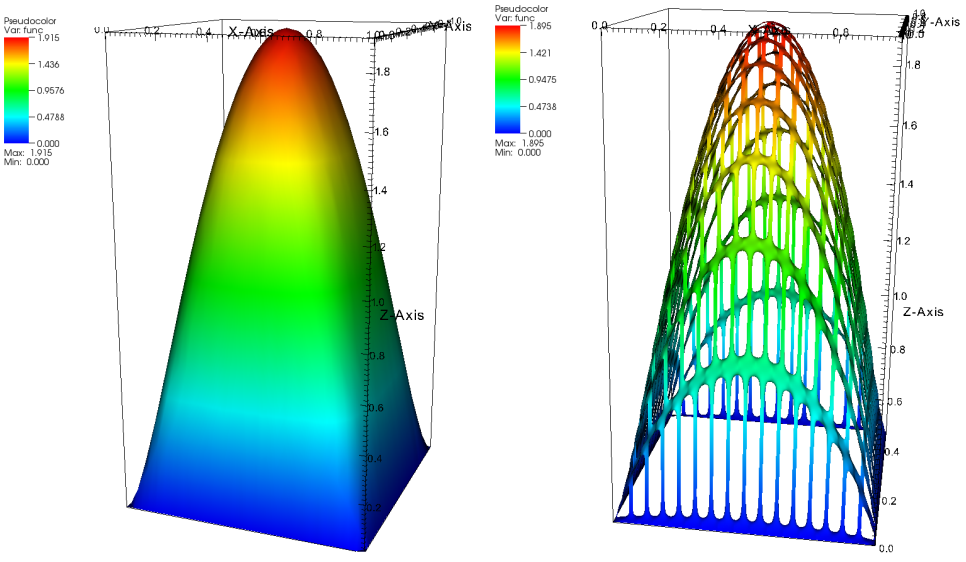

(a) Homogenized solution with 846 DOF and maximum value of 1.915

(b) Microscale solution with 372417 DOF and maximum value of 1.895

Figure 4.18: Comparison between the homogenized and the microscale solution

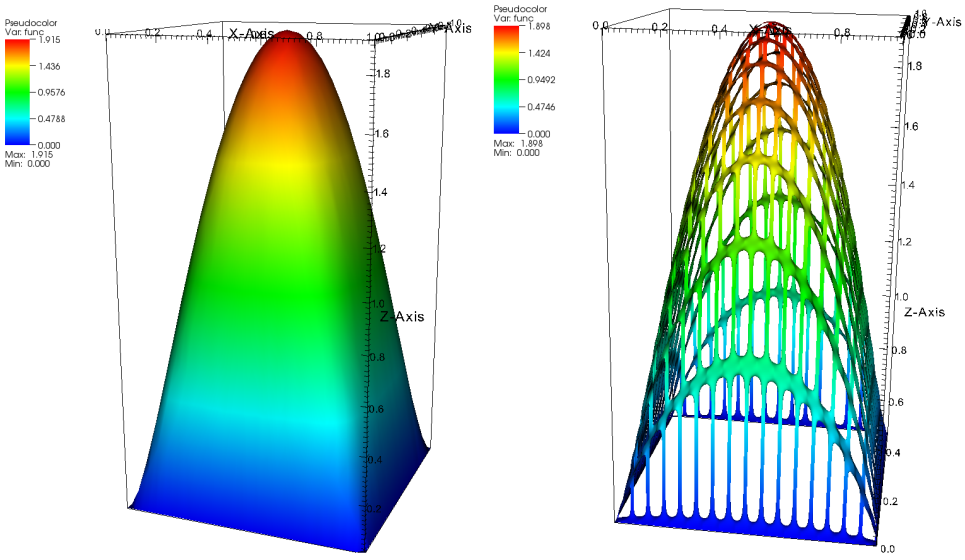

(a) Homogenized solution with 846 DOF and maximum value of 1.915

(b) Microscale solution with 742563 DOF and maximum value of 1.898

Figure 4.19: Comparison between the homogenized and the microscale solution

Chapter 5

Upscaling of the Li-ion Battery Model via the Homogenization Theory

5.1 Introduction

In this chapter we derive an upscaled Li-ion battery model on the lengthscale of the whole electrode starting from the microscale model [48] on the pore scale. We do this with the help of the asymptotic homogenization method. We follow and extend the work of Ciucci and Lai [45] who homogenize the microscale Li-ion battery model developed in [46]. Our main contribution is that we

- rigorously determine the asymptotic order of the interface exchange current densities
- derive a consistent upscaled Neumann boundary condition starting from the given microscale one (2.6.2) and, hence, develop a closed homogenized model
- perform a detailed numerical study to validate the upscaled model that we derive

For the homogenization of the isothermal Li-ion battery model (2.3.1)-(2.4.1) we apply the algorithm for homogenization in perforated domains, which was discussed in detail in the previous Chapter 4. Since each electrode consists of two phases - electrolyte and solid, we can think of these phases as two separate, self-complementary perforated domains. Therefore, the idea behind the asymptotic homogenization of the porous electrodes is to homogenize separately each phase as a detached perforated domain, where the two phases are coupled through the interface conditions (2.5.2). In order to validate the derived model we conduct a comprehensive numerical study for both simple and complex geometries of the battery cell electrodes. The results presented in this chapter were reported by the author at the Oberwolfach Mini-Workshop: Numerical Upscaling for Media with Deterministic and Stochastic Heterogeneity, held from 10 to 16 February 2013 and a contribution is published in [42].
The chapter is organized as follows. We start with the setting of the problem in Section 5.2. In Section 5.3 we discuss why the concentration of Li+ in the solid phase is not a

scale-separable function and we give the microscale solid phase equation in scale invariant form. We continue with the scale separable quantities in Section 5.4, where we treat the upscaling of the electrolyte phase equations and the solid phase equation for the potential. In Section 5.4.2 we approximate the nonlinear quantities with the zero order terms of the asymptotic expansions of the concentration and the potential. In this section we also derive the auxiliary cell problems and the homogenized model equations. Section 5.4.4 is devoted to the homogenization of the solid-electrolyte interface conditions, which is crucial for the correct upscaling of the microscale battery model. In Section 5.5 we derive an effective Neumann boundary condition for the electrical potential on the outer cathode boundary, starting from the microscale one. The full coupled macro-micro homogenized model is given in Section 5.6. In Section 5.7 we discuss the strategy for the numerical solving of the homogenized problem. In this section we also discuss the numerical methods that we use, we give the weak formulation of the problem, and we write the discretization and the linearization of the problem. We briefly consider the implementational aspects of the problem in Section 5.8. In Section 5.9 we present comprehensive numerical results. Numerical experiments for cut-off spherical particles and for various values of the small parameter ε are shown in Section 5.9.2 . Numerical results for complex geometry of the solid phase periodicity cell and different applied currents are given in Section 5.9.3. We outline the advantages of the proposed upscaling algorithm in Section 5.10 and we conclude with a short summary in Section 5.11.

5.2 Setting of the problem

We suppose periodic structure of the electrode medium in all three directions x_1, x_2 and x_3. Without loss of generality, we consider the solid phase to be composed of connected identical and periodically arranged cut-off spheres as shown in Figure 5.1. The exemplary two-phase periodicity cell is a cubic block, which is composed of one active particle surrounded by electrolyte as illustrated in Figure 5.2. Consequently, the solid phase period consists of one cut-off spherical particle, whereas the electrolyte phase period is the complement of the solid phase domain with respect to the two-phase periodicity cell. It is important to note that the solid phase periodicity cell may consist of many connected particles with different shape and size, as we will see in Section 5.9. Here we make the restriction regarding the solid phase geometry only for reasons of clarity and comprehensibility of the exposition.

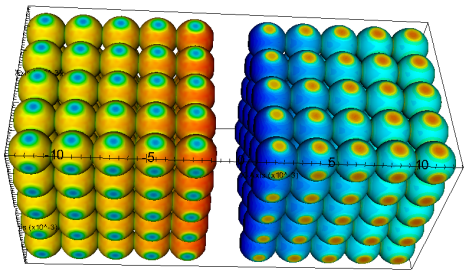

Figure 5.1: Battery cell with periodically arranged active particles, which are cut-off spheres

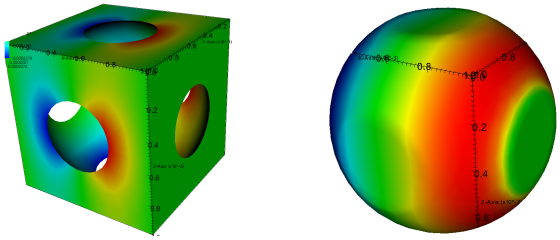

a. Electrolyte b. Solid

Figure 5.2: Geometry of the exemplary two-phase periodicity cell

With L we denote the characteristic length of the electrode and with l - the characteristic length of the two-phase periodicity cell. We introduce the small parameter ε as the ratio between the characteristic length of the two-phase periodicity cell and the characteristic length of the electrode, i.e., $\varepsilon = \dfrac{l}{L}$. Therefore, if x is the macroscopic "slow" variable, then we have that $y = \dfrac{x}{\varepsilon}$ is the microscopic "fast" variable. With $Y_i^\varepsilon = E_i^\varepsilon \cup S_i^\varepsilon \cup \Gamma_i^\varepsilon$ we denote the two-phase microscale periodicity cells, where $i = 1, 2, \ldots, M$, and M is the number of all periodicity cells in one electrode. With E_i^ε we denote the electrolyte phase domain in the two-phase microscale period cell (electrolyte phase periodicity cell), S_i^ε is the solid phase domain (solid phase periodicity cell), and Γ_i^ε is the interface boundary between the solid and the electrolyte. Then with $Y_i = E_i \cup S_i \cup \Gamma_i$ we denote the upscaled period cells after the change of variables

$$\upsilon : y = \frac{x}{\varepsilon}, \tag{5.2.1}$$

i.e.,

$$Y_i^\varepsilon \xrightarrow{\upsilon} Y_i \tag{5.2.2}$$

For each upscaled periodicity cell Y_i we make the following translation

$$\tau_i : y' = y + \xi_i \tag{5.2.3}$$

so that

$$Y_i \xrightarrow{\tau_i} Y, \tag{5.2.4}$$

where Y is the reference two-phase periodicity cell, which consists of electrolyte domain E, active particle domain S and interface boundary Γ, i.e., $Y = E \cup S \cup \Gamma$. It is clear that the characteristic length of the reference periodicity cell Y is L. We also note that the translation vector ξ_i is a constant vector for each $y \in Y_i$. From now on, unless specified otherwise, when we refer to the change of variables (5.2.1), we will mean implicitly that we make both changes of variables (5.2.1) and (5.2.3), but we will omit the translation. Thus, for a function $f(x)$, we should normally have the following notation for the two subsequent changes of variables

$$f(x) = f_1(y) = f_2(y') \tag{5.2.5}$$

or equivalently

$$\underbrace{f(x) = f\left(\varepsilon(y' - \xi_i)\right)} = \underbrace{f_2\left(\frac{x}{\varepsilon} + \xi_i\right) = f_2(y')}, \quad y' \in Y \tag{5.2.6}$$

where $x \in \Omega^{\varepsilon}_{electrode}$, $y \in \bigcup_{i=1}^{M} Y_i$, and $y' \in Y$, but we will write

$$f(x) = f_2\left(\frac{x}{\varepsilon}\right) = f_2(y), \quad y \in Y \tag{5.2.7}$$

where we skip to note the translation τ_i and we re-denote the variable $y' \in Y$ with y. We adopt the latter notation for brevity and simplicity.

5.3 Microscale equation for the concentration of Li+ in the solid phase

Based on physical considerations and microscale simulations [70] we can deduce that the spatial profile of the concentration c^s in a single particle depends strongly on the applied discharge/charge currents and on the size of the particle. For small currents or/and for very small particles this profile is uniform, whereas for higher currents or/and for bigger particles it is nonuniform. This means that above some critical discharge/charge current and particle size we do not have scale separation for c^s. Consequently, the behaviour of the function c^s can be captured adequately, and regardless of the regime in which the battery operates, only on the microscale. Therefore we do not upscale the equation for the concentration c^s of Lithium ions in the active particles. Instead, we solve the original microscale equation for the concentration c^s, given in scale invariant form in terms of the variable $y \in S$:

$$\frac{\partial c^s}{\partial t} - \nabla_y \cdot \left(\frac{D^s}{\varepsilon^2}\nabla_y c^s\right) = 0, \quad y \in S \tag{5.3.1a}$$

$$-\frac{D^s}{\varepsilon^2}\nabla_y c^s \cdot \mathbf{n_s} = \frac{1}{\varepsilon}\mathcal{N}(c_0^e, c^s, \phi_0^e, \phi_0^s), \quad y \in \Gamma. \tag{5.3.1b}$$

We impose periodic boundary conditions on $\partial S \backslash \Gamma$, i.e., on the part of the solid particles boundary where the particles are connected. With c_0^e, ϕ_0^e and ϕ_0^s we denote the respective upscaled quantities which are the solution of the homogenized model equations (5.6.1).

5.4 Upscaling of the electrolyte phase equations and the solid phase equation for the potential

Lithium ions have a very high mobility in the electrolyte, which means that their diffusion is very fast. Therefore in the electrolyte the concentration of ions and the electrochemical

potential are uniformly distributed functions with almost no spatial variation. We observe this behaviour of the concentration and the potential also in the numerical simulations on the microscale ([70]). The same consideration is also valid for the potential in the solid particles. This means that we have scale separation for the concentration c^e of Lithium ions in the electrolyte, for the potential ϕ^e in the electrolyte and for the potential ϕ^s in the particles, which allows us to derive macroscopic upscaled equations for these quantities. We start the homogenization procedure by introducing the following characteristic functions

$$\chi^e(x) = \begin{cases} 1, & x \in \Omega_e \\ 0, & x \in \Omega_s \end{cases} \quad \text{and} \quad \chi^s(x) = \begin{cases} 0, & x \in \Omega_e \\ 1, & x \in \Omega_s. \end{cases}$$

With the help of these characteristic functions we define the model equations that we want to upscale in the whole electrode domain $\Omega_{electrode}$, i.e., for $x \in \Omega_{electrode}$ we have

$$\frac{\partial\left(\chi^e(x)c^e\right)}{\partial t} - \nabla \cdot (k_{11}(x, c^e)\nabla c^e + k_{12}(x)\nabla\phi^e) = 0 \tag{5.4.1a}$$

$$-\nabla \cdot (k_{21}(x, c^e)\nabla c^e + k_{22}(x)\nabla\phi^e) = 0 \tag{5.4.1b}$$

$$-\nabla \cdot (\kappa(x)\nabla\phi^s) = 0 \tag{5.4.1c}$$

with the interface conditions (2.5.2) and boundary conditions

$$\phi^s(x) = E_1^s = const, \quad x \in \omega_1 \tag{5.4.2}$$

$$-(\kappa(x)\nabla\phi^s)\cdot\mathbf{n} = E_2(x) \quad x \in \omega_2 \tag{5.4.3}$$

$$\nabla c^s \cdot \mathbf{n} = 0, \quad x \in \omega_1 \cup \omega_2 \tag{5.4.4}$$

$$\mathbf{N}^e \cdot \mathbf{n} = \mathbf{J}^e \cdot \mathbf{n} = 0, \quad x \in \partial\Omega, \tag{5.4.5}$$

where $c^e(x), \phi^e(x) : \Omega^e_{anode/cathode} \longrightarrow \mathbb{R}$ and $\phi^s(x) : \Omega_s \longrightarrow \mathbb{R}$, and we define

$$k_{ij} = \chi^e(x)k^e_{ij}, \quad \kappa(x) = \chi^s(x)\kappa^s, \quad E_2(x) = \chi^s(x)E_2^s$$

for $i, j = 1, 2$.

5.4.1 Asymptotic analysis

Now for $x \in \Omega^\varepsilon_{electrode} = \left(\Omega^e_{anode/cathode}\right)^\varepsilon \cup \Omega^\varepsilon_{a/c}$ we write the electrolyte phase equations and the solid phase equation for the potential in terms of a dependence on the small parameter ε

$$\frac{\partial\left(\chi^e_\varepsilon(x)c^e_\varepsilon\right)}{\partial t} - \nabla \cdot (k^\varepsilon_{11}(x, c^e_\varepsilon)\nabla c^e_\varepsilon + k^\varepsilon_{12}(x)\nabla\phi^e_\varepsilon) = 0 \tag{5.4.6a}$$

$$-\nabla \cdot (k^\varepsilon_{21}(x, c^e_\varepsilon)\nabla c^e_\varepsilon + k^\varepsilon_{22}(x)\nabla\phi^e_\varepsilon) = 0, \tag{5.4.6b}$$

$$-\nabla \cdot (\kappa_\varepsilon(x)\nabla\phi^s_\varepsilon) = 0 \tag{5.4.6c}$$

where $c^e_\varepsilon(x), \phi^e_\varepsilon(x) : \left(\Omega^e_{anode/cathode}\right)^\varepsilon \longrightarrow \mathbb{R}$ and $\phi^s_\varepsilon(x) : \Omega^\varepsilon_s \longrightarrow \mathbb{R}$. We want to find the asymptotic limits of the resulting sequences of partial differential equations when ε goes to zero. For both perforated domains - the electrolyte phase and the solid phase, $\varepsilon \to 0$

is equivalent to the respective porous medium converging to a homogeneous one with no holes inside. This means that we look for a limit partial diffrential equation when $\varepsilon \to 0$ with effective transport coefficients, posed in a homogeneous domain where we do not distinguish anymore between perforated material and voids. Consequently, in contrast to problem (5.4.6), the solutions of the respective homogenized equations will be continuous functions defined for all $x \in \Omega_{electrode}$. Therefore, the homogenization reduces significantly the computational cost for the numerical solution of the problem because we need much coarser mesh and respectively less degrees of freedom for the homogenized problem compared to the high resolution, and respectively large number of degrees of freedom, that we would need to mesh the perforated domain in order to solve the microscale problem. Also, the homogenized problem is easy to solve numerically in contrast to the microscale one which is ill-conditioned and consequently complicated for numerical solving. The partial differential equations are closed with the following set of boundary conditions

$$\phi_\varepsilon^s(x) = E_1^s, \quad x \in \omega_1 \tag{5.4.7}$$
$$-(\kappa_\varepsilon(x)\nabla\phi_\varepsilon^s)\cdot\mathbf{n} = E_2^\varepsilon(x) = \chi_\varepsilon^s(x)E_2^s, \quad x \in \omega_2 \tag{5.4.8}$$
$$\nabla c_\varepsilon^s \cdot \mathbf{n} = 0, \quad x \in \omega_1 \cup \omega_2 \tag{5.4.9}$$
$$\mathbf{N}_\varepsilon^e \cdot \mathbf{n} = \mathbf{J}_\varepsilon^e \cdot \mathbf{n} = 0, \quad x \in \partial\Omega_\varepsilon \tag{5.4.10}$$

and interface conditions

$$-(k_{11}^\varepsilon \nabla c_\varepsilon^e + k_{12}^\varepsilon \nabla\phi_\varepsilon^e)\cdot\mathbf{n_s} = \mathcal{N}_\varepsilon, \quad x \in \gamma_\varepsilon \tag{5.4.11a}$$
$$-(k_{21}^\varepsilon \nabla c_\varepsilon^e + k_{22}^\varepsilon \nabla\phi_\varepsilon^e)\cdot\mathbf{n_s} = \mathcal{J}_\varepsilon, \quad x \in \gamma_\varepsilon \tag{5.4.11b}$$
$$-(\kappa_\varepsilon \nabla\phi_\varepsilon^s)\cdot\mathbf{n_s} = \mathcal{J}_\varepsilon, \quad x \in \gamma_\varepsilon, \tag{5.4.11c}$$

where we denote

$$\mathcal{N}_\varepsilon = \mathcal{N}\left(c_\varepsilon^e, c^s, \phi_\varepsilon^e, \phi_\varepsilon^s\right) \tag{5.4.12}$$
$$\mathcal{J}_\varepsilon = \mathcal{J}\left(c_\varepsilon^e, c^s, \phi_\varepsilon^e, \phi_\varepsilon^s\right) \tag{5.4.13}$$

For $x \in \Omega_{electrode}^\varepsilon$ and $y \in Y$, after the change of variables $x = \varepsilon y$, for the characteristic functions $\chi_\varepsilon^e(x)$ and $\chi_\varepsilon^s(x)$ we obtain

$$\chi_\varepsilon^e(x) = \begin{cases} 1, & x \in \Omega_e^\varepsilon \\ 0, & x \in \Omega_s^\varepsilon \end{cases} = \hat{\chi}^e\left(\frac{x}{\varepsilon}\right) = \hat{\chi}^e(y) = \begin{cases} 1, & y \in E \cup \Gamma \\ 0, & y \in S \end{cases} \tag{5.4.14}$$

and

$$\chi_\varepsilon^s(x) = \begin{cases} 0, & x \in \Omega_e^\varepsilon \\ 1, & x \in \Omega_s^\varepsilon \end{cases} = \hat{\chi}^s\left(\frac{x}{\varepsilon}\right) = \hat{\chi}^s(y) = \begin{cases} 0, & y \in E \\ 1, & y \in S \cup \Gamma, \end{cases} \tag{5.4.15}$$

where $\hat{\chi}^e(y)$ and $\hat{\chi}^s(y)$ are Y-periodic in the y variable functions. We recall that a function $f(x,y)$ is Y-periodic in the y variable if $f(x, y+L) = f(x,y)$, where L is the length of the

two-phase reference periodicity cell. Then, the coefficients in (5.4.6) are defined as follows

$$k_{11}^{\varepsilon}(x,c_{\varepsilon}^{e})=\chi_{\varepsilon}^{e}(x)k_{11}^{e}(c_{\varepsilon}^{e})=\hat{\chi}^{e}(y)k_{11}^{e}(c_{\varepsilon}^{e})=\hat{k}_{11}(y,c_{\varepsilon}^{e})=\begin{cases}k_{11}^{e}(c_{\varepsilon}^{e}), & y\in E\cup\Gamma,\\ 0, & y\in S\end{cases} \tag{5.4.16a}$$

$$k_{12}^{\varepsilon}(x)=\chi_{\varepsilon}^{e}(x)k_{12}^{e}=\hat{\chi}^{e}(y)k_{12}^{e}=\hat{k}_{12}(y)=\begin{cases}k_{12}^{e}, & y\in E\cup\Gamma,\\ 0, & y\in S\end{cases} \tag{5.4.16b}$$

$$k_{21}^{\varepsilon}(x,c_{\varepsilon}^{e})=\chi_{\varepsilon}^{e}(x)k_{21}^{e}(c_{\varepsilon}^{e})=\hat{\chi}^{e}(y)k_{21}^{e}(c_{\varepsilon}^{e})=\hat{k}_{21}(y,c_{\varepsilon}^{e})=\begin{cases}k_{21}^{e}(c_{\varepsilon}^{e}), & y\in E\cup\Gamma,\\ 0, & y\in S\end{cases} \tag{5.4.16c}$$

$$k_{22}^{\varepsilon}(x)=\chi_{\varepsilon}^{e}(x)k_{22}^{e}=\hat{\chi}^{e}(y)k_{22}^{e}=\hat{k}_{22}(y)=\begin{cases}k_{22}^{e}, & y\in E\cup\Gamma,\\ 0, & y\in S\end{cases} \tag{5.4.16d}$$

$$\kappa_{\varepsilon}(x)=\chi_{\varepsilon}^{s}(x)\kappa^{s}=\hat{\chi}^{s}(y)\kappa^{s}=\hat{\kappa}(y)=\begin{cases}0, & y\in E,\\ \kappa^{s}, & y\in S\cup\Gamma\end{cases} \tag{5.4.16e}$$

We suppose the following asymptotic expansions for the functions c_{ε}^{e}, ϕ_{ε}^{e} and ϕ_{ε}^{s}

$$c_{\varepsilon}^{e}(x,t)=c_{0}^{e}(x,t)+\varepsilon c_{1}^{e}\left(x,\frac{x}{\varepsilon},t\right)+\varepsilon^{2}c_{2}^{e}\left(x,\frac{x}{\varepsilon},t\right) \tag{5.4.17}$$

$$\phi_{\varepsilon}^{e}(x,t)=\phi_{0}^{e}(x,t)+\varepsilon\phi_{1}^{e}\left(x,\frac{x}{\varepsilon},t\right)+\varepsilon^{2}\phi_{2}^{e}\left(x,\frac{x}{\varepsilon},t\right) \tag{5.4.18}$$

$$\phi_{\varepsilon}^{s}(x,t)=\phi_{0}^{s}(x,t)+\varepsilon\phi_{1}^{s}\left(x,\frac{x}{\varepsilon},t\right)+\varepsilon^{2}\phi_{2}^{s}\left(x,\frac{x}{\varepsilon},t\right), \tag{5.4.19}$$

where $y=\dfrac{x}{\varepsilon}$ and for the differentiation operator we have

$$\nabla=\nabla_{x}+\frac{1}{\varepsilon}\nabla_{y}. \tag{5.4.20}$$

In the asymptotic expansions (5.4.17), (5.4.18) and (5.4.19) we postulate that the functions c_{0}^{e}, ϕ_{0}^{e} and ϕ_{0}^{s} depend only on the macroscopic (slow) variable x and all the other terms in the expansions are Y-periodic functions in the y variable. The fact that the zero order terms do not depend on the "fast" variable $y=\dfrac{x}{\varepsilon}$ means that we have scale separation for the concentration c^{e} and the potentials ϕ^{e}, and ϕ^{s}. More precisely, $c_{\varepsilon}^{e}(x,t)$ (and $\phi_{\varepsilon}^{e}(x,t)$, and $\phi_{\varepsilon}^{s}(x,t)$, respectively) is the smooth function $c_{0}^{e}(x,t)$ ($\phi_{0}^{e}(x,t)$, and $\phi_{0}^{s}(x,t)$, respectively), which represents the macroscopic behaviour of $c_{\varepsilon}^{e}(x,t)$ (and $\phi_{\varepsilon}^{e}(x,t)$, and $\phi_{\varepsilon}^{s}(x,t)$, respectively), plus a small, highly oscillating term. Let us consider the function $c_{\varepsilon}^{e}(x,t)$ and rewrite its asymptotic expansion (5.4.17) in the following way

$$c_{\varepsilon}^{e}(x,y,t)=c_{0}^{e}(x,t)+\varepsilon c_{1}^{e}\left(x,y,t\right)+\varepsilon^{2}c_{2}^{e}\left(x,y,t\right) \tag{5.4.21}$$

Then, since $c_{1}(x,y,t)$ and $c_{2}(x,y,t)$ are Y-periodic functions, we get that

$$\begin{aligned}c_{\varepsilon}^{e}(x,y+L,t)&=c_{0}^{e}(x,t)+\varepsilon c_{1}^{e}\left(x,y+L,t\right)+\varepsilon^{2}c_{2}^{e}\left(x,y+L,t\right)=\\&=c_{0}^{e}(x,t)+\varepsilon c_{1}^{e}\left(x,y,t\right)+\varepsilon^{2}c_{2}^{e}\left(x,y,t\right)=\\&=c_{\varepsilon}^{e}(x,y,t)\end{aligned} \tag{5.4.22}$$

which means that the function $c_{\varepsilon}^{e}(x,y,t)$, as well as the functions $\phi_{\varepsilon}^{e}(x,y,t)$, and $\phi_{\varepsilon}^{s}(x,y,t)$, are also Y-periodic. Furthermore, since the functions $\hat{\chi}^{e}(y)$ and $\hat{\chi}^{s}(y)$ are Y-periodic, it

follows that in the asymptotic analysis the coefficients (5.4.16) are Y-periodic in the y variable. This periodicity allows us to apply the asymptotic homogenization method in order to upscale equations (5.4.6) and to derive limit partial differential equations for $\varepsilon \to 0$.

To summarize, it is important to note that we can apply the asymptotic homogenization method to the Li-ion battery problem because the following criteria are satisfied:

- The electrode medium has a periodic microstructure with much smaller characteristic length than the size of the electrodes
- Two spatial lengthscales are present in the problem - one accounting for the variations within a single periodicity cell (the so-called "fast" scale), and one accounting for the variations within the domain of the whole electrode (the so-called "slow" scale)
- The coefficients of equations (5.4.6) are Y-periodic functions in the y variable

5.4.2 Approximation of the nonlinear quantities

Let us denote

$$\mathcal{C} = \{c^e(x) | c^e : \Omega_e \longrightarrow \mathbb{R}\} \tag{5.4.23}$$

Consequently we have that

$$k_{11}^e(c^e), k_{21}^e(c^e) : \mathcal{C} \longrightarrow \mathbb{R} \tag{5.4.24}$$

and

$$k_{12}^e, k_{22}^e \in \mathbb{R}, \quad such \quad that \quad k_{12}^e, k_{22}^e > 0 \tag{5.4.25}$$

Since we assume that $c^e(x) > 0 \ \forall x \in \Omega_e$, from (2.3.2) it follows that

$$k_{11}^e(c^e), k_{21}^e(c^e) \in C^\infty(\mathcal{C}) \quad with \tag{5.4.26a}$$

$$k_{11}^e(c^e), k_{21}^e(c^e) > 0, \forall c^e \in \mathcal{C} \tag{5.4.26b}$$

and

$$k_{12}^e, k_{22}^e \in \mathbb{R} \quad with \quad k_{12}^e, k_{22}^e > 0, \quad \forall x \in \Omega_e \tag{5.4.27a}$$

By analogy with (5.4.23) and (5.4.26a), if we denote

$$\mathcal{C}_\varepsilon = \left\{c_\varepsilon^e(x) | c_\varepsilon^e : \left(\Omega_{anode/cathode}^e\right)^\varepsilon \longrightarrow \mathbb{R}\right\} \tag{5.4.28}$$

we have that

$$k_{11}^e(c_\varepsilon^e), k_{21}^e(c_\varepsilon^e) \in C^\infty(\mathcal{C}_\varepsilon) \tag{5.4.29}$$

Since the coefficient $\hat{k}_{11}(y, c_\varepsilon^e) : Y \times \mathcal{C}_\varepsilon \longrightarrow \mathbb{R}$ (and $\hat{k}_{21}(y, c_\varepsilon^e)$, respectively) is defined by

$$\hat{k}_{11}(y, c_\varepsilon^e) = \hat{\chi}^e(y) k_{11}^e(c_\varepsilon^e) = \begin{cases} k_{11}^e(c_\varepsilon^e), & y \in E \cup \Gamma, \\ \\ 0, & y \in S \end{cases} \tag{5.4.30}$$

we need to approximate the function $k_{11}^e(c_\varepsilon^e)$. Therefore, for $y \in Y$, due to (5.4.29) and provided that the coefficient $k_{11}^e(c^e)$ (and $k_{21}^e(c^e)$ respectively) is C^1 with respect to c^e, and taking into account that $\varepsilon \to 0$, we can write the Taylor series of the function $k_{11}^e(c_\varepsilon^e)$ (and $k_{21}^e(c_\varepsilon^e)$ respectively) around the point c_0^e

$$\begin{aligned} k_{11}^e(c_\varepsilon^e) &= k_{11}^e\left(c_0^e(x,t) + \varepsilon c_1^e(x,y,t)\right) = \\ &= k_{11}^e(c_0^e) + \varepsilon c_1^e \frac{\partial k_{11}^e}{\partial c^e}(c_0^e) + \varepsilon^2 (c_1^e)^2 \frac{\partial^2 k_{11}^e}{\partial (c^e)^2}(c_0^e) + \ldots = \\ &= k_{11}^e(c_0^e) + O(\varepsilon) \end{aligned} \tag{5.4.31}$$

Consequently, we obtain that in the asymptotic limit when $\varepsilon \to 0$ we can approximate the nonlinear coefficient $\hat{k}_{11}(y, c_\varepsilon^e)$ with the zero order term of the expansion (5.4.17)

$$\hat{k}_{11}(y, c_\varepsilon^e) \approx \hat{\chi}^e(y) k_{11}^e(c_0^e) = \hat{k}_{11}(y, c_0^e) \tag{5.4.32}$$

By analogy for the interface exchange current density $\mathcal{N}_\varepsilon$ we obtain

$$\begin{aligned} \mathcal{N}_\varepsilon = \mathcal{N}\left(c_\varepsilon^e, c^s, \phi_\varepsilon^e, \phi_\varepsilon^s\right) &= \mathcal{N}\left(c_0^e + \varepsilon c_1^e, c^s, \phi_0^e + \varepsilon \phi_1^e, \phi_0^s + \varepsilon \phi_1^s\right) = \\ \\ &= \mathcal{N}\left(c_0^e, c^s, \phi_0^e, \phi_0^s\right) + \varepsilon c_1^e \frac{\partial \mathcal{N}}{\partial c^e}\left(c_0^e, c^s, \phi_0^e, \phi_0^s\right) + \\ \\ &+ \varepsilon \phi_1^e \frac{\partial \mathcal{N}}{\partial \phi^e}\left(c_0^e, c^s, \phi_0^e, \phi_0^s\right) + \varepsilon \phi_1^s \frac{\partial \mathcal{N}}{\partial \phi^s}\left(c_0^e, c^s, \phi_0^e, \phi_0^s\right) = \\ \\ &= \mathcal{N}\left(c_0^e, c^s, \phi_0^e, \phi_0^s\right) + O(\varepsilon^\alpha) \end{aligned} \tag{5.4.33}$$

with $\alpha \geq 1$ since we do not know what is the order of the function $\mathcal{N}\left(c_0^e, c^s, \phi_0^e, \phi_0^s\right)$ as well as of its first derivatives.

In summary, we approximate the the nonlinear coefficients, as well as the current densities $\mathcal{N}_\varepsilon$ and $\mathcal{J}_\varepsilon$ with the zero order terms of the asymptotic expansions of the concentration c_ε^e and the potentials ϕ_ε^e and ϕ_ε^s:

$$\hat{k}_{i1}(y, c_\varepsilon^e) = \hat{k}_{i1}(y, c_0^e) + O(\varepsilon) \tag{5.4.34}$$

$$\mathcal{N}_\varepsilon = \mathcal{N}\left(c_0^e, c^s, \phi_0^e, \phi_0^s\right) + O(\varepsilon^\alpha) \tag{5.4.35}$$

$$\mathcal{J}_\varepsilon = \mathcal{J}\left(c_0^e, c^s, \phi_0^e, \phi_0^s\right) + O(\varepsilon^\alpha) \tag{5.4.36}$$

where $\alpha \geq 1$ and $i = 1, 2$. We use the following notation for the zero order approximations of the interface exchange current densities

$$\mathcal{N}_0 = \mathcal{N}\left(c_0^e, c^s, \phi_0^e, \phi_0^s\right), \quad \mathcal{J}_0 = \mathcal{J}\left(c_0^e, c^s, \phi_0^e, \phi_0^s\right) \tag{5.4.37}$$

5.4.3 Homogenization procedure

After we substitute the asymptotic expansions (5.4.17), (5.4.18) and (5.4.19), as well as the differentiation operator (5.4.20) into the system of partial differential equations (5.4.6), we group like powers of ε and we obtain a cascade of partial differential equations for each term in the asymptotic expansions. Then we repeat the same procedure for the homogenization of the interface conditions (5.4.11), which is given in detail in the next section. Finally, we couple the $O(\varepsilon^{-1})$ and $O(\varepsilon^0)$ partial differential equations with the respective interface conditions and we derive the auxiliary cell problems and the homogenized model equations, respectively.

5.4.4 Homogenization of the interface conditions

Determining the asymptotic order of the interface exchange current densities

First we show that in each electrode the total flux over the whole interface boundary is preserved with respect to a change of the total interface surface. A similar idea is applied in [5] and [6] in order for the total flux across the interfaces to be properly scaled. In the asymptotic analysis of the problem we denote with γ_a^ε the interface boundary between the active particles and the electrolyte in the anode and with γ_c^ε - the interface boundary between the particles and the electrolyte in the cathode. Then we have that $\gamma_\varepsilon = \gamma_a^\varepsilon$ or γ_c^ε. Now we consider the equation for ϕ_ε^s in the cathode particles domain $\Omega_c^\varepsilon \subset \Omega_s^\varepsilon$ (and consequently $\chi_\varepsilon^s(x) = 1$ for $x \in \Omega_c^\varepsilon$) where we apply constant electrical current on the outer boundary $\omega_2 \cap \partial\Omega_c^\varepsilon$, i.e., we have the following boundary value problem

$$-\nabla \cdot (\kappa^s \nabla \phi_\varepsilon^s) = 0, \quad x \in \Omega_c^\varepsilon \tag{5.4.38a}$$

$$-\kappa^s \nabla \phi_\varepsilon^s \cdot \mathbf{n} = E_2^s, \quad x \in \{\omega_2 \cap \partial\Omega_c^\varepsilon\} \tag{5.4.38b}$$

$$-\kappa^s \nabla \phi_\varepsilon^s \cdot \mathbf{n} = 0, \quad x \in \partial\Omega_c^\varepsilon \tag{5.4.38c}$$

$$-\kappa^s \nabla \phi_\varepsilon^s \cdot \mathbf{n}_s = \mathcal{J}_\varepsilon, \quad x \in \gamma_c^\varepsilon. \tag{5.4.38d}$$

We integrate both sides of equation (5.4.38a) over the domain of the cathode particles Ω_c^ε. Then we apply the divergence theorem and after we account for the boundary conditions (5.4.38b) and (5.4.38c), as well as for the interface condition (5.4.38d), we obtain

$$\int\limits_{\Omega_c^\varepsilon} -\nabla \cdot (\kappa^s \nabla \phi_\varepsilon^s)\, dx = 0 \Leftrightarrow \int\limits_{\partial\Omega_c^\varepsilon} -\kappa^s \nabla \phi_\varepsilon^s \cdot \mathbf{n}\, ds = 0 \Leftrightarrow$$

$$\int\limits_{\gamma_c^\varepsilon} \mathcal{J}_\varepsilon\, ds + \int\limits_{\omega_2 \cap \partial\Omega_c^\varepsilon} E_2^s\, ds = 0 \Leftrightarrow \int\limits_{\gamma_c^\varepsilon} \mathcal{J}_\varepsilon\, ds = -|\omega_2 \cap \partial\Omega_c^\varepsilon| E_2^s. \tag{5.4.39}$$

We will show that the measure of $\omega_2 \cap \partial\Omega_c^\varepsilon$ does not change when we uniformly decrease the size of the periodicity cell. This means that the measure $\omega_2 \cap \partial\Omega_c^\varepsilon$ is constant with respect to ε. Even though this is true for random geometry of the solid domain in the periodicity cell, we will restrict our calculations to the type of exemplary active material domain that we consider (see Figure 5.2). In the case $\varepsilon = 1$ we have only one periodicity cell in each electrode and it coincides with the whole electrode. Taking into account

the type of particles we have (see Figure 5.2), it is clear that the intersection of a single particle with the outer battery cell boundary ω_1 or ω_2, is a circle. Let us denote the radius of this circle for $\varepsilon = 1$ with R_1. Therefore, for the measure of the cathode outer boundary we obtain (see Figure 5.3) $S_1 = |\omega_2 \cap \partial\Omega_c^\varepsilon| = \pi R_1^2$. Now let us decrease ε in such a way that we decrease the length of the periodicity cell twice. This means that in each electrode we will have 8 periodicity cells and thus 8 active particles. The side length of each periodicity cell is then $\frac{L}{2}$. Let us denote with R_2 the radius of the circle obtained from the intersection of the cathode particle with the outer boundary ω_2 (see Figure 5.3). Then $S_2 = |\omega_2 \cap \partial\Omega_c^\varepsilon| = 4\pi R_2^2$. Now taking into account that $\frac{R_2}{\frac{L}{2}} = \frac{R_1}{L}$, we obtain that $R_2 = \frac{R_1}{2}$ and consequently $S_2 = 4\pi\frac{R_1^2}{4} = \pi R_1^2 = S_1$. Thus we obtain that the measure $|\omega_2 \cap \partial\Omega_c^\varepsilon|$ does not change when we uniformly decrease ε, which together with (5.4.39) means that the total electrical flux across the interface is a constant and does not depend on ε.

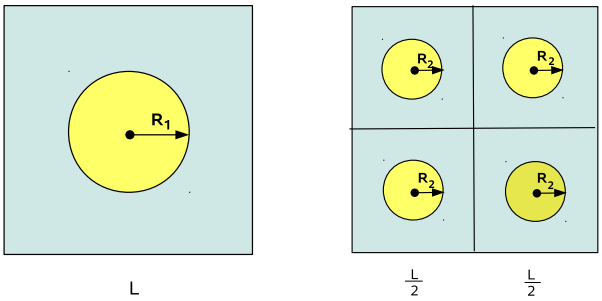

a. $\varepsilon = 1$ b. $\varepsilon = 0.5$

Figure 5.3: Cathode outer boundary given in yellow

From equation (5.4.6b), after we integrate over the electrolyte domain Ω_e^ε and apply the divergence theorem, we obtain

$$\int\limits_{\Omega_e^\varepsilon} \nabla \cdot \mathbf{J}_\varepsilon^e \, dx = 0 \Longleftrightarrow \underbrace{\int\limits_{\partial\Omega^\varepsilon \cap \partial\Omega_e^\varepsilon} \mathbf{J}_\varepsilon^e \cdot \mathbf{n} \, ds}_{=0} + \int\limits_{\gamma_\varepsilon} \mathbf{J}_\varepsilon^e \cdot \mathbf{n} \, ds = 0 \Longleftrightarrow$$

$$-\int\limits_{\gamma_\varepsilon} \underbrace{\mathbf{J}_\varepsilon^e \cdot \mathbf{n}_s}_{=-\mathcal{J}_\varepsilon} ds = 0 \Longleftrightarrow \int\limits_{\gamma_\varepsilon} \mathcal{J}_\varepsilon \, ds = 0 \Longleftrightarrow$$

$$\int\limits_{\gamma_a^\varepsilon} \mathcal{J}_\varepsilon \, ds + \int\limits_{\gamma_c^\varepsilon} \mathcal{J}_\varepsilon \, ds = 0 \Longleftrightarrow \int\limits_{\gamma_a^\varepsilon} \mathcal{J}_\varepsilon \, ds = -\int\limits_{\gamma_c^\varepsilon} \mathcal{J}_\varepsilon \, ds. \tag{5.4.40}$$

Consequently the electric current across the electrolyte-solid interface in the cathode is equal to the electric current in the anode. Then from (5.4.39) it follows that the electric current in the anode is also constant with respect to the small parameter ε. From (2.5.4) we have the following relation between the current density $\mathcal{J}$ and the flux $\mathcal{N}$ of Li+

$$\mathcal{J} = F\mathcal{N}$$

and consequently we obtain that

$$\int\limits_{\gamma_a^\varepsilon} \mathcal{N}_\varepsilon \, ds = \frac{1}{F} \int\limits_{\gamma_a^\varepsilon} \mathcal{J}_\varepsilon \, ds = \frac{1}{F} |\omega_2 \cap \partial\Omega_c^\varepsilon| E_2^s \tag{5.4.41}$$

$$\int\limits_{\gamma_c^\varepsilon} \mathcal{N}_\varepsilon \, ds = \frac{1}{F} \int\limits_{\gamma_c^\varepsilon} \mathcal{J}_\varepsilon \, ds = -\frac{1}{F} |\omega_2 \cap \partial\Omega_c^\varepsilon| E_2^s \tag{5.4.42}$$

which means that also the total flux of lithium ions across the electrolyte-particle interface in each electrode is a constant that does not depend on ε.
Let Π_ε be a parametrically defined surface in the three dimensionsional Euclidean space. Then we have the following formula for the change of variables $y = \dfrac{x}{\varepsilon}$

$$\int\limits_{\Pi_\varepsilon} f(x) \, ds_x = \varepsilon^2 \int\limits_{\Pi} g(y) \, ds_y, \tag{5.4.43}$$

where

$$f(x) = f(x(y)) = f(\varepsilon y) = g(y) \tag{5.4.44}$$

and the surface Π_ε transforms into the surface Π after the change of variables.
Now, for the functions $c_\varepsilon^e(x)$, $\phi_\varepsilon^e(x)$ and $\phi_\varepsilon^s(x)$ (here we intentionally omit the time dependence of the functions since it is not relevant for the spatial homogenization of the problem), given from (5.4.17), (5.4.18) and (5.4.19), after the subsequent changes of variables $y = \dfrac{x}{\varepsilon}$ and $y' = y + \xi_i$ (with ξ_i being a fixed vector for all $y \in Y_i$), we have

$$c_\varepsilon^e(x) = C_\varepsilon^e(y) = \hat{C}_\varepsilon^e(y') \tag{5.4.45a}$$

$$\phi_\varepsilon^e(x) = \Phi_\varepsilon^e(y) = \hat{\Phi}_\varepsilon^e(y') \tag{5.4.45b}$$

$$\phi_\varepsilon^s(x) = \Phi_\varepsilon^s(y) = \hat{\Phi}_\varepsilon^s(y') \tag{5.4.45c}$$

and for the concentration c^s of ions in the particles we obtain

$$c^s(x) = C^s(y) = \hat{C}^s(y'). \tag{5.4.46}$$

We recall that we denote with Γ_i^ε the interface boundary for each periodicity cell Y_i^ε and with $\gamma_\varepsilon = \bigcup\limits_{i=1}^{M} \Gamma_i^\varepsilon$ the whole interface boundary in the electrode. The electrode is a cube with length of the side L, or a parallelepiped with a charcteristic length of the sides L. Therefore the total number of all microscopic periodicity cells in the electrode is of order $\left(\dfrac{L}{l}\right)^3 = \dfrac{1}{\varepsilon^3}$, i.e., $M \sim O\left(\dfrac{1}{\varepsilon^3}\right)$. Then, for the total flux across the whole interface

boundary γ_ε in the asymptotic analysis we obtain

$$
\begin{aligned}
I &= \int\limits_{\gamma_\varepsilon} -\left(k_{11}^{\varepsilon}\nabla c_\varepsilon^e + k_{12}^{\varepsilon}\nabla\phi_\varepsilon^e\right)\cdot\mathbf{n_s}\,ds_x = \int\limits_{\gamma_\varepsilon}\mathcal{N}_\varepsilon\,ds_x = \\
&= \sum_{i=1}^{M}\int\limits_{\Gamma_i^\varepsilon}\mathcal{N}\left(c_\varepsilon^e(x), c^s(x), \phi_\varepsilon^e(x), \phi_\varepsilon^s(x)\right)\,ds_x = \\
&= \sum_{i=1}^{M}\varepsilon^2\int\limits_{\Gamma_i}\mathcal{N}\left(C_\varepsilon^e(y), C^s(y), \Phi_\varepsilon^e(y), \Phi_\varepsilon^s(y)\right)\,ds_y = \\
&= \sum_{i=1}^{M}\left(\varepsilon^2\int\limits_{\Gamma}\mathcal{N}\left(\hat{C}_\varepsilon^e(y'), \hat{C}^s(y'), \hat{\Phi}_\varepsilon^e(y'), \hat{\Phi}_\varepsilon^s(y')\right)\,ds_{y'}\right) = \\
&= O\left(\frac{1}{\varepsilon^3}\right)\left(\varepsilon^2\int\limits_{\Gamma}\mathcal{N}\left(\hat{C}_\varepsilon^e(y'), \hat{C}^s(y'), \hat{\Phi}_\varepsilon^e(y'), \hat{\Phi}_\varepsilon^s(y')\right)\,ds_{y'}\right) = \\
&= O\left(\frac{1}{\varepsilon}\right)\int\limits_{\Gamma}\mathcal{N}\left(\hat{C}_\varepsilon^e(y'), \hat{C}^s(y'), \hat{\Phi}_\varepsilon^e(y'), \hat{\Phi}_\varepsilon^s(y')\right)\,ds_{y'}. \qquad (5.4.47)
\end{aligned}
$$

We showed that the total flux across the interface does not depend on ε (see (5.4.41) and (5.4.42)). Consequently, the total flux I does not depend on ε if and only if

$$\mathcal{N}\left(\hat{C}_\varepsilon^e(y'), \hat{C}^s(y'), \hat{\Phi}_\varepsilon^e(y'), \hat{\Phi}_\varepsilon^s(y')\right) = O(\varepsilon) \qquad (5.4.48)$$

which due to (5.4.45) is equivalent to

$$\mathcal{N}_\varepsilon = \mathcal{N}\left(c_\varepsilon^e(x), c^s(x), \phi_\varepsilon^e(x), \phi_\varepsilon^s(x)\right) = O(\varepsilon). \qquad (5.4.49)$$

From (5.4.35) we have that

$$\mathcal{N}_\varepsilon = \mathcal{N}\left(c_0^e, c^s, \phi_0^e, \phi_0^s\right) + O(\varepsilon^\alpha) \qquad (5.4.50)$$

which together with (5.4.49) gives

$$\mathcal{N}_0 = \mathcal{N}\left(c_0^e, c^s, \phi_0^e, \phi_0^s\right) = O(\varepsilon). \qquad (5.4.51)$$

Thus we obtained that the interface exchange current densities $\mathcal{N}_\varepsilon$ and $\mathcal{J}_\varepsilon$, as well as $\mathcal{N}_0$ and $\mathcal{J}_0$, are of order ε.

Grouping like powers of ε

Finally, for the homogenization of the interface conditions we obtain

$$
\begin{aligned}
&\mathcal{N}_\varepsilon = \mathbf{N}_\varepsilon^{\mathbf{e}}\cdot\mathbf{n_s} = -\left\{\hat{k}_{11}\left(y, c_\varepsilon^e\right)\nabla c_\varepsilon^e + \hat{k}_{12}(y)\nabla\phi_\varepsilon^e\right\}\cdot\mathbf{n_s} = \\
&-\left\{\hat{k}_{11}\left(y, c_0^e\right)\left(\nabla_x + \frac{1}{\varepsilon}\nabla_y\right)\left(c_0^e + \varepsilon c_1^e + \varepsilon^2 c_2^e\right) + \hat{k}_{12}(y)\left(\nabla_x + \frac{1}{\varepsilon}\nabla_y\right)\left(\phi_0^e + \varepsilon\phi_1^e + \varepsilon^2\phi_2^e\right)\right\}\cdot\mathbf{n_s} \qquad (5.4.52)
\end{aligned}
$$

which is equivalent to

$$\frac{1}{\varepsilon}\mathcal{N}_\varepsilon = -\Bigg[\quad \frac{1}{\varepsilon^2}\left(\hat{k}_{11}\left(y, c_0^e\right)\nabla_y c_0^e + \hat{k}_{12}(y)\nabla_y \phi_0^e\right) +$$

$$\frac{1}{\varepsilon}\left(\hat{k}_{11}\left(y, c_0^e\right)\left(\nabla_x c_0^e + \nabla_y c_1^e\right) + \hat{k}_{12}(y)\left(\nabla_x \phi_0^e + \nabla_y \phi_1^e\right)\right) +$$

$$\varepsilon^0\left(\hat{k}_{11}\left(y, c_0^e\right)\left(\nabla_x c_1^e + \nabla_y c_2^e\right) + \hat{k}_{12}(y)\left(\nabla_x \phi_1^e + \nabla_y \phi_2^e\right)\right) +$$

$$\varepsilon(\ldots)\Bigg] \cdot \mathbf{n_s}. \tag{5.4.53}$$

Now taking into account that $\mathcal{N}_0 = \mathcal{N}\left(c_0^e, c^s, \phi_0^e, \phi_0^s\right) = O(\varepsilon)$, it follows that $\frac{1}{\varepsilon}\mathcal{N}_0 = O(1)$. Then, by grouping equal powers of ε, we obtain

$$\varepsilon^{-2}: \quad \left[\hat{k}_{11}\left(y, c_0^e\right)\underbrace{\nabla_y c_0^e}_{=0} + \hat{k}_{12}(y)\underbrace{\nabla_y \phi_0^e}_{=0}\right] \cdot \mathbf{n_s} = 0 \Longleftrightarrow 0 = 0 \tag{5.4.54a}$$

$$\varepsilon^{-1}: \quad \left[\hat{k}_{11}\left(y, c_0^e\right)\left(\nabla_x c_0^e + \nabla_y c_1^e\right) + \hat{k}_{12}(y)\left(\nabla_x \phi_0^e + \nabla_y \phi_1^e\right)\right] \cdot \mathbf{n_s} = 0 \tag{5.4.54b}$$

$$\varepsilon^0: \quad -\left[\hat{k}_{11}\left(y, c_0^e\right)\nabla_x c_1^e + \hat{k}_{11}\left(y, c_0^e\right)\nabla_y c_2^e + \hat{k}_{12}(y)\nabla_x \phi_1^e + \hat{k}_{12}(y)\nabla_y \phi_2^e\right] \cdot \mathbf{n_s} =$$
$$= \frac{1}{\varepsilon}\mathcal{N}\left(c_0^e, c^s, \phi_0^e, \phi_0^s\right), \tag{5.4.54c}$$

where we account for the fact that the functions c_0^e and ϕ_0^e depend only on x and do not depend on y. By analogy, from $\mathbf{J}_\varepsilon^{\mathbf{e}} \cdot \mathbf{n_s} = \mathcal{J}_\varepsilon$ we obtain

$$\varepsilon^{-2}: \quad \left[\hat{k}_{21}\left(y, c_0^e\right)\underbrace{\nabla_y c_0^e}_{=0} + \hat{k}_{22}(y)\underbrace{\nabla_y \phi_0^e}_{=0}\right] \cdot \mathbf{n_s} = 0 \Longleftrightarrow 0 = 0 \tag{5.4.55a}$$

$$\varepsilon^{-1}: \quad \left[\hat{k}_{21}\left(y, c_0^e\right)\left(\nabla_x c_0^e + \nabla_y c_1^e\right) + \hat{k}_{22}(y)\left(\nabla_x \phi_0^e + \nabla_y \phi_1^e\right)\right] \cdot \mathbf{n_s} = 0 \tag{5.4.55b}$$

$$\varepsilon^0: \quad -\left[\hat{k}_{21}\left(y, c_0^e\right)\nabla_x c_1^e + \hat{k}_{21}\left(y, c_0^e\right)\nabla_y c_2^e + \hat{k}_{22}(y)\nabla_x \phi_1^e + \hat{k}_{22}(y)\nabla_y \phi_2^e\right] \cdot \mathbf{n_s} =$$
$$= \frac{1}{\varepsilon}\mathcal{J}\left(c_0^e, c^s, \phi_0^e, \phi_0^s\right) \tag{5.4.55c}$$

We account for the upscaled interface conditions (5.4.54c) and (5.4.55c) in the final step of the homogenization procedure, when we average with respect to y the differential equations obtained by grouping like powers of order ε^0.

5.4.5 Homogenization of the electrolyte phase equations

First we consider the electrolyte phase equations (5.4.6a)-(5.4.6b), and, more precisely, we start with equation (5.4.6a). Since

$$\begin{aligned}\frac{\partial\left(\chi_\varepsilon^e(x)c_\varepsilon^e\right)}{\partial t} &= \frac{\partial\left(\hat{\chi}^e(y)c_\varepsilon^e\right)}{\partial t} = \frac{\partial}{\partial t}\left(\hat{\chi}^e(y)\left(c_0^e(x,t)+\varepsilon c_1^e\left(x,y,t\right)+\varepsilon^2 c_2^e\left(x,y,t\right)\right)\right) = \\ &= \frac{\partial}{\partial t}\left(\hat{\chi}^e(y)c_0^e(x,t)\right)+\varepsilon\frac{\partial}{\partial t}\left(\hat{\chi}^e(y)c_1^e\left(x,y,t\right)\right)+\varepsilon^2\frac{\partial}{\partial t}\left(\hat{\chi}^e(y)c_2^e\left(x,y,t\right)\right) = \\ &= \frac{\partial\left(\hat{\chi}^e(y)\partial c_0\right)}{\partial t}+O(\varepsilon),\end{aligned}$$

we can approximate the time derivative with the zero order term of the concentration c_ε^e, i.e., we take $\frac{\partial\left(\chi_\varepsilon^e(x)c_\varepsilon^e\right)}{\partial t} \approx \frac{\partial\left(\hat{\chi}^e(y)c_0\right)}{\partial t}$. We have that $y \in Y = E \cup S$ and $x \in \Omega$. Therefore for equation (5.4.6a) we obtain

$$\frac{\partial\left(\hat{\chi}^e(y)c_0\right)}{\partial t} = \nabla\cdot\left(k_{11}^\varepsilon\left(x,c_\varepsilon^e\right)\nabla c_\varepsilon^e + k_{12}^\varepsilon(x)\nabla\phi_\varepsilon^e\right) =$$

$$= \left(\nabla_x+\frac{1}{\varepsilon}\nabla_y\right)\cdot\left[\hat{k}_{11}(y,c_0^e)\left(\nabla_x+\frac{1}{\varepsilon}\nabla_y\right)\left(c_0^e(x,t)+\varepsilon c_1^e(x,y,t)+\varepsilon^2 c_2^e(x,y,t)\right)+\right.$$

$$\left.+\,\hat{k}_{12}(y)\left(\nabla_x+\frac{1}{\varepsilon}\nabla_y\right)\left(\phi_0^e(x,t)+\varepsilon\phi_1^e(x,y,t)+\varepsilon^2\phi_2^e(x,y,t)\right)\right] =$$

$$= \left(\nabla_x+\frac{1}{\varepsilon}\nabla_y\right)\cdot\left[\hat{k}_{11}(y,c_0^e)\nabla_x c_0^e+\varepsilon\hat{k}_{11}(y,c_0^e)\nabla_x c_1^e+\varepsilon^2\hat{k}_{11}(y,c_0^e)\nabla_x c_2^e+\frac{1}{\varepsilon}\hat{k}_{11}(y,c_0^e)\nabla_y c_0^e+\right.$$

$$+\,\hat{k}_{11}(y,c_0^e)\nabla_y c_1^e+\varepsilon\hat{k}_{11}(y,c_0^e)\nabla_y c_2^e+\hat{k}_{12}(y)\nabla_x\phi_0^e+\varepsilon\hat{k}_{12}(y)\nabla_x\phi_1^e+\varepsilon^2\hat{k}_{12}(y)\nabla_x\phi_2^e+$$

$$\left.+\,\frac{1}{\varepsilon}\hat{k}_{12}(y)\nabla_y\phi_0^e+\hat{k}_{12}(y)\nabla_y\phi_1^e+\varepsilon\hat{k}_{12}(y)\nabla_y\phi_2^e\right] =$$

$$= \left(\nabla_x+\frac{1}{\varepsilon}\nabla_y\right)\cdot\left\{\hat{k}_{11}(y,c_0^e)\left(\nabla_x c_0^e+\nabla_y c_1^e\right)+\hat{k}_{12}(y)\left(\nabla_x\phi_0^e+\nabla_y\phi_1^e\right)+\right.$$

$$+\,\varepsilon\left[\hat{k}_{11}(y,c_0^e)\left(\nabla_x c_1^e+\nabla_y c_2^e\right)+\hat{k}_{12}(y)\left(\nabla_x\phi_1^e+\nabla_y\phi_2^e\right)\right]+$$

$$\left.+\,\varepsilon^2\left(\hat{k}_{11}(y,c_0^e)\nabla_x c_2^e+\hat{k}_{12}(y)\nabla_x\phi_2^e\right)+\frac{1}{\varepsilon}\left(\hat{k}_{11}(y,c_0^e)\nabla_y c_0^e+\hat{k}_{12}(y)\nabla_y\phi_0^e\right)\right\} =$$

$$
\begin{aligned}
&= \frac{1}{\varepsilon^2}\nabla_y \cdot \left\{ \hat{k}_{11}(y, c_0^e)\nabla_y c_0^e + \hat{k}_{12}(y)\nabla_y \phi_0^e \right\} + \\
&+ \frac{1}{\varepsilon}\left\{ \nabla_x \cdot \left(\hat{k}_{11}(y, c_0^e)\nabla_y c_0^e + \hat{k}_{12}(y)\nabla_y \phi_0^e \right) + \right. \\
&+ \quad \left. \nabla_y \cdot \left(\hat{k}_{11}(y, c_0^e)\nabla_x c_0^e + \hat{k}_{11}(y, c_0^e)\nabla_y c_1^e + \hat{k}_{12}(y)\nabla_x \phi_0^e + \hat{k}_{12}(y)\nabla_y \phi_1^e \right) \right\} + \\
&+ \varepsilon^0 \left\{ \nabla_x \cdot \left[\hat{k}_{11}(y, c_0^e)\nabla_x c_0^e + \hat{k}_{11}(y, c_0^e)\nabla_y c_1^e + \hat{k}_{12}(y)\nabla_x \phi_0^e + \hat{k}_{12}(y)\nabla_y \phi_1^e \right] + \right. \\
&+ \quad \left. \nabla_y \cdot \left[\hat{k}_{11}(y, c_0^e)\nabla_x c_1^e + \hat{k}_{11}(y, c_0^e)\nabla_y c_2^e + \hat{k}_{12}(y)\nabla_x \phi_1^e + \hat{k}_{12}(y)\nabla_y \phi_2^e \right] \right\} + \\
&+ \varepsilon \left\{ \nabla_x \cdot \left(\hat{k}_{11}(y, c_0^e)\nabla_x c_1^e + \hat{k}_{11}(y, c_0^e)\nabla_y c_2^e + \hat{k}_{12}(y)\nabla_x \phi_1^e + \hat{k}_{12}(y)\nabla_y \phi_2^e \right) + \right. \\
&+ \quad \left. \nabla_y \cdot \left(\hat{k}_{11}(y, c_0^e)\nabla_x c_2^e + \hat{k}_{12}(y)\nabla_x \phi_2^e \right) \right\} + \\
&+ \varepsilon^2 \nabla_x \cdot \left\{ \hat{k}_{11}(y, c_0^e)\nabla_x c_2^e + \hat{k}_{12}(y)\nabla_x \phi_2^e \right\}
\end{aligned} \tag{5.4.56}
$$

which is equivalent to

$$
\begin{aligned}
\frac{\partial \left(\hat{\chi}^e(y) c_0\right)}{\partial t} =& \varepsilon^{-2}\nabla_y \cdot \left\{ \hat{k}_{11}(y, c_0^e)\nabla_y c_0^e + \hat{k}_{12}(y)\nabla_y \phi_0^e \right\} + \\
&+ \varepsilon^{-1}\left\{ \nabla_x \cdot \left(\hat{k}_{11}(y, c_0^e)\nabla_y c_0^e + \hat{k}_{12}(y)\nabla_y \phi_0^e \right) + \right. \\
&+ \quad \left. \nabla_y \cdot \left(\hat{k}_{11}(y, c_0^e)\nabla_x c_0^e + \hat{k}_{11}(y, c_0^e)\nabla_y c_1^e + \hat{k}_{12}(y)\nabla_x \phi_0^e + \hat{k}_{12}(y)\nabla_y \phi_1^e \right) \right\} + \\
&+ \varepsilon^0 \left\{ \nabla_x \cdot \left[\hat{k}_{11}(y, c_0^e)\nabla_x c_0^e + \hat{k}_{11}(y, c_0^e)\nabla_y c_1^e + \hat{k}_{12}(y)\nabla_x \phi_0^e + \hat{k}_{12}(y)\nabla_y \phi_1^e \right] + \right. \\
&+ \quad \left. \nabla_y \cdot \left[\hat{k}_{11}(y, c_0^e)\nabla_x c_1^e + \hat{k}_{11}(y, c_0^e)\nabla_y c_2^e + \hat{k}_{12}(y)\nabla_x \phi_1^e + \hat{k}_{12}(y)\nabla_y \phi_2^e \right] \right\} + \\
&+ O(\varepsilon)
\end{aligned} \tag{5.4.57}
$$

Now, after we match equal powers of ε from both sides of the latter equality, and after we take into account the fact that $\nabla_y c_0^e = 0$, and $\nabla_y \phi_0^e = 0$, we obtain

$$\varepsilon^{-2}: \quad \nabla_y \cdot \left(\hat{k}_{11}(y, c_0^e) \underbrace{\nabla_y c_0^e}_{=0} + \hat{k}_{12}(y) \underbrace{\nabla_y \phi_0^e}_{=0} \right) = 0 \Longleftrightarrow 0 = 0 \tag{5.4.58a}$$

$$\varepsilon^{-1}: \quad \nabla_y \cdot \left(\hat{k}_{11}(y, c_0^e) \nabla_x c_0^e + \hat{k}_{11}(y, c_0^e) \nabla_y c_1^e + \hat{k}_{12}(y) \nabla_x \phi_0^e + \hat{k}_{12}(y) \nabla_y \phi_1^e \right) = 0 \tag{5.4.58b}$$

$$\begin{aligned} \varepsilon^{0}: \quad \hat{\chi}^e(y) \frac{\partial c_0^e}{\partial t} = \nabla_x \cdot \left[\hat{k}_{11}(y, c_0^e) \nabla_x c_0^e + \hat{k}_{11}(y, c_0^e) \nabla_y c_1^e + \hat{k}_{12}(y) \nabla_x \phi_0^e + \hat{k}_{12}(y) \nabla_y \phi_1^e \right] + \\ + \nabla_y \cdot \left[\hat{k}_{11}(y, c_0^e) \nabla_x c_1^e + \hat{k}_{11}(y, c_0^e) \nabla_y c_2^e + \hat{k}_{12}(y) \nabla_x \phi_1^e + \hat{k}_{12}(y) \nabla_y \phi_2^e \right] \end{aligned} \tag{5.4.58c}$$

We have analogous result for the second partial differential equation (5.4.6b) from the electrolyte system of equations

$$\varepsilon^{-2}: \quad \nabla_y \cdot \left(\hat{k}_{21}(y, c_0^e) \underbrace{\nabla_y c_0^e}_{=0} + \hat{k}_{22}(y) \underbrace{\nabla_y \phi_0^e}_{=0} \right) = 0 \Longleftrightarrow 0 = 0 \tag{5.4.59a}$$

$$\varepsilon^{-1}: \quad \nabla_y \cdot \left(\hat{k}_{21}(y, c_0^e) \nabla_x c_0^e + \hat{k}_{21}(y, c_0^e) \nabla_y c_1^e + \hat{k}_{22}(y) \nabla_x \phi_0^e + \hat{k}_{22}(y) \nabla_y \phi_1^e \right) = 0 \tag{5.4.59b}$$

$$\begin{aligned} \varepsilon^{0}: \quad 0 = \nabla_x \cdot \left[\hat{k}_{21}(y, c_0^e) \nabla_x c_0^e + \hat{k}_{21}(y, c_0^e) \nabla_y c_1^e + \hat{k}_{22}(y) \nabla_x \phi_0^e + \hat{k}_{22}(y) \nabla_y \phi_1^e \right] + \\ + \nabla_y \cdot \left[\hat{k}_{21}(y, c_0^e) \nabla_x c_1^e + \hat{k}_{21}(y, c_0^e) \nabla_y c_2^e + \hat{k}_{22}(y) \nabla_x \phi_1^e + \hat{k}_{22}(y) \nabla_y \phi_2^e \right] \end{aligned} \tag{5.4.59c}$$

Order ε^{-1}: Derivation of the auxiliary cell problems

From the ε^{-1} order partial differential equations (5.4.58b) and (5.4.59b), we obtain the following system of equations for $y \in Y$ and $x \in \Omega$

$$\nabla_y \cdot \left(\hat{k}_{11}(y, c_0^e) \nabla_x c_0^e + \hat{k}_{11}(y, c_0^e) \nabla_y c_1^e + \hat{k}_{12}(y) \nabla_x \phi_0^e + \hat{k}_{12}(y) \nabla_y \phi_1^e \right) = 0 \tag{5.4.60a}$$

$$\nabla_y \cdot \left(\hat{k}_{21}(y, c_0^e) \nabla_x c_0^e + \hat{k}_{21}(y, c_0^e) \nabla_y c_1^e + \hat{k}_{22}(y) \nabla_x \phi_0^e + \hat{k}_{22}(y) \nabla_y \phi_1^e \right) = 0 \tag{5.4.60b}$$

where we think of the functions $c_1^e(x, y, t)$ and $\phi_1^e(x, y, t)$ as the unknowns with $c_0^e(x, t)$ and $\phi_0^e(x, t)$ being given functions and x, and t being parameters. The system of equations

(5.4.60) is equivalent to

$$\nabla_y \cdot \left(\hat{k}_{11}(y, c_0^e)\nabla_y c_1^e + \hat{k}_{12}(y)\nabla_y \phi_1^e\right) = -\nabla_y \cdot \left(\hat{k}_{11}(y, c_0^e)\nabla_x c_0^e + \hat{k}_{12}(y)\nabla_x \phi_0^e\right) \quad (5.4.61a)$$

$$\nabla_y \cdot \left(\hat{k}_{21}(y, c_0^e)\nabla_y c_1^e + \hat{k}_{22}(y)\nabla_y \phi_1^e\right) = -\nabla_y \cdot \left(\hat{k}_{21}(y, c_0^e)\nabla_x c_0^e + \hat{k}_{22}(y)\nabla_x \phi_0^e\right) \quad (5.4.61b)$$

with the following boundary conditions for $y \in \Gamma$

$$\left(\hat{k}_{11}(y, c_0^e)\nabla_y c_1^e + \hat{k}_{12}(y)\nabla_y \phi_1^e\right) \cdot \mathbf{n}_s = -\left(\hat{k}_{11}(y, c_0^e)\nabla_x c_0^e + \hat{k}_{12}(y)\nabla_x \phi_0^e\right) \cdot \mathbf{n}_s \quad (5.4.62a)$$

$$\left(\hat{k}_{21}(y, c_0^e)\nabla_y c_1^e + \hat{k}_{22}(y)\nabla_y \phi_1^e\right) \cdot \mathbf{n}_s = -\left(\hat{k}_{21}(y, c_0^e)\nabla_x c_0^e + \hat{k}_{22}(y)\nabla_x \phi_0^e\right) \cdot \mathbf{n}_s \quad (5.4.62b)$$

which are the interface conditions (5.4.54b) and (5.4.55b), corresponding to the ε^{-1} order of the asymptotic analysis.
We look for the solution of system (5.4.61) in the following scale separable form

$$c_1^e(x, y, t) = \sum_{i=1}^{3} \frac{\partial c_0^e}{\partial x_i}(x, t) w_i(y) \quad (5.4.63a)$$

$$\phi_1^e(x, y, t) = \sum_{i=1}^{3} \frac{\partial \phi_0^e}{\partial x_i}(x, t) \psi_i(y) \quad (5.4.63b)$$

where $w_i(y)$ and $\psi_i(y)$, for $i = 1, 2, 3$, are Y-periodic functions in the y variable.
Now we substitute the functions c_1^e and ϕ_1^e with their scale separable representation (5.4.63) in the system of equations (5.4.61)

$$\left|\begin{array}{l} \nabla_y \cdot \left(\hat{k}_{11}(y, c_0^e) \displaystyle\sum_{i=1}^{3} \frac{\partial c_0^e}{\partial x_i}(x)\nabla_y w_i + \hat{k}_{12}(y) \sum_{i=1}^{3} \frac{\partial \phi_0^e}{\partial x_i}(x)\nabla_y \psi_i\right) = \\ = -\nabla_y \cdot \left(\hat{k}_{11}(y, c_0^e)\nabla_x c_0^e + \hat{k}_{12}(y)\nabla_x \phi_0^e\right) \\ \\ \nabla_y \cdot \left(\hat{k}_{21}(y, c_0^e) \displaystyle\sum_{i=1}^{3} \frac{\partial c_0^e}{\partial x_i}(x)\nabla_y w_i + \hat{k}_{22}(y) \sum_{i=1}^{3} \frac{\partial \phi_0^e}{\partial x_i}(x)\nabla_y \psi_i\right) = \\ = -\nabla_y \cdot \left(\hat{k}_{21}(y, c_0^e)\nabla_x c_0^e + \hat{k}_{22}(y)\nabla_x \phi_0^e\right) \end{array}\right. \quad (5.4.64)$$

and in the interface conditions (5.4.62)

$$\left|\begin{array}{l} \left(\hat{k}_{11}(y, c_0^e) \displaystyle\sum_{i=1}^{3} \frac{\partial c_0^e}{\partial x_i}(x)\nabla_y w_i + \hat{k}_{12}(y) \sum_{i=1}^{3} \frac{\partial \phi_0^e}{\partial x_i}(x)\nabla_y \psi_i\right) \cdot \mathbf{n}_s = \\ = -\left(\hat{k}_{11}(y, c_0^e)\nabla_x c_0^e + \hat{k}_{12}(y)\nabla_x \phi_0^e\right) \cdot \mathbf{n}_s \\ \\ \left(\hat{k}_{21}(y, c_0^e) \displaystyle\sum_{i=1}^{3} \frac{\partial c_0^e}{\partial x_i}(x)\nabla_y w_i + \hat{k}_{22}(y) \sum_{i=1}^{3} \frac{\partial \phi_0^e}{\partial x_i}(x)\nabla_y \psi_i\right) \cdot \mathbf{n}_s = \\ = -\left(\hat{k}_{21}(y, c_0^e)\nabla_x c_0^e + \hat{k}_{22}(y)\nabla_x \phi_0^e\right) \cdot \mathbf{n}_s \end{array}\right. \quad (5.4.65)$$

For the gradients of the zero order terms c_0^e and ϕ_0^e we can write

$$\nabla_x c_0^e = \sum_{i=1}^{3} \frac{\partial c_0^e}{\partial x_i}\vec{\mathbf{e}}_i, \quad \nabla_x \phi_0^e = \sum_{i=1}^{3} \frac{\partial \phi_0^e}{\partial x_i}\vec{\mathbf{e}}_i$$

where $\vec{\mathbf{e}_1} = (1,0,0)$, $\vec{\mathbf{e}_2} = (0,1,0)$ and $\vec{\mathbf{e}_3} = (0,0,1)$, and then we substitute these expressions in (5.4.64) and (5.4.65) to arrive at

$$\left|\begin{array}{l} \nabla_y \cdot \left(\hat{k}_{11}(y, c_0^e) \sum_{i=1}^{3} \frac{\partial c_0^e}{\partial x_i}(x) \nabla_y w_i + \hat{k}_{12}(y) \sum_{i=1}^{3} \frac{\partial \phi_0^e}{\partial x_i}(x) \nabla_y \psi_i \right) = \\ = -\nabla_y \cdot \left(\hat{k}_{11}(y, c_0^e) \sum_{i=1}^{3} \frac{\partial c_0^e}{\partial x_i}\vec{\mathbf{e}}_i + \hat{k}_{12}(y) \sum_{i=1}^{3} \frac{\partial \phi_0^e}{\partial x_i}\vec{\mathbf{e}}_i \right) \\ \nabla_y \cdot \left(\hat{k}_{21}(y, c_0^e) \sum_{i=1}^{3} \frac{\partial c_0^e}{\partial x_i}(x) \nabla_y w_i + \hat{k}_{22}(y) \sum_{i=1}^{3} \frac{\partial \phi_0^e}{\partial x_i}(x) \nabla_y \psi_i \right) = \\ = -\nabla_y \cdot \left(\hat{k}_{21}(y, c_0^e) \sum_{i=1}^{3} \frac{\partial c_0^e}{\partial x_i}\vec{\mathbf{e}}_i + \hat{k}_{22}(y) \sum_{i=1}^{3} \frac{\partial \phi_0^e}{\partial x_i}\vec{\mathbf{e}}_i \right) \end{array}\right. \tag{5.4.66}$$

and for the interface conditions

$$\left|\begin{array}{l} \left(\hat{k}_{11}(y, c_0^e) \sum_{i=1}^{3} \frac{\partial c_0^e}{\partial x_i}(x) \nabla_y w_i + \hat{k}_{12}(y) \sum_{i=1}^{3} \frac{\partial \phi_0^e}{\partial x_i}(x) \nabla_y \psi_i \right) \cdot \mathbf{n}_s = \\ = - \left(\hat{k}_{11}(y, c_0^e) \sum_{i=1}^{3} \frac{\partial c_0^e}{\partial x_i}\vec{\mathbf{e}}_i + \hat{k}_{12}(y) \sum_{i=1}^{3} \frac{\partial \phi_0^e}{\partial x_i}\vec{\mathbf{e}}_i \right) \cdot \mathbf{n}_s \\ \left(\hat{k}_{21}(y, c_0^e) \sum_{i=1}^{3} \frac{\partial c_0^e}{\partial x_i}(x) \nabla_y w_i + \hat{k}_{22}(y) \sum_{i=1}^{3} \frac{\partial \phi_0^e}{\partial x_i}(x) \nabla_y \psi_i \right) \cdot \mathbf{n}_s = \\ = - \left(\hat{k}_{21}(y, c_0^e) \sum_{i=1}^{3} \frac{\partial c_0^e}{\partial x_i}\vec{\mathbf{e}}_i + \hat{k}_{22}(y) \sum_{i=1}^{3} \frac{\partial \phi_0^e}{\partial x_i}\vec{\mathbf{e}}_i \right) \cdot \mathbf{n}_s \end{array}\right. \tag{5.4.67}$$

which is equivalent to

$$\left|\begin{array}{l} \nabla_y \cdot \left(\hat{k}_{11}(y, c_0^e) \sum_{i=1}^{3} \frac{\partial c_0^e}{\partial x_i}(x) \left(\nabla_y w_i + \vec{\mathbf{e}}_i \right) + \hat{k}_{12}(y) \sum_{i=1}^{3} \frac{\partial \phi_0^e}{\partial x_i}(x) \left(\nabla_y \psi_i + \vec{\mathbf{e}}_i \right) \right) = 0 \\ \nabla_y \cdot \left(\hat{k}_{21}(y, c_0^e) \sum_{i=1}^{3} \frac{\partial c_0^e}{\partial x_i}(x) \left(\nabla_y w_i + \vec{\mathbf{e}}_i \right) + \hat{k}_{22}(y) \sum_{i=1}^{3} \frac{\partial \phi_0^e}{\partial x_i}(x) \left(\nabla_y \psi_i + \vec{\mathbf{e}}_i \right) \right) = 0 \end{array}\right. \tag{5.4.68}$$

and on the interface

$$\left|\begin{array}{l}\left(\hat{k}_{11}(y,c_0^e)\sum_{i=1}^{3}\frac{\partial c_0^e}{\partial x_i}(x)\left(\nabla_y w_i+\vec{\mathbf{e}_i}\right)+\hat{k}_{12}(y)\sum_{i=1}^{3}\frac{\partial \phi_0^e}{\partial x_i}(x)\left(\nabla_y \psi_i+\vec{\mathbf{e}_i}\right)\right)\cdot\mathbf{n}_s=0\\ \left(\hat{k}_{21}(y,c_0^e)\sum_{i=1}^{3}\frac{\partial c_0^e}{\partial x_i}(x)\left(\nabla_y w_i+\vec{\mathbf{e}_i}\right)+\hat{k}_{22}(y)\sum_{i=1}^{3}\frac{\partial \phi_0^e}{\partial x_i}(x)\left(\nabla_y \psi_i+\vec{\mathbf{e}_i}\right)\right)\cdot\mathbf{n}_s=0\end{array}\right. \tag{5.4.69}$$

The latter is equivalent to

$$\left|\begin{array}{l}\sum_{i=1}^{3}\frac{\partial c_0^e}{\partial x_i}(x)\nabla_y\cdot\left(\hat{k}_{11}(y,c_0^e)\left(\nabla_y w_i+\vec{\mathbf{e}_i}\right)\right)+\sum_{i=1}^{3}\frac{\partial \phi_0^e}{\partial x_i}(x)\nabla_y\cdot\left(\hat{k}_{12}(y)\left(\nabla_y \psi_i+\vec{\mathbf{e}_i}\right)\right)=0\\ \sum_{i=1}^{3}\frac{\partial c_0^e}{\partial x_i}(x)\nabla_y\cdot\left(\hat{k}_{21}(y,c_0^e)\left(\nabla_y w_i+\vec{\mathbf{e}_i}\right)\right)+\sum_{i=1}^{3}\frac{\partial \phi_0^e}{\partial x_i}(x)\nabla_y\cdot\left(\hat{k}_{22}(y)\left(\nabla_y \psi_i+\vec{\mathbf{e}_i}\right)\right)=0\end{array}\right. \tag{5.4.70}$$

and

$$\left|\begin{array}{l}\hat{k}_{11}(y,c_0^e)\sum_{i=1}^{3}\frac{\partial c_0^e}{\partial x_i}(x)\left(\nabla_y w_i+\vec{\mathbf{e}_i}\right)\cdot\mathbf{n}_s+\hat{k}_{12}(y)\sum_{i=1}^{3}\frac{\partial \phi_0^e}{\partial x_i}(x)\left(\nabla_y \psi_i+\vec{\mathbf{e}_i}\right)\cdot\mathbf{n}_s=0\\ \hat{k}_{21}(y,c_0^e)\sum_{i=1}^{3}\frac{\partial c_0^e}{\partial x_i}(x)\left(\nabla_y w_i+\vec{\mathbf{e}_i}\right)\cdot\mathbf{n}_s+\hat{k}_{22}(y)\sum_{i=1}^{3}\frac{\partial \phi_0^e}{\partial x_i}(x)\left(\nabla_y \psi_i+\vec{\mathbf{e}_i}\right)\cdot\mathbf{n}_s=0\end{array}\right. \tag{5.4.71}$$

Since $y\in Y=E\cup S$, and we want to derive the electrolyte phase cell problems, we must consider only $y\in E$, which leads to

$$\begin{aligned}\hat{k}_{11}(y,c_0^e)&=k_{11}^e(c_0^e),\\ \hat{k}_{12}(y)&=k_{12}^e,\\ \hat{k}_{21}(y,c_0^e)&=k_{21}^e(c_0^e),\\ \hat{k}_{22}(y)&=k_{22}^e\end{aligned}$$

and the system of equations (5.4.70) and the interface conditions (5.4.71) become respectively

$$\left|\begin{array}{l}\sum_{i=1}^{3}\frac{\partial c_0^e}{\partial x_i}(x)\nabla_y\cdot\left(k_{11}^e(c_0^e)\left(\nabla_y w_i+\vec{\mathbf{e}_i}\right)\right)+\sum_{i=1}^{3}\frac{\partial \phi_0^e}{\partial x_i}(x)\nabla_y\cdot\left(k_{12}^e\left(\nabla_y \psi_i+\vec{\mathbf{e}_i}\right)\right)=0\\ \sum_{i=1}^{3}\frac{\partial c_0^e}{\partial x_i}(x)\nabla_y\cdot\left(k_{21}^e(c_0^e)\left(\nabla_y w_i+\vec{\mathbf{e}_i}\right)\right)+\sum_{i=1}^{3}\frac{\partial \phi_0^e}{\partial x_i}(x)\nabla_y\cdot\left(k_{22}^e\left(\nabla_y \psi_i+\vec{\mathbf{e}_i}\right)\right)=0\end{array}\right. \tag{5.4.72}$$

and

$$\left|\begin{array}{l} \displaystyle\sum_{i=1}^{3} k_{11}^{e}(c_0^e)\frac{\partial c_0^e}{\partial x_i}(x)\left(\nabla_y w_i + \vec{\mathbf{e}_i}\right)\cdot\mathbf{n}_s + \sum_{i=1}^{3} k_{12}^{e}\frac{\partial \phi_0^e}{\partial x_i}(x)\left(\nabla_y \psi_i + \vec{\mathbf{e}_i}\right)\cdot\mathbf{n}_s = 0 \\ \displaystyle\sum_{i=1}^{3} k_{21}^{e}(c_0^e)\frac{\partial c_0^e}{\partial x_i}(x)\left(\nabla_y w_i + \vec{\mathbf{e}_i}\right)\cdot\mathbf{n}_s + \sum_{i=1}^{3} k_{22}^{e}\frac{\partial \phi_0^e}{\partial x_i}(x)\left(\nabla_y \psi_i + \vec{\mathbf{e}_i}\right)\cdot\mathbf{n}_s = 0 \end{array}\right. \tag{5.4.73}$$

Because $c_0^e = c_0^e(x)$ is a function of x only and the electrolyte coefficients k_{12}^e and k_{22}^e are constants, the system of equations (5.4.72) becomes

$$\left|\begin{array}{l} \displaystyle\sum_{i=1}^{3} k_{11}^{e}(c_0^e)\frac{\partial c_0^e}{\partial x_i}(x)\nabla_y\cdot\left(\nabla_y w_i + \vec{\mathbf{e}_i}\right) + \sum_{i=1}^{3} k_{12}^{e}\frac{\partial \phi_0^e}{\partial x_i}(x)\nabla_y\cdot\left(\nabla_y \psi_i + \vec{\mathbf{e}_i}\right) = 0 \\ \displaystyle\sum_{i=1}^{3} k_{21}^{e}(c_0^e)\frac{\partial c_0^e}{\partial x_i}(x)\nabla_y\cdot\left(\nabla_y w_i + \vec{\mathbf{e}_i}\right) + \sum_{i=1}^{3} k_{22}^{e}\frac{\partial \phi_0^e}{\partial x_i}(x)\nabla_y\cdot\left(\nabla_y \psi_i + \vec{\mathbf{e}_i}\right) = 0 \end{array}\right. \tag{5.4.74}$$

We want the resulting equalities (5.4.74) and (5.4.73) to be satisfied for all $x \in \Omega_{electrode}$ and this is fulfilled if and only if

$$\left|\begin{array}{l} \nabla_y\cdot\left(\nabla_y w_i + \vec{\mathbf{e}_i}\right) = 0 \\ \nabla_y\cdot\left(\nabla_y \psi_i + \vec{\mathbf{e}_i}\right) = 0 \\ \left(\nabla_y w_i + \vec{\mathbf{e}_i}\right)\cdot\mathbf{n}_s = 0 \\ \left(\nabla_y \psi_i + \vec{\mathbf{e}_i}\right)\cdot\mathbf{n}_s = 0 \end{array}\right. \tag{5.4.75}$$

which is equivalent to

$$\left|\begin{array}{l} \nabla_y\cdot\left(\nabla_y w_i\right) + \underbrace{\nabla_y\cdot\vec{\mathbf{e}_i}}_{=0} = 0 \\ \nabla_y\cdot\left(\nabla_y \psi_i\right) + \underbrace{\nabla_y\cdot\vec{\mathbf{e}_i}}_{=0} = 0 \\ \nabla_y w_i\cdot\mathbf{n}_s = -\vec{\mathbf{e}_i}\cdot\mathbf{n}_s \\ \nabla_y \psi_i\cdot\mathbf{n}_s = -\vec{\mathbf{e}_i}\cdot\mathbf{n}_s \end{array}\right. \iff \left|\begin{array}{l} \nabla_y\cdot\left(\nabla_y w_i\right) = 0 \\ \nabla_y w_i\cdot\mathbf{n}_s = -\vec{\mathbf{e}_i}\cdot\mathbf{n}_s \\ \nabla_y\cdot\left(\nabla_y \psi_i\right) = 0 \\ \nabla_y \psi_i\cdot\mathbf{n}_s = -\vec{\mathbf{e}_i}\cdot\mathbf{n}_s \end{array}\right. \tag{5.4.76}$$

Finally we obtain that we have equivalent cell problems for c_1^e and ϕ_1^e, and these cell problems have the following form

$$\nabla_y\cdot\left(\nabla_y w_i\right) = 0, \quad y \in E \tag{5.4.77a}$$

$$\nabla_y w_i\cdot\mathbf{n}_s = -\vec{\mathbf{e}_i}\cdot\mathbf{n}_s, \quad y \in \Gamma \tag{5.4.77b}$$

where $w_i(y)$ are Y-periodic functions and $i = 1, 2, 3$, i.e., we have one auxiliary cell problem corresponding to each of the three directions y_1, y_2 and y_3. The boundary condition

(5.4.77b) is imposed on the boundary Γ, which is the interface in the two-phase reference periodicity cell $Y = E \cup S$, and as before, $\mathbf{n}_s$ is the unit normal vector to the boundary Γ pointing in direction from the solid domain into the electrolyte domain. Since $w_i(y)$ are Y-periodic functions, on the "outer" boundary of the electrolyte domain E we impose periodic boundary conditions for $w_i(y)$ and we also take $\int_E w_i(y)\,dy = 0$ in order to fix the solution.
Taking into account the fact that $w_i(y) \equiv \psi_i(y)$ for all $y \in E$, we can rewrite the scale-separable representation (5.4.63) of c_1^e and ϕ_1^e in the following way

$$c_1^e(x,y,t) = \sum_{i=1}^{3} \frac{\partial c_0^e}{\partial x_i}(x,t) w_i(y) \tag{5.4.78a}$$

$$\phi_1^e(x,y,t) = \sum_{i=1}^{3} \frac{\partial \phi_0^e}{\partial x_i}(x,t) w_i(y) \tag{5.4.78b}$$

It is easy to show that if the functions $w_i(y)$ are solution to problems (5.4.77), then the functions c_1^e and ϕ_1^e, having the scale separable form (5.4.63), are solution to problem (5.4.61)-(5.4.62). Thus, we showed that the scale separable representation (5.4.63) of c_1^e and ϕ_1^e that we introduced is solution to problem (5.4.61)-(5.4.62) if and only if the functions $w_i(y)$ are solution to the auxiliary cell problems (5.4.77).
The cell problems are very easy to solve numerically and they are time-independent, which means that we have to solve them only once and then we can reuse them at each time step.

Order ε^0: Derivation of the homogenized equations

For the zero order terms c_0^s and ϕ_0^s of the asymptotic expansions (5.4.17) and (5.4.18), from (5.4.58c) and (5.4.59c), we obtain the following system of partial differential equations for $y \in Y = E \cup S$ and $x \in \Omega_{electrode}$

$$\begin{aligned}\hat{\chi}^e(y)\frac{\partial c_0^e}{\partial t} = {} & \nabla_x \cdot \left[\hat{k}_{11}(y, c_0^e)\left(\nabla_x c_0^e + \nabla_y c_1^e\right) + \hat{k}_{12}(y)\left(\nabla_x \phi_0^e + \nabla_y \phi_1^e\right)\right] + \\ & + \nabla_y \cdot \left[\hat{k}_{11}(y, c_0^e)\nabla_x c_1^e + \hat{k}_{11}(y, c_0^e)\nabla_y c_2^e + \hat{k}_{12}(y)\nabla_x \phi_1^e + \hat{k}_{12}(y)\nabla_y \phi_2^e\right]\end{aligned} \tag{5.4.79a}$$

$$\begin{aligned}& \nabla_x \cdot \left[\hat{k}_{21}(y, c_0^e)\left(\nabla_x c_0^e + \nabla_y c_1^e\right) + \hat{k}_{22}(y)\left(\nabla_x \phi_0^e + \nabla_y \phi_1^e\right)\right] + \\ & + \nabla_y \cdot \left[\hat{k}_{21}(y, c_0^e)\nabla_x c_1^e + \hat{k}_{21}(y, c_0^e)\nabla_y c_2^e + \hat{k}_{22}(y)\nabla_x \phi_1^e + \hat{k}_{22}(y)\nabla_y \phi_2^e\right] = 0\end{aligned} \tag{5.4.79b}$$

with their matching ε^0 order interface conditions (5.4.55c) on Γ

$$-\left[\hat{k}_{11}(y,c_0^e)\nabla_x c_1^e+\hat{k}_{11}(y,c_0^e)\nabla_y c_2^e+\hat{k}_{12}(y)\nabla_x\phi_1^e+\hat{k}_{12}(y)\nabla_y\phi_2^e\right]\cdot\mathbf{n_s}=\frac{1}{\varepsilon}\mathcal{N}(c_0^e,c^s,\phi_0^e,\phi_0^s) \tag{5.4.80a}$$

$$-\left[\hat{k}_{21}(y,c_0^e)\nabla_x c_1^e+\hat{k}_{21}(y,c_0^e)\nabla_y c_2^e+\hat{k}_{22}(y)\nabla_x\phi_1^e+\hat{k}_{22}(y)\nabla_y\phi_2^e\right]\cdot\mathbf{n_s}=\frac{1}{\varepsilon}\mathcal{J}(c_0^e,c^s,\phi_0^e,\phi_0^s) \tag{5.4.80b}$$

We integrate both sides of equations (5.4.79) over the domain of the two-phase reference periodicity cell Y and then we divide by the measure of Y to arrive at

$$\begin{aligned}\frac{|E|}{|Y|}\frac{\partial c_0^e}{\partial t}=&\frac{1}{|Y|}\int\limits_Y\nabla_x\cdot\left[\hat{k}_{11}(y,c_0^e)\left(\nabla_x c_0^e+\nabla_y c_1^e\right)+\hat{k}_{12}(y)\left(\nabla_x\phi_0^e+\nabla_y\phi_1^e\right)\right]\,dy+\\&+\frac{1}{|Y|}\int\limits_Y\nabla_y\cdot\left[\hat{k}_{11}(y,c_0^e)\nabla_x c_1^e+\hat{k}_{11}(y,c_0^e)\nabla_y c_2^e+\hat{k}_{12}(y)\nabla_x\phi_1^e+\hat{k}_{12}(y)\nabla_y\phi_2^e\right]\,dy\end{aligned} \tag{5.4.81a}$$

$$\begin{aligned}&\frac{1}{|Y|}\int\limits_Y\nabla_x\cdot\left[\hat{k}_{21}(y,c_0^e)\left(\nabla_x c_0^e+\nabla_y c_1^e\right)+\hat{k}_{22}(y)\left(\nabla_x\phi_0^e+\nabla_y\phi_1^e\right)\right]\,dy+\\&+\frac{1}{|Y|}\int\limits_Y\nabla_y\cdot\left[\hat{k}_{21}(y,c_0^e)\nabla_x c_1^e+\hat{k}_{21}(y)\nabla_y c_2^e+\hat{k}_{22}(y)\nabla_x\phi_1^e+\hat{k}_{22}(y)\nabla_y\phi_2^e\right]\,dy=0\end{aligned} \tag{5.4.81b}$$

where for the left hand side of equation (5.4.81a) we calculated

$$\frac{1}{|Y|}\int\limits_Y\hat{\chi}^e(y)\frac{\partial c_0^e}{\partial t}(x,t)\,dy=\frac{1}{|Y|}\frac{\partial c_0^e}{\partial t}\int\limits_Y\hat{\chi}^e(y)\,dy=\frac{1}{|Y|}\frac{\partial c_0^e}{\partial t}\left(\int\limits_E 1\,dy+\int\limits_S 0\,dy\right)=\frac{|E|}{|Y|}\frac{\partial c_0^e}{\partial t} \tag{5.4.82}$$

Since $Y=E\cup S$ and consequently $\hat{k}_{ij}(y,c_0^e)=\hat{\chi}^e(y)k_{ij}^e=\left\{\begin{array}{ll}k_{ij}^e, & y\in E\\ 0, & y\in S\end{array}\right.$ it follows that

$$\frac{1}{|Y|}\int\limits_Y\hat{k}_{ij}(y,c_0^e)(\ldots)\,dy=\frac{1}{|Y|}\left(\int\limits_E k_{ij}^e(\ldots)\,dy+\underbrace{\int\limits_S 0(\ldots)\,dy}_{=0}\right)=\frac{1}{|Y|}\int\limits_E k_{ij}^e(\ldots)\,dy$$

We will consider in details the homogenization only of the first equation (5.4.81a) of the considered system of partial differential equations. We recall that the functions $c_1^e(x,y)$, $\phi_1^e(x,y)$, and $c_2^e(x,y)$, $\phi_2^e(x,y)$, are Y-periodic in the y variable.

Now we consider the second integral of the right hand side of equation (5.4.81a), where we arrive at integration over the electrolyte reference periodicity cell E

$$\begin{aligned}
&\frac{1}{|Y|}\int\limits_{E}\nabla_y\cdot[k_{11}^e(c_0^e)\nabla_x c_1^e+k_{11}^e(c_0^e)\nabla_y c_2^e+k_{12}^e\nabla_x\phi_1^e+k_{12}^e\nabla_y\phi_2^e]\;dy=\\
&=\frac{1}{|Y|}\int\limits_{\partial E}[k_{11}^e(c_0^e)\nabla_x c_1^e+k_{11}^e(c_0^e)\nabla_y c_2^e+k_{12}^e\nabla_x\phi_1^e+k_{12}^e\nabla_y\phi_2^e]\cdot\mathbf{n}\,ds=\\
&=\underbrace{\frac{1}{|Y|}\int\limits_{\partial E\cap\partial Y}[k_{11}^e(c_0^e)\nabla_x c_1^e+k_{11}^e(c_0^e)\nabla_y c_2^e+k_{12}^e\nabla_x\phi_1^e+k_{12}^e\nabla_y\phi_2^e]\cdot\mathbf{n}\,ds}_{=0}+\\
&+\frac{1}{|Y|}\int\limits_{\Gamma}[k_{11}^e(c_0^e)\nabla_x c_1^e+k_{11}^e(c_0^e)\nabla_y c_2^e+k_{12}^e\nabla_x\phi_1^e+k_{12}^e\nabla_y\phi_2^e]\cdot\mathbf{n_e}\,ds=\\
&=0-\frac{1}{|Y|}\int\limits_{\Gamma}\underbrace{[k_{11}^e(c_0^e)\nabla_x c_1^e+k_{11}^e(c_0^e)\nabla_y c_2^e+k_{12}^e\nabla_x\phi_1^e+k_{12}^e\nabla_y\phi_2^e]\cdot\mathbf{n_s}}_{=-\frac{1}{\varepsilon}\mathcal{N}(c_0^e,c^s,\phi_0^e,\phi_0^s)}\;ds=\\
&=\frac{1}{\varepsilon\,|Y|}\int\limits_{\Gamma}\mathcal{N}(c_0^e,c^s,\phi_0^e,\phi_0^s)\,ds
\end{aligned}\tag{5.4.83}$$

In the latter calculations we apply the divergence theorem and as a result we obtain two surface integrals - one over the outer boundary of the electrolyte domain E, which vanishes due to symmetry and periodicity, and one over the interface boundary Γ. Then, as integrand in the surface integral over Γ, we obtain exactly the $O(\varepsilon^0)$ interface exchange current density from (5.4.54). Therefore, we substitute this integrand with its equal expression, i.e., with $\frac{1}{\varepsilon}\mathcal{N}\,(c_0^e,c^s,\phi_0^e,\phi_0^s)$, which is also the interface condition (5.4.80a). Finally, we obtain the term $\frac{1}{|Y|}\int\limits_{\Gamma}\frac{1}{\varepsilon}\mathcal{N}\,(c_0^e,c^s,\phi_0^e,\phi_0^s)\;ds$ which later goes as a right-hand side in the homogenized equations.
Finally, we consider the first integral in the right hand side of equation (5.4.81a), where we

substitute the functions c_1^e and ϕ_1^e with their scale separable form (5.4.78), and we obtain

$$\frac{1}{|Y|}\int\limits_E \nabla_x \cdot [k_{11}^e \nabla_y c_1^e + k_{12}^e \nabla_y \phi_1^e + k_{11}^e \nabla_x c_0^e + k_{12}^e \nabla_x \phi_0^e]\, dy =$$

$$= \frac{1}{|Y|}\int\limits_E \nabla_x \cdot \left[k_{11}^e \sum_{i=1}^{3} \frac{\partial c_0^e}{\partial x_i} \nabla_y w_i + k_{12}^e \sum_{i=1}^{3} \frac{\partial \phi_0^e}{\partial x_i} \nabla_y w_i + k_{11}^e \nabla_x c_0^e + k_{12}^e \nabla_x \phi_0^e \right] dy =$$

$$= \nabla_x \cdot \left\{ \frac{1}{|Y|}\int\limits_E \left[k_{11}^e \sum_{i=1}^{3} \frac{\partial c_0^e}{\partial x_i} \nabla_y w_i + k_{12}^e \sum_{i=1}^{3} \frac{\partial \phi_0^e}{\partial x_i} \nabla_y w_i + k_{11}^e \nabla_x c_0^e + k_{12}^e \nabla_x \phi_0^e \right] dy \right\} =$$

$$= \nabla_x \cdot \left\{ \sum_{i=1}^{3} \frac{1}{|Y|}\int\limits_E k_{11}^e \frac{\partial c_0^e}{\partial x_i}(x) \nabla_y w_i \, dy + \sum_{i=1}^{3} \frac{1}{|Y|}\int\limits_E k_{12}^e \frac{\partial \phi_0^e}{\partial x_i}(x) \nabla_y w_i \, dy + \right.$$

$$\left. + \frac{1}{|Y|}\int\limits_E k_{11}^e \nabla_x c_0^e \, dy + \frac{1}{|Y|}\int\limits_E k_{12}^e \nabla_x \phi_0^e \, dy \right\} =$$

$$= \nabla_x \cdot \left\{ \sum_{i=1}^{3} \left(\frac{1}{|Y|}\int\limits_E k_{11}^e \nabla_y w_i \, dy \right) \frac{\partial c_0^e}{\partial x_i}(x) + \sum_{i=1}^{3} \left(\frac{1}{|Y|}\int\limits_E k_{12}^e \nabla_y w_i \, dy \right) \frac{\partial \phi_0^e}{\partial x_i}(x) + \right.$$

$$\left. + \left(\frac{1}{|Y|}\int\limits_E k_{11}^e \, dy \right) \nabla_x c_0^e + \left(\frac{1}{|Y|}\int\limits_E k_{12}^e \, dy \right) \nabla_x \phi_0^e \right\} =$$

$$= \nabla_x \cdot \left\{ \mathbf{A} \nabla_x c_0^e + \mathbf{B} \nabla_x \phi_0^e + k_{11}^e \frac{|E|}{|Y|} \mathbf{I} \nabla_x c_0^e + k_{12}^e \frac{|E|}{|Y|} \mathbf{I} \nabla_x \phi_0^e \right\} =$$

$$= \nabla_x \cdot \left\{ \left(\mathbf{A} + k_{11}^e \frac{|E|}{|Y|} \mathbf{I} \right) \nabla_x c_0^e + \left(\mathbf{B} + k_{12}^e \frac{|E|}{|Y|} \mathbf{I} \right) \nabla_x \phi_0^e \right\}$$

In the latter $\mathbf{I}$ is the identity matrix and we also denoted

$$\mathbf{A} = (a_{ij})_{i,j=1}^{3} = \frac{1}{|Y|} \int\limits_{E} k_{11}^{e} \frac{\partial w_j}{\partial y_i}(y)\, dy$$

$$\mathbf{B} = (b_{ij})_{i,j=1}^{3} = \frac{1}{|Y|} \int\limits_{E} k_{12}^{e} \frac{\partial w_j}{\partial y_i}(y)\, dy$$

Now we denote

$$\mathbf{K_{11}} = \mathbf{A} + k_{11}^{e} \frac{|E|}{|Y|} \mathbf{I}$$

$$\mathbf{K_{12}} = \mathbf{B} + k_{12}^{e} \frac{|E|}{|Y|} \mathbf{I}$$

where the elements of the matrices $\mathbf{K_{1m}}$, $m = 1, 2$ have the following form

$$(\mathbf{K_{1m}})_{ij} = \frac{1}{|Y|} \int\limits_{E} k_{1m}^{e} \frac{\partial w_j}{\partial y_i}(y)\, dy + k_{1m}^{e} \frac{|E|}{|Y|} \delta_{ij} =$$

$$= \frac{k_{1m}^{e}}{|Y|} \int\limits_{E} \frac{\partial w_j}{\partial y_i}(y)\, dy + \frac{k_{1m}^{e}}{|Y|} \delta_{ij} \int\limits_{E} 1\, dy =$$

$$= \frac{k_{1m}^{e}}{|Y|} \int\limits_{E} \left(\frac{\partial w_j}{\partial y_i}(y) + \delta_{ij} \right) dy \tag{5.4.84}$$

By analogy with the first equation (5.4.81a) of the system (5.4.79), we average and the second equation (5.4.81b). Finally, we obtain the following system of homogenized electrolyte phase equations

$$\frac{|E|}{|Y|} \frac{\partial c_0^e}{\partial t} - \nabla_x \cdot (\mathbf{K_{11}} \nabla_x c_0^e + \mathbf{K_{12}} \nabla_x \phi_0^e) = \frac{1}{\varepsilon |Y|} \int\limits_{\Gamma} \mathcal{N}(c_0^e, c^s, \phi_0^e, \phi_0^s)\, ds \tag{5.4.85}$$

$$-\nabla_x \cdot (\mathbf{K_{21}} \nabla_x c_0^e + \mathbf{K_{22}} \nabla_x \phi_0^e) = \frac{1}{\varepsilon |Y|} \int\limits_{\Gamma} \mathcal{J}(c_0^e, c^s, \phi_0^e, \phi_0^s)\, ds \tag{5.4.86}$$

where Γ is the interface boundary between the electrolyte and the solid in the reference two-phase periodicity cell $Y = E \cup S$ and the ***effective (homogenized) transport***

coefficients $\mathbf{K_{11}}$, $\mathbf{K_{12}}$, $\mathbf{K_{21}}$, and $\mathbf{K_{22}}$ are tensors with elements

$$(\mathbf{K_{11}})_{ij} = \frac{k^e_{11}(c^e_0)}{|Y|}\int\limits_E \left(\delta_{ij} + \frac{\partial w_j}{\partial y_i}(y)\right) dy, \quad (\mathbf{K_{12}})_{ij} = \frac{k^e_{12}}{|Y|}\int\limits_E \left(\delta_{ij} + \frac{\partial w_j}{\partial y_i}(y)\right) dy$$

$$(\mathbf{K_{21}})_{ij} = \frac{k^e_{21}(c^e_0)}{|Y|}\int\limits_E \left(\delta_{ij} + \frac{\partial w_j}{\partial y_i}(y)\right) dy, \quad (\mathbf{K_{22}})_{ij} = \frac{k^e_{22}}{|Y|}\int\limits_E \left(\delta_{ij} + \frac{\partial w_j}{\partial y_i}(y)\right) dy \tag{5.4.87}$$

where $i, j = 1, 2, 3$. It is important to make the following

Remark: The effective homogenized coefficients given by the analytical formulas (5.4.87) describe the macroscopic properties of the medium and at the same time incorporate microscale information, such as the anisotropy of the medium. Since for each direction of the three-dimensional Euclidean space we solve one auxiliary cell problem (5.4.77), we can think of their solutions - the functions $w_i(y)$ as an "indicator" for the ***tortuosity*** of the underlying microstructure of the porous electrodes. The tortuosity is a geometrical property of medium and, roughly speaking, accounts for the curvity of the medium.

5.4.6 Homogenization of the solid phase equation for the electrical potential

Since the derivation of the upscaled solid phase equation for the potential ϕ^s is analogical to that of the electrolyte phase equations, here we give directly the homogenized equation for $y \in Y$, and $x \in \Omega_{electrode}$,

$$-\nabla_x \cdot (\mathbf{\Lambda^s} \nabla_x \phi^s_0) = -\frac{1}{\varepsilon\,|Y|}\int\limits_\Gamma \mathcal{J}(c^e_0, c^s, \phi^e_0, \phi^s_0)\, ds \tag{5.4.88}$$

where the effective electronic conductivity $\mathbf{\Lambda^s}$ is a tensor with elements

$$(\mathbf{\Lambda^s})_{ij} = \frac{1}{|Y|}\int\limits_S \kappa^s \left(\delta_{ij} + \frac{\partial \xi_j}{\partial y_i}\right) dy, \quad i, j = 1, 2, 3 \tag{5.4.89}$$

and the Y-periodic functions $\xi_j(y)$, $j = 1, 2, 3$ are solutions to the following cell problems

$$\nabla \cdot (\nabla_y \xi_j) = 0, \quad y \in S \tag{5.4.90a}$$

$$\nabla_y \xi_j \cdot \mathbf{n_s} = -\vec{\mathbf{e}}_j \cdot \mathbf{n_s}, \quad y \in \Gamma \tag{5.4.90b}$$

In the cell problems we have periodic boundary conditions on $\partial S \backslash \Gamma$, i.e., on the boundary of the particles where the particles are connected and we take $\int\limits_S \xi_j(y)\, dy = 0$ for all $j = 1, 2, 3$ in order to fix the solution.

We recall that when calculating the efficient coefficient (5.4.89), we have to take into account in which homogenized electrode we are, since

$$\kappa^s = \begin{cases} \kappa^s_{anode}, & x \in \Omega_{anode} \\ \\ \kappa^s_{cathode}, & x \in \Omega_{cathode} \end{cases} \tag{5.4.91}$$

5.5 Upscaling of the Neumann boundary condition

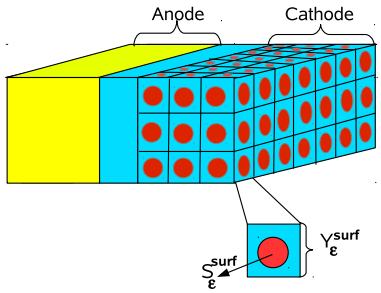

Figure 5.4: Electrode outer boundary

We have the following Neumann boundary condition in the ε-setting of the microscale problem

$$-\kappa^s \nabla \phi_\varepsilon^s \cdot \mathbf{n} = E_2^s, \quad x \in \{\omega_2 \cap \Omega_c^\varepsilon\} \tag{5.5.1}$$

and we need to derive the respective upscaled boundary condition for the homogenized flux $-\mathbf{\Lambda^s} \nabla \phi_0^s \cdot \mathbf{n}$ in equation (5.6.1c). Since we apply constant current E_2^s on the cathode boundary $\omega_2 \cap \Omega_c^\varepsilon$, it is clear that the applied current $-\mathbf{\Lambda^s} \nabla \phi_0^s \cdot \mathbf{n}$ on the whole wall ω_2 in the homogenized problem (5.6.1) is also a constant. Consequently if we denote $-\mathbf{\Lambda^s} \nabla \phi_0^s \cdot \mathbf{n} = C$, then C is a constant. Let us also denote with p_ε the number of all microscopic periodicity cells which have a wall on the external battery cell boundary ω_2. With S_ε^{surf} we denote a single periodicity cell cathode boundary (which is a circle in our exemplary geometry), and with Y_ε^{surf} - the boundary wall of a single microscopic periodicity cell, as shown in Figure 5.4. Due to the constant applied current E_2^s on the cathode boundary ω_2, the total flux across ω_2 should be preserved no matter how many periodicity cells we have in the cathode. This means that the total flux across ω_2 must be the same in both the upscaled problem and the microscopic one. Therefore we want to ensure that the following surface integrals are equal

$$\int\limits_{\omega_2 \cap \partial\Omega_c^\varepsilon} -\kappa^s \nabla \phi_\varepsilon^s \cdot \mathbf{n} \, dS = \int\limits_{\omega_2} -\mathbf{\Lambda^s} \nabla \phi_0^s \cdot \mathbf{n} \, dS \tag{5.5.2}$$

which is equivalent to

$$\int\limits_{\omega_2 \cap \partial\Omega_c^\varepsilon} E_2^s \, dS = \int\limits_{\omega_2} C \, dS \quad \Longleftrightarrow \quad E_2^s \left|\omega_2 \cap \partial\Omega_c^\varepsilon\right| = C \left|\omega_2\right| \quad \Longleftrightarrow$$

$$E_2^s p_\varepsilon \left|S_\varepsilon^{surf}\right| = C p_\varepsilon \left|Y_\varepsilon^{surf}\right| \quad \Longleftrightarrow \quad C = \frac{\left|S_\varepsilon^{surf}\right|}{\left|Y_\varepsilon^{surf}\right|} E_2^s.$$

Finally, after we account for the fact that $\frac{\left|S^{surf}\right|}{|Y^{surf}|} = \frac{\left|S_\varepsilon^{surf}\right|}{\left|Y_\varepsilon^{surf}\right|}$, where S^{surf} and Y^{surf} are the respective domains in the two-phase reference periodicity cell Y, we obtain the final form of the upscaled Neumann boundary condition on the outer cathode boundary ω_2

$$-\mathbf{\Lambda^s}\nabla_x\phi_0^s\cdot\mathbf{n} = \frac{\left|S^{surf}\right|}{|Y^{surf}|}E_2^s, \quad x\in\omega_2 \tag{5.5.3}$$

$$\tag{5.5.4}$$

5.6 Homogenized model: coupled macro-micro problem

We obtain the following homogenized equations for the concentration c^e of ions in the electrolyte, the potential ϕ^e in the electrolyte and for the potential ϕ^s in the electrode particles, for $x\in\Omega_{electrode}$

$$\frac{|E|}{|Y|}\frac{\partial c_0^e}{\partial t} - \nabla_x\cdot(\mathbf{K_{11}}\nabla_x c_0^e + \mathbf{K_{12}}\nabla_x\phi_0^e) = \frac{1}{\varepsilon\,|Y|}\int\limits_\Gamma \mathcal{N}(c_0^e, c^s, \phi_0^e, \phi_0^s)\,ds \tag{5.6.1a}$$

$$-\nabla_x\cdot(\mathbf{K_{21}}\nabla_x c_0^e + \mathbf{K_{22}}\nabla_x\phi_0^e) = \frac{1}{\varepsilon\,|Y|}\int\limits_\Gamma \mathcal{J}(c_0^e, c^s, \phi_0^e, \phi_0^s)\,ds \tag{5.6.1b}$$

$$-\nabla_x\cdot(\mathbf{\Lambda^s}\nabla_x\phi_0^s) = -\frac{1}{\varepsilon\,|Y|}\int\limits_\Gamma \mathcal{J}(c_0^e, c^s, \phi_0^e, \phi_0^s)\,ds, \tag{5.6.1c}$$

with the corresponding set of boundary conditions

$$\phi_0^s = E_1^s, \quad x\in\omega_1 \tag{5.6.2a}$$

$$-\mathbf{\Lambda^s}\nabla_x\phi_0^s\cdot\mathbf{n} = \frac{\left|S^{surf}\right|}{|Y^{surf}|}E_2^s, \quad x\in\omega_2 \tag{5.6.2b}$$

$$\mathbf{N_e^h}\cdot\mathbf{n} = 0, \quad x\in\partial\Omega \tag{5.6.2c}$$

$$\mathbf{J_e^h}\cdot\mathbf{n} = \mathbf{J_s^h}\cdot\mathbf{n} = 0, \quad x\in\partial\Omega \tag{5.6.2d}$$

where we denote $\mathbf{N_e^h} = -(\mathbf{K_{11}}\nabla_x c_0^e + \mathbf{K_{12}}\nabla_x\phi_0^e)$, $\mathbf{J_e^h} = -(\mathbf{K_{21}}\nabla_x c_0^e + \mathbf{K_{22}}\nabla_x\phi_0^e)$, and $\mathbf{J_s^h} = -\mathbf{\Lambda^s}\nabla_x\phi_0^s$.

The term $\frac{|E|}{|Y|}$ in front of the time derivative in equation (5.6.1a) is the ***porosity*** of the electrodes. For each $x\in\Omega_{electrode}$ we have to solve the following microscale problem for the concentration of ions in the electrode particles

$$\frac{\partial c^s}{\partial t} - \nabla_y\cdot\left(\frac{D^s}{\varepsilon^2}\nabla_y c^s\right) = 0, \quad y\in S \tag{5.6.3a}$$

$$-\frac{D^s}{\varepsilon^2}\nabla_y c^s\cdot\mathbf{n_s} = \frac{1}{\varepsilon}\mathcal{N}(c_0^e, c^s, \phi_0^e, \phi_0^s), \quad y\in\Gamma, \tag{5.6.3b}$$

where we have periodic boundary conditions on $\partial S \backslash \Gamma$, i.e. on the boundary of the solid particle where the particles are connected to each other. The two models - macro (5.6.1) and micro (5.6.3) are coupled via the interface exchange current densities $\mathcal{N}_0 = \mathcal{N}(c_0^e, c^s, \phi_0^e, \phi_0^s)$ and $\mathcal{J}_0 = \mathcal{J}(c_0^e, c^s, \phi_0^e, \phi_0^s)$. We recall that the homogenized effective transport coefficients are tensors and have the following form

$$(\mathbf{K_{lm}})_{ij} = \frac{k_{lm}^e(c_0^e)}{|Y|} \int\limits_E \left(\delta_{ij} + \frac{\partial w_j}{\partial y_i}(y) \right) dy, \tag{5.6.4a}$$

$$(\mathbf{\Lambda^s})_{ij} = \frac{1}{|Y|} \int\limits_S \kappa^s \left(\delta_{ij} + \frac{\partial \xi_j}{\partial y_i} \right) dy \tag{5.6.4b}$$

where $l, m = 1, 2$ and $i, j = 1, 2, 3$ with $w_j(y)$, and $\xi_j(y)$ being the solutions of the auxiliary cell problems (5.4.77) and (5.4.90), respectively, which account for the ***tortuosity***. We solve the cell problems only once and then using their solutions, by formula (5.6.4) we compute the effective macroscopic transport coefficients.

5.7 Strategy for the numerical solution of the homogenized model

We want to solve the following system of electrolyte phase equations, which is defined in the whole domain $\Omega = \Omega_{anode} \cup \Omega_{separator}^e \cup \Omega_{cathode}$

$$\alpha \frac{\partial \tilde{c}^e}{\partial t} - \nabla_x \cdot \left(\mathcal{K}_{11}^e \nabla_x \tilde{c}^e + \mathcal{K}_{12}^e \nabla_x \tilde{\phi}^e \right) = f_1(x), \quad x \in \Omega \tag{5.7.1a}$$

$$-\nabla_x \cdot \left(\mathcal{K}_{21}^e \nabla_x \tilde{c}^e + \mathcal{K}_{22}^e \nabla_x \tilde{\phi}^e \right) = f_2(x), \quad x \in \Omega \tag{5.7.1b}$$

with boundary condtions

$$-\left(\mathcal{K}_{11}^e \nabla_x \tilde{c}^e + \mathcal{K}_{12}^e \nabla_x \tilde{\phi}^e \right) \cdot \mathbf{n} = 0, \quad x \in \partial\Omega \tag{5.7.2a}$$

$$-\left(\mathcal{K}_{21}^e \nabla_x \tilde{c}^e + \mathcal{K}_{22}^e \nabla_x \tilde{\phi}^e \right) \cdot \mathbf{n} = 0, \quad x \in \partial\Omega \tag{5.7.2b}$$

where

$$\alpha = \begin{cases} 1, & x \in \Omega_{separator}^e, \\ \dfrac{|E|}{|Y|}, & x \in \Omega_{anode} \cup \Omega_{cathode} \end{cases} \tag{5.7.3}$$

the right-hand sides are given by

$$f_1(x) = \begin{cases} 0, & x \in \Omega_{separator}^e, \\ \dfrac{1}{\varepsilon\,|Y|} \displaystyle\int\limits_\Gamma \mathcal{N}\left(c_0^e, \phi_0^e, c^s, \phi_0^s\right)\, ds, & x \in \Omega_{anode} \cup \Omega_{cathode} \end{cases} \tag{5.7.4}$$

$$f_2(x) = \begin{cases} 0, & x \in \Omega^e_{separator}, \\ \dfrac{1}{\varepsilon\,|Y|} \displaystyle\int_\Gamma \mathcal{J}\left(c_0^e, \phi_0^e, c^s, \phi_0^s\right)\, ds, & x \in \Omega_{anode} \cup \Omega_{cathode} \end{cases} \tag{5.7.5}$$

and the equations' coefficients are the subsequent tensors

$$\mathcal{K}^e_{ij} = \begin{cases} \mathbf{K_{ij}^{micro}} := \begin{pmatrix} k^e_{ij} & 0 & 0 \\ 0 & k^e_{ij} & 0 \\ 0 & 0 & k^e_{ij} \end{pmatrix}, & x \in \Omega^e_{separator}, \\ \mathbf{K_{ij}}, & x \in \Omega_{anode} \cup \Omega_{cathode} \end{cases} \tag{5.7.6}$$

for $i, j = 1, 2$. The functions $\tilde{c}^e(x,t)$ and $\tilde{\phi}^e(x,t)$ are continuous across the electrode-separator interface, which is denoted by ρ_1 and ρ_2 in Figure 5.5. Strictly speaking, we have that

$$\tilde{c}^e|_{\rho_1^-} = \tilde{c}^e|_{\rho_1^+}, \quad \tilde{c}^e|_{\rho_2^-} = \tilde{c}^e|_{\rho_2^+} \tag{5.7.7a}$$

$$\tilde{\phi}^e|_{\rho_1^-} = \tilde{\phi}^e|_{\rho_1^+}, \quad \tilde{\phi}^e|_{\rho_2^-} = \tilde{\phi}^e|_{\rho_2^+} \tag{5.7.7b}$$

where with $\tilde{c}^e|_{\rho_1^-}$ we denote the values of the concentration on the interface wall ρ_1 in the anode domain, and with $\tilde{c}^e|_{\rho_1^+}$ - the values of the concentration on the wall ρ_1 on the side of the pure electrolyte domain. By analogy, with $\tilde{c}^e|_{\rho_2^-}$ we denote the values of the concentration on the interface wall ρ_2 on the side of the pure electrolyte domain $\Omega^e_{separator}$, and with $\tilde{c}^e|_{\rho_2^+}$ - the values of the concentration on the interface wall ρ_2 in the cathode domain $\Omega_{cathode}$. For the electrochemical potential $\tilde{\phi}^e$ we use the same notation.

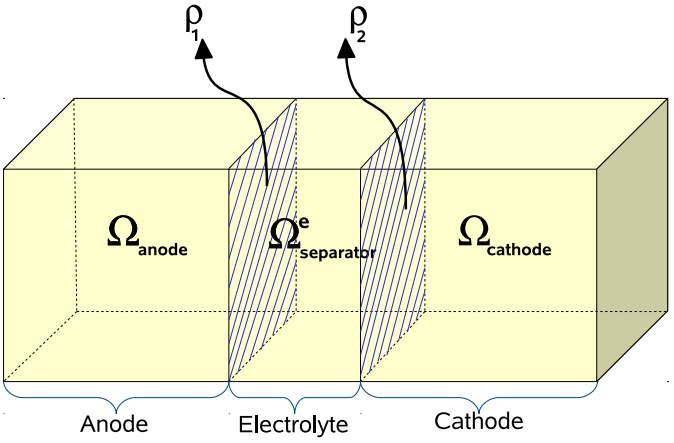

Figure 5.5: Schematic domain of the battery cell

Since the electrical potential ϕ_0^s and the solid phase concentration c^s are defined only for $x \in \Omega_{electrode}$, we solve the homogenized equation (5.6.1c) and the microscale equation (5.6.3) only in the electrodes Ω_{anode} and $\Omega_{cathode}$. Therefore, for the potential ϕ_0^s we solve the following boundary value problem in the anode

$$-\nabla_x \cdot (\mathbf{\Lambda^s} \nabla_x \phi_0^s) = -\frac{1}{\varepsilon\,|Y|} \int\limits_{\Gamma} \mathcal{J}(c_0^e, c^s, \phi_0^e, \phi_0^s)\, ds, \quad x \in \Omega_{anode} \tag{5.7.8a}$$

$$\phi_0^s = E_1^s, \quad x \in \omega_1 \tag{5.7.8b}$$

$$-\mathbf{\Lambda^s} \nabla_x \phi_0^s \cdot \mathbf{n} = 0, \quad x \in \rho_1 \tag{5.7.8c}$$

$$-\mathbf{\Lambda^s} \nabla_x \phi_0^s \cdot \mathbf{n} = 0, \quad x \in \{\partial\Omega_{anode} \backslash \omega_1\} \tag{5.7.8d}$$

and in the cathode

$$-\nabla_x \cdot (\mathbf{\Lambda^s} \nabla_x \phi_0^s) = -\frac{1}{\varepsilon\,|Y|} \int\limits_{\Gamma} \mathcal{J}(c_0^e, c^s, \phi_0^e, \phi_0^s)\, ds, \quad x \in \Omega_{cathode} \tag{5.7.9a}$$

$$-\mathbf{\Lambda^s} \nabla_x \phi_0^s \cdot \mathbf{n} = 0, \quad x \in \rho_2 \tag{5.7.9b}$$

$$-\mathbf{\Lambda^s} \nabla_x \phi_0^s \cdot \mathbf{n} = 0, \quad x \in \{\partial\Omega_{cathode} \backslash \omega_2\} \tag{5.7.9c}$$

$$-\mathbf{\Lambda^s} \nabla_x \phi_0^s \cdot \mathbf{n} = \frac{|S^{surf}|}{|Y^{surf}|} E_2^s, \quad x \in \omega_2 \tag{5.7.9d}$$

With $\mathbf{n}$ we denote the respective unit outward normal vectors. In problems (5.7.8) and (5.7.9) we impose zero Neumann (no flux) boundary condition for the homogenized electrical flux $-\mathbf{\Lambda^s} \nabla_x \phi_0^s$ on the electrode-separator interface boundaries ρ_1 and ρ_2. We do not need to account additionally for the Butler-Volmer interface conditions, because they are accounted for naturally in the homogenized equations (5.7.8a) and (5.7.9a) in the right-hand side as part of the homogenization procedure.
We solve the boundary value problems (5.7.8) and (5.7.9) for the electrical homogenized potential ϕ_0^s, and the electrolyte phase problem (5.7.1) as a single system of equations, where the coupling between the two sets of problems is due to the interface exchange current densities $\mathcal{N}$ and $\mathcal{J}$ in their right-hand sides. Additionally, for each $x \in \Omega_{electrode}$ we have to solve the microscale problem (5.6.3).

5.7.1 Numerical methods

For the space discretization of the homogenized problem we use the Finite Element Method with linear Lagrange elements and for the time discretization we apply the Backward Euler method. We use the Newton-Raphson method for the linearization of the resulting system of nonlinear algebraic equations. More details on the numerical methods that we use can be found in [9], [13], [60], [33] and [43].

5.7.2 Weak formulation of the problem

As usual, in order to obtain the weak formulation of problem (5.7.1)-(5.7.8) ((5.7.9)) we multiply both sides of the equations by appropriate sufficiently smooth test functions and

then we integrate over the respective solution domains:

$$\int_\Omega \alpha \frac{\partial \tilde{c}^e}{\partial t} v(x)\,dx - \int_\Omega \nabla_x \cdot \left(\mathcal{K}_{11}^e \nabla_x \tilde{c}^e + \mathcal{K}_{12}^e \nabla_x \tilde{\phi}^e \right) v(x)\,dx =$$

$$= \int_\Omega f_1(x) v(x)\,dx \tag{5.7.10a}$$

$$- \int_\Omega \nabla_x \cdot \left(\mathcal{K}_{21}^e \nabla_x \tilde{c}^e + \mathcal{K}_{22}^e \nabla_x \tilde{\phi}^e \right) v(x)\,dx = \int_\Omega f_2(x) v(x)\,dx \tag{5.7.10b}$$

$$- \int_{\Omega_{electrode}} \nabla_x \cdot \left(\mathbf{\Lambda^s} \nabla_x \phi_0^s \right) w(x)\,dx = - \int_{\Omega_{electrode}} \left(\frac{1}{\varepsilon\,|Y|} \int_\Gamma \mathcal{J}_0\,ds \right) w(x)\,dx \tag{5.7.10c}$$

where we recall that $\Omega_{electrode} = \Omega_{anode}$ or $\Omega_{electrode} = \Omega_{cathode}$. Equations (5.7.10) are equivalent to

$$\alpha \int_\Omega \frac{\partial \tilde{c}^e}{\partial t} v\,dx - \int_\Omega \nabla_x \cdot \left(v \mathcal{K}_{11}^e \nabla_x \tilde{c}^e + v \mathcal{K}_{12}^e \nabla_x \tilde{\phi}^e \right) dx +$$

$$+ \int_\Omega \left((\mathcal{K}_{11}^e \nabla_x \tilde{c}^e) \cdot \nabla v + \left(\mathcal{K}_{12}^e \nabla_x \tilde{\phi}^e \right) \cdot \nabla v \right) dx = \int_\Omega f_1 v\,dx \tag{5.7.11a}$$

$$- \int_\Omega \nabla_x \cdot \left(v \mathcal{K}_{21}^e \nabla_x \tilde{c}^e + v \mathcal{K}_{22}^e \nabla_x \tilde{\phi}^e \right) dx +$$

$$+ \int_\Omega \left((\mathcal{K}_{21}^e \nabla_x \tilde{c}^e) \cdot \nabla v + \left(\mathcal{K}_{22}^e \nabla_x \tilde{\phi}^e \right) \cdot \nabla v \right) dx = \int_\Omega f_2 v\,dx \tag{5.7.11b}$$

$$\int_{\Omega_{electrode}} \nabla_x \cdot \left(w \mathbf{\Lambda^s} \nabla_x \phi_0^s \right) dx - \int_{\Omega_{electrode}} (\mathbf{\Lambda^s} \nabla_x \phi_0^s) \cdot \nabla w\,dx = \int_{\Omega_{electrode}} \left(\frac{1}{\varepsilon\,|Y|} \int_\Gamma \mathcal{J}_0\,ds \right) w\,dx \tag{5.7.11c}$$

Now we apply the divergence theorem and taking into account the boundary conditions (5.7.2), equations (5.7.11) become

$$\alpha \int_\Omega \frac{\partial \tilde{c}^e}{\partial t} v\,dx + \int_\Omega \left((\mathcal{K}_{11}^e \nabla_x \tilde{c}^e) \cdot \nabla v + \left(\mathcal{K}_{12}^e \nabla_x \tilde{\phi}^e \right) \cdot \nabla v \right) dx = \int_\Omega f_1 v\,dx \tag{5.7.12a}$$

$$\int_\Omega \left((\mathcal{K}_{21}^e \nabla_x \tilde{c}^e) \cdot \nabla v + \left(\mathcal{K}_{22}^e \nabla_x \tilde{\phi}^e \right) \cdot \nabla v \right) dx = \int_\Omega f_2 v\,dx \tag{5.7.12b}$$

$$\int_{\partial\Omega_{electrode}} w \mathbf{\Lambda^s} \nabla_x \phi_0^s \cdot \mathbf{n}\,ds - \int_{\Omega_{electrode}} (\mathbf{\Lambda^s} \nabla_x \phi_0^s) \cdot \nabla w\,dx = \int_{\Omega_{electrode}} \left(\frac{1}{\varepsilon\,|Y|} \int_\Gamma \mathcal{J}_0\,ds \right) w\,dx \tag{5.7.12c}$$

In the anode, due to boundary conditions (5.7.8b)-(5.7.8d), and w having zero trace on the Dirichlet boundary, the boundary integral in equation (5.7.12c) vanishes. Hence, in the anode (5.7.12c) becomes

$$-\int\limits_{\Omega_{anode}} (\mathbf{\Lambda^s}\nabla_x\phi_0^s)\cdot\nabla w\,dx = \int\limits_{\Omega_{anode}} \left(\frac{1}{\varepsilon\,|Y|}\int\limits_{\Gamma}\mathcal{J}_0\,ds\right) w\,dx \tag{5.7.13}$$

and we impose the Dirichlet data directly in the final resulting system of linear algebraic equations.
In the cathode, taking into account the Neumann boundary conditions (5.7.9b)-(5.7.9d), the boundary integral in equation (5.7.12c) is equivalent to

$$\int\limits_{\partial\Omega_{cathode}\setminus\omega_2} w\mathbf{\Lambda^s}\nabla_x\phi_0^s\cdot\mathbf{n}\,ds + \int\limits_{\omega_2} w\mathbf{\Lambda^s}\nabla_x\phi_0^s\cdot\mathbf{n}\,ds = \int\limits_{\omega_2} w\frac{\left|S^{surf}\right|}{\left|Y^{surf}\right|}E_2^s\,ds \tag{5.7.14}$$

and the equation itself becomes

$$\int\limits_{\omega_2} w\frac{\left|S^{surf}\right|}{\left|Y^{surf}\right|}E_2^s\,ds - \int\limits_{\Omega_{cathode}} (\mathbf{\Lambda^s}\nabla_x\phi_0^s)\cdot\nabla w\,dx = \int\limits_{\Omega_{cathode}} \left(\frac{1}{\varepsilon\,|Y|}\int\limits_{\Gamma}\mathcal{J}_0\,ds\right) w\,dx \tag{5.7.15}$$

Finally, for the weak form of the homogenized problem we obtain: find $\tilde{c}^e$, $\tilde{\phi}^e \in H^1(\Omega)$ and $\phi_0^s \in H^1(\Omega_{electrode})$, so that the following integral equalities are satisfied for all functions $v \in H^1(\Omega)$ and $w \in H^1(\Omega_{electrode})$

$$\alpha\int\limits_{\Omega}\frac{\partial\tilde{c}^e}{\partial t}v\,dx + \int\limits_{\Omega}\left((\mathcal{K}_{11}^e\nabla_x\tilde{c}^e)\cdot\nabla v + \left(\mathcal{K}_{12}^e\nabla_x\tilde{\phi}^e\right)\cdot\nabla v\right)dx = \int\limits_{\Omega} f_1 v\,dx \tag{5.7.16a}$$

$$\int\limits_{\Omega}\left((\mathcal{K}_{21}^e\nabla_x\tilde{c}^e)\cdot\nabla v + \left(\mathcal{K}_{22}^e\nabla_x\tilde{\phi}^e\right)\cdot\nabla v\right)dx = \int\limits_{\Omega} f_2 v\,dx \tag{5.7.16b}$$

$$I - \int\limits_{\Omega_{electrode}} (\mathbf{\Lambda^s}\nabla_x\phi_0^s)\cdot\nabla w\,dx = \int\limits_{\Omega_{electrode}} \left(\frac{1}{\varepsilon\,|Y|}\int\limits_{\Gamma}\mathcal{J}_0\,ds\right) w\,dx \tag{5.7.16c}$$

where

$$I = \begin{cases} \displaystyle\int\limits_{\omega_2} w\frac{\left|S^{surf}\right|}{\left|Y^{surf}\right|}E_2^s\,ds, & x\in\Omega_{cathode} \\ \\ 0, & x\in\Omega_{anode} \end{cases} \tag{5.7.17}$$

5.7.3 Discretization of the problem

Space discretization

In order to solve numerically the homogenized probelm, we need to restrict its weak form (5.7.16) to a finite dimensional approximation subspace $V^h \subset H^1(\Omega)$ and $V^h_{electrode} \subset H^1(\Omega_{electrode})$. Let $dim(V^h) = N$ and $dim(V^h_{electrode}) = n < N$. Then the discretized weak formulation of the homogenized problem reads as: find $(\tilde{c}^e)^h$, $\left(\tilde{\phi}^e\right)^h \in V^h$ and $(\phi_0^s)^h \in V^h_{electrode}$, so that the following integral equalities are true for all functions $v^h \in V^h$ and $w^h \in V^h_{electrode}$

$$\alpha \int\limits_{\Omega} \frac{\partial \left(\tilde{c}^e\right)^h}{\partial t} v^h \, dx + \int\limits_{\Omega} \left(\left(\mathcal{K}^e_{11} \nabla_x \left(\tilde{c}^e\right)^h \right) \cdot \nabla v^h + \left(\mathcal{K}^e_{12} \nabla_x \left(\tilde{\phi}^e\right)^h \right) \cdot \nabla v^h \right) dx = \int\limits_{\Omega} f_1 v^h \, dx \tag{5.7.18a}$$

$$\int\limits_{\Omega} \left(\left(\mathcal{K}^e_{21} \nabla_x \left(\tilde{c}^e\right)^h \right) \cdot \nabla v^h + \left(\mathcal{K}^e_{22} \nabla_x \left(\tilde{\phi}^e\right)^h \right) \cdot \nabla v^h \right) dx = \int\limits_{\Omega} f_2 v^h \, dx \tag{5.7.18b}$$

$$I - \int\limits_{\Omega_{electrode}} \left(\mathbf{\Lambda^s} \nabla_x \left(\phi_0^s\right)^h \right) \cdot \nabla w^h \, dx = \int\limits_{\Omega_{electrode}} \left(\frac{1}{\varepsilon \left|Y\right|} \int\limits_{\Gamma} \mathcal{J}_0^h \, ds \right) w^h \, dx \tag{5.7.18c}$$

where

$$I = \begin{cases} \displaystyle\int\limits_{\omega_2} w^h(x) \frac{\left|S^{surf}\right|}{\left|Y^{surf}\right|} E_2^s \, ds, & x \in \Omega_{cathode} \\ \\ 0, & x \in \Omega_{anode} \end{cases} \tag{5.7.19}$$

and

$$f_1(x) = \begin{cases} 0, & x \in \Omega^e_{separator}, \\ \\ \dfrac{1}{\varepsilon \left|Y\right|} \displaystyle\int\limits_{\Gamma} \mathcal{N} \left(\left(\tilde{c}^e\right)^h, \left(\tilde{\phi}^e\right)^h, c^s, \left(\phi_0^s\right)^h \right) ds, & x \in \Omega_{anode} \cup \Omega_{cathode} \end{cases} \tag{5.7.20}$$

$$f_2(x) = \begin{cases} 0, & x \in \Omega^e_{separator}, \\ \\ \dfrac{1}{\varepsilon \left|Y\right|} \displaystyle\int\limits_{\Gamma} \mathcal{J} \left(\left(\tilde{c}^e\right)^h, \left(\tilde{\phi}^e\right)^h, c^s, \left(\phi_0^s\right)^h \right) ds, & x \in \Omega_{anode} \cup \Omega_{cathode} \end{cases} \tag{5.7.21}$$

$$\mathcal{K}_{lm}^{e} = \mathcal{K}_{lm}^{e}\left((\tilde{c}^{e})^{h}\right) = \begin{cases} \mathbf{K}_{\mathbf{lm}}^{\mathbf{micro}}\left((c^{e})^{h}\right), & x \in \Omega_{separator}^{e}, \\ \mathbf{K}_{\mathbf{lm}}\left((c_0^{e})^{h}\right), & x \in \Omega_{anode} \cup \Omega_{cathode} \end{cases} \tag{5.7.22}$$

for $l, m = 1, 2$, and we denote

$$\mathcal{J}_0^h = \mathcal{J}\left((\tilde{c}^{e})^{h}, \left(\tilde{\phi}^{e}\right)^{h}, c^{s}, (\phi_0^{s})^{h}\right) \tag{5.7.23}$$

$$\mathcal{N}_0^h = \mathcal{N}\left((\tilde{c}^{e})^{h}, \left(\tilde{\phi}^{e}\right)^{h}, c^{s}, (\phi_0^{s})^{h}\right) \tag{5.7.24}$$

For the space discretization of the homogenized problem we use the Finite Element Method with linear Lagrange finite elements (for more details on the method see [9], [13] and [60]). The FEM has a convergence rate of $O(h^2)$ in the L^2 norm and $O(h)$ in the H^1 norm, where h is the size of the mesh. We consider a partition $\mathcal{T}^h$ of the solution domain Ω into finite elements T, i.e., $\mathcal{T}^h = \bigcup_{T \in \mathcal{T}^h} T$. Let $V^h = span\left\{\varphi_i(x)\right\}_{i=1}^{N}$ where $\left\{\varphi_i(x)\right\}_{i=1}^{N}$ are the finite element basis functions such that

$$\varphi_i(x^j) = \begin{cases} 1, & i = j, \\ 0, & i \neq j \end{cases} \tag{5.7.25}$$

where $x^j = (x_1^j, x_2^j, x_3^j)$ for $j = 1, \ldots, N$ are the nodes of the discretization mesh. The basis functions are piecewise linear polynomials and have local supports. A two-dimensional basis hat function is shown in Figure 5.7. We discretize separately the three subdomains Ω_{anode}, $\Omega_{separator}^{e}$ and $\Omega_{cathode}$ in such a way that they share the same mesh points on the inner electrode-electrolyte boundaries ρ_1 and ρ_2 (see Figure 5.5) with no element lying simultaneously in two different subdomains as shown in the two-dimensional example with triangular elements in Figure 5.6. Now, we expand the discretized approximate solutions $(\tilde{c}^{e})^{h}$, $\left(\tilde{\phi}^{e}\right)^{h}$, and $(\phi_0^{s})^{h}$ with respect to the standard linear basis

$$(\tilde{c}^{e})^{h}(x,t) = \sum_{i=1}^{N} \tilde{C}_i^{e}(t)\varphi_i(x) \tag{5.7.26a}$$

$$\left(\tilde{\phi}^{e}\right)^{h}(x,t) = \sum_{i=1}^{N} \tilde{\Phi}_i^{e}(t)\varphi_i(x) \tag{5.7.26b}$$

$$(\phi_0^{s})^{h}(x,t) = \sum_{i=1}^{n} \Phi_i^{s}(t)\varphi_i(x) \tag{5.7.26c}$$

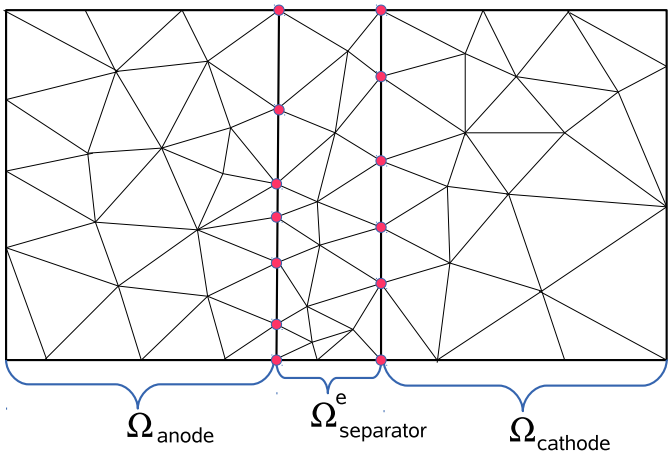

Figure 5.6: Exemplary triangulation of a 2D schematic solution domain Ω

where for $(\phi_0^s)^h$ we use only the basis functions, that are defined over the electrodes and, respectively, for the basis functions corresponding to a node belonging to ρ_1 or ρ_2 (see Figure 5.5), we use only their restriction to the electrode domain. We use the basis functions $\varphi_i(x)$ also as test functions in the discretized weak form (5.7.18), i.e., we take $v^h(x) = \varphi_j(x)$ for all $j = 1, \dots, N$ and $w^h(x) = \varphi_k(x)$ for all $k = 1, \dots, n$. Thus, we obtain

$$\alpha \int_\Omega \frac{\partial}{\partial t}\left(\sum_{i=1}^{N} \tilde{C}_i^e(t)\varphi_i(x)\right)\varphi_j(x)\,dx + \int_\Omega \left(\left(\mathcal{K}_{11}^e \sum_{i=1}^{N} \tilde{C}_i^e(t)\nabla\varphi_i\right)\cdot\nabla\varphi_j + \left(\mathcal{K}_{12}^e \sum_{i=1}^{N} \tilde{\Phi}_i^e(t)\nabla\varphi_i\right)\cdot\nabla\varphi_j\right)dx = \int_\Omega f_1\varphi_j(x)\,dx \tag{5.7.27a}$$

$$\int_\Omega \left(\left(\mathcal{K}_{21}^e \sum_{i=1}^{N} \tilde{C}_i^e(t)\nabla\varphi_i\right)\cdot\nabla\varphi_j + \left(\mathcal{K}_{22}^e \sum_{i=1}^{N} \tilde{\Phi}_i^e(t)\nabla\varphi_i\right)\cdot\nabla\varphi_j\right)dx = \int_\Omega f_2\varphi_j(x)\,dx \tag{5.7.27b}$$

$$I - \int_{\Omega_{electrode}} \left(\mathbf{\Lambda^s}\sum_{i=1}^{n} \Phi_i^s(t)\nabla\varphi_i\right)\cdot\nabla\varphi_k\,dx = \int_{\Omega_{electrode}} \left(\frac{1}{\varepsilon\,|Y|}\int_\Gamma \mathcal{J}_0^h\,ds\right)\varphi_k(x)\,dx \tag{5.7.27c}$$

for all $j = 1, \dots, N$ and $k = 1, \dots, n$, and where

$$I = \begin{cases} \dfrac{|S^{surf}|}{|Y^{surf}|} E_2^s \displaystyle\int_{\omega_2} \varphi_k(x)\,ds, & x \in \Omega_{cathode} \\ \\ 0, & x \in \Omega_{anode} \end{cases} \tag{5.7.28}$$

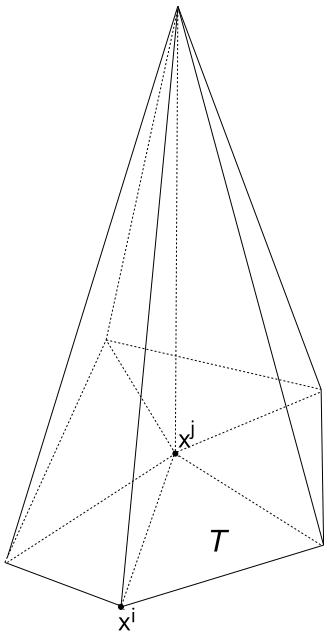

Figure 5.7: The 2D basis hat function $\varphi_j(x)$ with its support

Time discretization

For the time discretization we use the Backward Euler Method, which is an implicit scheme and is shown to be stable for nonlinear problems [33]. The method has a convergence rate $O(\tau)$, where τ is the time step.
Equation (5.7.27a) is equivalent to

$$\alpha \int_\Omega \sum_{i=1}^{N} \frac{\partial \tilde{C}_i^e(t)}{\partial t} \varphi_i(x)\varphi_j(x)\,dx + \\ + \int_\Omega \left(\left(\mathcal{K}_{11}^e \sum_{i=1}^{N} \tilde{C}_i^e(t) \nabla\varphi_i \right) \cdot \nabla\varphi_j + \left(\mathcal{K}_{12}^e \sum_{i=1}^{N} \tilde{\Phi}_i^e(t) \nabla\varphi_i \right) \cdot \nabla\varphi_j \right) dx = \int_\Omega f_1 \varphi_j(x)\,dx \tag{5.7.29}$$

Now we approximate the time derivative

$$\frac{\partial \tilde{C}_i^e(t)}{\partial t} \approx \frac{\tilde{C}_i^{e,(m)} - \tilde{C}_i^{e,(m-1)}}{\tau} \tag{5.7.30}$$

where we denote

$$\tilde{C}_i^{e,(m)} = \tilde{C}_i^e(t_m) \tag{5.7.31}$$
$$\tilde{\Phi}_i^{e,(m)} = \tilde{\Phi}_i^e(t_m) \tag{5.7.32}$$
$$\Phi_i^{s,(m)} = \Phi_i^s(t_m) \tag{5.7.33}$$

with t_m being the discrete time moments and

$$\tau = t_m - t_{m-1} \tag{5.7.34}$$

is the time step. We also take all other quantities on the m-th time step and obtain the following system of nonlinear algebraic equations

$$\alpha \int\limits_{\Omega} \sum_{i=1}^{N} \frac{\tilde{C}_i^{e,(m)} - \tilde{C}_i^{e,(m-1)}}{\tau} \varphi_i(x)\varphi_j(x)\,dx + \\ + \int\limits_{\Omega} \left(\left(\mathcal{K}_{11}^e \sum_{i=1}^{N} \tilde{C}_i^{e,(m)} \nabla\varphi_i \right) \cdot \nabla\varphi_j + \left(\mathcal{K}_{12}^e \sum_{i=1}^{N} \tilde{\Phi}_i^{e,(m)} \nabla\varphi_i \right) \cdot \nabla\varphi_j \right) dx - \int\limits_{\Omega} f_1\varphi_j(x)\,dx = 0 \tag{5.7.35a}$$

$$\int\limits_{\Omega} \left(\left(\mathcal{K}_{21}^e \sum_{i=1}^{N} \tilde{C}_i^{e,(m)} \nabla\varphi_i \right) \cdot \nabla\varphi_j + \left(\mathcal{K}_{22}^e \sum_{i=1}^{N} \tilde{\Phi}_i^{e,(m)} \nabla\varphi_i \right) \cdot \nabla\varphi_j \right) dx - \int\limits_{\Omega} f_2\varphi_j(x)\,dx = 0 \tag{5.7.35b}$$

$$I - \int\limits_{\Omega_{electrode}} \left(\mathbf{\Lambda^s} \sum_{i=1}^{n} \Phi_i^{s,(m)} \nabla\varphi_i \right) \cdot \nabla\varphi_k\,dx - \int\limits_{\Omega_{electrode}} \left(\frac{1}{\varepsilon\,|Y|} \int\limits_{\Gamma} \mathcal{J}_0^{h,(m)}\,ds \right) \varphi_k(x)\,dx = 0 \tag{5.7.35c}$$

for all $j = 1, \ldots, N$ and $k = 1, \ldots, n$, and with

$$f_1(x) = \begin{cases} 0, & x \in \Omega_{separator}^e, \\ \dfrac{1}{\varepsilon\,|Y|} \displaystyle\int\limits_{\Gamma} \mathcal{N}\left(\left(\tilde{c}^e\right)^{h,(m)}, \left(\tilde{\phi}^e\right)^{h,(m)}, c^s, \left(\phi^s\right)^{h,(m)} \right) ds, & x \in \Omega_{anode} \cup \Omega_{cathode} \end{cases} \tag{5.7.36}$$

$$f_2(x) = \begin{cases} 0, & x \in \Omega_{separator}^e, \\ \dfrac{1}{\varepsilon\,|Y|} \displaystyle\int\limits_{\Gamma} \mathcal{J}\left(\left(\tilde{c}^e\right)^{h,(m)}, \left(\tilde{\phi}^e\right)^{h,(m)}, c^s, \left(\phi^s\right)^{h,(m)} \right) ds, & x \in \Omega_{anode} \cup \Omega_{cathode} \end{cases} \tag{5.7.37}$$

$$\mathcal{K}_{lm}^e = \mathcal{K}_{lm}^e \left(\left(\tilde{c}^e\right)^{h,(m)} \right) \tag{5.7.38}$$

for $l, m = 1, 2$, and

$$\mathcal{J}_0^{h,(m)} = \mathcal{J}\left(\left(\tilde{c}^e\right)^{h,(m)}, \left(\tilde{\phi}^e\right)^{h,(m)}, c^s, \left(\phi^s\right)^{h,(m)} \right) \tag{5.7.39}$$

where we use the following notation

$$\left(\tilde{c}^e\right)^{h,(m)}(x) = \left(\tilde{c}^e\right)^h(x,t_m) = \sum_{i=1}^{N} \tilde{C}_i^{e,(m)} \varphi_i(x) \tag{5.7.40a}$$

$$\left(\tilde{\phi}^e\right)^{h,(m)}(x) = \left(\tilde{\phi}^e\right)^h(x,t_m) = \sum_{i=1}^{N} \tilde{\Phi}_i^{e,(m)} \varphi_i(x) \tag{5.7.40b}$$

$$\left(\phi^s\right)^{h,(m)}(x) = \left(\phi^s\right)^h(x,t_m) = \sum_{i=1}^{n} \Phi_i^{s,(m)} \varphi_i(x) \tag{5.7.40c}$$

We denote with $G_1^j = G_1^j\left(\tilde{\mathbf{C}}^{\mathbf{e},(\mathbf{m})}, \tilde{\mathbf{\Phi}}^{\mathbf{e},(\mathbf{m})}, \mathbf{\Phi}^{\mathbf{s},(\mathbf{m})}\right)$, $G_2^j = G_2^j\left(\tilde{\mathbf{C}}^{\mathbf{e},(\mathbf{m})}, \tilde{\mathbf{\Phi}}^{\mathbf{e},(\mathbf{m})}, \mathbf{\Phi}^{\mathbf{s},(\mathbf{m})}\right)$ and $G_3^k = G_3^k\left(\tilde{\mathbf{C}}^{\mathbf{e},(\mathbf{m})}, \tilde{\mathbf{\Phi}}^{\mathbf{e},(\mathbf{m})}, \mathbf{\Phi}^{\mathbf{s},(\mathbf{m})}\right)$ the following functions

$$\begin{aligned} G_1^j = & \int_\Omega \alpha \sum_{i=1}^{N} \frac{\tilde{C}_i^{e,(m)} - \tilde{C}_i^{e,(m-1)}}{\tau} \varphi_i(x)\varphi_j(x)\,dx + \\ & + \int_\Omega \left(\left(\mathcal{K}_{11}^e \sum_{i=1}^{N} \tilde{C}_i^{e,(m)} \nabla\varphi_i \right) \cdot \nabla\varphi_j + \left(\mathcal{K}_{12}^e \sum_{i=1}^{N} \tilde{\Phi}_i^{e,(m)} \nabla\varphi_i \right) \cdot \nabla\varphi_j \right) dx - \int_\Omega f_1 \varphi_j(x)\,dx \end{aligned} \tag{5.7.41}$$

$$G_2^j = \int_\Omega \left(\left(\mathcal{K}_{21}^e \sum_{i=1}^{N} \tilde{C}_i^{e,(m)} \nabla\varphi_i \right) \cdot \nabla\varphi_j + \left(\mathcal{K}_{22}^e \sum_{i=1}^{N} \tilde{\Phi}_i^{e,(m)} \nabla\varphi_i \right) \cdot \nabla\varphi_j \right) dx - \int_\Omega f_2 \varphi_j(x)\,dx \tag{5.7.42}$$

$$G_3^k = I - \int_{\Omega_{electrode}} \left(\mathbf{\Lambda}^{\mathbf{s}} \sum_{i=1}^{n} \Phi_i^{s,(m)} \nabla\varphi_i \right) \cdot \nabla\varphi_k\,dx - \int_{\Omega_{electrode}} \left(\frac{1}{\varepsilon\,|Y|} \int_\Gamma \mathcal{J}_0^{h,(m)}\,ds \right) \varphi_k(x)\,dx \tag{5.7.43}$$

where

$$\tilde{\mathbf{C}}^{\mathbf{e},(\mathbf{m})} = \left(\tilde{C}_1^{e,(m)}, \tilde{C}_2^{e,(m)}, \ldots, \tilde{C}_N^{e,(m)} \right) \tag{5.7.44a}$$

$$\tilde{\mathbf{\Phi}}^{\mathbf{e},(\mathbf{m})} = \left(\tilde{\Phi}_1^{e,(m)}, \tilde{\Phi}_2^{e,(m)}, \ldots, \tilde{\Phi}_N^{e,(m)} \right) \tag{5.7.44b}$$

$$\mathbf{\Phi}^{\mathbf{s},(\mathbf{m})} = \left(\Phi_1^{s,(m)}, \Phi_2^{s,(m)}, \ldots, \Phi_n^{s,(m)} \right) \tag{5.7.44c}$$

are the unknowns at the current time step.

Linearization

Now, we have to solve the following system of nonlinear algebraic equations at each time step of the Backward Euler method time iterations

$$\left|\begin{array}{l} G_1^j\left(\tilde{\mathbf{C}}^{\mathbf{e},(\mathbf{m})}, \tilde{\mathbf{\Phi}}^{\mathbf{e},(\mathbf{m})}, \mathbf{\Phi}^{\mathbf{s},(\mathbf{m})}\right) = 0 \\ G_2^j\left(\tilde{\mathbf{C}}^{\mathbf{e},(\mathbf{m})}, \tilde{\mathbf{\Phi}}^{\mathbf{e},(\mathbf{m})}, \mathbf{\Phi}^{\mathbf{s},(\mathbf{m})}\right) = 0 \\ G_3^k\left(\tilde{\mathbf{C}}^{\mathbf{e},(\mathbf{m})}, \tilde{\mathbf{\Phi}}^{\mathbf{e},(\mathbf{m})}, \mathbf{\Phi}^{\mathbf{s},(\mathbf{m})}\right) = 0 \end{array}\right. \tag{5.7.45}$$

In order to linearize the system we apply the Newton-Raphson method [43]. The Jacobian is a $(2N+n)\times(2N+n)$ sparse matrix and has the following form

$$J = \begin{pmatrix} \dfrac{\partial G_1^j}{\partial \tilde{C}_l^{e,(m)}} & \dfrac{\partial G_1^j}{\partial \tilde{\Phi}_l^{e,(m)}} & \dfrac{\partial G_1^j}{\partial \Phi_p^{s,(m)}} \\ \dfrac{\partial G_2^j}{\partial \tilde{C}_l^{e,(m)}} & \dfrac{\partial G_2^j}{\partial \tilde{\Phi}_l^{e,(m)}} & \dfrac{\partial G_2^j}{\partial \Phi_p^{s,(m)}} \\ \dfrac{\partial G_3^k}{\partial \tilde{C}_l^{e,(m)}} & \dfrac{\partial G_3^k}{\partial \tilde{\Phi}_l^{e,(m)}} & \dfrac{\partial G_3^k}{\partial \Phi_p^{s,(m)}} \end{pmatrix} \tag{5.7.46}$$

where $j,l = 1,\ldots,N$ and $k,p = 1,\ldots,n$. We solve the following system of equations at each Netwon-Raphson iteration

$$J\left(\mathbf{U}^{(r-1)}\right)\left(\mathbf{U}^{(r)} - \mathbf{U}^{(r-1)}\right) = -\mathbf{G}\left(\mathbf{U}^{(r-1)}\right) \tag{5.7.47}$$

where with

$$\mathbf{U}^{(r)} = \left(\left(\tilde{\mathbf{C}}^{\mathbf{e},(\mathbf{m})}\right)^{(r)}, \left(\tilde{\mathbf{\Phi}}^{\mathbf{e},(\mathbf{m})}\right)^{(r)}, \left(\mathbf{\Phi}^{\mathbf{s},(\mathbf{m})}\right)^{(r)}\right)^T \tag{5.7.48}$$

we denote the solution at the current Newton-Raphson iteration, and the right-hand side is given by

$$\mathbf{G}\left(\mathbf{U}^{(r-1)}\right) = \left(G_1^j\left(\mathbf{U}^{(r-1)}\right), G_2^j\left(\mathbf{U}^{(r-1)}\right), G_3^k\left(\mathbf{U}^{(r-1)}\right)\right)^T \tag{5.7.49}$$

Let us denote

$$\mathcal{I}_{electrodes} = \left\{i |\ T_i \in \mathcal{T}^h :\ T_i \in \Omega_{anode} \cup \Omega_{cathode}\right\} \tag{5.7.50}$$

(5.7.51)

and

$$(\mathcal{P}_1, p_1) = \left(\tilde{C}_l^{e,(m)}, c^e\right) \tag{5.7.52a}$$

$$(\mathcal{P}_2, p_2) = \left(\tilde{\Phi}_l^{e,(m)}, \phi^e\right) \tag{5.7.52b}$$

$$(\mathcal{P}_3, p_3) = \left(\Phi_p^{s,(m)}, \phi^s\right) \tag{5.7.52c}$$

Then for $i = 1, 2, 3$ we have that

$$\int_{\Omega} \frac{\partial f_1}{\partial \mathcal{P}_i} \varphi_j(x)\, dx = \int_{\Omega_{anode}} \frac{\partial f_1}{\partial \mathcal{P}_i} \varphi_j(x)\, dx + \int_{\Omega^e_{separator}} \underbrace{\frac{\partial f_1}{\partial \mathcal{P}_i}}_{=0} \varphi_j(x)\, dx + \int_{\Omega_{cathode}} \frac{\partial f_1}{\partial \mathcal{P}_i} \varphi_j(x)\, dx =$$

$$= \sum_{r \in \mathcal{I}_{electrodes}} \int_{T_r} \left(\frac{1}{\varepsilon\, |Y|} \int_{\Gamma} \frac{\partial \mathcal{N}}{\partial p_i} \left((\tilde{c}^e)^{h,(m)}, \left(\tilde{\phi}^e\right)^{h,(m)}, c^s, (\phi^s)^{h,(m)} \right) ds \right) \varphi_l(x) \varphi_j(x)\, dx \tag{5.7.53}$$

and

$$\int_{\Omega} \frac{\partial f_2}{\partial \mathcal{P}_i} \varphi_j(x)\, dx = \int_{\Omega_{anode}} \frac{\partial f_2}{\partial \mathcal{P}_i} \varphi_j(x)\, dx + \int_{\Omega^e_{separator}} \underbrace{\frac{\partial f_2}{\partial \mathcal{P}_i}}_{=0} \varphi_j(x)\, dx + \int_{\Omega_{cathode}} \frac{\partial f_2}{\partial \mathcal{P}_i} \varphi_j(x)\, dx =$$

$$= \sum_{r \in \mathcal{I}_{electrodes}} \int_{T_r} \left(\frac{1}{\varepsilon\, |Y|} \int_{\Gamma} \frac{\partial \mathcal{J}}{\partial p_i} \left((\tilde{c}^e)^{h,(m)}, \left(\tilde{\phi}^e\right)^{h,(m)}, c^s, (\phi^s)^{h,(m)} \right) ds \right) \varphi_l(x) \varphi_j(x)\, dx \tag{5.7.54}$$

Taking into account (5.7.53) and (5.7.54), for the elements of the Jacobian matrix we obtain

$$\frac{\partial G_1^j}{\partial \tilde{C}_l^{e,(m)}} = \frac{1}{\tau} \sum_{T \in \mathcal{T}^h} \int_T \alpha \varphi_l(x) \varphi_j(x)\, dx +$$

$$+ \sum_{T \in \mathcal{T}^h} \int_T \left(\frac{\partial \mathcal{K}^e_{11}}{\partial \tilde{c}^e} \left((\tilde{c}^e)^h \right) \varphi_l(x) \sum_{i=1}^{N} \tilde{C}_i^{e,(m)} \nabla \varphi_i \right) \cdot \nabla \varphi_j\, dx +$$

$$+ \sum_{T \in \mathcal{T}^h} \int_T \left(\mathcal{K}^e_{11} \left((\tilde{c}^e)^h \right) \nabla \varphi_l \right) \cdot \nabla \varphi_j\, dx - \sum_{T \in \mathcal{T}^h} \int_T \frac{\partial f_1}{\partial \tilde{C}_l^{e,(m)}} \varphi_j(x)\, dx \tag{5.7.55}$$

$$\frac{\partial G_1^j}{\partial \tilde{\Phi}_l^{e,(m)}} = \sum_{T \in \mathcal{T}^h} \int_T (\mathcal{K}^e_{12} \nabla \varphi_l) \cdot \nabla \varphi_j\, dx - \sum_{T \in \mathcal{T}^h} \int_T \frac{\partial f_1}{\partial \tilde{\Phi}_l^{e,(m)}} \varphi_j(x)\, dx \tag{5.7.56}$$

$$\frac{\partial G_1^j}{\partial \Phi_p^{s,(m)}} = - \sum_{T \in \mathcal{T}^h} \int_T \frac{\partial f_1}{\partial \Phi_p^{s,(m)}} \varphi_j(x)\, dx \tag{5.7.57}$$

$$\frac{\partial G_2^j}{\partial \tilde{C}_l^{e,(m)}} = \sum_{T\in\mathcal{T}^h} \int_T \left(\frac{\partial \mathcal{K}_{21}^e}{\partial \tilde{c}^e} \left((\tilde{c}^e)^h \right) \varphi_l(x) \sum_{i=1}^N \tilde{C}_i^{e,(m)} \nabla\varphi_i \right) \cdot \nabla\varphi_j \, dx +$$

$$+ \sum_{T\in\mathcal{T}^h} \int_T \left(\mathcal{K}_{21}^e \left((\tilde{c}^e)^h \right) \nabla\varphi_l \right) \cdot \nabla\varphi_j \, dx - \sum_{T\in\mathcal{T}^h} \int_T \frac{\partial f_2}{\partial \tilde{C}_l^{e,(m)}} \varphi_j(x) \, dx \tag{5.7.58}$$

$$\frac{\partial G_2^j}{\partial \tilde{\Phi}_l^{e,(m)}} = \sum_{T\in\mathcal{T}^h} \int_T (\mathcal{K}_{22}^e \nabla\varphi_l) \cdot \nabla\varphi_j \, dx - \sum_{T\in\mathcal{T}^h} \int_T \frac{\partial f_2}{\partial \tilde{\Phi}_l^{e,(m)}} \varphi_j(x) \, dx \tag{5.7.59}$$

$$\frac{\partial G_2^j}{\partial \Phi_p^{s,(m)}} = - \sum_{T\in\mathcal{T}^h} \int_T \frac{\partial f_2}{\partial \Phi_p^{s,(m)}} \varphi_j(x) \, dx \tag{5.7.60}$$

$$\frac{\partial G_3^k}{\partial \tilde{C}_l^{e,(m)}} = - \sum_{r\in\mathcal{I}_{electrodes}} \int_{T_r} \frac{\partial f_2}{\partial \tilde{C}_l^{e,(m)}} \varphi_k(x) \, dx \tag{5.7.61}$$

$$\frac{\partial G_3^k}{\partial \tilde{\Phi}_l^{e,(m)}} = - \sum_{r\in\mathcal{I}_{electrodes}} \int_{T_r} \frac{\partial f_2}{\partial \tilde{\Phi}_l^{e,(m)}} \varphi_k(x) \, dx \tag{5.7.62}$$

$$\frac{\partial G_3^k}{\partial \Phi_p^{s,(m)}} = - \sum_{r\in\mathcal{I}_{electrodes}} \int_{T_r} \mathbf{\Lambda^s} \nabla\varphi_p \cdot \nabla\varphi_k \, dx - \sum_{r\in\mathcal{I}_{electrodes}} \int_{T_r} \frac{\partial f_2}{\partial \Phi_p^{s,(m)}} \varphi_k(x) \, dx \tag{5.7.63}$$

for $j, l = 1, \ldots, N$ and $k, p = 1, \ldots, n$. The derivatives of the coefficients of equation (5.7.1), given by (5.7.6) and (5.6.4), are

$$\frac{\partial \mathcal{K}_{11}^e}{\partial \tilde{c}^e} = \begin{cases} \dfrac{\partial}{\partial c^e} \left(k_{11}^e \mathbf{I} \right), \text{where} \quad \dfrac{\partial k_{11}^e}{\partial c^e} = -\dfrac{RT}{F^2} \dfrac{(t_+)^2 \kappa^e}{(c^e)^2}, \quad x \in \Omega_{separator}^e, \\ \dfrac{\partial \mathbf{K_{11}}}{\partial c_0^e} = \dfrac{\partial}{\partial c_0^e} \left(\mathbf{K_{11}} \right)_{i,j=1}^3 = \dfrac{\partial k_{11}^e}{\partial c^e} \left(c_0^e \right) \dfrac{1}{|Y|} \displaystyle\int_E \left(\delta_{ij} + \frac{\partial w_j}{\partial y_i}(y) \right) dy = \\ = -\dfrac{RT}{F^2} \dfrac{(t_+)^2 \kappa^e}{(c_0^e)^2} \dfrac{1}{|Y|} \displaystyle\int_E \left(\delta_{ij} + \frac{\partial w_j}{\partial y_i}(y) \right) dy, \quad x \in \Omega_{anode} \cup \Omega_{cathode} \end{cases}$$

$$\frac{\partial \mathcal{K}_{12}^e}{\partial \tilde{c}^e} = 0 \tag{5.7.64}$$

$$\frac{\partial \mathcal{K}^e_{21}}{\partial \tilde{c}^e} = \begin{cases} \dfrac{\partial}{\partial c^e}\left(k^e_{21}\mathbf{I}\right), \text{where} \quad \dfrac{\partial k^e_{21}}{\partial c^e} = -\dfrac{RT}{F}\dfrac{t_+\kappa^e}{\left(c^e\right)^2}, \quad x \in \Omega^e_{separator}, \\ \dfrac{\partial \mathbf{K_{21}}}{\partial c^e_0} = \dfrac{\partial}{\partial c^e_0}\left(\mathbf{K_{21}}\right)^3_{i,j=1} = \dfrac{\partial k^e_{21}}{\partial c^e}\left(c^e_0\right)\dfrac{1}{|Y|}\displaystyle\int_E \left(\delta_{ij} + \frac{\partial w_j}{\partial y_i}(y)\right) dy = \\ = -\dfrac{RT}{F}\dfrac{t_+\kappa^e}{\left(c^e_0\right)^2}\dfrac{1}{|Y|}\displaystyle\int_E \left(\delta_{ij} + \frac{\partial w_j}{\partial y_i}(y)\right) dy, \quad x \in \Omega_{anode} \cup \Omega_{cathode} \end{cases}$$

$$\frac{\partial \mathcal{K}^e_{22}}{\partial \tilde{c}^e} = 0 \tag{5.7.65}$$

where $\mathbf{I}$ is the identity matrix.
The interface exchange current densities are given by

$$\mathcal{N} = \frac{k}{F}\sqrt{c^e c^s\left(c^s_{max} - c^s\right)}\left[\exp^{\frac{F}{2RT}(\phi^s - \phi^e - U_0(c^s))} - \exp^{-\frac{F}{2RT}(\phi^s - \phi^e - U_0(c^s))}\right] \tag{5.7.66}$$

$$\mathcal{J} = F\mathcal{N} \tag{5.7.67}$$

and for their derivatives we obtain

$$\frac{\partial \mathcal{N}}{\partial c^e} = \frac{k}{2F}\frac{1}{\sqrt{c^e}}\sqrt{c^s\left(c^s_{max} - c^s\right)}\left[\exp^{\frac{F}{2RT}(\phi^s - \phi^e - U_0(c^s))} - \exp^{-\frac{F}{2RT}(\phi^s - \phi^e - U_0(c^s))}\right] =$$

$$= \frac{k}{2F}\frac{1}{\sqrt{c^e}}\sqrt{c^s\left(c^s_{max} - c^s\right)}\left[\exp^{\frac{F}{2RT}(\phi^s - \phi^e)}\exp^{-\frac{F}{2RT}U_0(c^s)} - \exp^{-\frac{F}{2RT}(\phi^s - \phi^e)}\exp^{\frac{F}{2RT}U_0(c^s)}\right] =$$

$$= \underbrace{\frac{k}{2F}\frac{1}{\sqrt{c^e}}\exp^{\frac{F}{2RT}(\phi^s - \phi^e)}}_{=\mathcal{F}_{11}(c^e,\phi^e,\phi^s)}\underbrace{\sqrt{c^s\left(c^s_{max} - c^s\right)}\exp^{-\frac{F}{2RT}U_0(c^s)}}_{=\mathcal{G}_{11}(c^s)} -$$

$$- \underbrace{\frac{k}{2F}\frac{1}{\sqrt{c^e}}\exp^{-\frac{F}{2RT}(\phi^s - \phi^e)}}_{=\mathcal{F}_{12}(c^e,\phi^e,\phi^s)}\underbrace{\sqrt{c^s\left(c^s_{max} - c^s\right)}\exp^{\frac{F}{2RT}U_0(c^s)}}_{=\mathcal{G}_{12}(c^s)} =$$

$$= \mathcal{F}_{11}\left(c^e, \phi^e, \phi^s\right)\mathcal{G}_{11}\left(c^s\right) - \mathcal{F}_{12}\left(c^e, \phi^e, \phi^s\right)\mathcal{G}_{12}\left(c^s\right) \tag{5.7.68}$$

$$\frac{\partial \mathcal{N}}{\partial \phi^e} = \frac{-k}{2RT}\sqrt{c^e}\sqrt{c^s\left(c^s_{max}-c^s\right)}\left[\exp^{\frac{F}{2RT}(\phi^s-\phi^e-U_0(c^s))}+\exp^{-\frac{F}{2RT}(\phi^s-\phi^e-U_0(c^s))}\right] =$$

$$= \underbrace{\frac{-k}{2RT}\sqrt{c^e}\exp^{\frac{F}{2RT}(\phi^s-\phi^e)}}_{=\mathcal{F}_{21}(c^e,\phi^e,\phi^s)}\underbrace{\sqrt{c^s\left(c^s_{max}-c^s\right)}\exp^{-\frac{F}{2RT}U_0(c^s)}}_{=\mathcal{G}_{21}(c^s)}+$$

$$+\underbrace{\frac{-k}{2RT}\sqrt{c^e}\exp^{-\frac{F}{2RT}(\phi^s-\phi^e)}}_{=\mathcal{F}_{22}(c^e,\phi^e,\phi^s)}\underbrace{\sqrt{c^s\left(c^s_{max}-c^s\right)}\exp^{\frac{F}{2RT}U_0(c^s)}}_{=\mathcal{G}_{22}(c^s)} =$$

$$= \mathcal{F}_{21}\left(c^e,\phi^e,\phi^s\right)\mathcal{G}_{21}\left(c^s\right)-\mathcal{F}_{22}\left(c^e,\phi^e,\phi^s\right)\mathcal{G}_{22}\left(c^s\right) \tag{5.7.69}$$

$$\frac{\partial \mathcal{N}}{\partial \phi^s} = -\frac{\partial \mathcal{N}}{\partial \phi^e} := \mathcal{F}_{31}\left(c^e,\phi^e,\phi^s\right)\mathcal{G}_{31}(c^s)-\mathcal{F}_{32}\left(c^e,\phi^e,\phi^s\right)\mathcal{G}_{32}(c^s) \tag{5.7.70}$$

where we introduce the functions $\mathcal{F}_{31}\left(c^e,\phi^e,\phi^s\right),\mathcal{G}_{31}(c^s),\mathcal{F}_{32}\left(c^e,\phi^e,\phi^s\right)$ and $\mathcal{G}_{32}(c^s)$ formally for the purpose of a consistent with (5.7.52) notation. It is clear that, up to a sign, these functions are equal to the respective ones in (5.7.69). The exact form of the open circuit potential $U_0(c^s)$ as a function of the concentration c^s is given in the next section. By analogy with their derivatives, we can write down the interface exchange current densities $\mathcal{N}$ and $\mathcal{J}$ in the following way

$$\mathcal{N} = \frac{k}{F}\sqrt{c^e c^s\left(c^s_{max}-c^s\right)}\left[\exp^{\frac{F}{2RT}(\phi^s-\phi^e-U_0(c^s))}-\exp^{-\frac{F}{2RT}(\phi^s-\phi^e-U_0(c^s))}\right] =$$

$$= \mathcal{F}_{01}\left(c^e,\phi^e,\phi^s\right)\mathcal{G}_{01}\left(c^s\right)-\mathcal{F}_{02}\left(c^e,\phi^e,\phi^s\right)\mathcal{G}_{02}\left(c^s\right) \tag{5.7.71a}$$

$$\mathcal{J} = F\mathcal{N} \tag{5.7.71b}$$

where

$$\mathcal{F}_{01}\left(c^e,\phi^e,\phi^s\right) = \frac{k}{F}\sqrt{c^e}\exp^{\frac{F}{2RT}(\phi^s-\phi^e)} \tag{5.7.72a}$$

$$\mathcal{G}_{01}\left(c^e,\phi^e,\phi^s\right) = \sqrt{c^s\left(c^s_{max}-c^s\right)}\exp^{-\frac{F}{2RT}U_0(c^s)} \tag{5.7.72b}$$

$$\mathcal{F}_{02}\left(c^e,\phi^e,\phi^s\right) = \frac{k}{F}\sqrt{c^e}\exp^{-\frac{F}{2RT}(\phi^s-\phi^e)} \tag{5.7.72c}$$

$$\mathcal{G}_{02}\left(c^e,\phi^e,\phi^s\right) = \sqrt{c^s\left(c^s_{max}-c^s\right)}\exp^{\frac{F}{2RT}U_0(c^s)} \tag{5.7.72d}$$

Since from (5.7.53) we have that

$$\int\limits_{\Omega} \frac{\partial f_1}{\partial \mathcal{P}_i}\varphi_j(x)\,dx =$$

$$= \underbrace{\int\limits_{\Omega_{anode}} \left(\frac{1}{\varepsilon\,|Y|} \int\limits_{\Gamma} \frac{\partial \mathcal{N}}{\partial p_i} \left((\tilde{c}^e)^{h,(m)}, \left(\tilde{\phi}^e\right)^{h,(m)}, c^s, (\phi^s)^{h,(m)} \right) ds \right) \varphi_l(x)\varphi_j(x)\,dx}_{=I^1_{anode}} +$$

$$+ \underbrace{\int\limits_{\Omega_{cathode}} \left(\frac{1}{\varepsilon\,|Y|} \int\limits_{\Gamma} \frac{\partial \mathcal{N}}{\partial p_i} \left((\tilde{c}^e)^{h,(m)}, \left(\tilde{\phi}^e\right)^{h,(m)}, c^s, (\phi^s)^{h,(m)} \right) ds \right) \varphi_l(x)\varphi_j(x)\,dx}_{=I^1_{cathode}} =$$

$$= I^1_{anode} + I^1_{cathode} \tag{5.7.73}$$

and by analogy

$$\int\limits_{\Omega} \frac{\partial f_2}{\partial \mathcal{P}_i}\varphi_j(x)\,dx = I^2_{anode} + I^2_{cathode} \tag{5.7.74}$$

Due to (5.7.68), (5.7.69) and (5.7.70), for the latter integrals over the domains of the two electrodes - $I^1_{anode/cathode}$ (and $I^2_{anode/cathode}$) we obtain

$$I^1_{electrode} = \int\limits_{\Omega_{electrode}} \left(\frac{1}{\varepsilon\,|Y|} \int\limits_{\Gamma} \frac{\partial \mathcal{N}}{\partial p_i} \left((\tilde{c}^e)^{h,(m)}, \left(\tilde{\phi}^e\right)^{h,(m)}, c^s, (\phi^s)^{h,(m)} \right) ds \right) \varphi_l(x)\varphi_j(x)\,dx =$$

$$= \int\limits_{\Omega_{electrode}} \left(\frac{1}{\varepsilon\,|Y|} \int\limits_{\Gamma} \left(\mathcal{F}_{i1}\left(c^e_0, \phi^e_0, \phi^s_0\right) \mathcal{G}_{i1}(c^s) - \mathcal{F}_{i2}\left(c^e_0, \phi^e_0, \phi^s_0\right) \mathcal{G}_{i2}(c^s) \right) ds \right) \varphi_l(x)\varphi_j(x)\,dx =$$

$$= \int\limits_{\Omega_{electrode}} \left(\frac{1}{\varepsilon\,|Y|} \int\limits_{\Gamma} \mathcal{F}_{i1}\left(c^e_0, \phi^e_0, \phi^s_0\right) \mathcal{G}_{i1}(c^s)\,ds - \frac{1}{\varepsilon\,|Y|} \int\limits_{\Gamma} \mathcal{F}_{i2}\left(c^e_0, \phi^e_0, \phi^s_0\right) \mathcal{G}_{i2}(c^s)\,ds \right) \varphi_l(x)\varphi_j(x)\,dx =$$

$$= \int\limits_{\Omega_{electrode}} \left(\mathcal{F}_{i1}\left(c^e_0, \phi^e_0, \phi^s_0\right) \frac{1}{\varepsilon\,|Y|} \int\limits_{\Gamma} \mathcal{G}_{i1}(c^s)\,ds - \mathcal{F}_{i2}\left(c^e_0, \phi^e_0, \phi^s_0\right) \frac{1}{\varepsilon\,|Y|} \int\limits_{\Gamma} \mathcal{G}_{i2}(c^s)\,ds \right) \varphi_l(x)\varphi_j(x)\,dx =$$

$$= \int\limits_{\Omega_{electrode}} \left(\frac{1}{\varepsilon\,|Y|} \int\limits_{\Gamma} \mathcal{G}_{i1}(c^s)\,ds \right) \mathcal{F}_{i1}\left(c^e_0, \phi^e_0, \phi^s_0\right) \varphi_l(x)\varphi_j(x)\,dx -$$

$$- \int\limits_{\Omega_{electrode}} \left(\frac{1}{\varepsilon\,|Y|} \int\limits_{\Gamma} \mathcal{G}_{i2}(c^s)\,ds \right) \mathcal{F}_{i2}\left(c^e_0, \phi^e_0, \phi^s_0\right) \varphi_l(x)\varphi_j(x)\,dx \tag{5.7.75}$$

where $i = 1, 2, 3$, and we recall that $\Omega_{electrode} = \Omega_{anode}$ or $\Omega_{electrode} = \Omega_{cathode}$. In the latter calculations we make use of the fact that the functions $\mathcal{F}_{i1}$ and $\mathcal{F}_{i2}$ depend only on the the "slow" macroscale variable x because the macroscopic qunatities are functions only of x, i.e., $c_0^e = c_0^e(x,t)$, $\phi_0^e = \phi_0^e(x,t)$, $\phi_0^s = \phi_0^s(x,t)$, and that $c^s = c^s(y,t)$ is a function of the "fast" variable y. We compute the integral $\dfrac{1}{\varepsilon\,|Y|}\displaystyle\int_\Gamma \mathcal{G}_{ij}(c^s)\,ds$, for $j = 1, 2$, on the microscale when we solve the 3D microscale problem (5.3.1) for finding the concentration of ions c^s in the solid phase. Due to (5.7.68), (5.7.69), (5.7.70), (5.7.71), (5.7.73) and (5.7.74), we make use of the same arguments as above when calculating the integrals $\displaystyle\int_\Gamma \mathcal{N}\left((\tilde{c}^e)^{h,(m)}, \left(\tilde{\phi}^e\right)^{h,(m)}, c^s, (\phi^s)^{h,(m)}\right) ds$, $\displaystyle\int_\Gamma \mathcal{J}\left((\tilde{c}^e)^{h,(m)}, \left(\tilde{\phi}^e\right)^{h,(m)}, c^s, (\phi^s)^{h,(m)}\right) ds$ and $\displaystyle\int_\Omega \frac{\partial f_{1,2}}{\partial \mathcal{P}_i}\varphi_j(x)\,dx$ participating in the right-hand side $\mathbf{G}\left(\mathbf{U}^{(r-1)}\right)$ and the Jacobian, respectively.

Weak form of the microscale problem for the concentration c^s

For each $x \in \Omega_{electrode}$ we have to solve the following microscale problem for the concentration of ions in the electrode particles

$$\frac{\partial c^s}{\partial t} - \nabla_y \cdot \left(\frac{D^s}{\varepsilon^2}\nabla_y c^s\right) = 0, \quad y \in S \tag{5.7.76a}$$

$$-\frac{D^s}{\varepsilon^2}\nabla_y c^s \cdot \mathbf{n_s} = \frac{1}{\varepsilon}\mathcal{N}(c_0^e, c^s, \phi_0^e, \phi_0^s), \quad y \in \Gamma, \tag{5.7.76b}$$

where we have periodic boundary conditions on $\partial S^{periodic} = \partial S \backslash \Gamma$, i.e. on the boundary of the solid phase domain where the periodicity cells are connected to each other. The two models - macro (5.6.1) and micro (5.6.3) are coupled via the interface exchange current densities $\mathcal{N}_0 = \mathcal{N}(c_0^e, c^s, \phi_0^e, \phi_0^s)$ and $\mathcal{J}_0 = \mathcal{J}(c_0^e, c^s, \phi_0^e, \phi_0^s)$.
We denote

$$H^1_{\#}(S) = \left\{v(y) \in H^1(S) |\, v \quad \text{are periodic on} \quad \partial S^{periodic}\right\} \tag{5.7.77}$$

We proceed with writing the problem in a weak form by multiplying equation (5.7.76a) with a test function and integrating over S

$$\int_S \frac{\partial c^s}{\partial t} v(y)\,dy - \int_S \nabla_y \cdot \left(\frac{D^s}{\varepsilon^2}\nabla_y c^s\right) v(y)\,dy = 0 \tag{5.7.78}$$

which is equivalent to

$$\int_S \frac{\partial c^s}{\partial t} v(y)\, dy - \int_S \nabla_y \cdot \left(v \frac{D^s}{\varepsilon^2} \nabla_y c^s \right) dy + \int_S \frac{D^s}{\varepsilon^2} \nabla_y c^s \cdot \nabla_y v \, dy = 0 \Longleftrightarrow$$

$$\int_S \frac{\partial c^s}{\partial t} v \, dy - \int_{\partial S} v \frac{D^s}{\varepsilon^2} \nabla_y c^s \cdot \mathbf{n_s} \, dy + \int_S \frac{D^s}{\varepsilon^2} \nabla_y c^s \cdot \nabla_y v \, dy = 0 \Longleftrightarrow$$

$$\int_S \frac{\partial c^s}{\partial t} v \, dy - \int_\Gamma v \underbrace{\frac{D^s}{\varepsilon^2} \nabla_y c^s \cdot \mathbf{n_s}}_{= -\frac{1}{\varepsilon}\mathcal{N}(c_0^e, c^s, \phi_0^e, \phi_0^s)} ds_y - \int_{\partial S^{periodic}} v \frac{D^s}{\varepsilon^2} \nabla_y c^s \cdot \mathbf{n_s} \, ds_y + \int_S \frac{D^s}{\varepsilon^2} \nabla_y c^s \cdot \nabla_y v \, dy = 0 \tag{5.7.79}$$

The latter is equivalent to

$$\int_S \frac{\partial c^s}{\partial t} v \, dy + \int_\Gamma \frac{1}{\varepsilon} \mathcal{N}(c_0^e, c^s, \phi_0^e, \phi_0^s) v \, ds_y + \int_S \frac{D^s}{\varepsilon^2} \nabla_y c^s \cdot \nabla_y v \, dy = 0 \tag{5.7.80}$$

because the term $\int_{\partial S^{periodic}} v(y) \frac{D^s}{\varepsilon^2} \nabla_y c^s \cdot \mathbf{n_s} \, ds_y$ vanishes due to periodicity and symmetry, and we later impose explicitly the periodic boundary conditions in the resulting system of linear algebraic equations. Then, the weak formulation of the problem is: find $c^s \in H^1_\#(S)$, such that the following integral equality is true for all $v(y) \in H^1_\#(S)$

$$\int_S \frac{\partial c^s}{\partial t} v \, dy + \int_\Gamma \frac{1}{\varepsilon} \mathcal{N}(c_0^e, c^s, \phi_0^e, \phi_0^s) v \, ds_y + \int_S \frac{D^s}{\varepsilon^2} \nabla_y c^s \cdot \nabla_y v \, dy = 0 \tag{5.7.81}$$

Now we restrict the weak form (5.7.81) to a finite dimensional approximation space $V_S^h \subset H^1_\#(S)$: find $(c^s)^h \in V_S^h$, such that the following integral equality is true for all $v^h \in V_S^h$

$$\int_S \frac{\partial \left(c^s\right)^h}{\partial t} v^h \, dy + \int_\Gamma \frac{1}{\varepsilon} \mathcal{N}(c_0^e, \left(c^s\right)^h, \phi_0^e, \phi_0^s) v^h \, ds_y + \int_S \frac{D^s}{\varepsilon^2} \nabla_y \left(c^s\right)^h \cdot \nabla_y v^h \, dy = 0 \tag{5.7.82}$$

Let $\{\varphi_i^s(y)\}_{i=1}^{N_s}$ be the standard finite element basis of the space V_S^h with $dim\left(V_S^h\right) = N_s$. Then, we expand the approximate discretized solution $\left(c^s(y,t)\right)^h$ with respect to this basis

$$\left(c^s(y,t)\right)^h = \sum_{i=1}^{N_s} C_i^s(t) \varphi_i^s(y) \tag{5.7.83}$$

Now we take $v^h(y) = \varphi_j^s(y)$ for all $j = 1, 2, \ldots, N_s$ and we obtain the following system of equations

$$\int_S \sum_{i=1}^{N_s} \frac{\partial C_i^s}{\partial t} \varphi_i^s(y) \varphi_j^s(y)\, dy + \frac{1}{\varepsilon} \int_\Gamma \mathcal{N}(c_0^e, (c^s)^h, \phi_0^e, \phi_0^s) \varphi_j^s(y)\, ds_y +$$

$$+ \int_S \frac{D^s}{\varepsilon^2} \sum_{i=1}^{N_s} C_i^s(t) \nabla \varphi_i^s \cdot \nabla \varphi_j^s\, dy = 0 \tag{5.7.84}$$

As before, we apply the Backward Euler method for the time discretization and we use the same time step and discrete time moments as in the homogenized macro problem

$$\int_S \sum_{i=1}^{N_s} \frac{C_i^{s,(m)} - C_i^{s,(m-1)}}{\tau} \varphi_i^s(y) \varphi_j^s(y)\, dy + \frac{1}{\varepsilon} \int_\Gamma \mathcal{N}(c_0^e, (c^s)^{h,(m)}, \phi_0^e, \phi_0^s) \varphi_j^s(y)\, ds_y +$$

$$+ \frac{D^s}{\varepsilon^2} \int_S \sum_{i=1}^{N_s} C_i^{s,(m)} \nabla \varphi_i^s \cdot \nabla \varphi_j^s\, dy = 0 \tag{5.7.85}$$

where $C_i^s(t_m) = C_i^{s,(m)}$ and $(c^s)^{h,(m)} = (c^s)^h(y, t_m)$. We denote

$$G_j^s \left(C_1^{s,(m)}, C_2^{s,(m)}, \ldots, C_{N_s}^{s,(m)} \right) =$$

$$= \int_S \sum_{i=1}^{N_s} \frac{C_i^{s,(m)} - C_i^{s,(m-1)}}{\tau} \varphi_i^s(y) \varphi_j^s(y)\, dy + \frac{1}{\varepsilon} \int_\Gamma \mathcal{N}(c_0^e, (c^s)^{h,(m)}, \phi_0^e, \phi_0^s) \varphi_j^s(y)\, ds_y +$$

$$+ \frac{D^s}{\varepsilon^2} \int_S \sum_{i=1}^{N_s} C_i^{s,(m)} \nabla \varphi_i^s \cdot \nabla \varphi_j^s\, dy \tag{5.7.86}$$

for all $j = 1, 2, \ldots, N_s$ and we want to solve the following system of nonlinear algebraic equations

$$\left| \begin{array}{l} G_1^s \left(C_1^{s,(m)}, C_2^{s,(m)}, \ldots, C_{N_s}^{s,(m)} \right) = 0 \\ G_2^s \left(C_1^{s,(m)}, C_2^{s,(m)}, \ldots, C_{N_s}^{s,(m)} \right) = 0 \\ \ldots \\ G_{N_s}^s \left(C_1^{s,(m)}, C_2^{s,(m)}, \ldots, C_{N_s}^{s,(m)} \right) = 0 \end{array} \right. \tag{5.7.87}$$

Again we apply the Newton-Raphson method for linearization of the problem at each time step of the Backward Euler method. Hence, we end up solving the following system of

equations at each Netwon-Raphson iteration

$$\mathbf{J^s}\left(\mathbf{C}^{(k-1)}\right)\left(\mathbf{C}^{(k)}-\mathbf{C}^{(k-1)}\right)=-\mathbf{G^s}\left(\mathbf{C}^{(k-1)}\right) \tag{5.7.88}$$

where the solution at the current Newton-Raphson iteration (and current time step) is denoted by

$$\mathbf{C}^{(k)}=\left(\left(C_1^{s,(m)}\right)^{(k)},\left(C_2^{s,(m)}\right)^{(k)},\ldots,\left(C_{N_s}^{s,(m)}\right)^{(k)}\right)^T \tag{5.7.89}$$

The Jacobian matrix is denoted by $\mathbf{J^s}$ and the right-hand side is given by

$$\mathbf{G^s}\left(\mathbf{C}^{(k-1)}\right)=\left(G_1^s\left(\mathbf{C}^{(k-1)}\right),G_2^s\left(\mathbf{C}^{(k-1)}\right),\ldots,G_{N_s}^s\left(\mathbf{C}^{(k-1)}\right)\right)^T \tag{5.7.90}$$

The elements of the Jacobian have the following form

$$\mathbf{J^s}_{jl}=\frac{\partial G_j^s}{\partial C_l^{s,(m)}}=\frac{1}{\tau}\int\limits_S\varphi_l^s(y)\varphi_j^s(y)\,dy+\frac{1}{\varepsilon}\int\limits_\Gamma\frac{\partial\mathcal{N}}{\partial c^s}(c_0^e,(c^s)^{h,(m)},\phi_0^e,\phi_0^s)\varphi_l^s(y)\varphi_j^s(y)\,ds_y+$$

$$+\frac{D^s}{\varepsilon^2}\int\limits_S\nabla\varphi_l^s\cdot\nabla\varphi_j^s\,dy \tag{5.7.91}$$

for $l,j=1,2,\ldots,N_s$.
Finally we couple the micro problem for c^s and the homogenized problem by the interface integrals over Γ, which are part of the elements of the Jacobian matrix and the right-hand side in both problems.

5.8 Implementation

The straightforward approach to couple the macroscale homogenized equations and the microscale equation (5.7.76) for c^s is to solve one 3D microscale problem at each time step and at each Newton-Raphson iteration for all integration points $x\in\Omega_{electrode}$. We use the following semi-implicit time-stepping scheme:

- First we solve the homogenized equations (5.6.1) with the help of the Backward Euler method and using the values of c^s from the previous time step.
- Then we use the obtained values for c_0^e, ϕ_0^e and ϕ_0^s to solve the microscale problem for c^s.

Here we discuss different strategies on how to avoid solving the microscale problem for each $x\in\Omega_{electrode}$ which is computationally expensive. For example, by computing the effective transport coefficients ((5.9.6) and (5.9.8)), which are tensors, for certain types of solid phase geometries, we see that the homogenized medium is almost isotropic for the considered test cases. Furthermore, due to the zero Neumann boundary conditions for the fluxes on all of the battery cell walls, except for ω_1 and ω_2, the transport of Li+

and charges is essentially one-dimensional, in direction from one electrode to the other. Therefore we can solve the homogenized equations in 1D but we leave the microscale problem for c^s in 3D and use a semi-implicit time scheme. Another option is to solve microscale solid problems only in selected regions of the electrodes. This can be done by choosing slices of the electrodes based on the specific geometry of the periodicity cell and subsequently the dominant terms in the effective tensors.
We impose the periodic boundary conditions in the auxiliary cell problems (5.4.77) and (5.4.90) in the following manner. In the finite element formulation of the problem we use the same numeration for the corresponding symmetric (periodic) mesh nodes on the opposite faces of the reference periodicity cell. This allows us to account naturally for the equal values of the periodic solution directly in the resulting system of linear algebraic equations.
In the numerical experiments presented in the thesis we consider only the case when the diagonal elements of the effective tensors are dominant and approximately equal to one another. We assume to have one solid phase periodicity cell per node in the finite element discretization of the 1D homogenized equations (5.6.1) as shown in Figure 5.8. Consequently we solve as many microscale problems for the concentration c^s of lithium ions in the electrode particles as there are nodes in the FEM discretization of equations (5.6.1). We use our own implemented C++ code, based on the Finite Element Method framework developed for the "FEMLion" library in Fraunhofer ITWM by Maxim Taralov, a PhD student at the Technical University of Kaiserslautern and Fraunhofer ITWM. We use the same software to run the numerical simulations of the microscale Li-ion battery model [48]. The 3D geometry of the solid phase solution domain is generated with the software tool Netgen [66]([65]) and we use linear tetrahedral finite elements. The linear solver is preconditioned BiCGSTAB (Stabilized Biconjugate Gradient), which is an iterative solver. In terms of computational time, we achieve 7 times acceleration with the homogenized model compared to the full microscale simulation.

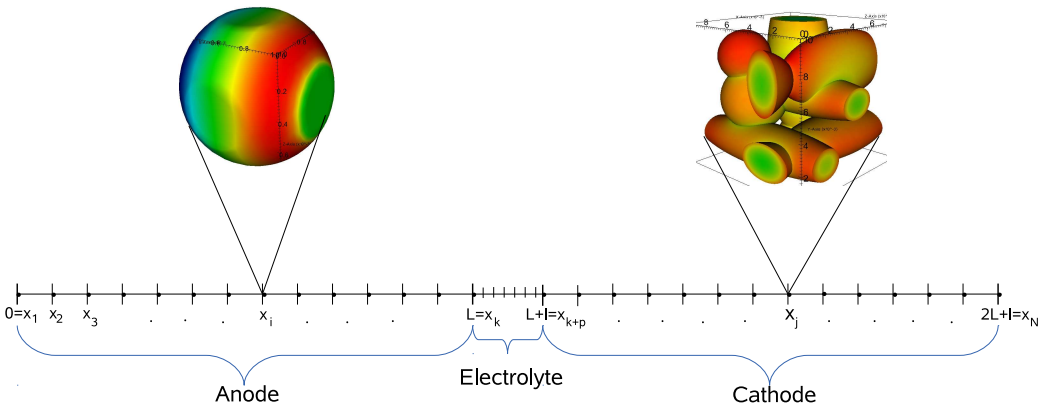

Figure 5.8: 1D solution domain and FEM discretization for the homogenized equations

A better approximation of the microscale concentration c^s can be achieved by a better interpolation of the macroscopic quantities c_0^e, ϕ_0^e and ϕ_0^s. For example, instead of taking only one value of c_0^e, ϕ_0^e and ϕ_0^s - that in the "center" of the solid phase periodicity cell,

i.e., in one node of the 1D discretization of the homogenized problem, we can take the linear interpolation of the values of the macroscale quantities between two adjacent nodes of the 1D mesh.

5.9 Numerical results

We show numerical results for two types of periodicity cell geometries. In the first test case we consider a simple geometry of the solid domain in the periodicity cell, consisting only of one cut-off spherical particle as shown in Figure 5.2 and Figure 5.10. In the second test case we have a periodicity cell with complex solid geometry consisitng of randomly arranged intersecting ellipsoid and spherical particles with different size, as shown in Figure 5.20, 5.21, 5.22, 5.23 and Figure 5.24. The results of the numerical simulations are given in Section 5.9.2 and Section 5.9.3, respectively. In both test cases we observe a very good agreement between the homogenized solution and the microscale one.

5.9.1 Setting of the numerical experiments

In all of the numerical experiments we have a battery cell which consists of two electrodes - anode and cathode, each of them being a parallelepiped, or in the 1D case – a line. Between the two electrodes there is a layer of pure electrolyte (see Figure 5.9). We simulate charging of the battery. In Table 5.9.1 we give the values of all the parameters which we use in the simulations. We show numerical results for the cell voltage and cell voltage difference versus transferred charge, as well as for the concentration of Li+ in the electrolyte phase, the electrochemical potential ϕ^e, the electrical potential ϕ^s, and the concentration of ions in the solid phase. We compare the one-dimensional homogenized concentration c_0^e with the three-dimensional microscale one with the help of the visualization program VisIt [14]([50]), version 2.7.1.
The cell voltage is defined as the difference between the potential in the cathode and the potential in the anode measured on the external walls of the electrodes (in our case these are the walls ω_1 and ω_2), i.e.

$$cell \quad voltage = \phi^s_{cathode}(x)|_{\omega_2} - \phi^s_{anode}(x)|_{\omega_1} \tag{5.9.1}$$

We provide numerical results for the battery cell voltage because in real industrial applications the cell voltage is an important quantity of interest which can be measured in a non-destructive way. Therefore it is preferred by engineers as an indicator for the battery cell performance. The cell voltage difference is the difference between the microscale cell voltage and the homogenized one. The transferred charge is given by

$$transferred \quad charge = i_{appl} \cdot S_{cathode} \cdot N \tag{5.9.2}$$

where $i_{appl} = E_2^s$ (in A/cm^2) is the applied current density on the cathode,
$S_{cathode} = |\omega_2 \cap \Omega_c^\varepsilon|$ (in cm^2) is the surface area of the outer cathode boundary and N is the number of seconds for which we run the simulation.

Table 5.9.1: Values of the parameters used for the simulations

	Electrolyte	Cathode	Anode
$D \quad cm^2/s$	7.5×10^{-7}	1.0×10^{-9}	3.9×10^{-10}
t_+	0.363	0	0
$\kappa \quad S/cm$	0.002	0.038	1.0
$c_{max} \quad mol/cm^3$	-	0.023671	0.024681
$c_{initial} \quad mol/cm^3$	0.001	0.9^*c_{max}	0.1^*c_{max}
$k \quad Acm^{2.5}/mol^{1.5}$	-	0.2	0.002

The Faraday constant is $F = 96486 \quad \frac{A \cdot s}{mol}$ and the universal gas constant is $R = 8.3144621 \quad \frac{J}{mol \cdot K}$. The temperature is $T = 300 \quad K$. The open circuit potential U_0 is given by

$$U_0(c^s) = -0.132 + 1.41e^{-3.52soc}, \quad x \in \Omega_a \tag{5.9.3a}$$

$$U_0(c^s) = 4.06279 - 0.045e^{-71.69soc^8} + 0.0677504\tanh(-21.8502soc + 12.8268) - 0.105734\left(\frac{1}{(1.00167 - soc)^{0.379571}} - 1.576\right) + 0.01e^{-200(soc-0.19)}, \quad x \in \Omega_c, \tag{5.9.3b}$$

where

$$soc = \frac{c^s}{c^s_{max}}. \tag{5.9.4}$$

The exact form of the open circuit potential (5.9.3) is taken from [56] and is the one used by Fuller et. al. in [31]. Furthermore, the parameters from Table 5.9.1 are of the same order as those given in [31], i.e., they are in agreement with the provided data for the open circuit potential.
For the potential ϕ^s, given in V, on the anode outer boundary we impose the following value

$$\phi^s_0 = E^s_1 = U_0(c^s_{initial}) = 0.8596 \quad V, \quad x \in \omega_1. \tag{5.9.5}$$

In Table 5.9.2 we give the specifications of the setup of our numerical simulations in the two different test cases.

Table 5.9.2: Specifications of the numerical simulations

	Cut-off spherical particle	Complex geometry
Dimensions of the electrodes	1) $100\mu m \times 10\mu m \times 10\mu m$ 2) $100\mu m \times 5\mu m \times 5\mu m$ 3) $100\mu m \times 2.5\mu m \times 2.5\mu m$	$100\mu m \times 20\mu m \times 20\mu m$
Thickness of the separator	1) $10\mu m$ 2) $5\mu m$ 3) $2.5\mu m$	$20\mu m$
Dimensions of the battery cell	1) $210\mu m \times 10\mu m \times 10\mu m$ 2) $205\mu m \times 5\mu m \times 5\mu m$ 3) $202.5\mu m \times 2.5\mu m \times 2.5\mu m$	$220\mu m \times 20\mu m \times 20\mu m$
Dimension of the periodicity cell	1) $10\mu m \times 10\mu m \times 10\mu m$ 2) $5\mu m \times 5\mu m \times 5\mu m$ 3) $2.5\mu m \times 2.5\mu m \times 2.5\mu m$	$20\mu m \times 20\mu m \times 20\mu m$
Applied current density	$E_2^s = 0.01\ A/cm^2$	1) $E_2^s = 0.03224985\ A/cm^2$ 2) $E_2^s = 0.3224985\ A/cm^2$
C rate	0.384808 C	1) 1C 2) 10 C
Time step	2s	1) 2s 2) 1s
Porosity	33.09%	55.52%

5.9.2 Numerical experiments for cut-off spherical particles

In each of the experiments we run simulations varying the size of the active particles and we compare the homogenized and microscale cell voltage, potential and concentration of Li+ in the electrolyte and in the solid. We begin with particles having a characteristic size of 10 μm and we decrease this size up to 2.5 μm in the last experiment. In Figure 5.10 we show the electrode geometry in the case of 5 periodicity cells per electrode.

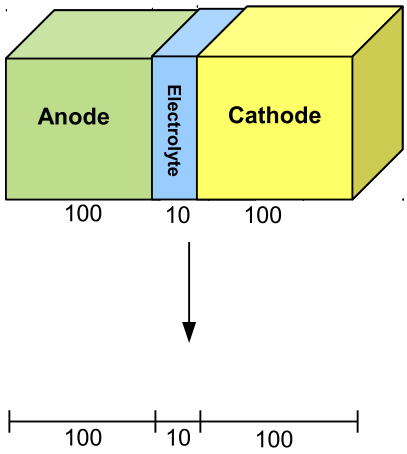

Figure 5.9: Exemplary battery cell dimensions

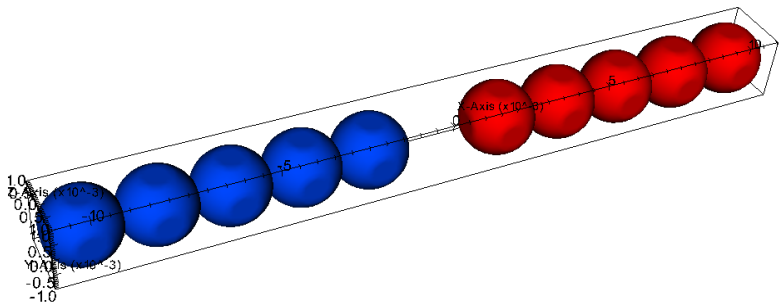

Figure 5.10: Electrodes consisting of spherical particles arranged in strings

In Figures 5.12, 5.15 and 5.17 we show the concentration of Li+ in the electrolyte throughout the whole battery cell. Furthermore, on the x-axis is given the battery cell length in cm and on the y-axis - the values of the concentration in mol/cm^3.
By formula (5.6.4) we compute the following *effective macroscopic coefficients* for $i, j = 1, 2$

$$\mathbf{K_{ij}} = k_{ij}^e \begin{pmatrix} 0.196084 & 0.0000967534 & -0.0000258525 \\ 0.0000967533 & 0.196317 & -0.0000447355 \\ -0.0000258525 & -0.0000447356 & 0.196349 \end{pmatrix} \tag{5.9.6a}$$

$$\mathbf{\Lambda^s} = \kappa^s \begin{pmatrix} 0.890891 & 0.0000208619 & 0.0000762248 \\ 0.000020862 & 0.891478 & -0.0000363849 \\ 0.0000762249 & -0.0000363847 & 0.890049 \end{pmatrix} \tag{5.9.6b}$$

where k_{ij}^e and κ^s are the microscale transport coefficients from the microscale model equations (2.3.1) and (2.4.1). The tensors (5.9.6a) and (5.9.6b) are diagonally dominated with approximately equal diagonal elements and almost zero off-diagonal elements. This means that we have an almost isotropic medium. For this reason we make the following approximation: we neglect the off-diagonal elements and we reduce the three-dimensional homogenized problem (5.6.1) to one-dimensional one, as shown in Figure 5.9, where as effective transport coefficients we take $K_{ij} = 0.196084 k_{ij}^e$ and $\Lambda^s = 0.890891 \kappa^s$ (i.e. the original microscale coefficients multiplied by the first diagonal element of the tensors).

Experiment 1: $\varepsilon = 0.1$

In this experiment we run simulations for 10 active particles in each electrode, arranged in a string . Therefore the characteristic size of the particles is $l = 10$ μm whereas the size of the whole electrode is $L = 100$ μm and consequently $\varepsilon = \dfrac{l}{L} = 0.1$. In Figure 5.11 we see that the cell voltages for the homogenized and the microscale model basically coincide. We show the concentration of Li+ in the electrolyte for different time steps in Figure 5.12 where one can observe that there is a very good agreement between the homogenized and the microscale model. The electrochemical potential in the electrolyte at different time steps is illustrated in Figure 5.13, where the x-axis is the battery cell length in cm.

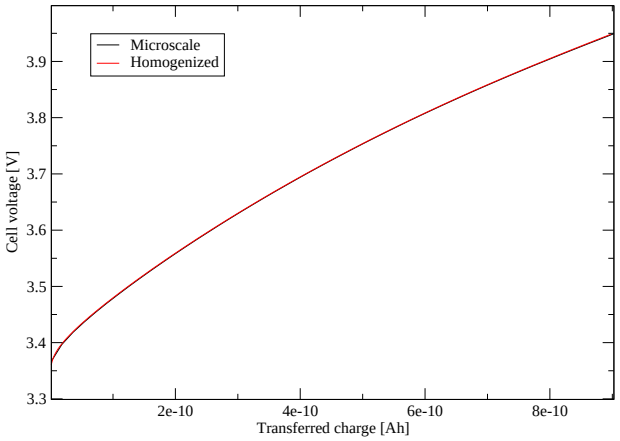

Figure 5.11: Cell voltage in V

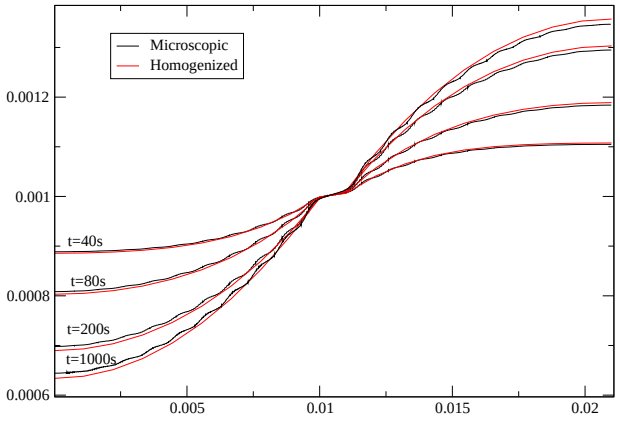

Figure 5.12: Concentration of Li+ in the electrolyte at different time steps

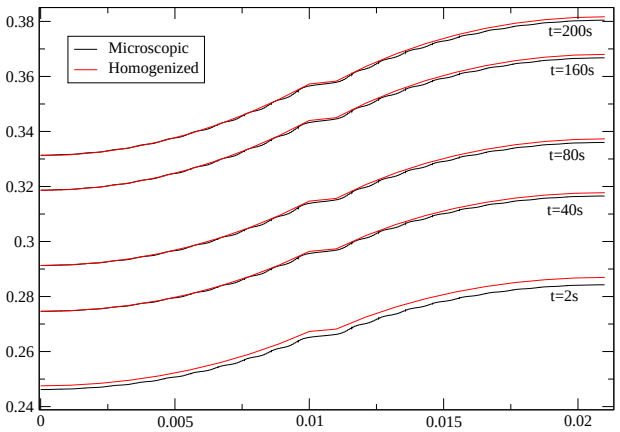

Figure 5.13: Potential in the electrolyte in volts for different time steps

Experiment 2: $\varepsilon = 0.05$

Here we run simulations for 20 active particles in each electrode, arranged in a string. The characteristic size of the particles is 5μm and the small parameter is $\varepsilon = 0.05$. The results from the microscale simulation and from the homogenized problem are given in Figure 5.14, Figure 5.15 and 5.16. In Figure 5.16 we show the concentration c^s of Li+ in a representative anode particle after 80 time steps (160s), and as we can see from the picture, the values of the microscale and the homogenized solution are pretty close.

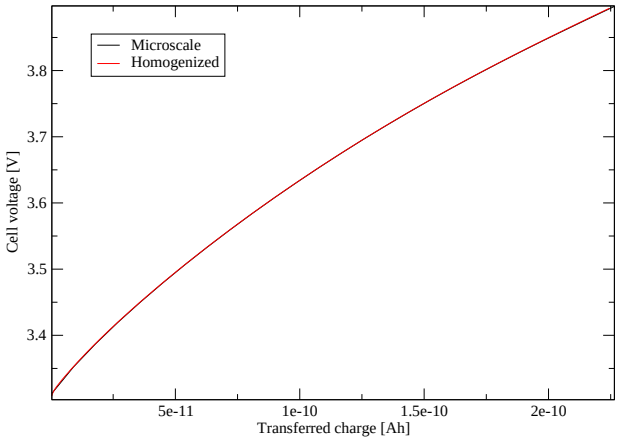

Figure 5.14: Cell voltage in V

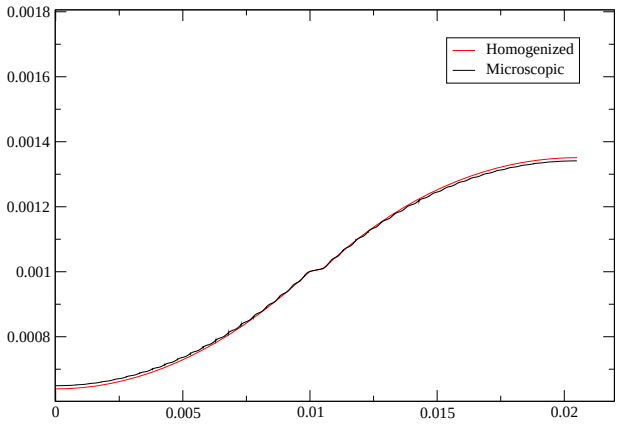

Figure 5.15: Concentration of Li+ in the electrolyte after 800s

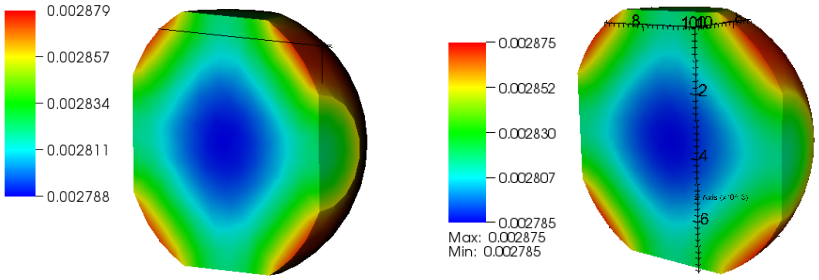

a. Microscale reference solution b. Homogenized solution

Figure 5.16: Concentration in a single representative anode particle after 160s (80 time steps)

Experiment 3: $\varepsilon = 0.025$

In this experiment we run simulations for 40 active particles in each electrode, arranged in a string and the typical size of the particles is 2.5μm. Consequently we have that $\varepsilon = 0.025$. The results from the microscale simulation and the homogenized problem are given in Figure 5.17, 5.18 and 5.19..

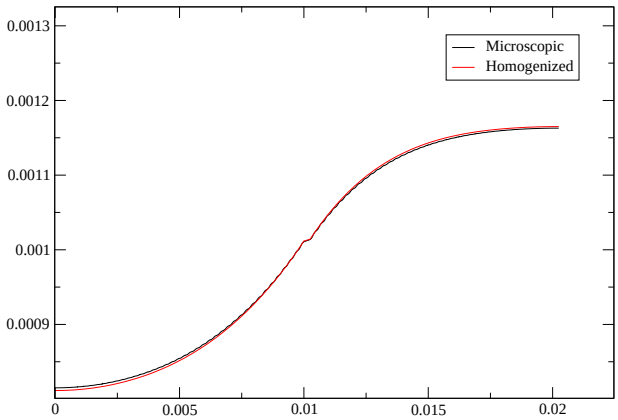

Figure 5.17: Concentration of Li+ in the electrolyte after 80s

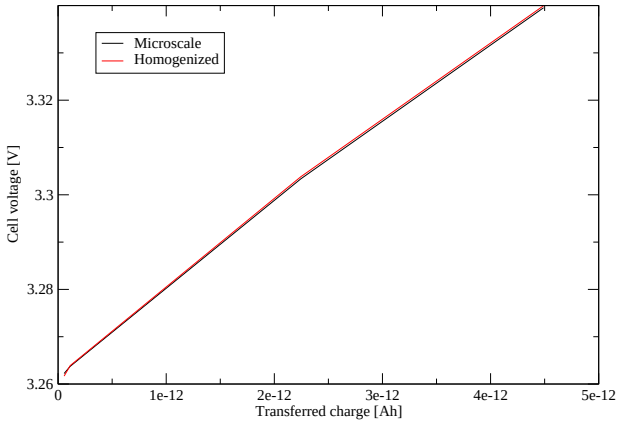

Figure 5.18: Cell volatge in V

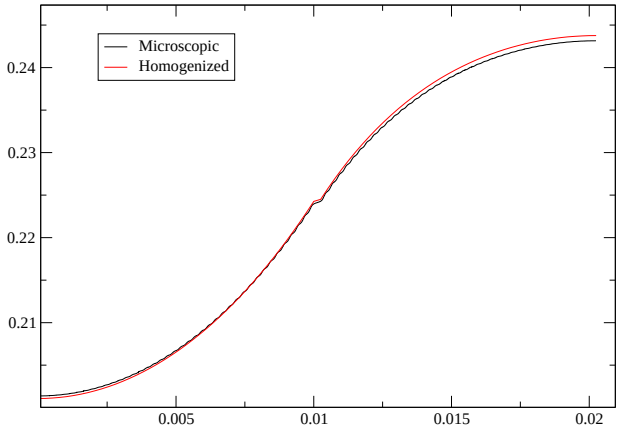

Figure 5.19: Potential in the electrolyte in V after 80s (40 time steps)

Summary of the numerical results

The convergence result (3.5.9) in L^2 for linear elliptic problems was

$$\|u_\varepsilon - u_0\|_{L^2(\Omega)} \longrightarrow 0, \quad when \quad \varepsilon \to 0 \tag{5.9.7}$$

where u_ε is the microscopic solution and u_0 is the solution of the homogenized problem. In Tables 5.9.3, 5.9.4 and 5.9.5 we show the L^2 norm of the difference between the homogenized and the microscale concentration c^e in the electrolyte, potential ϕ^e in the electrolyte and potential ϕ^s in the solid. We observe a steady convergence rate as $\varepsilon \to 0$ which confirms the asymptotic analysis behind the homogenization method.

Table 5.9.3: L^2 norms for the concentration of Li+ in the electrolyte at time step 40

ε	$\|c_0^e - c_\varepsilon^e\|_{L^2}$	Convergence rate
0.2	8.73508e-07	-
0.1	5.60168e-07	0.64
0.05	4.41375e-07	0.34
0.025	3.66711e-07	0.27

Table 5.9.4: L^2 norms for the potential in the electrolyte at time step 40

ε	$\|\phi_0^e - \phi_\varepsilon^e\|_{L^2}$	Convergence rate
0.2	3.76515e-04	-
0.1	1.114424e-04	1.76
0.05	7.49176e-05	0.57
0.025	5.82417e-05	0.36

Table 5.9.5: L^2 norms for the potential in the cathode at time step 40

ε	$\|\phi_0^s - \phi_\varepsilon^s\|_{L^2}$	Convergence rate
0.2	0.000393077	-
0.1	0.000139498	1.494518
0.05	7.30204e-05	0.93
0.025	3.5623e-05	1.04

5.9.3 Numerical experiments for random complex geometry of the periodicity cell

The geometry of the battery cell electrodes is shown in Figure 5.24 and the solid phase periodicity cell is given in Figures 5.20, 5.21, 5.22 and 5.23. Here we do not run simulations for different values of the small parameter ε due to the complexity of the problem and, respectively, the big computational time needed for the microscale simulations. Instead, we show numerical results for $\varepsilon = 0.2$, which in our case corresponds to having only 5 periodicity cells in each electrode. Even for this big value of ε in the context of the homogenization method, we obtain very good agreement between the homogenized and the microscale problem both for low and very high applied currents. We show numerical results for 1C and 10C rates. The C-rate is defined as the measure of the rate at which a battery is discharged (respectively charged) relative to its maximum capacity. A 1C rate corresponds to the current necessary to discharge (charge) the entire battery in one hour.

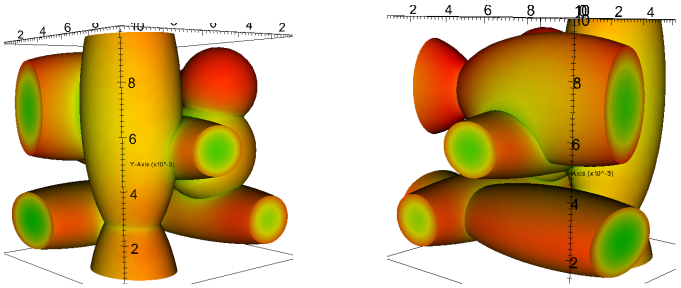

Figure 5.20: Geometry of the periodicity cell - View 1

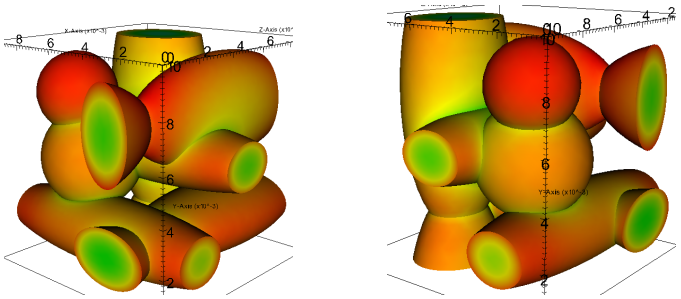

Figure 5.21: Geometry of the periodicity cell - View 2

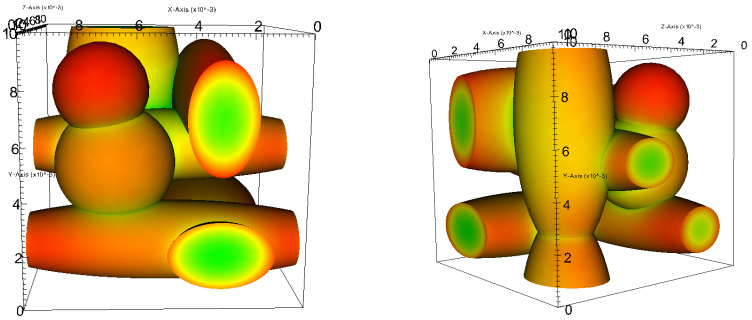

Figure 5.22: Geometry of the periodicity cell - View 3

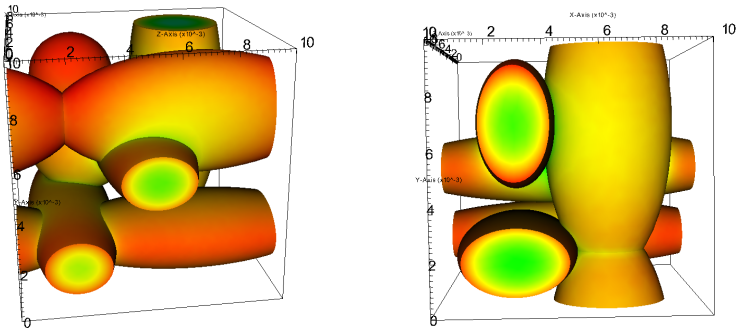

Figure 5.23: Geometry of the periodicity cell - View 4

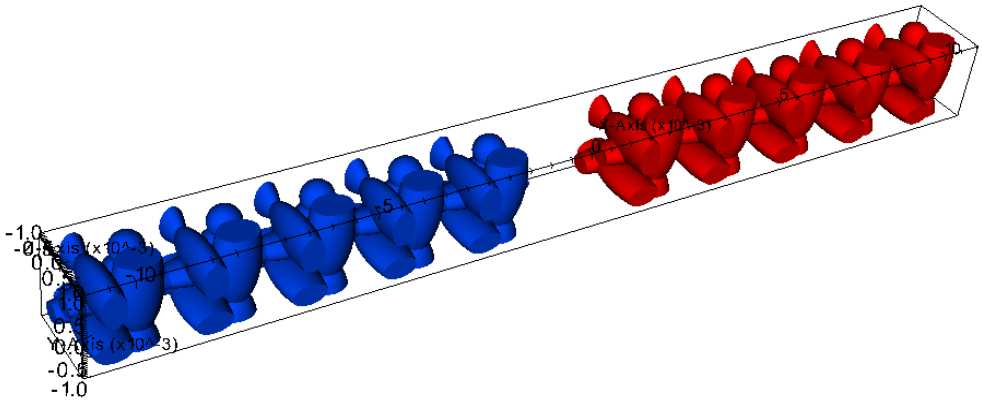

Figure 5.24: Electrodes consisting of 5 complex periodicity cells arranged in a string

The *effective macroscopic coefficients* in this test case are

$$\mathbf{K_{ij}} = k_{ij}^{e} \begin{pmatrix} 0.414526 & 0.00379188 & -0.00320872 \\ 0.00379188 & 0.393643 & 0.0189317 \\ -0.00320872 & 0.0189317 & 0.410734 \end{pmatrix} \tag{5.9.8a}$$

$$\mathbf{\Lambda^{s}} = \kappa^{s} \begin{pmatrix} 0.707535 & 0.0021711 & 0.0111428 \\ 0.0021711 & 0.754764 & -0.0120859 \\ 0.0111428 & -0.0120859 & 0.706042 \end{pmatrix} \tag{5.9.8b}$$

where $i, j = 1, 2$. Because of shape changes of the active material, there is some more pronounced anisotropy in the effective tensors compared to the cut-off spherical particles geometry. Nevertheless, the off-diagonal elements are still much smaller than the diagonal ones due to the fact that the particles' orientations are parallel to the coordinate axes. Therefore we still solve the homogenized problem in 1D.

Results for 1C rate

Here we run the simulations for 400s. In Figure 5.25 and Figure 5.26 we show numerical results for the cell voltage and cell voltage difference, respectively, versus the transferred charge. The computational time for the full microscale simulation was approximately 27 hours and for the homogenized problem - 3h 40min.
As we can see from Figure 5.26, the cell voltage difference between the microscale and the homogenized solution is only about 10 mV. More precisely, the microscale cell voltage is in the interval $[3.44256V, 3.80986V]$, which means that it increases throughout the considered time frame with a total of 367.3 mV. On the other hand, the maximum cell voltage difference (see Figure 5.26) is less than 12.5 mV. Consequently, the relative error between the microscale and the homogenized cell voltage is only 3.4% with respect to the total change in the microscale cell voltage.
The concentration of Li+ in the electrolyte is shown in Figure 5.27 and we can see that the homogenized solution is in a very good agreement with the microscale one.

In Figure 5.28 we show the electrochemical potential in the electrolyte and in Figure 5.29 - the electrical potential in the cathode measured on the current collector, i.e., on the wall ω_2. In the three-dimensional microscale simulation, the value of ϕ^s on $\partial\Omega_c \cap \omega_2$ is virtually constant due to the fast electroconductivity and hence the negligible variations of the potential inside the cathode active particles. Therefore, we can take the value of the potential on $\partial\Omega_c \cap \omega_2$ at an arbitrary point. As we can see in Figure 5.28, the spatial profile of the homogenized potential ϕ^e coincides with that of the microscale one and there is a constant shift between the two curves. The same is valid and for ϕ^s with a little bigger offset at the end of the simulation.
In Figures 5.30, 5.31, 5.32, 5.33 and 5.34 we show the concentration of Li+ in the active material at different times, in the innermost cathode periodicity cell situated right next to the layer of pure electrolyte which separates the two electrodes. The values of the concentration c^s in the microscale problem and in the homogenized one are in a good agreement but there are some discrepancies in the spatial distribution of the concentration due to the following reasons

- Due to the good agreement between the macroscopic homogenized quantities and the microscale ones in this test case, in the homogenized problem we do not impose the real Butler-Volmer interface conditions on the part of the solid phase domain which is in contact with the layer of pure electrolyte separating the electrodes. Instead, we impose periodic boundary conditions there, as you can see in Figure 5.35, where we show the two opposite, periodic in the x_1-direction, sides of the periodicity cell. Therefore, in the microscale solution the distribution of c^s on this part of the active material surface differs from that in the homogenized solution.

- Since we apply constant current on the outer cathode boundary, the lithium ions move from the cathode to the anode, i.e., from right to left in the pictures below. Therefore in the microscale solution we observe bigger concentration of Li+ on the right side of the periodicity cell (see Figure 5.36). The depletion of ions from the solid into the electrolyte is faster where there are "edges" and the active material surface is more "curvy". Hence in the simulations below the "flat" regions of the solid domain are with higher concentrations of Li+, whereas the more "curvy" and "edgy" ones are with lower concentrations of ions. The same is valid for the homogenized solution, except for the part of the active material where we have periodicity of the solution in the x_1-direction (see Figure 5.35 and Figure 5.36).

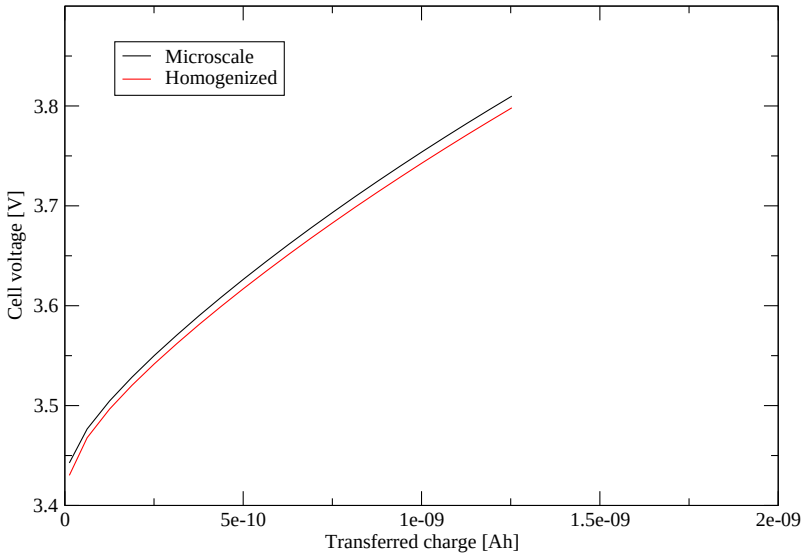

Figure 5.25: Cell voltage in V

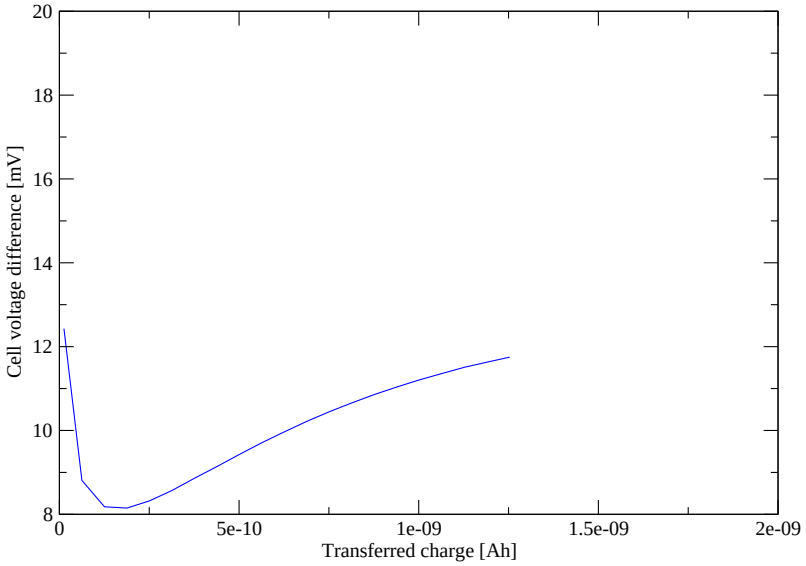

Figure 5.26: Cell voltage difference in mV

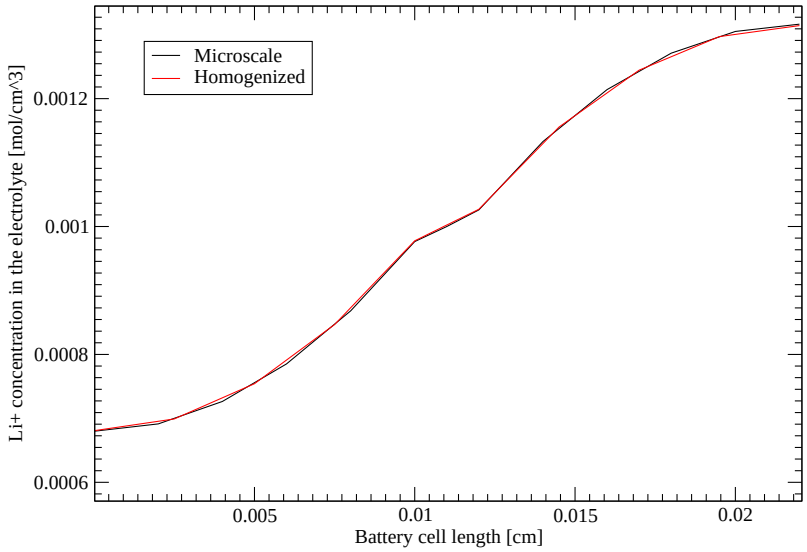

Figure 5.27: Concentration of Li+ in the electrolyte after 400s

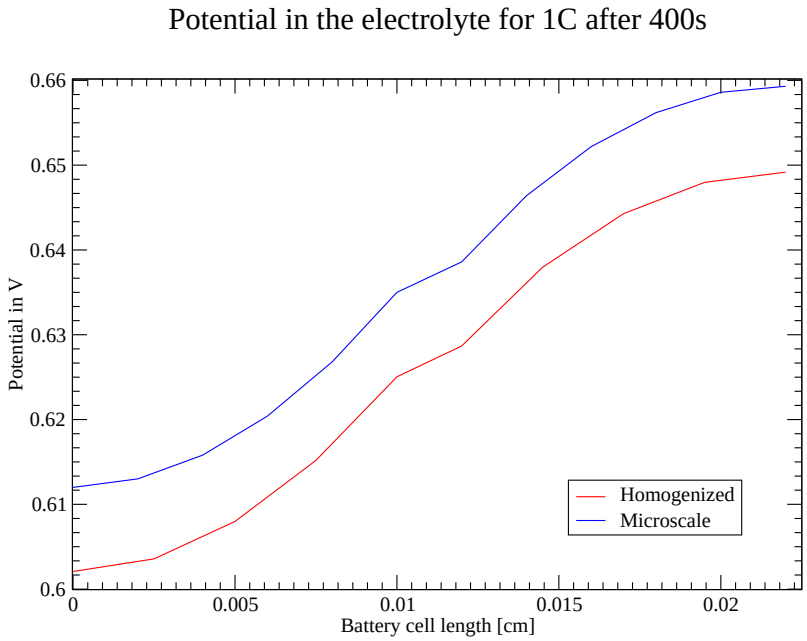

Figure 5.28: Potential in the electrolyte in V

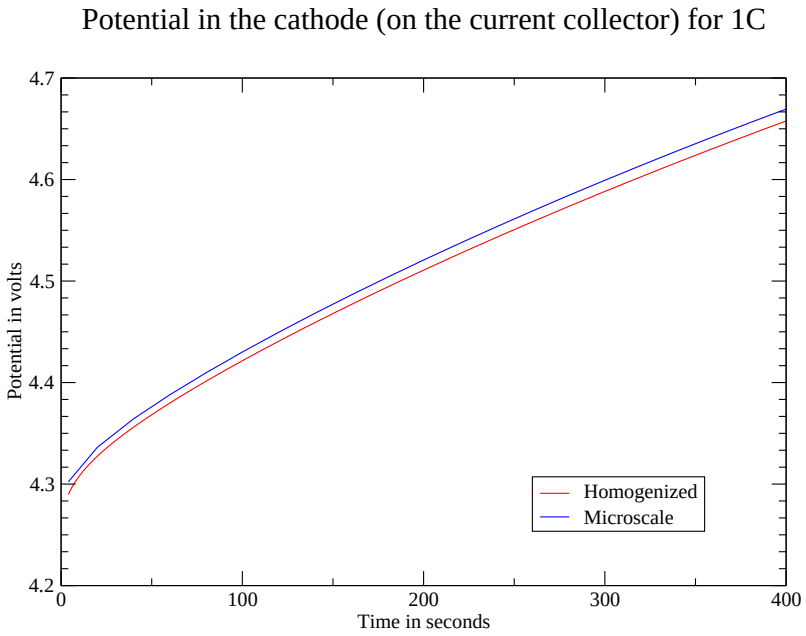

Figure 5.29: Potential in the cathode in V

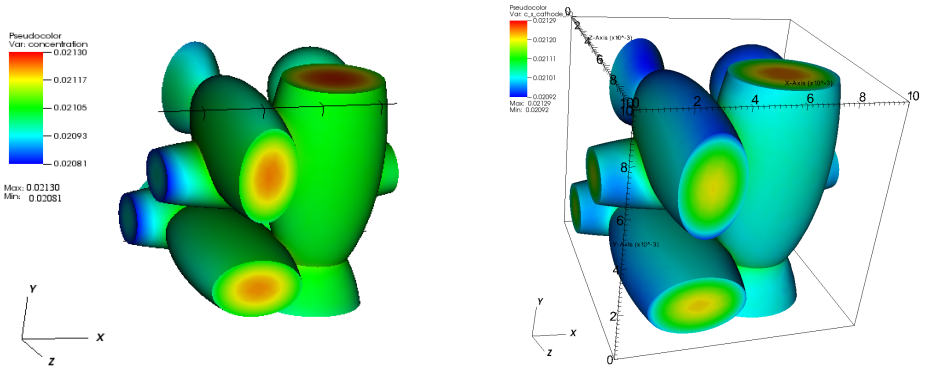

a. Microscale reference solution with values in $[0.02081, 0.02130]$

b. Homogenized solution with values in $[0.02092, 0.02129]$

Figure 5.30: Concentration of Li+ in a single cathode periodicity cell after 20s

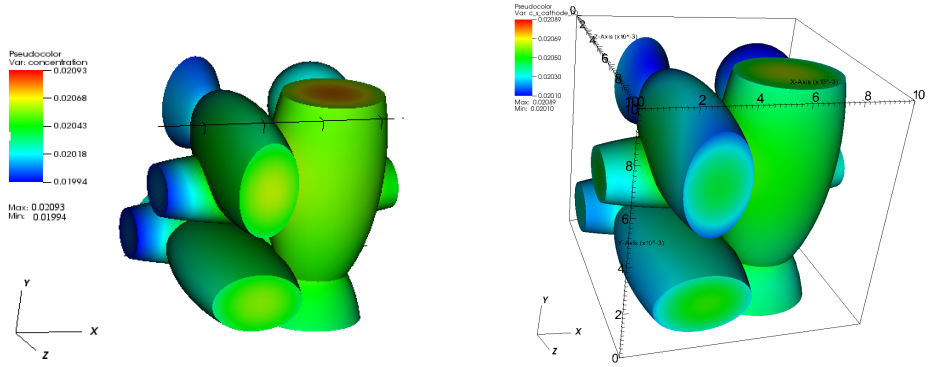

a. Microscale reference solution with values in $[0.01994, 0.02093]$

b. Homogenized solution with values in $[0.02010, 0.02089]$

Figure 5.31: Concentration of Li+ in a single cathode periodicity cell after 100s

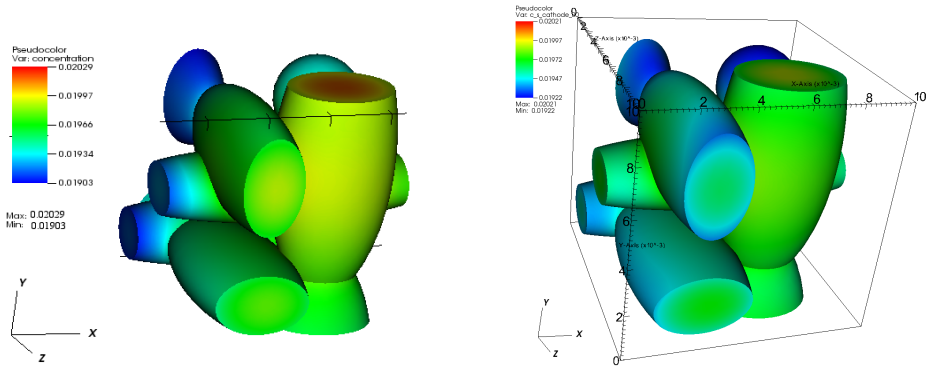

a. Microscale reference solution with values in $[0.01903, 0.02029]$

b. Homogenized solution with values in $[0.01922, 0.02021]$

Figure 5.32: Concentration of Li+ in a single cathode periodicity cell after 200s

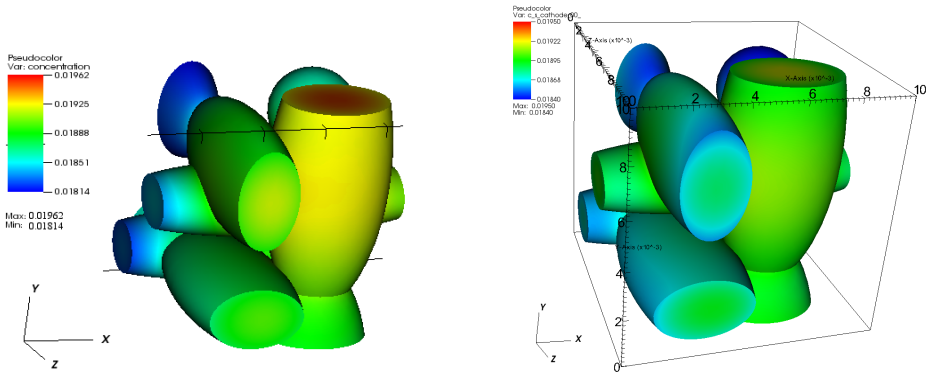

a. Microscale reference solution with values in $[0.01814, 0.01962]$

b. Homogenized solution with values in $[0.01840, 0.01950]$

Figure 5.33: Concentration of Li+ in a single cathode periodicity cell after 300s

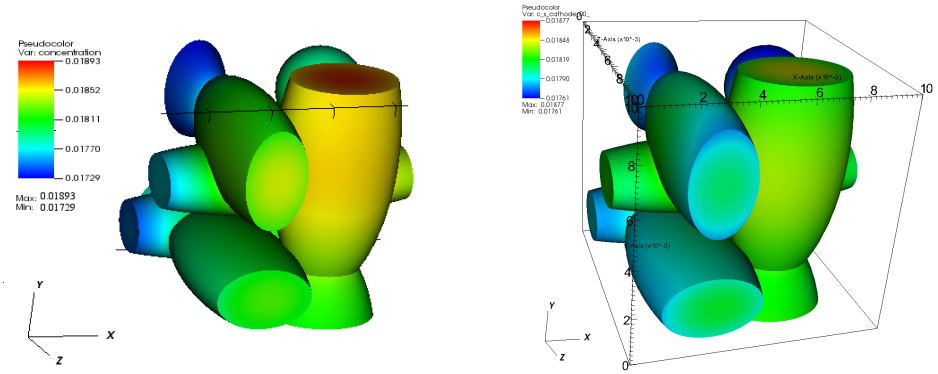

a. Microscale reference solution with values in $[0.01729, 0.01893]$

b. Homogenized solution with values in $[0.01761, 0.01877]$

Figure 5.34: Concentration of Li+ in a single cathode periodicity cell after 400s

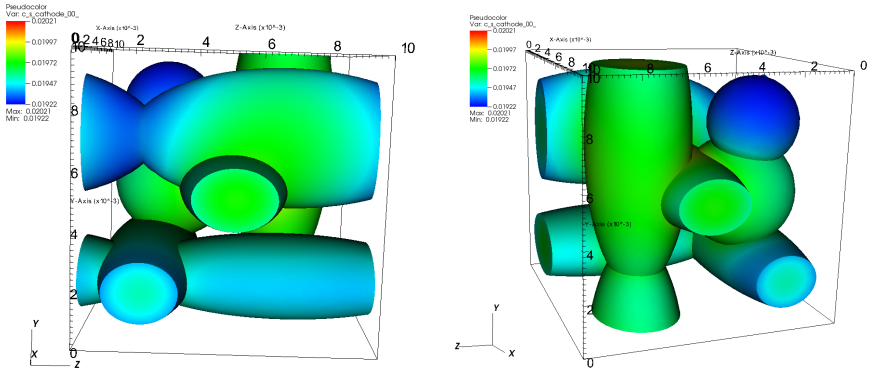

a. Left side

b. Right side

Figure 5.35: Homogenized concentration of Li+ in a single cathode periodicity cell after 200s

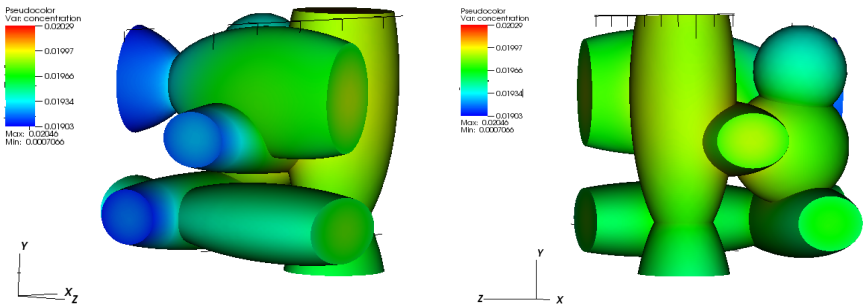

a. Left side

b. Right side

Figure 5.36: Microscale concentration of Li+ in a single cathode periodicity cell after 200s

Results for 10C rate

Here we run the simulations until the battery is fully charged. The very high applied current in this test case leads to steeper gradients of the concentration c^s near the solid-electrolyte interface. This results in less uniform spatial profile of c^s compared to the 1C case. Consequently, we need better approximation for c^s in the active material near the layer of pure electrolyte because there we have the biggest solid-electrolyte interface surface area. Therefore we do some optimizations in the numerics. First, we impose the real interface conditions for the two innermost periodicity cells (the ones right next to the layer of pure electrolyte) - one in the cathode and one in the anode, instead of periodic boundary conditions as we do in the case for 1C. Second, since we solve the coupled macro-micro model semi-implicit in time, at each time step we iterate several times between macro (5.6.1) and micro (5.6.3) problem solution until they converge. In all of the figures below we show numerical results for both the improved and non-improved solution of the homogenized problem.
We show numerical results for the cell voltage in Figure 5.37, and cell voltage difference in Figure 5.38, respectively, versus the transferred charge. The concentration of Li+ in the electrolyte is given in Figure 5.39 and we can see that even in this regime of 10C rate, the homogenized solution is a very good approximation of the microscale one. The electrochemical potential in the electrolyte is given in Figure 5.40, and the electrical potential, measured on the outer cathode boundary $\partial\Omega_c \cap \omega_2$ (where the current collector is usually placed) is given in Figure 5.41.
The computational time for the full microscale simulation was approximately 14 hours and that for the homogenized problem was 1h 30min for the non-optimized version and 2h 40min for the optimized version.
The microscale cell voltage is given in Figure 5.37 and it varies in the interval $[3.88742V, 4.6587V]$, which means that the total increase in the cell voltage over the considered time period is 771.28 mV. The maximum value of the difference between the microscale cell voltage and the improved homogenized one is less than 76.5 mV as we can see in Figure 5.38. Therefore the relative error between the microscale and the homogenized cell voltage is approximately 10%. Here the bigger difference between the reference solution and the homogenized one, compared to the test case of 1C rate, is due to the fact we solve a coupled macro-micro problem and we need better approximation of the macroscale quantities when solving the microscale 3D problem for c^s.
In Figures 5.42, 5.43 and 5.44 we show the solid phase concentration of Li+ at different times in the innermost cathode periodicity cell, located right next to the layer of pure electrolyte. We observe a good agreement between the microscale and the improved homogenized solution. We also compare the spatial distribution of ions in both the improved and non-improved homogenized solution in Figures 5.45, 5.46, and 5.47. We can see that when we impose the Butler-Volmer interface conditions in the microscale problem (5.3.1) for c^s (Figure 5.46), instead of periodic boundary conditions (Figure 5.47), we obtain a better approximation of the reference microscale solution which is shown in Figure 5.45.

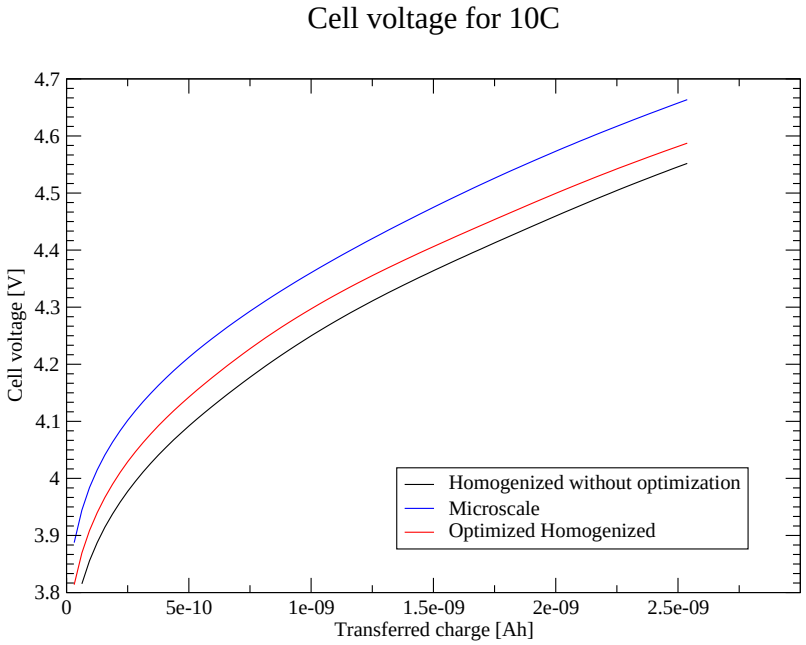

Figure 5.37: Cell voltage in V

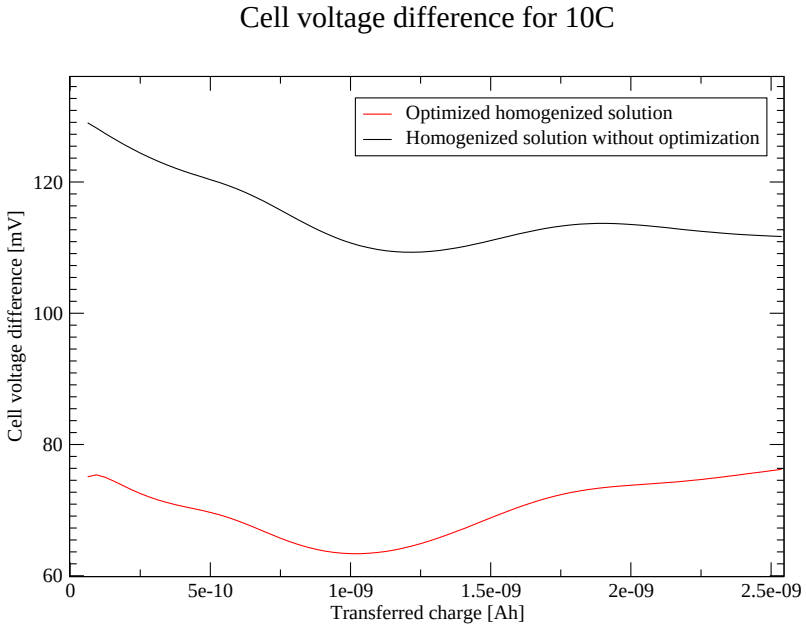

Figure 5.38: Cell voltage difference in mV

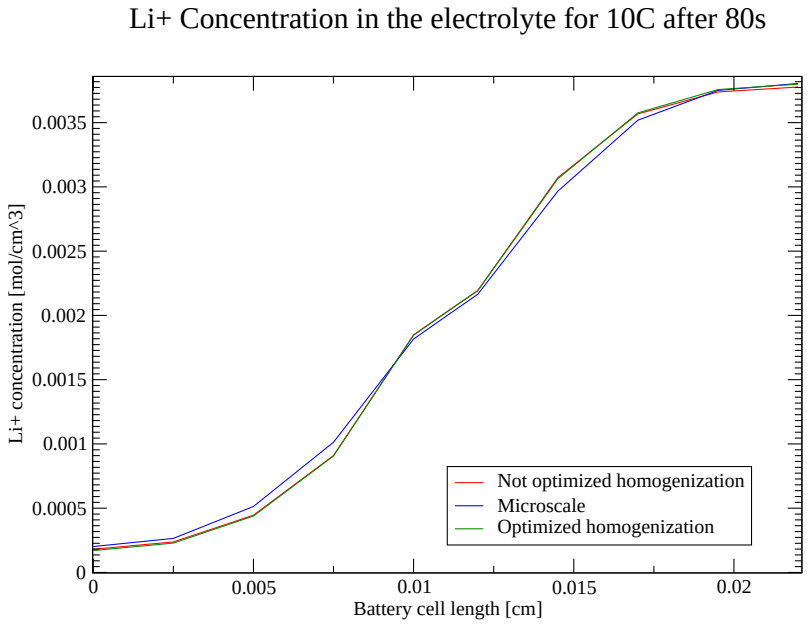

Figure 5.39: Concentration of Li+ in the electrolyte after 80s

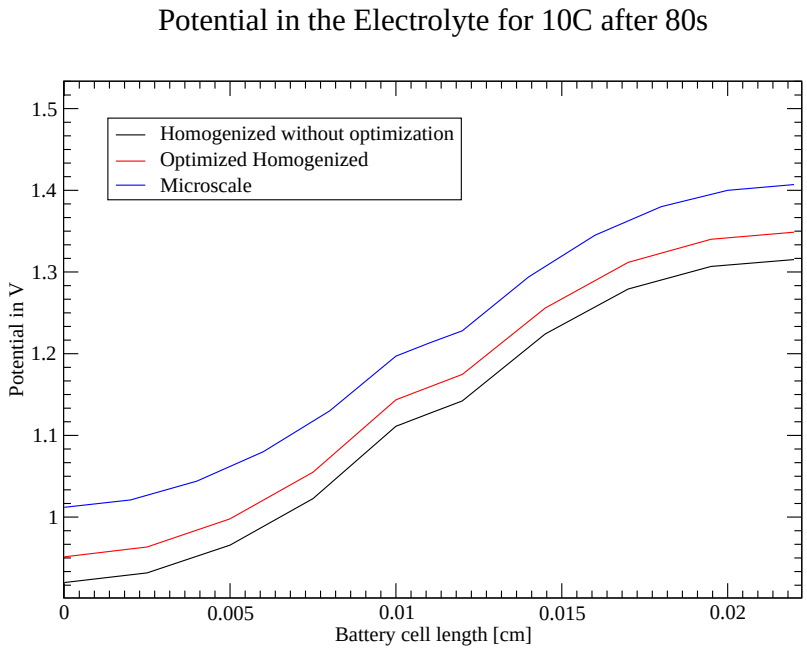

Figure 5.40: Potential in the electrolyte in V after 80s

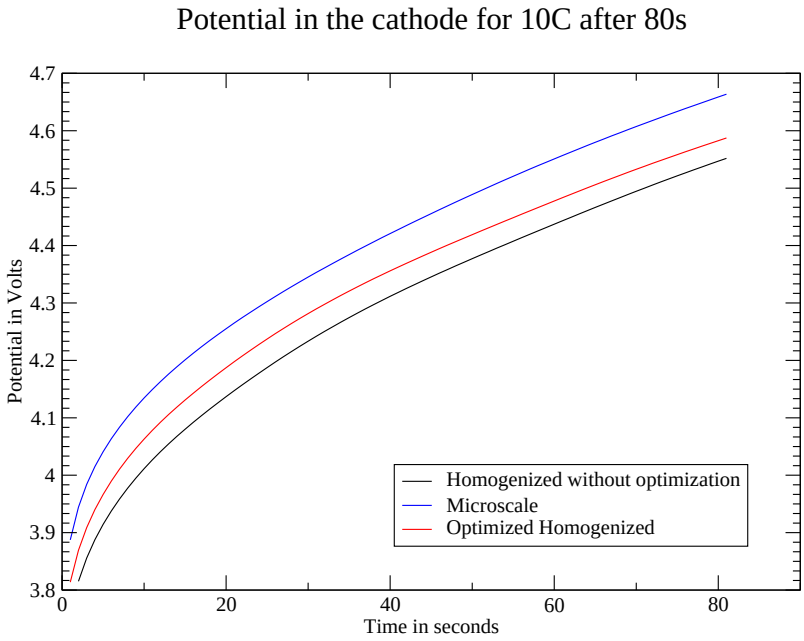

Figure 5.41: Potential in the cathode in V for 80s of simulation

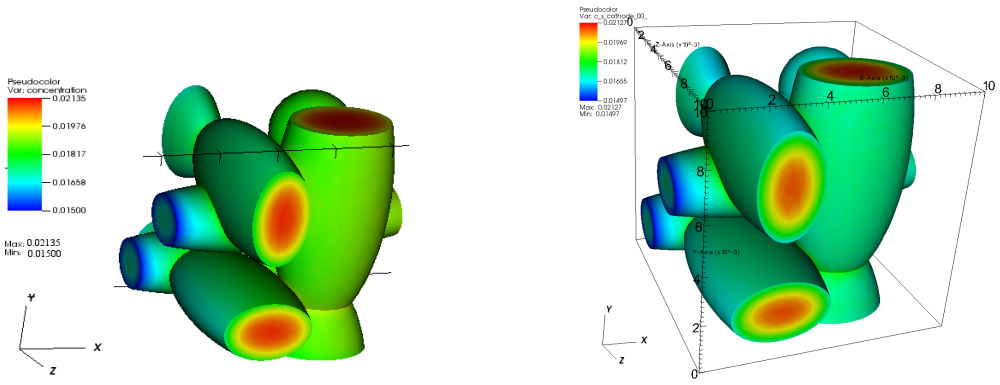

a. Microscale reference solution with values in $[0.01500, 0.02135]$

b. Optimized homogenized solution with values in $[0.01497, 0.02127]$

Figure 5.42: Concentration of Li+ in a single cathode periodicity cell after 10s

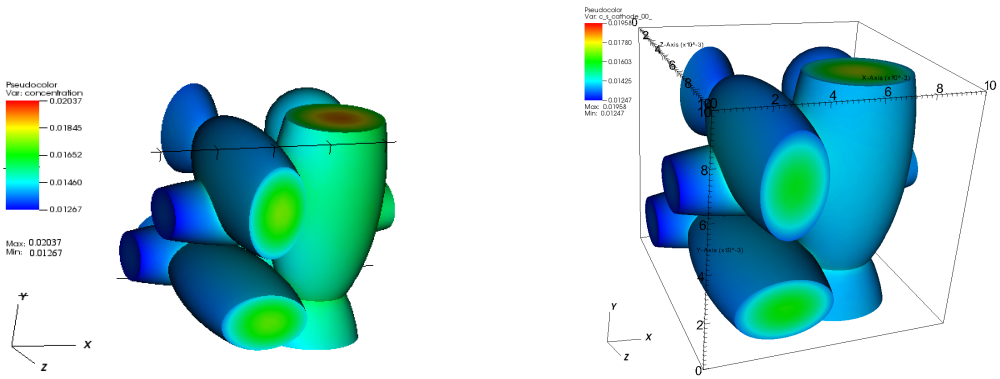

a. Microscale reference solution with values in $[0.01267, 0.02037]$

b. Optimized homogenized solution with values in $[0.01247, 0.01958]$

Figure 5.43: Concentration of Li+ in a single cathode periodicity cell after 40s

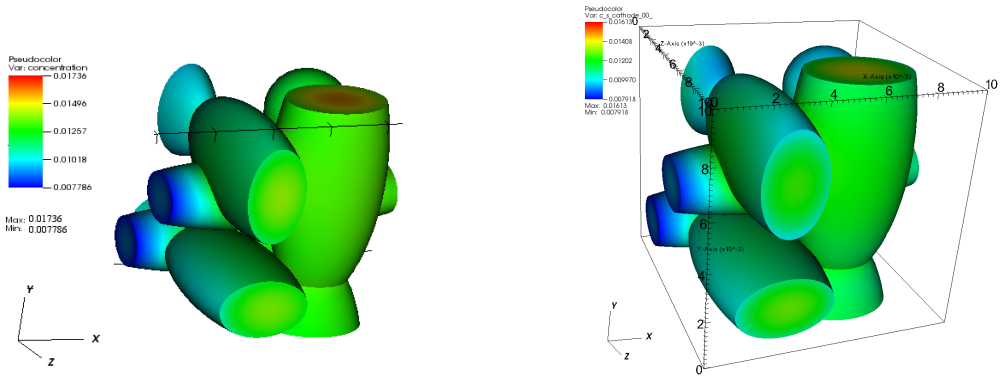

a. Microscale reference solution with values in $[0.007786, 0.01736]$

b. Optimized homogenized solution with values in $[0.007918, 0.01613]$

Figure 5.44: Concentration of Li+ in a single cathode periodicity cell after 80s

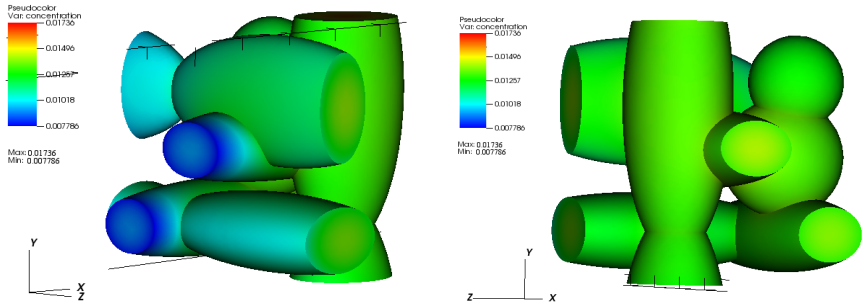

a. Left side

b. Right side

Figure 5.45: Microscale concentration of Li+ in a single cathode periodicity cell after 80s, with values in $[0.007786, 0.01736]$

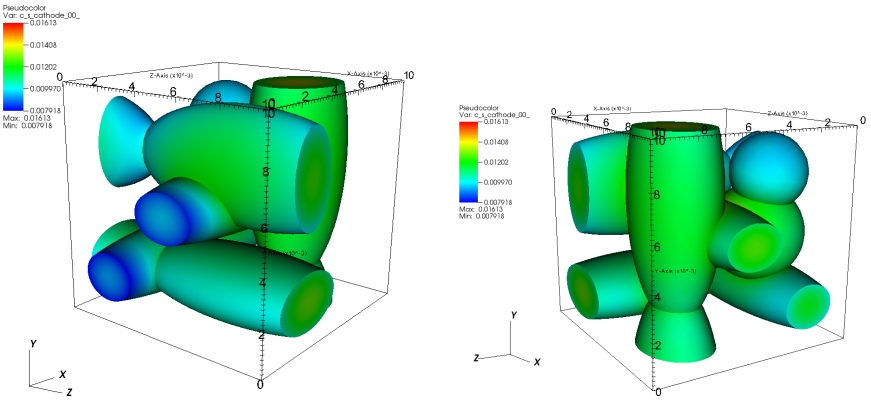

a. Left side b. Right side

Figure 5.46: Optimized homogenized concentration of Li+ in a single cathode periodicity cell after 80s, with values in $[0.007918, 0.01613]$

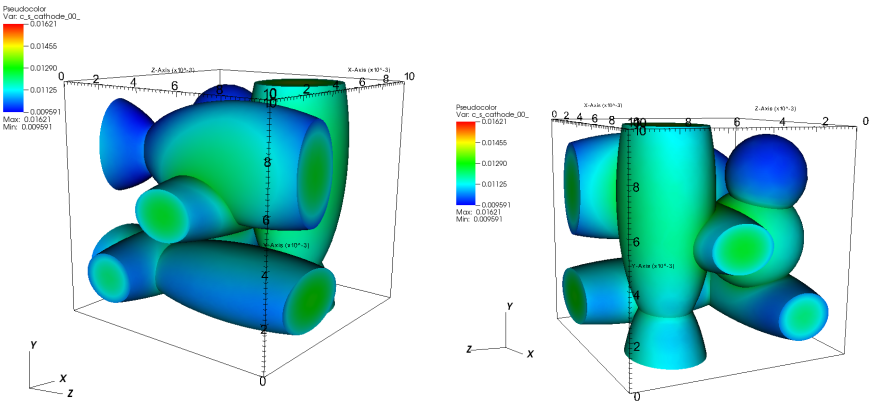

a. Left side b. Right side

Figure 5.47: Non-optimized homogenized concentration of Li+ in a single cathode periodicity cell after 80s, with values in $[0.009591, 0.01621]$

5.10 Advantages of the proposed upscaling algorithm

The developed upscaling approach which is based on the asymptotic homogenization theory has the following benefits:

- Averaged macroscopic partial differential equations that capture the behaviour of the concentration and the potential on the lengthscale of the whole battery cell
- Effective transport coefficients describing the macroscopic properties of the battery electrodes
- No restrictions on the geometry of the active material inside the periodicity cell unlike the assumption for spherical particles in Newman's model [22]

- No restrictions on the applied currents
- Significantly reduced number of degrees of freedom due to the fact that with the homogenized equations we do not need to resolve the porous microscale structure of the electrodes
- Faster numerical simulations thanks to the very little number of unknowns and the well-posed homogenized model
- The proposed solution algorithm, which is semi-implicit in time, allows for solving very efficiently in parallel the three-dimensional microscale problems for c^s
- Computationally shown proximity of the the upscaled problem to the microscale one

5.11 Conclusion

We have successfully derived an upscaled coupled macro-microscale Li-ion battery model starting from the isothermal microscale model [48]. We showed rigorously the asymptotic order of the interface exchange current densities with respect to the small parameter, which is crucial for the homogenization of the microscopic model. We also derived upscaled Neumann boundary conditions for the homogenized problem using the specified microscale boundary conditions. Finally, we performed a series of numerical simulations in order to validate our upscaled model. The results of the numerical experiments showed very good agreement between the homogenized and the microscale model, even for complex geometry of the periodicity cell and for very high applied currents. Also, with the homogenized model we achieved seven times acceleration in terms of computational time. Moreover, the numerical algorithm that we proposed allows for parallel implementations, which in turn will speed up even further the computer simulations. The computations for the coupled macro-micro model can also be significantly simplified by applying the reduced basis method (studied for example in [76], [51], [53]) which is a subject of future research.

Chapter 6

Multiscale Finite Element Method (MsFEM)

6.1 Introduction

As we have already discussed in Chapter 3, multiscale problems arise as a result of the mathematical modelling of many physical processes, such as flows in porous media (for example in groundwater transport) and electrical or thermal conductivity in composite materials. The coefficients of such problems, as well as their solutions, are highly oscillatory, not necessarily periodic functions and may spread over multiple spatial scales, leading to very expensive direct numerical simulations when standard methods, such as the Finite Element Method ([9], [13], [60]), Finite Volume Method ([30], [7], [49]) or Finite Difference Method ([52]), are applied. This computational complexity is due to the huge number of degrees of freedom needed to resolve all the scales involved in order to obtain a relevant solution. While resolving in detail all scales of the multiscale problem is preferred (if the available computer resources allow it), in many practical applications it is often sufficient to know the macroscopic properties of a given quantity. As an upscaling technique, this is also the idea behind the Multiscale Finite Element Method. The MsFEM was introduced by Hou and Wu in the mid 90's in [68], and some of the most prominent works on the topic are [69], [73], [74], [72] and [25]. The MsFEM is based on the Finite Element Method and it provides a systematic and easy to analyze and apply framework. Namely, the method is designed to effectively capture the macroscopic behaviour of highly oscillating multiscale solutions without fully resolving all small-scale features. This is achieved by constructing special finite element basis functions which incorporate the local properties of the differential operator.

There are no original results presented in this chapter. It serves as a short introduction to the standard Multiscale Finite Element Method, which we expand in the next chapters to problems in perforated domains and apply it to the considered in this work microscale Li-ion battery model [48]. The chapter is organized as follows. We begin with the framework of the method in Section 6.2, where we present the basics of the MsFEM by applying it to a simple model problem. Then, in Section 6.3 we briefly discuss the choice of boundary conditions for the local problems which are being solved in order to construct the multiscale

basis functions. In Section 6.4 we address the choice of the coarse grid size H and the concept of scale separation in the context of the MsFEM. We give the main convergence result in Section 6.5. We illustrate the method with a simple numerical example in Section 6.6.

6.2 Framework of the method

In order to illustrate the method, we consider the following model elliptic problem

$$-\nabla \cdot (k_\varepsilon(x)\nabla u_\varepsilon) = f(x), \quad x \in \Omega = [0,1] \times [0,1] \subset \mathbb{R}^2 \tag{6.2.1a}$$

$$u_\varepsilon(x) = 0, \quad x \in \partial\Omega \tag{6.2.1b}$$

where $k_\varepsilon(x)$ is some highly oscillating, not necessarily periodic, coefficient. The ε in problem (6.2.1) stands for indicating that the coefficient $k_\varepsilon(x)$ and the solution $u_\varepsilon(x)$ are spatially oscillating functions with oscillations of order ε, where $\varepsilon \ll 1$. Let us denote the differential operator in (6.2.1) with $\mathcal{L}_\varepsilon$, i.e., $\mathcal{L}_\varepsilon = -\nabla \cdot (k_\varepsilon(x)\nabla)$.
The weak formulation of the problem reads: find $u_\varepsilon \in H_0^1(\Omega)$ such that the following integral equality is true for all functions $v \in H_0^1(\Omega)$

$$\int_\Omega k_\varepsilon(x)\nabla u_\varepsilon \cdot \nabla v \, dx = \int_\Omega f v \, dx \tag{6.2.2}$$

In order to apply the Finite Element Method, we need to restrict the weak formulation (6.2.2) to a finite dimensional approximation subspace of $H_0^1(\Omega)$. Let $\mathcal{T}^H$ be a partition of the solution domain Ω into coarse rectangular finite elements K as shown in Figure 6.1(a), where $0 < H \leq 1$, such that $H \gg \varepsilon$, is the diameter of the partition. We denote with N the number of nodes (vertices of coarse finite elements) in the mesh of finite elements. The idea of the MsFEM is to solve local problems in each coarse grid finite element $K \in \mathcal{T}^H$ in order to construct special basis functions which capture the local properties of the differential operator $\mathcal{L}_\varepsilon$. We denote the multiscale basis functions by $\phi_i^M(x)$, where $i = 1, 2, \ldots, N$. We require that $\phi_i^M(\mathbf{x^j}) = \delta_{ij}$ (the Kronecker delta symbol), where $\mathbf{x^j}$ for $j = 1, 2, \ldots, N$ are the vertices of the coarse finite elements K. This means that $\{\phi_i^M\}_{i=1}^N$ form a nodal basis. Hence, the multiscale basis functions have localized supports consisting of the four striped squares, given in Figure 6.1(a), which share the common vertex $\mathbf{x^i}$. A single coarse grid finite element K is illustrated in Figure 6.1(b). Finally, we define the multiscale basis functions as the solution to the following local poblems $\forall K \in \mathcal{T}^H : K \in supp\{\phi_i^M(x)\}$:

$$-\nabla \cdot \left(k_\varepsilon(x)\nabla \phi_i^M\right) = 0, \quad x \in K, \tag{6.2.3a}$$

$$\phi_i^M(x) = \phi_i^L(x), \quad x \in \partial K \tag{6.2.3b}$$

where $i = 1, 2, \ldots, N$ and $\{\phi_i^L(x)\}_{i=1}^N$ is the standard piecewise linear basis. We solve numerically the local problems (6.2.3) using the Finite Element Method with linear Lagrange elements. Let us denote with τ_K^h the partition of each coarse grid block $K \in \mathcal{T}^H$

into finite elements e_K as shown in Figure 6.1(c). We call these partitions $\tau_K^h = \bigcup_{e_K \in \tau_K^h} e_K$ "the fine mesh". With $\left(\phi_i^M\right)^h$ we denote the expansion of the discretized approximate solution to (6.2.3) with respect to the fine mesh basis over a given coarse grid block.
The Dirichlet boundary condition (6.2.3b) assures that the multiscale basis functions are continuous across the edges of the coarse finite elements, i.e., the finite element method is conforming. Therefore, we have that

$$V^H = span\{\phi_i^M(x)\}_{i=1}^N \subset H_0^1(\Omega) \tag{6.2.4}$$

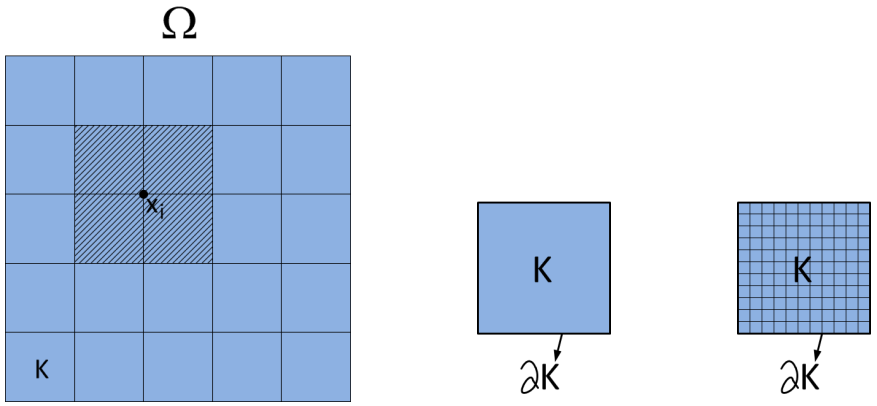

(a) Coarse grid

(b) Single coarse grid finite element K

(c) Discretized coarse finite element K

Figure 6.1: Discretized 2D solution domain with coarse grid rectangular finite elements K

Now we restrict the weak form (6.2.2) to the finite dimensional approximation space $V^H \subset H_0^1(\Omega)$. Then the weak formulation in the space V^H becomes: find $u_\varepsilon^H \in V^H$ such that the following integral equality is satisfied for all functions $v^H \in V^H$

$$\int_\Omega k_\varepsilon(x) \nabla u_\varepsilon^H \cdot \nabla v^H \, dx = \int_\Omega f v^H \, dx \tag{6.2.5}$$

and we can apply the Finite Element Method. Consequently, we expand the approximate discretized solution u_ε^H with respect to the multiscale basis $\left\{\phi_i^M(x)\right\}_{i=1}^N$

$$u_\varepsilon^H(x) = \sum_{i=1}^N U_i \phi_i^M(x) \tag{6.2.6}$$

and after we substitute this expansion in the weak form (6.2.5), together with $v^H = \phi_j^M$ for all $j = 1, 2, \ldots, N$, we get the following system of N equations

$$\int_\Omega k_\varepsilon(x) \sum_{i=1}^N U_i \nabla \phi_i^M \cdot \nabla \phi_j^M \, dx = \int_\Omega f \phi_j^M \, dx \tag{6.2.7}$$

Finally we obtain the system of linear algebraic equations $\mathbf{AU} = \mathbf{F}$, where the elements of the stiffness matrix $\mathbf{A} = (a_{ij})_{i,j=1}^{N}$ are given by

$$a_{ji} = \sum_{K \in \mathcal{T}^H} \left(\sum_{e_K \in \tau_K^h} \int_{e_K} k_\varepsilon(x) \nabla \left(\phi_i^M\right)^h \cdot \nabla \left(\phi_j^M\right)^h \, dx \right) \tag{6.2.8}$$

The right-hand side is the vector $\mathbf{F} = (F_1, F_2, \ldots, F_N)^T$ with elements

$$F_j = \sum_{K \in \mathcal{T}^H} \left(\sum_{e_K \in \tau_K^h} \int_{e_K} f \left(\phi_j^M\right)^h \, dx \right), \tag{6.2.9}$$

and the solution vector is $\mathbf{U} = (U_1, U_2, \ldots, U_N)^T$. In order to calculate the elements of the stiffness matrix and the right-hand side, we have to integrate over the fine mesh τ_K^h for each $K \in \mathcal{T}^H$ and consequently we have to store the solutions of all local problems for the multiscale basis functions ϕ_i^M. The MsFEM method is suitable for parallel implementations due to the fact that the multiscale basis functions are computed independently of one another in each coarse grid block.

6.3 The choice of boundary conditions for the multiscale basis functions

In the local problems (6.2.3) for constructing the multiscale basis functions, we impose linear boundary conditions on the edges of the coarse grid blocks K. This leads to a very rough approximation of the oscillations of the solution u_ε on the edges ∂K of the coarse grid finite elements. Another possibility, discussed in [69], is to impose so called "oscillatory boundary conditions". The idea is to solve the reduced 1-D elliptic equations (6.2.3a) on each coarse grid edge ∂K with boundary conditions 0 and 1 at the vertices of the edge, and then to use the solution to these reduced problems as a boundary condition for the multiscale basis functions $\phi_i^M(x)$.
In the present work we use only the linear boundary conditions (6.2.3b) because the focus of the thesis is to develop a general framework for MsFEM in perforated domains with Neumann data on the holes. Therefore we do not study the effect on the convergence rate of the method caused by imposing different boundary conditions in the local problems.

6.4 Choice of coarse grid size

Here we would like to discuss the nature of the oscillations of the solution u_ε to the multiscale problem (6.2.1) as well as the choice of the size H of the coarse mesh. Let us make an analogy with the asymptotic homogenization method from Chapter 3 and consider only the case when the solution to problem (6.2.1) spans over two spatial scales. In the homogenization, the solution of (3.4.1) is scale separable in the sense that it can be decomposed into an averaged macroscopic part u_0 and an oscillatory part εu_1, with

oscillations of order ε, where the small parameter ε characterizes the periodic microstructure of the medium and is much smaller than the characteristic size of the solution domain. Therefore, the two lengthscales in the homogenization problem are the lenghtscale of the whole solution domain and the lengthscale of the periodic microstructures, which is characterized by ε. Thus, in the asymptotic limit, when $\varepsilon \to 0$, the oscillations decay and the oscillatory solution u_ε to problem (3.4.1) can be approximated by the $O(1)$ term u_0. On the other hand, if the solution u_ε has oscillations of $O(1)$, then it is not scale-separable and the asymptotic homogenization method cannot be applied. In the case of the MsFEM, we have similar reasoning. Namely, if the solution to (6.2.1) has oscillations of $O(1)$ (as shown in Figure 6.3), then, the MsFEM will capture correctly the oscillatory solution only if $H \ll \varepsilon$, which is equivalent to applying the standard FEM. And vice versa, if the solution to (6.2.1) has oscillations only of order ε (as shown in the example in Figure 6.2), then we can take $H \gg \varepsilon$, which is the reasonable and efficient regime of the MsFEM. From now on, unless specified otherwise, we will consider only the latter case and we will always have in mind that $H \gg \varepsilon$. Thus, the advantage of the MsFEM is when applied to PDEs with highly oscillating, not necessarily periodic, coefficients with magnitude of the oscillations of order ε.

We illustrate the concept with two examples in 1-D. The upscalable function $u_\varepsilon(x) = x(2-x) + \varepsilon \sin\left(\frac{\pi x}{\varepsilon}\right)$ is shown in black, in Figure 6.2, for different values of the small parameter ε. As we can see from the picture, when $\varepsilon \to 0$, the oscillations decay and u_ε can be approximated by the function $u_0(x) = x(2-x)$, which is given in red and is plotted both in Figure 6.2 and 6.3. In Figure 6.3 we show the function $v_\varepsilon(x) = x(2-x) + \sin\left(\frac{\pi x}{\varepsilon}\right)$, given in black, which is not upscalable because the magnitude of its oscillations is not of order ε.

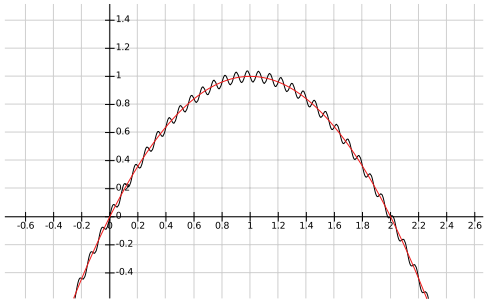

(a) $\varepsilon = 0.04$

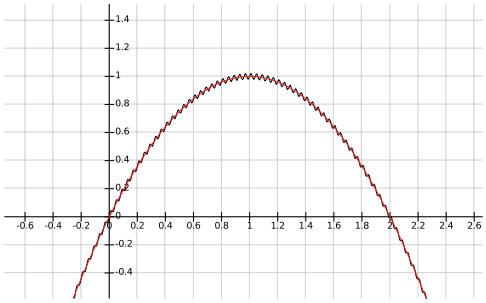

(b) $\varepsilon = 0.02$

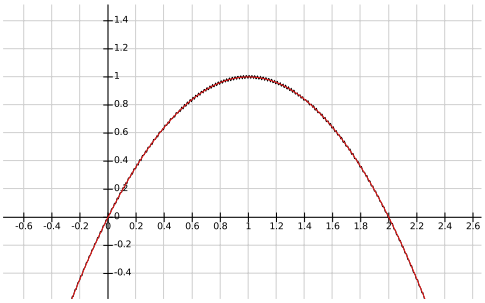

(c) $\varepsilon = 0.01$

Figure 6.2: Example for an upscalable function

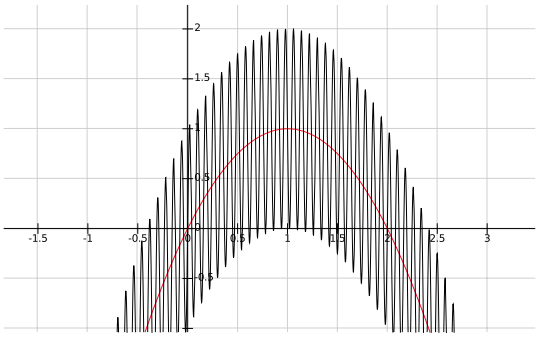

(a) $\varepsilon = 0.04$

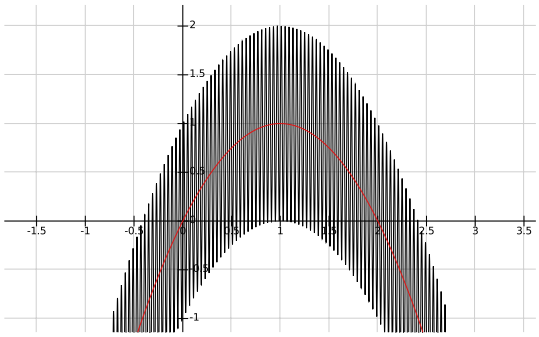

(b) $\varepsilon = 0.02$

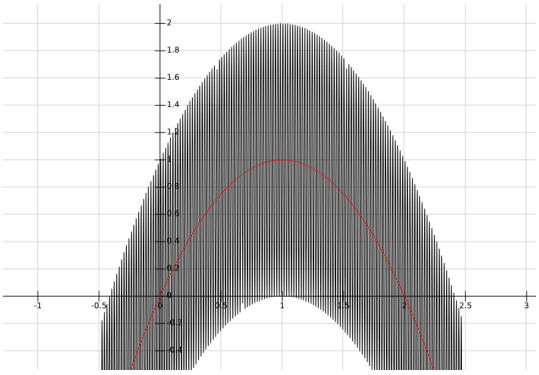

(c) $\varepsilon = 0.01$

Figure 6.3: Example for a function that is not upscalable

6.5 Main convergence result

In the work of Hou, Wu and Cai [69], for $H > \varepsilon$ we have the following

Theorem 4. *We make the following assumptions*

(1) $k_\varepsilon(x) = \left(k_{ij}^\varepsilon(x)\right)_{i,j=1}^2$, *with* $k_{ij}^\varepsilon(x) \in W^{1,p}(\Omega)$ $(p > 2)$ *and for all* $\xi \in \mathbb{R}^2$, *with* $0 < \alpha < \beta$, *it satisfies the following conditions*

1. $\xi k_\varepsilon \xi^T \geq \alpha |\xi|^2$,
2. $|k_\varepsilon \xi| \leq \beta |\xi|$
3. $k_{ij}^\varepsilon = k_{ji}^\varepsilon, \quad \forall i, j = 1, 2$
4. $k_{ij}^\varepsilon(x + \varepsilon) = k_{ij}^\varepsilon(x), \quad \forall x \in \Omega$
5. $k_{ij}^\varepsilon(x) = k_{ij}\left(\dfrac{x}{\varepsilon}\right) = k_{ij}(y), \quad where \quad y = \dfrac{x}{\varepsilon}$
6. $k_{ij}(y) \in W^{1,p}(Y) \quad is \quad Y - periodic \quad in \quad y, \quad where \quad Y = [0,1] \times [0,1]$

(2) $f \in L^2(\Omega)$

If, under assumptions (1) and (2), u_ε *is the solution to problem* (6.2.1) *and* u_ε^H *is the solution to problem* (6.2.5), *then there exist constants* C_1 *and* C_2, *independent of* ε *and* H, *such that*

$$\|u_\varepsilon - u_\varepsilon^H\|_{H^1(\Omega)} \leq C_1 H \|f\|_{L^2(\Omega)} + C_2 \sqrt{\frac{\varepsilon}{H}} \tag{6.5.1}$$

Also the following L^2 *error estimate holds*

$$\|u_\varepsilon - u_\varepsilon^H\|_{L^2(\Omega)} \leq C_1 H^2 \|f\|_{L^2(\Omega)} + C_2 \sqrt{\frac{\varepsilon}{H}} \tag{6.5.2}$$

We point out that the convergence result is proven only in the periodic case, when $k_\varepsilon(x)$ is a periodically oscillating coefficient with period ε and the proof is carried out with the help of the asymptotic homogenization method. We must also note that the result in Theorem 4 is derived under the assumption that the local problems (6.2.3) for computing the multiscale basis functions are solved exactly.
In [69] numerically is shown also the following improved error estimate

$$\|u_\varepsilon - u_\varepsilon^H\|_{L^2(\Omega)} \leq C_1 H^2 \|f\|_{L^2(\Omega)} + C_2 \frac{\varepsilon}{H} + C_3 \varepsilon \tag{6.5.3}$$

As we can see from the error estimates (6.5.1) and (6.5.2), the error is the biggest when $H = \varepsilon$. This is the so-called "resonance effect" and it occurs when the wavelength of the oscillations coincides with the coarse mesh size H. Therefore, in the case when $H > \varepsilon$ and in the presence of scale separation of the solution u_ε, the latter convergence results show that H must be sufficiently larger than ε in order for the multiscale basis functions to capture correctly the averaged behaviour of the differential operator $\mathcal{L}_\varepsilon$.
In the case when $H < \varepsilon$, the following result from [69] holds

Theorem 5. *If, under assumptions (1) and (2) from Theorem 4, u_ε is the solution to problem (6.2.1) and u_ε^H is the solution to problem (6.2.5), then there exists a constant C, independent of ε and H, such that*

$$\|u_\varepsilon - u_\varepsilon^H\|_{H^1(\Omega)} \leq C\frac{H}{\varepsilon}\|f\|_{L^2(\Omega)} \tag{6.5.4}$$

and also

$$\|u_\varepsilon - u_\varepsilon^H\|_{L^2(\Omega)} \leq C\left(\frac{H}{\varepsilon}\right)^2\|f\|_{L^2(\Omega)} \tag{6.5.5}$$

6.6 Numerical example

We solve the linear elliptic boundary value problem (6.2.1) with coefficient $k_\varepsilon(x) = \cos(128\pi x_1)\cos(128\pi x_2) + 1.1$ and right-hand side $f(x) = 16$. Consequently, since we solve the problem in the unit square, we have that $\varepsilon = \dfrac{1}{64}$. In the direct microscale simulation we have 792991 elements and 3954904 nodes. We use triangular finite elements both for the coarse and the fine grid, and the triangulation of the domain is generated with the program Triangle [67]. We have 259 coarse grid finite elements with approximately 4000 elements and 2500 nodes per macro element. The results of the simulation are shown in Figure 6.4. Due to the linear boundary conditions (6.2.3b), in Figure 6.4(b), we can clearly see where the edges of the coarse grid finite elements $K \in \mathcal{T}^H$ are. In Figure 6.5 we show how the multiscale basis function looks like.

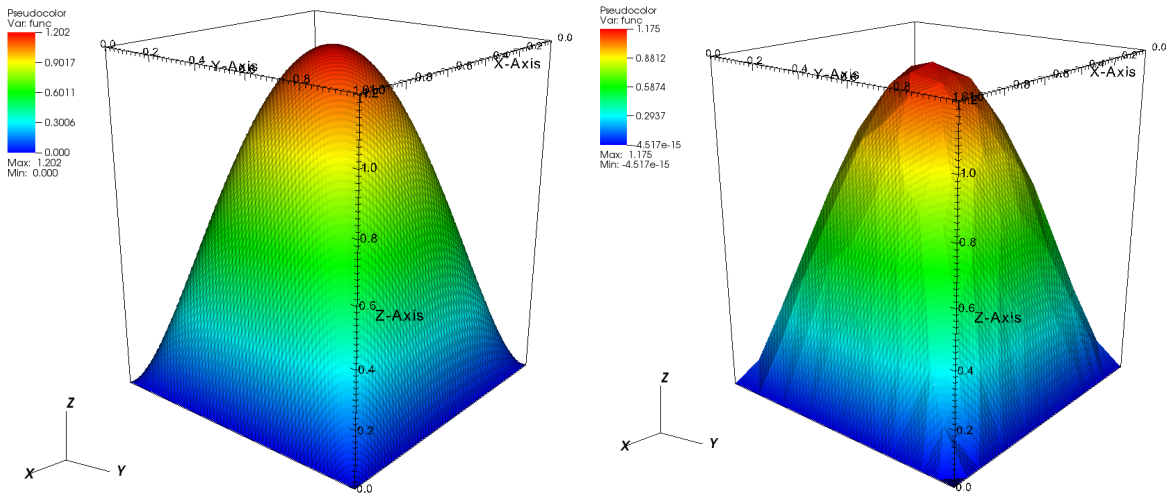

(a) Microscale solution with maximum value 1.202 (b) MsFEM solution with maximum value 1.175

Figure 6.4: Microscale solution and MsFEM solution

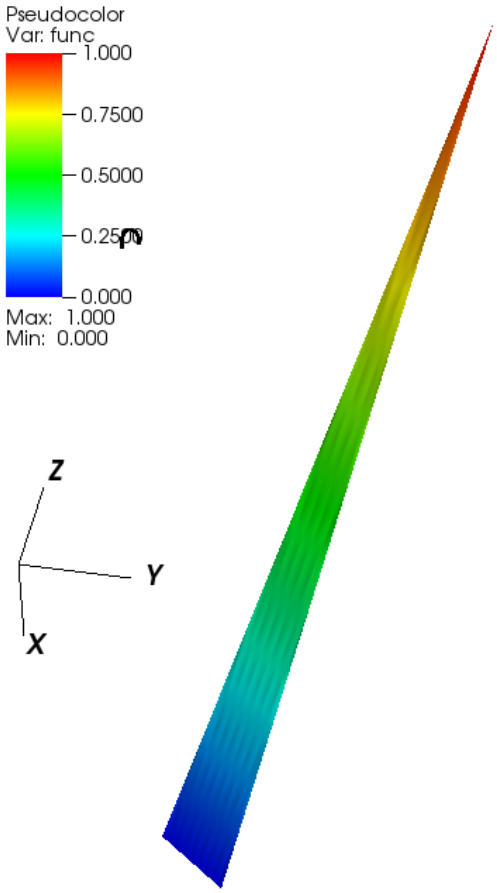

Figure 6.5: Multiscale basis function (Shape function)

Chapter 7

Multiscale Finite Element Method in Perforated Domains

7.1 Introduction

In this chapter we extend the Multiscale Finite Element Method to problems in perforated domains with Neumann boundary condition on the boundary of the perforations, which is a new contribution of the thesis. The necessity for developing a MsFEM for perforated domains originates from the nature of the Li-ion battery model, which cannot be solved by simply applying the standard MsFEM. Therefore, in Section 7.2 we begin with motivation why we need to build up a MsFEM for perforated domains in the context of the considered Li-ion battery model and we lay out the idea of how to solve the battery problem with the MsFEM for domains with holes. In the next sections we systematically build the MsFEM for perforated domains, starting from the simplest case in Section 7.3 where we have zero Neumann boundary condition on the holes. Then we move forward to nonzero linear Neumann in Section 7.4 to finally reach in Section 7.6 nonlinear Neumann boundary conditions on the holes, which are similar to the Butler-Volmer interface conditions in the microscale Li-ion battery model [48]. More specifically, in Section 7.6 we solve a system of parabolic PDEs in a perforated domain with nonlinear Neumann boundary conditions on the holes. We consider different test cases for holes entirely included in the coarse grid finite elements and for holes intersecting the edges and vertices of the macro elements. In all of the experiments we demonstrate numerical convergence of the proposed method with a convergence rate which coincides with either the theoretical one – (6.5.2) or the improved one – (6.5.3) for the standard MsFEM, given in Section 6.5 from the previous chapter. Moreover, we show that the convergence rate is independent of the size and positioning of the perforations. Hence, in this chapter we apply the developed MsFEM in perforated domains for a class of problems which gradually approach the full Li-ion battery model and we verify their convergence numerically. We provide numerical results only in 2D because for the convergence analysis we need to run a series of nested simulations with rapidly increasing number of unknowns, which would be too computationally expensive to do on a desktop machine for 3D problems. Other than that, the numerical algorithm does not depend on the dimension of the problem and can be straightforwardly applied to 3D

problems.

7.2 Lithium-ion battery model and the MsFEM in perforated domains

7.2.1 Setup of the problem

The concentration and the potential are discontinous functions across the solid-electrolyte interface. Therefore, if we straightforwardly apply the standard MsFEM to the Li-ion battery model, we will end up with discontinuous multiscale "basis" functions, which have jumps on the interface between the electrolyte and the solid phase. Therefore our idea is to consider each phase - the electrolyte and the solid, as two separate domains with holes and to apply for each phase the MsFEM adapted to perforated domains. The two perforated domains will be coupled via the nonlinear Butler-Volmer interface conditions (2.5.2). We recall that we employed the same idea in the asymptotic homogenization of the battery model in Chapter 5. To the best of our knowledge, there is very little done in this direction. The only available papers are [12] and [57], and in these papers a zero Dirichlet boundary condition on the holes is considered, whereas for the Li-ion battery model we need to impose nonlinear Neumann conditions for the fluxes across the perforations' boundary.
It is important to note that the concept behind the MsFEM for perforated domains is not to mesh only the connected, non-perforated domain which we obtain after removing the holes. This is expensive and reduces the setup of the problem more or less to its original form. The idea is to mesh the solution domain together with the perforations into coarse blocks, independently of the position of the perforations. This way not only the coarse blocks will contain holes but the perforations may or may not intersect the edges and vertices of the coarse grid finite elements. This means that the coarse grid blocks will be domains with randomly distributed holes. In Figure 7.1 we show a schematic 2D domain, where the blue part represents the electrolyte and the inclusions are the active material. As we can see in the picture, the solution domain is discretized into coarse finite elements K, which contain both electrolyte and solid phase. Figure 7.1 serves only to illustrate the concenpt of two distinct media being present in a single coarse grid finite element. We can think of the solid particles as perforations with the electrolyte being the perforated solution domain. For meaningful simulations of actual batteries the solution domain must be three-dimensional with the electrolyte and the solid phase being connected domains due to the fact that there cannot exist an isolated solid material.

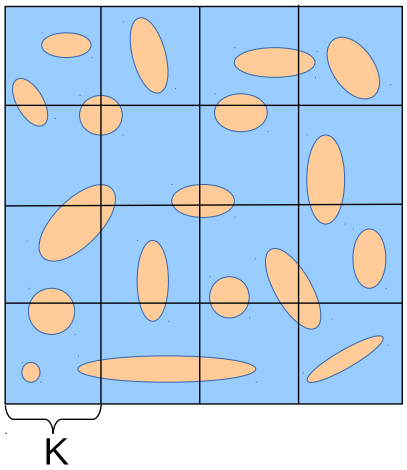

Figure 7.1: Schematic 2D Li-ion battery electrode domain with coarse grid

7.2.2 Idea for solving the Li-ion battery model via the MsFEM for perforated domains

As we discussed in Chapter 5, not all of the variables in the microscale Li-ion battery model [48] are scale-separable. We have scale-separation for the concentration and the potential in the electrolyte, as well as for the potential in the solid and we want to apply the MsFEM only for these quantities. Namely, we want to solve the electrolyte phase equations and the solid phase equation for the potential on the macroscale with the help of the MsFEM. We will then couple these equations to the microscale equation for the concentration in the solid via the Butler-Volmer interface conditions (2.5.2). For this purpose, we have to construct two sets of multiscale basis functions - one for the electrolyte phase and one for the solid phase. The coarse grid will be the same for all upscaled quantities and for both sets of basis functions, but the local problems for constructing the multiscale bases will be posed in different subdomains of the coarse grid finite element K - the solid and the electrolyte subdomain. Another issue is the nonlinear differential operator in the electrolyte PDEs (the coefficients depend on the concentration of Li+ in the electrolyte), which means that we have to recompute the multiscale basis at each time step and at each Newton-Raphson iteration. This is very expensive procedure and we want to avoid it. Our idea is to construct the multiscale basis only once by solving the elliptic part of the PDEs with linearized, time-independent coefficients, and then to reuse it at each time step and each Newton iteration. For example, we can approximate the equation coefficients (2.3.2) with coefficients that depend on the initial concentration $c^e_{initial}$ in the electrolyte, which is a given constant. Another option is to recompute the multiscale basis at chosen time steps. Also, if we use a semi-implicit time scheme to solve the coupled macro-micro problem, we can decouple the solid phase microscale problem for c^s into local problems defined in each coarse finite element K. This domain decomposition of the microscale solid phase problem will allow for a parallel solving.
We can summarize the basic idea for solving the Li-ion battery model with the MsFEM for perforated domains as follows:

- Consider the electrolyte and the solid phase as two separate perforated domains

- Solve the PDEs for the scale-separable quantities on a coarse grid (macroscale) with the MsFEM for perforated domains

- Construct two sets of multiscale basis functions by solving the elliptic part of the electrolyte equations and the solid phase equation for the potential

- Solve the solid phase equation for the concentration c^s on the microscale and couple it to the macroscale equations via the Butler-Volmer interface conditions

- Compute only once the electrolyte phase multiscale basis by solving the elliptic part of the electrolyte PDEs with constant coefficients (take the initial concentration c^e of Li+ in the electrolyte, for example)

- Solve semi-implicit in time the coupled macro-micro problem, so that the microscale solid phase problems for c^s to be solved separately, in parallel, in each coarse grid finite element K

7.3 Zero Neumann boundary condition on the holes

7.3.1 Setup of the problem

We consider the following model boundary value problem in the perforated domain $\Omega_\varepsilon = \Omega \backslash B_\varepsilon$, where $\Omega = [0,1] \times [0,1] \subset \mathbb{R}^2$ and B_ε is the domain of the perforations as shown in Figure 7.2

$$-\nabla \cdot (k_\varepsilon(x) \nabla u_\varepsilon) = f(x), \quad x \in \Omega_\varepsilon, \tag{7.3.1a}$$

$$-k_\varepsilon(x) \nabla u_\varepsilon \cdot \mathbf{n} = 0, \quad x \in \partial B_\varepsilon, \tag{7.3.1b}$$

$$u_\varepsilon(x) = 0, \quad x \in \partial\Omega \backslash \partial B_\varepsilon \tag{7.3.1c}$$

Although in Figure 7.2 the perforations do not intersect the boundary of Ω, we do not exlude such types of domains and we even give numerical results for a domain with perforations on the outer boundary.

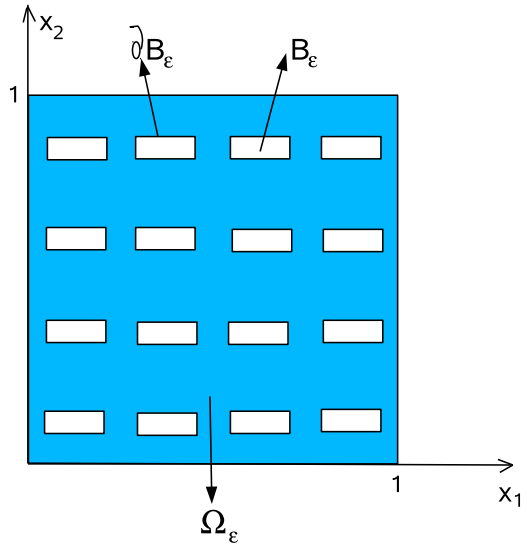

Figure 7.2: Perforated solution domain

7.3.2 Weak formulation of the problem

As standard, we first multiply equation (7.3.1a) by a test function $v(x)$, which vanishes on $\partial\Omega\backslash\partial B_\varepsilon$, and then we integrate over Ω_ε

$$-\int_{\Omega_\varepsilon} \nabla\cdot(k_\varepsilon(x)\nabla u_\varepsilon)\, v(x)\, dx = \int_{\Omega_\varepsilon} f(x)v(x)\, dx \Longleftrightarrow \tag{7.3.2}$$

$$-\int_{\Omega_\varepsilon} \nabla\cdot(v(x)k_\varepsilon(x)\nabla u_\varepsilon)\; dx + \int_{\Omega_\varepsilon} k_\varepsilon(x)\nabla u_\varepsilon\cdot\nabla v\, dx = \int_{\Omega_\varepsilon} f(x)v(x)\, dx \tag{7.3.3}$$

Now we apply the divergence theorem for the first integral on the left hand side and we obtain

$$-\int_{\partial\Omega_\varepsilon} v(x)k_\varepsilon(x)\nabla u_\varepsilon\cdot\mathbf{n}\, ds + \int_{\Omega_\varepsilon} k_\varepsilon(x)\nabla u_\varepsilon\cdot\nabla v\, dx = \int_{\Omega_\varepsilon} f(x)v(x)\, dx \tag{7.3.4}$$

Taking into account that $v(x)=0$ on $\partial\Omega\backslash\partial B_\varepsilon$, we get

$$-\int_{\partial\Omega\backslash\partial B_\varepsilon} \underbrace{v(x)}_{=0} k_\varepsilon(x)\nabla u_\varepsilon\cdot\mathbf{n}\, ds - \int_{\partial B_\varepsilon} v(x)k_\varepsilon(x)\nabla u_\varepsilon\cdot\mathbf{n}\, ds + \int_{\Omega_\varepsilon} k_\varepsilon(x)\nabla u_\varepsilon\cdot\nabla v\, dx = \int_{\Omega_\varepsilon} f(x)v(x)\, dx \tag{7.3.5}$$

which is equivalent to

$$-\int_{\partial B_\varepsilon} v(x)\underbrace{k_\varepsilon(x)\nabla u_\varepsilon\cdot\mathbf{n}}_{=0}\, ds + \int_{\Omega_\varepsilon} k_\varepsilon(x)\nabla u_\varepsilon\cdot\nabla v\, dx = \int_{\Omega_\varepsilon} f(x)v(x)\, dx \tag{7.3.6}$$

Finally, the weak form of the problem reads: find $u_\varepsilon \in H_0^1(\Omega_\varepsilon) = \left\{ u_\varepsilon \in L_2(\Omega_\varepsilon), \quad \dfrac{\partial u_\varepsilon}{\partial x_i} \in L_2(\Omega_\varepsilon), \quad u_\varepsilon(x)|_{\partial\Omega\setminus\partial B_\varepsilon} = 0 \right\}$, so that the following integral equality is true for all $v \in H_0^1(\Omega_\varepsilon)$

$$\int\limits_{\Omega_\varepsilon} k_\varepsilon(x)\nabla u_\varepsilon \cdot \nabla v \, dx = \int\limits_{\Omega_\varepsilon} f(x)v(x) \, dx \tag{7.3.7}$$

The weak form, restricted to a finite dimensional approximation space $V^H \subset H_0^1(\Omega_\varepsilon)$, is: find $u_\varepsilon^H \in V^H$, so that the following integral equality is true for all $v^H \in V^H$

$$\int\limits_{\Omega_\varepsilon} k_\varepsilon(x)\nabla u_\varepsilon^H \cdot \nabla v^H \, dx = \int\limits_{\Omega_\varepsilon} f(x)v^H \, dx, \quad \forall v^H \in V^H \tag{7.3.8}$$

Due to the zero Neumann boundary condition (7.3.1b), the latter weak form is the same as the weak form (6.2.5) that we obtain in the standard case for non-perforated domains from the previous chapter. Therefore, we do not go into more details here. The only difference with the model problem (6.2.1) is that here we test with specially constructed multiscale basis functions for perforated domains, which we show in the next Section 7.3.3.

7.3.3 Construction of the multiscale basis functions

Let $\Omega_\varepsilon = \bigcup\limits_{K\in\mathcal{T}_H} K$, where $\mathcal{T}_H$ is a partition of the perforated domain Ω_ε into ***perforated finite elements*** K as shown in Figure 7.3. This perforated element does not violate the definition of a finite element, because its domain is a bounded closed set with nonempty interior and piecewise smooth boundary (for reference see [9]). We denote with B the domain of the perforation inside the finite element K, and with ∂B - its boundary. In Figure 7.3(a) with "$\bullet$" we indicate the vertices of the square $\hat{K} = K \cup B$, where the nodal values are calculated. We denote with N the number of all these vertices in the mesh of coarse finite elements K. Hence, it is clear that $dim(V^H) = N$. Then, the multiscale basis functions ϕ_i^M are solutions to the following local problems, which we solve for each coarse finite element $K \in \mathcal{T}_H$, such that $K \in supp\{\phi_i^M(x)\}$, and for all $i = 1, 2, \ldots, N = dim(V^H)$

$$-\nabla \cdot \left(k_\varepsilon(x)\nabla\phi_i^M\right) = 0, \quad x \in K, \tag{7.3.9a}$$

$$-k_\varepsilon(x)\nabla\phi_i^M \cdot \mathbf{n} = 0, \quad x \in \partial B \tag{7.3.9b}$$

$$\phi_i^M(x) = \phi_i^L(x), \quad x \in \partial K\setminus\partial B \tag{7.3.9c}$$

where, as before, $\{\phi_i^L(x)\}_{i=1}^N$ is the standard piecewise linear basis. We note that, since the problem which we consider is with Neumann data on the holes, we also impose Neumann boundary conditions (7.3.9b) in the local problems (7.3.9). If in (7.3.9), for example, we impose Dirichlet boundary conditions on the perforations, we will fix the solution on the holes in contrast to problem (7.3.1). Therefore, the most reasonable choice of boundary conditions for the local problems is Neumann since this is the nature of the problem we

solve. In Figure 7.4 we show how perforated multiscale basis functions with 9 holes look like.

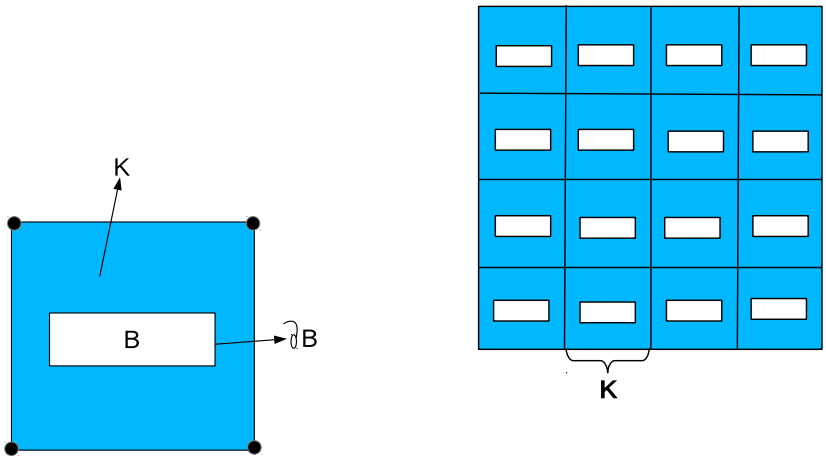

(a) A single perforated coarse grid finite element

(b) Coarse grid finite element discretization

Figure 7.3: Perforated coarse block and discretized solution domain

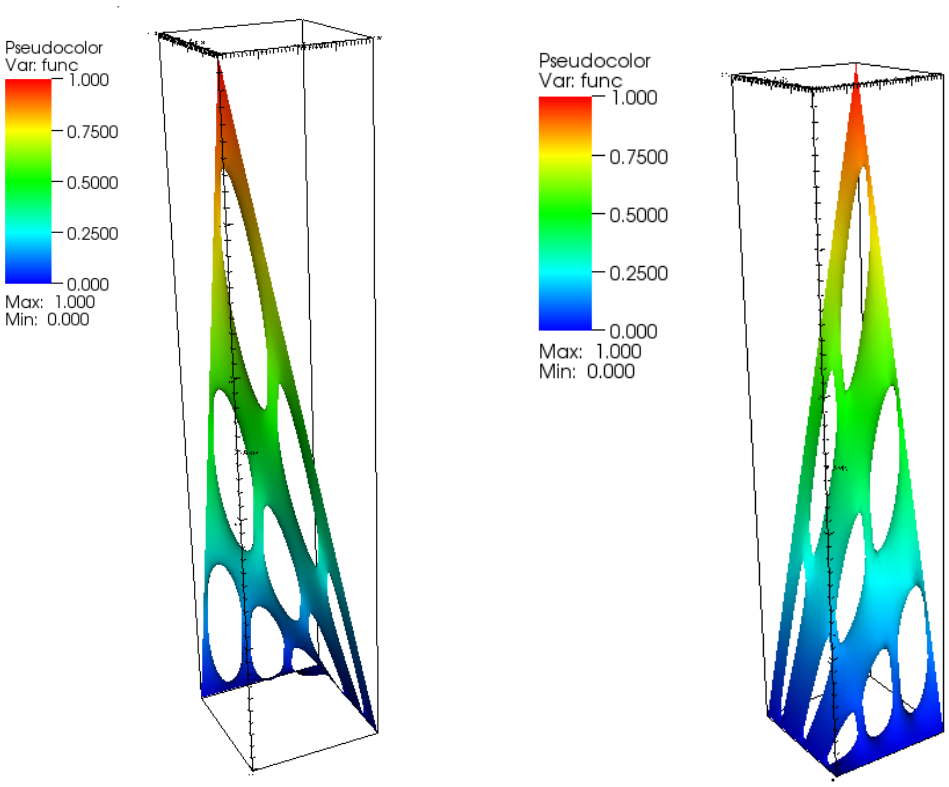

(a) MsFEM Basis Function

(b) MsFEM Basis Function

Figure 7.4: Multiscale shape function

7.4 Nonzero Neumann boundary condition on the holes

7.4.1 Setup of the problem

We solve the following model problem in the perforated domain $\Omega_\varepsilon = \Omega \backslash B_\varepsilon$, where $\Omega = [0,1] \times [0,1]$ and B_ε is the domain of the perforations

$$-\nabla \cdot (k_\varepsilon(x) \nabla u_\varepsilon) = f(x), \quad x \in \Omega_\varepsilon \subset \mathbb{R}^2, \tag{7.4.1a}$$

$$-k_\varepsilon(x) \nabla u_\varepsilon \cdot \mathbf{n} = \varepsilon g(x), \quad x \in \partial B_\varepsilon, \tag{7.4.1b}$$

$$u_\varepsilon(x) = 0, \quad x \in \partial\Omega \backslash \partial B_\varepsilon \tag{7.4.1c}$$

In order to conduct a rigorous numerical investigation of the convergence of the method when $\varepsilon \to 0$, we need to properly scale the flux across the perforations' boundary. Here we employ the same considerations as in the asymptotic homogenization method for perforated domains that we discussed in Chapter 4. Namely, we require that the total flux across ∂B_ε is conserved, so that we converge to some limit solution u_0 when $\varepsilon \to 0$. In Chapter 4 we showed rigorously that if we do not scale with ε the flux across the boundary of the perforations, the total flux across the holes blows up when $\varepsilon \to 0$. Therefore, the Neumann boundary condition (7.4.1b) is scaled with the small parameter ε.

7.4.2 Weak formulation of the problem

Again, as in the zero Neumann case, we first multiply equation (7.4.1a) by a test function $v(x)$, which vanishes on $\partial\Omega \backslash \partial B_\varepsilon$, and then we integrate over Ω_ε

$$-\int_{\Omega_\varepsilon} \nabla \cdot (k_\varepsilon(x) \nabla u_\varepsilon)\, v(x)\, dx = \int_{\Omega_\varepsilon} f(x) v(x)\, dx \iff \tag{7.4.2}$$

$$-\int_{\Omega_\varepsilon} \nabla \cdot (v(x) k_\varepsilon(x) \nabla u_\varepsilon)\, dx + \int_{\Omega_\varepsilon} k_\varepsilon(x) \nabla u_\varepsilon \cdot \nabla v\, dx = \int_{\Omega_\varepsilon} f(x) v(x)\, dx \tag{7.4.3}$$

Now we apply the divergence theorem for the first integral on the left hand side and we obtain

$$-\int_{\partial\Omega_\varepsilon} v(x) k_\varepsilon(x) \nabla u_\varepsilon \cdot \mathbf{n}\, ds + \int_{\Omega_\varepsilon} k_\varepsilon(x) \nabla u_\varepsilon \cdot \nabla v\, dx = \int_{\Omega_\varepsilon} f(x) v(x)\, dx \tag{7.4.4}$$

Taking into account that $v(x) = 0$ on $\partial\Omega \backslash \partial B_\varepsilon$, we get

$$-\int_{\partial\Omega \backslash \partial B_\varepsilon} \underbrace{v(x)}_{=0} k_\varepsilon(x) \nabla u_\varepsilon \cdot \mathbf{n}\, ds - \int_{\partial B_\varepsilon} v(x) k_\varepsilon(x) \nabla u_\varepsilon \cdot \mathbf{n}\, ds + \int_{\Omega_\varepsilon} k_\varepsilon(x) \nabla u_\varepsilon \cdot \nabla v\, dx = \int_{\Omega_\varepsilon} f(x) v(x)\, dx \tag{7.4.5}$$

which is equivalent to

$$-\int_{\partial B_\varepsilon} v(x)\underbrace{k_\varepsilon(x)\nabla u_\varepsilon\cdot\mathbf{n}}_{=-\varepsilon g(x)}\,ds+\int_{\Omega_\varepsilon}k_\varepsilon(x)\nabla u_\varepsilon\cdot\nabla v\,dx=\int_{\Omega_\varepsilon}f(x)v(x)\,dx\Longleftrightarrow \tag{7.4.6}$$

$$\int_{\partial B_\varepsilon}\varepsilon g(x)v(x)\,ds+\int_{\Omega_\varepsilon}k_\varepsilon(x)\nabla u_\varepsilon\cdot\nabla v\,dx=\int_{\Omega_\varepsilon}f(x)v(x)\,dx \tag{7.4.7}$$

Finally, the weak form of the problem reads: find $u_\varepsilon\in H_0^1(\Omega_\varepsilon)=\left\{u_\varepsilon\in L_2(\Omega_\varepsilon),\quad \dfrac{\partial u_\varepsilon}{\partial x_i}\in L_2(\Omega_\varepsilon),\quad u_\varepsilon(x)|_{\partial\Omega\setminus\partial B_\varepsilon}=0\right\}$, so that the following integral equality is true for all $v\in H_0^1(\Omega_\varepsilon)$

$$\int_{\Omega_\varepsilon}k_\varepsilon(x)\nabla u_\varepsilon\cdot\nabla v\,dx+\int_{\partial B_\varepsilon}\varepsilon g(x)v(x)\,ds=\int_{\Omega_\varepsilon}f(x)v(x)\,dx \tag{7.4.8}$$

The weak form, restricted to a finite dimensional approximation space is: find $u_\varepsilon^H\in V^H\subset H_0^1(\Omega_\varepsilon)$, so that the following integral equality is true for all $v^H\in V^H$

$$\int_{\Omega_\varepsilon}k_\varepsilon(x)\nabla u_\varepsilon^H\cdot\nabla v^H\,dx+\int_{\partial B_\varepsilon}\varepsilon g(x)v^H\,ds=\int_{\Omega_\varepsilon}f(x)v^H\,dx,\quad\forall v^H\in V^H \tag{7.4.9}$$

Now we take $v^H=\phi_j^M(x)$, for all $j=1,2,\ldots,N$, we expand the function with respect to the multiscale basis $u_\varepsilon^H=\sum_{i=1}^N U_i\phi_i^M(x)$, and we obtain the following system of algebraic equations

$$\int_{\Omega_\varepsilon}k_\varepsilon(x)\sum_{i=1}^N U_i\nabla\phi_i^M\cdot\nabla\phi_j^M\,dx=\int_{\Omega_\varepsilon}f(x)\phi_j^M(x)\,dx-\int_{\partial B_\varepsilon}\varepsilon g(x)\phi_j^M(x)\,ds,\quad\forall j=1,N \tag{7.4.10}$$

which is equivalent to

$$\mathbf{AU}=\mathbf{F} \tag{7.4.11}$$

where $\mathbf{A}=(a_{ij})_{i,j=1}^N$ is the stiffness matrix, $\mathbf{U}=(U_1,U_2,\ldots,U_N)^T$ is the solution vector and $\mathbf{F}=(F_1,F_2,\ldots,F_N)^T$ is the right-hand side. As in the zero Neumann case, let $\Omega_\varepsilon=\bigcup_{K\in\mathcal{T}_H}K$, where $\mathcal{T}_H$ is the partition of the perforated domain Ω_ε into perforated finite elements K as shown in Figure 7.3. Let also τ_h^K be the partition of each macro finite element K into triangular finite elements e, i.e., $K=\bigcup_{e\in\tau_h^K}e$. We denote with e_Γ the following set of fine elements $e\in\tau_h^K$

$$e_\Gamma=\left\{e\in\tau_h^K:e\quad has\quad an\quad edge\quad\mathcal{E}_\Gamma\in\partial B\right\} \tag{7.4.12}$$

Consequently, the elements of the stiffness matrix $\mathbf{A}$ are given by

$$a_{ij} = \sum_{K\in\mathcal{T}_H} \int\limits_K k_\varepsilon(x)\nabla\phi_i^M \cdot \nabla\phi_j^M \, dx =$$

$$= \sum_{K\in\mathcal{T}_H} \left(\sum_{e\in\tau_h^K} \int\limits_e k_\varepsilon(x)\nabla \left(\phi_i^M\right)^h \cdot \nabla \left(\phi_j^M\right)^h \, dx \right) \tag{7.4.13}$$

and the right-hand side elements are

$$F_j = \int\limits_{\Omega_\varepsilon} f(x)\phi_j^M(x)\, dx - \int\limits_{\partial B_\varepsilon} \varepsilon g(x)\phi_j^M(x)\, ds =$$

$$= \sum_{K\in\mathcal{T}_H} \int\limits_K f(x)\phi_j^M(x)\, dx - \sum_{K\in\mathcal{T}_H} \int\limits_{\partial B^K} \varepsilon g(x)\phi_j^M(x)\, ds =$$

$$= \sum_{K\in\mathcal{T}_H} \left(\sum_{e\in\tau_h^K} \int\limits_e f(x) \left(\phi_j^M\right)^h \, dx \right) - \sum_{K\in\mathcal{T}_H} \left(\sum_{e_\Gamma\in\tau_h^K} \int\limits_{\mathcal{E}_\Gamma} \varepsilon g(x) \left(\phi_j^M\right)^h \, ds \right) \tag{7.4.14}$$

for $i, j = 1, 2, \ldots, N$ and we use the notation ∂B^K for the perforations' boundary in the coarse element K. As we have already mentioned, because we compute numerically the multiscale basis functions, we need to integrate on the fine mesh in order to calculate the stiffness matrix and the right-hand side. Therefore, calculating the integral over the perforations' boundary ∂B_ε in (7.4.14) does not require additional computational effort, except for identifying the edges of the fine elements which belong to ∂B_ε.

7.4.3 Construction of the multiscale basis functions

We construct the multiscale basis functions in the following way. For each coarse grid finite element $K \in \mathcal{T}_H$ and for all $i = 1, 2, \ldots, N = dim(V_H)$, $V_H \subset H_0^1(\Omega)$, the basis functions ϕ_i^M are solutions to the following local problems

$$-\nabla \cdot \left(k_\varepsilon(x)\nabla\phi_i^M\right) = 0, \quad x \in K, \forall K \in \mathcal{T}_H, such \quad that \quad K \in supp\left(\phi_i(x)\right), \tag{7.4.15a}$$

$$-k_\varepsilon(x)\nabla\phi_i^M \cdot \mathbf{n} = 0, \quad x \in \partial B \tag{7.4.15b}$$

$$\phi_i^M(x) = \phi_i^L(x), \quad x \in \partial K \backslash \partial B \tag{7.4.15c}$$

where $\{\phi_i^L(x)\}_{i=1}^N$ is the standard piecewise linear basis. This way we account naturally for the Neumann data in the global weak formulation (7.4.9) of the problem and in the construction of the multiscale basis functions we impose zero Neumann boundary condition on the holes. In Section 7.5.3 we show numerical results for the L^2 norm of the error and we obtain a good convergence rate, which is in accordance with the theoretical one for

the standard MsFEM. It is well known that the standard linear basis $\{\phi_i^L(x)\}_{i=1}^N$ forms a partition of unity. We will show that the multiscale basis $\{\phi_i^M(x)\}_{i=1}^N$, constructed by solving (7.4.15), also forms a partition of unity. For completeness, here we give a definition for partition of unity.

Definition 14 (Partition of Unity)**.** Let X be a topological space, $\mathbf{U} = \{U_1, U_2, \ldots, U_n\}$ a finite open cover of X. A partition of unity, subordinated to $\mathbf{U}$, is a family of functions $\eta_i : X \longrightarrow [0,1]$ satisfying: $\eta_1 + \eta_2 + \ldots + \eta_n = 1$, $supp\,(\eta_i) \subset U_i$. Given $\mathcal{A} \subset C(X)$, we say that $\{\eta_i\}$ is an $\mathcal{A}$ - partiton of unity if $\eta_i \in \mathcal{A}$ for all i. $\mathcal{A}$ is a set of continuous functions $C(X) = C(X, \mathbb{R}) = \{f : X \longrightarrow \mathbb{R} : f \quad is \quad continuous\}$.

Now, if we assume that we can impose some nonzero Neumann boundary condition on ∂B in (7.4.15), we obtain the following local problems for the multiscale basis functions for all $i = 1, 2, \ldots, N$

$$-\nabla \cdot (k_\varepsilon(x)\nabla\phi_i) = 0, \quad x \in K, \forall K \in \mathcal{T}_H, such \quad that \quad K \in supp\,(\phi_i(x)) \tag{7.4.16a}$$

$$-k_\varepsilon(x)\nabla\phi_i \cdot \mathbf{n} = G(x), \quad x \in \partial B \tag{7.4.16b}$$

$$\phi_i(x) = \phi_i^L(x), \quad x \in \partial K \backslash \partial B \tag{7.4.16c}$$

where for convenience we omit the superscript "M" in the basis functions. Let us consider a single coarse grid finite element $K \in \mathcal{T}_H$ and the corresponding multiscale basis functions $\phi_1^K(x)$, $\phi_2^K(x)$, $\phi_3^K(x)$ and $\phi_4^K(x)$, whose supports contain the finite element K. In our case the coarse element K is a perforated square (a multiply connected open bounded domain). Each function $\phi_l^K(x)$, for $l = 1, 2, 3, 4$, satisfies problem (7.4.16) in K

$$-\nabla \cdot \left(k_\varepsilon(x)\nabla\phi_l^K\right) = 0, \quad x \in K, \tag{7.4.17a}$$

$$-k_\varepsilon(x)\nabla\phi_l^K \cdot \mathbf{n} = G(x), \quad x \in \partial B \tag{7.4.17b}$$

$$\phi_l^K(x) = \phi_i^L(x), \quad x \in \partial K \backslash \partial B \tag{7.4.17c}$$

and since the differential operator in (7.4.16a) is linear, we can sum up the four differential equations for $\phi_1^K(x)$, $\phi_2^K(x)$, $\phi_3^K(x)$ and $\phi_4^K(x)$ to obtain

$$-\nabla \cdot \left(k_\varepsilon(x)\left(\nabla\phi_1^K + \nabla\phi_2^K + \nabla\phi_3^K + \nabla\phi_4^K\right)\right) = 0 \tag{7.4.18}$$

We denote

$$\Phi_K(x) = \phi_1^K(x) + \phi_2^K(x) + \phi_3^K(x) + \phi_4^K(x) \tag{7.4.19}$$

and consequently we obtain

$$-\nabla \cdot (k_\varepsilon(x)\nabla\Phi_K) = 0 \tag{7.4.20}$$

If $G(x) = 0$ for $x \in \partial B$, it follows that we have the following Neumann boundary condition for the function $\Phi_K(x)$ on the perforations' boundary ∂B

$$-k_\varepsilon(x)\nabla\Phi_K \cdot \mathbf{n} = \underbrace{4G(x)}_{} = 0, \quad x \in \partial B \tag{7.4.21}$$

On the edges of the finite element K the function Φ_K satisfies the following Dirichlet boundary condition

$$\Phi_K(x) = \sum_{i=1}^{4} \phi_i^L(x) = 1, \quad x \in \partial K \tag{7.4.22}$$

because we know that for the standard linear basis functions $\phi_i^L(x)$, $i = 1, 2, 3, 4$, we have that $\sum_{i=1}^{4} \phi_i^L(x) = 1, \quad \forall x \in \partial K$.
Thus, in the case of $G(x) = 0$, we obtain the following boundary value problem

$$-\nabla \cdot (k_\varepsilon(x)\nabla\Phi_K) = 0, \quad x \in K, \tag{7.4.23a}$$
$$-k_\varepsilon(x)\nabla\Phi_K \cdot \mathbf{n} = 0, \quad x \in \partial B, \tag{7.4.23b}$$
$$\Phi_K(x) = 1, \quad x \in \partial K \backslash \partial B \tag{7.4.23c}$$

It is obvious that $\Phi_K(x) \equiv 1$ satisfies the partial differential equation (7.4.23a) and since problem (7.4.23) has an unique solution, see [29], it follows that $\Phi_K(x) \equiv 1$ is the unique solution to (7.4.23). This means that $\Phi_K(x) = 1, \quad \forall x \in \bar{K} = K \cup \partial K$, which is equivalent to

$$\phi_1^K(x) + \phi_2^K(x) + \phi_3^K(x) + \phi_4^K(x) = 1, \quad \forall x \in \bar{K}, \tag{7.4.24}$$

Since each multiscale basis function $\phi_i(x)$ has a compact support $supp\,(\phi_i(x)) \subset \Omega_\varepsilon$, then

$$\sum_{i=1}^{N} \phi_i(x) = 1, \quad \forall x \in \Omega_\varepsilon \tag{7.4.25}$$

and also

$$0 \leq \phi_i(x) \leq 1, \quad \forall x \in \Omega_\varepsilon \tag{7.4.26}$$

Consequently the multiscale basis functions form a partition of unity in Ω_ε.
Remark: We showed that the multiscale basis $\{\phi_i^M(x)\}_{i=1}^N$ forms a partition of unity only when $G(x) = 0$, i.e., when we impose zero Neumann boundary condition on the holes in the local problems (7.4.15). Hence, the constructed multiscale basis is a partition of unity.

7.5 Numerical results

7.5.1 Setup of the experiments and numerical methods

We solve problem (7.3.1) in the perforated unit square domain. We take $k_\varepsilon(x)$ to be a constant. We do not consider the case when k_ε depends on x and is a highly oscillating function because we are interested only in oscillations coming from the perforations, which is also the case in the Li-ion battery model where the oscillations come from the geometry. In order to conduct a consistent numerical analysis of the convergence, we need to decrease

uniformly H and ε. Therefore, we consider solution domains with periodically arranged identical holes, but the method is not restricted to periodic media. The coarse grid size H and the small parameter ε indicate the number of coarse finite elements and the size of the periodic microstructures, respectively. In our case $\left(\frac{1}{H}\right)^2$ is the number of coarse elements and $\left(\frac{1}{\varepsilon}\right)^2$ is the number of holes in the solution domain Ω_ε.

In all of the following numerical experiments, with N_{micro} we denote the number of finite elements that we use to obtain the reference microscale solution, and with n we denote the number of finite elements per single coarse grid element in the MsFEM formulation of the problem. We run the experiments with $N_{micro} \approx n\left(\frac{1}{H}\right)^2$, i.e., the total number of fine mesh elements in all of the coarse elements is equal to the number of finite elements in the microscale simulation.

The coarse grid consists of finite elements which are perforated squares and we run numerical simulations with different number of holes per coarse element. Exemplary geometries of the coarse grid elements are given in Figure 7.5. In Figure 7.5(a) and Figure 7.5(b) we show a coarse element with smaller and bigger holes, respectively, on the edges and vertices, and in Figure 7.5(c) are shown elements with 4 holes, which are entirely included in the macro element. More specifically, in Figure 7.6 and Figure 7.7 is given the geometry of the perforated coarse grid block for different number of holes per coarse element in the case when the holes intersect the edges and vertices of the macro element. Since in our numerical experiments we decrease uniformly H and ε, in order to have consistent perforated geometries when the perforations are on the edges of the element, we define the case $H = \varepsilon$ as shown in Figure 7.6(a). Then, for $H > \varepsilon$ we construct accordingly the perforated coarse finite elements with holes on the edges.

We solve the local problems (7.3.9) using the Finite Element Method with linear Lagrange triangular elements and we use Triangle [67] to generate the mesh. For the numerical integration we use a Gaussian quadrature rule. The linear solver that we use is iterative. More specifically, we use the preconditioned Stabilized Biconjugate Gradient Method. We show numerical results for the L^2 norm and the L^∞ norm. We recall that for the standard MsFEM , the following L^2 error estimate holds:

$$\|u_\varepsilon - u_\varepsilon^H\|_{L^2(\Omega)} \leq C_1 H^2 \|f\|_{L^2(\Omega)} + C_2 \varepsilon^{\frac{1}{2}} H^{-\frac{1}{2}} \tag{7.5.1}$$

We should keep in mind that estimate (7.5.1) is not sharp and when we analyze the numerical results we must take into account also the improved estimate

$$\|u_\varepsilon - u_\varepsilon^H\|_{L^2(\Omega)} \leq C_1 H^2 \|f\|_{L^2(\Omega)} + C_2 \varepsilon H^{-1} + C_3 \varepsilon \tag{7.5.2}$$

which is not rigorously proven. In all of the test cases that we consider we show numerically that the solution obtained with the MsFEM for perforated domains converges to the reference microscale solution with a convergence rate which coincides with either the theoretical one (7.5.1) or the improved one (7.5.2).

The numerical experiments are organized as follows. We begin with numerical results for zero Neumann boundary conditions on the holes in Section 7.5.2. First we consider

test cases for holes entirely included in the coarse grid finite elements. Then we show numerical results for smaller and bigger perforations which intersect the edges and vertices of the macro elements. In both scenarios for the positioning of the holes we run numerical simulations for fixed H and varying ε and then for fixed ε, and varying H. We show numerical results for different size and distribution of the perforations in order to test if the convergence of the method depends on these factors. As we will see, it turns out that the size and arrangement of the holes do not affect the convergence rate.
In Section 7.5.3 we show numerical convergence of the proposed method in the case when we have nonzero Neumann boundary conditions on the perforations. This section is also divided into two subsections – holes entirely included in the macro finite elements and holes intersecting the edges and vertices of the coarse elements. Again, as in Section 7.5.2, we test the convergence of the numerical algorithm by fixing H and decreasing ε, and vice versa. In Section 7.5.2 for the test case with holes entirely included in the coarse elements, we give examples for different values of H fixed in order to illustrate the behaviour of the MsFEM also for big values of H. In the subsequent numerical experiments we consider only the value $\frac{1}{16}$ for H fixed and $\frac{1}{128}$ for ε fixed.
In both Section 7.5.2 and Section 7.5.3 we give only a few figures with comparison between the microscale reference solutions and the solutions computed with the MsFEM for perforated domains. A complete list with pictures from all of the numerical simulations is given in the appendix.

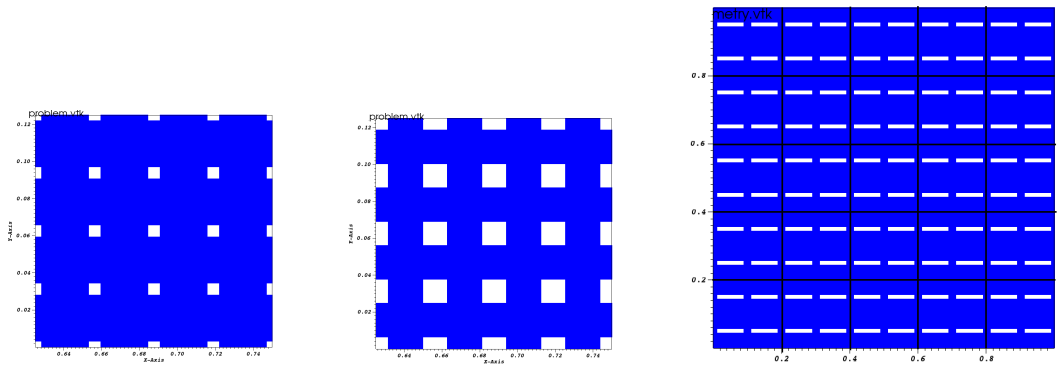

(a) Coarse element with holes on the edges and vertices

(b) Coarse element with bigger holes on the edges and vertices

(c) Coarse elements with 4 holes entirely included in the element

Figure 7.5: Perforated coarse grid finite elements

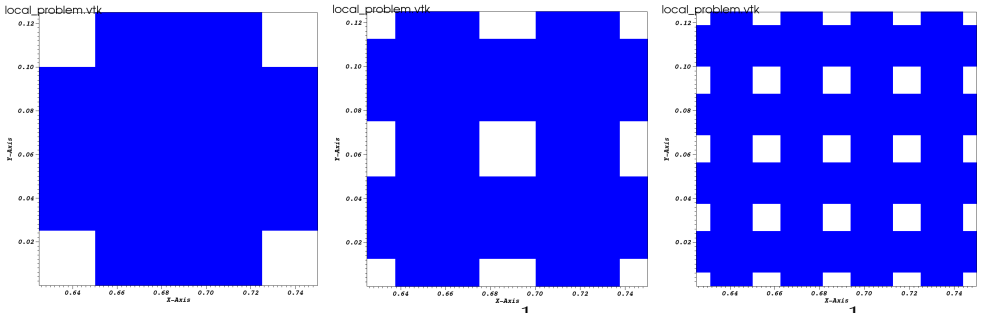

(a) $H = \varepsilon$ (b) $\varepsilon = \frac{1}{2}H$ (c) $\varepsilon = \frac{1}{4}H$

Figure 7.6: Coarse grid blocks with different number of perforations per block

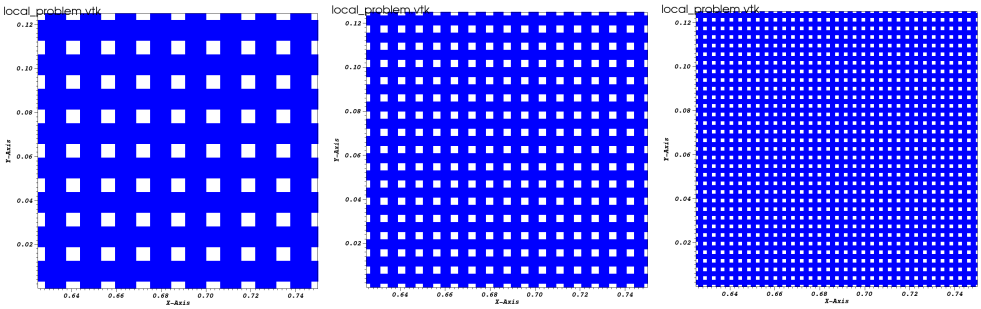

(a) $\varepsilon = \frac{1}{8}H$ (b) $\varepsilon = \frac{1}{16}H$ (c) $\varepsilon = \frac{1}{32}H$

Figure 7.7: Coarse grid blocks with different number of perforations per block

7.5.2 Zero Neumann boundary condition on the holes

Numerical results for holes entirely included in the coarse grid finite elements

Here we take the coefficient to be $k_\varepsilon(x) = 5$ and the right-hand side is $f(x) = 16$.

- **Fixed $H = \frac{1}{4}$ and decreasing ε**

  In this experiment we have only $4 \times 4 = 16$ coarse grid blocks with different number of holes per block. More specifically, we start with 1 hole per element, then we have $2^2 = 4$, $4^2 = 16$ and finally $8^2 = 64$ holes per block. As we can see from the results in Table 7.5.1, since the coarse grid size H is very big, the term $C_1 H^2 \|f\|_{L^2(\Omega)}$ in (7.5.1) dominates the error, and therefore the convergence rate that we obtain is very far from the theoretical one, which is 0.5. We show the microscale reference solution and the MsFEM one for $\varepsilon = \frac{1}{16}$ in Figure 7.8. The results of the rest of the experiments are illustrated in Figures A.1, A.2, and A.4.

Table 7.5.1: Fixed $H = \frac{1}{4}$ and decreasing ε

ε	N_{micro}	n	$\|u_\varepsilon - u_\varepsilon^H\|_{L^2(\Omega)}$	Rate	$\|u_\varepsilon - u_\varepsilon^H\|_\infty$	Rate
$\varepsilon = \frac{1}{4}$	14547	906	0.0696443	-	0.1595	-
$\varepsilon = \frac{1}{8}$	58074	3623	0.0845571	-0.28	0.1902	-0.25
$\varepsilon = \frac{1}{16}$	227727	14209	0.0827109	0.031	0.1689	0.17
$\varepsilon = \frac{1}{32}$	932586	58074	0.0808739	0.032	0.1659	0.026

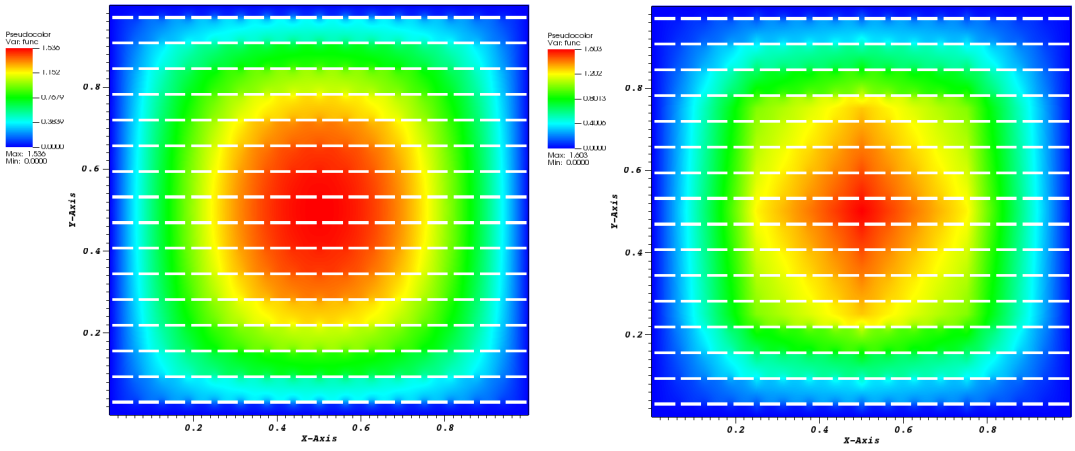

(a) Microscale solution with maximum=1.536 (b) MsFEM solution with maximum=1.603

Figure 7.8: Comparison between the microscale and the MsFEM solution for $\varepsilon = \frac{1}{16}$

- **Fixed $H = \frac{1}{8}$ and decreasing ε**

  In this test case, H is smaller and, as we can see from Table 7.5.2, we have an improvement in the convergence rate, compared to the case when we had $H = \frac{1}{4}$. Nevertheless, H is still not small enough and it seems that the H^2 term again dominates the error. Here we demonstrate the reference microscale solution and the MsFEM one only for $\varepsilon = \frac{1}{32}$ in Figure 7.9. The remaining simulations are shown in Figures A.5, A.6, and A.8.

Table 7.5.2: Fixed $H = \frac{1}{8}$ and decreasing ε

ε	N_{micro}	n	$\|u_\varepsilon - u_\varepsilon^H\|_{L^2(\Omega)}$	Rate	$\|u_\varepsilon - u_\varepsilon^H\|_\infty$	Rate
$\varepsilon = \frac{1}{8}$	32156	497	0.0365996	-	0.1036	-
$\varepsilon = \frac{1}{16}$	126517	1858	0.0304484	0.27	0.08003	0.37
$\varepsilon = \frac{1}{32}$	517806	7985	0.0250537	0.28	0.06463	0.31
$\varepsilon = \frac{1}{64}$	2072411	32156	0.0224074	0.16	0.05392	0.26

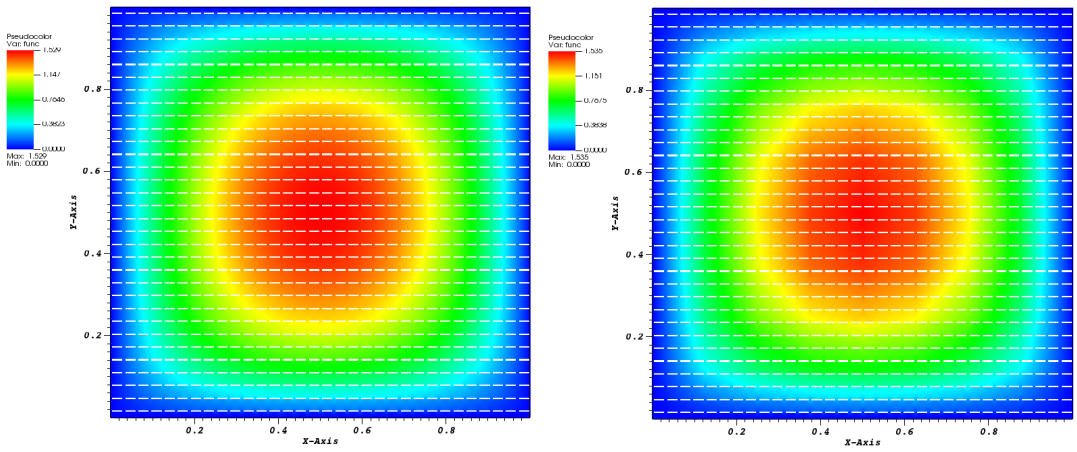

(a) Microscale solution with maximum=1.529 (b) MsFEM solution with maximum=1.535

Figure 7.9: Comparison between the microscale and the MsFEM solution for $\varepsilon = \frac{1}{32}$

- **Fixed $H = \frac{1}{16}$ and decreasing ε**

  Here we have $16^2 = 256$ coarse grid blocks with varying number of holes per block. We start with 1 hole per macro element and we reach $8^2 = 64$ holes per block in the last experiment. In this test case we start with sufficiently small H so that the $O(H^2)$ term in (7.5.1) does not dominate the error initially. Moreover, the results from Table 7.5.3 show a convergence rate, which is even better than the theoretical one (6.5.2) and approaching the improved one (6.5.3). We also observe that when ε becomes very small, which means that the $\sqrt{\frac{\varepsilon}{H}}$ term is getting very small, the convergence rate starts to decline. This phenomenon is most likely due to the fact that the H^2 term becomes dominant for very small values of ε. In Figure 7.10 we show the comparison between the microscale and the MsFEM solution for $\varepsilon = \frac{1}{128}$. The rest of the numerical experiments are given in Figure A.9, A.10, and A.11.

Table 7.5.3: Fixed $H = \dfrac{1}{16}$ and decreasing ε

ε	N_{micro}	n	$\|u_\varepsilon - u_\varepsilon^H\|_{L^2(\Omega)}$	Rate	$\|u_\varepsilon - u_\varepsilon^H\|_\infty$	Rate
$\varepsilon = \dfrac{1}{16}$	131806	500	0.0284502	-	0.05975	-
$\varepsilon = \dfrac{1}{32}$	517806	2003	0.0173716	0.71	0.03544	0.75
$\varepsilon = \dfrac{1}{64}$	2072411	7985	0.0110185	0.66	0.02425	0.55
$\varepsilon = \dfrac{1}{128}$	7279206	28257	0.00781583	0.5	0.01840	0.4

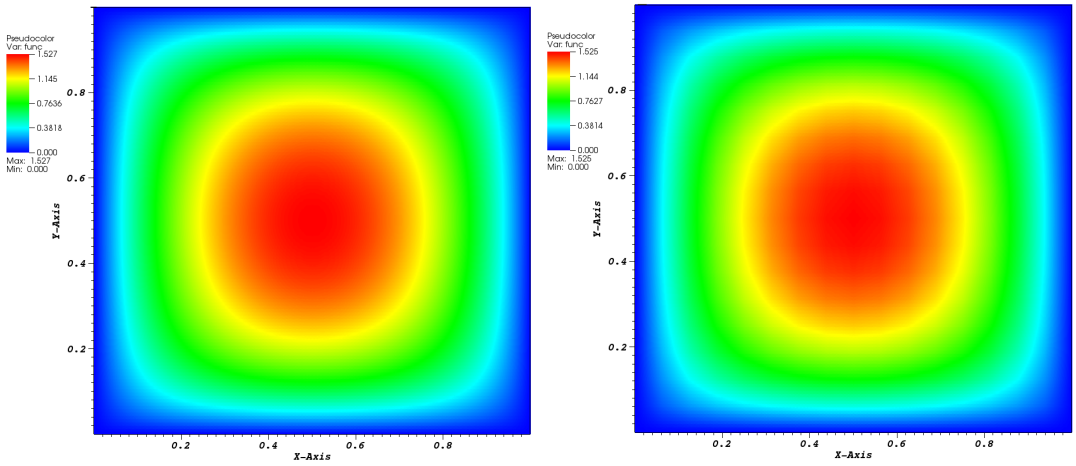

(a) Microscale solution with maximum=1.527 (b) MsFEM solution with maximum=1.525

Figure 7.10: Comparison between the microscale and the MsFEM solution for $\varepsilon = \dfrac{1}{128}$

- **Fixed $\varepsilon = \dfrac{1}{64}$ and decreasing H**

  Here we have a total of $\left(\dfrac{1}{\varepsilon}\right)^2 = 64^2 = 4096$ holes and a different number of coarse finite elements. As we can see from the results in Table 7.5.4, first, when we decrease H, the error also decreases due to the fact that we start with a very big H and consequently the H^2 term dominates the error. Then, when H becomes sufficiently small and we further decrease it, the error increases with a convergence rate close to the theoretical one, that is $-\dfrac{1}{2}$, and even approaching -1, which is the improved rate (6.5.3). The comparison between the reference microscale solution and the MsFEM solution is given in Figure A.13, A.14, A.15 and A.16.

Table 7.5.4: Fixed $\varepsilon = \frac{1}{64}$ and decreasing H

H	N_{micro}	n	$\|u_\varepsilon - u_\varepsilon^H\|_{L^2(\Omega)}$	Rate	$\|u_\varepsilon - u_\varepsilon^H\|_\infty$	Rate
$H = \frac{1}{8}$	2072411	32156	0.0224074	-	0.05392	-
$H = \frac{1}{16}$	2072411	7985	0.0110185	1.02	0.02425	1.15
$H = \frac{1}{32}$	2072411	1941	0.014923	−0.44	0.02722	−0.17
$H = \frac{1}{64}$	2072411	497	0.0271371	−0.86	0.04815	−0.82

- **Fixed $\varepsilon = \frac{1}{128}$ and decreasing H**

  In this experiment we have $128^2 = 16384$ holes in the unit square and a varying number of coarse grid blocks. The norms of the error are given in Table 7.5.5. Again, when H is relatively big, the error first decreases, and then, when H becomes small enough, the error starts to increase as predicted by the theoretical estimate with a convergence rate close to the improved one from (6.5.3). The microscale and the MsFEM solutions are shown in Figures A.17, A.18, A.19, A.20 and A.21.

Table 7.5.5: Fixed $\varepsilon = \frac{1}{128}$ and decreasing H

H	N_{micro}	n	$\|u_\varepsilon - u_\varepsilon^H\|_{L^2(\Omega)}$	Rate	$\|u_\varepsilon - u_\varepsilon^H\|_\infty$	Rate
$H = \frac{1}{8}$	7279206	113391	0.021233	-	0.04982	-
$H = \frac{1}{16}$	7279206	28257	0.00781583	1.44	0.01840	1.44
$H = \frac{1}{32}$	7279206	6943	0.00822288	−0.07	0.01457	0.34
$H = \frac{1}{64}$	7279206	1763	0.0145742	−0.83	0.02565	−0.82
$H = \frac{1}{128}$	7279206	451	0.0266223	−0.87	0.04651	−0.86

- **Fixed $H = \frac{1}{64}$ and $\varepsilon = \frac{1}{64}, \frac{1}{128}$**

  Here, in Table 7.5.6, we summarize the results from Table 7.5.4 and Table 7.5.5. We observe that for very small coarse grid size $H \geq \varepsilon$, the converges rate is almost 1, which coincides with the improved estimate (6.5.3).

Table 7.5.6: Fixed $H = \frac{1}{64}$ and decreasing ε

ε	N_{micro}	n	$\|u_\varepsilon - u_\varepsilon^H\|_{L^2(\Omega)}$	Rate	$\|u_\varepsilon - u_\varepsilon^H\|_\infty$	Rate
$\varepsilon = \frac{1}{64}$	2072411	497	0.0271371	-	0.04815	-
$\varepsilon = \frac{1}{128}$	7279206	1763	0.0145742	0.9	0.02565	0.91

Numerical results for holes on the vertices and intersecting the edges of the coarse grid finite elements

Here we take $k_\varepsilon = 5$ and $f(x) = 13$.

- **Fixed $H = \frac{1}{16}$ and decreasing ε**

  Here we have $16^2 = 256$ coarse grid blocks with different number of holes per block. The norms of the error are given in Table 7.5.7. For $\varepsilon = \frac{1}{16}, \frac{1}{32}, \frac{1}{64}$ we have a good convergence rate which resembles the theoretical one. When ε becomes very small, or, equivalently, the $\sqrt{\frac{\varepsilon}{H}}$ term in (7.5.1) becomes very small, the error seems to be dominated again by the H^2 term. The numerical results are shown in Figures A.22, A.23, A.24 and A.25.

Table 7.5.7: Fixed $H = \frac{1}{16}$ and decreasing ε

ε	N_{micro}	n	$\|u_\varepsilon - u_\varepsilon^H\|_{L^2(\Omega)}$	Rate	$\|u_\varepsilon - u_\varepsilon^H\|_\infty$	Rate
$\varepsilon = \frac{1}{16}$	110252	423	0.00168992	-	0.005044	-
$\varepsilon = \frac{1}{32}$	447242	1741	0.00100534	0.75	0.003088	0.71
$\varepsilon = \frac{1}{64}$	1789204	6960	0.000796352	0.34	0.002168	0.51
$\varepsilon = \frac{1}{128}$	7120901	27797	0.000721315	0.14	0.001663	0.38

- **Fixed $\varepsilon = \frac{1}{128}$ and decreasing H**

  We have a total of $128^2 = 16384$ holes in the whole domain wtih varying number of coarse grid blocks. As we can see in Table 7.5.8, for the relatively big $H = \frac{1}{16}$ and $H = \frac{1}{32}$ the error decreases because it is dominated by the H^2 term. Then, when H becomes smaller and does not dominate the error anymore, the error starts to increase as the $\sqrt{\frac{\varepsilon}{H}}$ (or $\frac{\varepsilon}{H}$ in the improved estimate) term is getting bigger and the convergence rate reaches the theoretically estimated one. We show the microscale and the MsFEM solution in Figure A.26, A.27, A.28 and A.29.

Table 7.5.8: Fixed $\varepsilon = \frac{1}{128}$ and decreasing H

H	N_{micro}	n	$\|u_\varepsilon - u_\varepsilon^H\|_{L^2(\Omega)}$	Rate	$\|u_\varepsilon - u_\varepsilon^H\|_\infty$	Rate
$H = \frac{1}{16}$	7120901	27797	0.000721315	-	0.001663	-
$H = \frac{1}{32}$	7120901	6951	0.000319653	1.17	0.0008293	1
$H = \frac{1}{64}$	7120901	1721	0.000413392	-0.37	0.0007698	0.11
$H = \frac{1}{128}$	7120901	433	0.000866028	-1.07	0.001571	-1.03

Numerical results for bigger holes on the vertices and edges of the coarse finite elements

The shape and size of the perforations for this test case is given in Figure 7.5(b).

- **Fixed $H = \frac{1}{16}$ and decreasing ε**

  We have $16^2 = 256$ coarse grid blocks with different number of holes per block. In this test case H is sufficiently small and, as we can see from Table 7.5.9, we obtain a very good convergence rate, which is even better than the theoretical result from (6.5.2) and coincides with the improved one (6.5.3). The microscale and the MsFEM solutions are given in Figures A.30, A.31, A.32 and A.33.

Table 7.5.9: Fixed $H = \frac{1}{16}$ and decreasing ε

ε	N_{micro}	n	$\|u_\varepsilon - u_\varepsilon^H\|_{L^2(\Omega)}$	Rate	$\|u_\varepsilon - u_\varepsilon^H\|_\infty$	Rate
$\varepsilon = \frac{1}{16}$	118434	448	0.0137621	-	0.02730	-
$\varepsilon = \frac{1}{32}$	472373	1842	0.00733666	0.91	0.01452	0.91
$\varepsilon = \frac{1}{64}$	1875022	7294	0.00403372	0.86	0.008011	0.86
$\varepsilon = \frac{1}{128}$	7479234	28950	0.00236792	0.77	0.004607	0.8

- **Fixed $\varepsilon = \frac{1}{128}$ and decreasing H**

  In this experiment we have a fixed number of $128^2 = 16384$ holes in the solution domain and we vary the size of the coarse grid. As we can see from Table 7.5.10, we obtain a convergence rate, which coincides with the improved one (6.5.3). The microscale and the MsFEM solutions are given in Figures A.34, A.35, A.36, A.37 and A.38.

Table 7.5.10: Fixed $\varepsilon = \frac{1}{128}$ and decreasing H

H	N_{micro}	n	$\|u_\varepsilon - u_\varepsilon^H\|_{L^2(\Omega)}$	Rate	$\|u_\varepsilon - u_\varepsilon^H\|_\infty$	Rate
$H = \frac{1}{8}$	7479234	116050	0.00404241	-	0.008052	-
$H = \frac{1}{16}$	7479234	28950	0.00236792	0.77	0.004607	0.81
$H = \frac{1}{32}$	7479234	7168	0.00355501	-0.59	0.007261	-0.66
$H = \frac{1}{64}$	7479234	1806	0.00664181	-0.9	0.01364	-0.91
$H = \frac{1}{128}$	7479234	424	0.0128549	-1	0.02646	-0.96

7.5.3 Nonzero Neumann boundary condition on the holes

Numerical results for perforations entirely included in the coarse grid finite elements

In these numerical experiments we take $k_\varepsilon(x) = 5$, $f(x) = 16$ and $g(x) = -0.5$.

- **Fixed $H = \frac{1}{16}$ and decreasing ε**

  We have $16^2 = 256$ coarse grid blocks with different number of holes per block. In this test case H is sufficiently small and, as we can see from Table 7.5.11, we obtain a very good convergence rate, which coincides with the theoretical one. The microscale and the MsFEM solutions are given in Figures A.39, A.40, A.41 and A.42.

Table 7.5.11: Fixed $H = \frac{1}{16}$ and decreasing ε

ε	N_{micro}	n	$\|u_\varepsilon - u_\varepsilon^H\|_{L^2(\Omega)}$	Rate	$\|u_\varepsilon - u_\varepsilon^H\|_\infty$	Rate
$\varepsilon = \frac{1}{16}$	104758	405	0.00593531	-	0.01275	-
$\varepsilon = \frac{1}{32}$	418092	1587	0.00376737	0.66	0.007679	0.73
$\varepsilon = \frac{1}{64}$	1704034	6452	0.00234438	0.69	0.005109	0.58
$\varepsilon = \frac{1}{128}$	7858530	30239	0.00164513	0.52	0.003912	0.39

- **Fixed $\varepsilon = \frac{1}{128}$ and decreasing H**

  In this test case we have a total of $128^2 = 16384$ holes in the whole domain wtih varying number of coarse grid blocks. The norms of the error are given in Table 7.5.12, and we observe a convergence rate close to -1, which is the improved estimate (6.5.3). The comparison between the microscale and the MsFEM solution is given in Figure A.43, A.44, A.45 and A.46.

Table 7.5.12: Fixed $\varepsilon = \frac{1}{128}$ and decreasing H

H	N_{micro}	n	$\|u_\varepsilon - u_\varepsilon^H\|_{L^2(\Omega)}$	Rate	$\|u_\varepsilon - u_\varepsilon^H\|_\infty$	Rate
$H = \frac{1}{16}$	7858530	30239	0.00164513	-	0.003912	-
$H = \frac{1}{32}$	7858530	7565	0.00165395	-0.008	0.002957	0.4
$H = \frac{1}{64}$	7858530	1880	0.00307981	-0.90	0.005415	-0.87
$H = \frac{1}{128}$	7858530	470	0.00555299	-0.85	0.009689	-0.84

Numerical results for perforations on the vertices and edges of the coarse grid finite elements

In the following experiments we take $k_\varepsilon(x) = 5$, $f(x) = 16$ and $g(x) = -0.5$. The geometry of the perforated solution domain and coarse finite elements is the same as in Section 7.5.2.

- **Fixed $H = \frac{1}{16}$ and decreasing ε**

  We have $16^2 = 256$ coarse grid blocks with different number of holes per block. We also notice that when ε is getting smaller, the convergence rate starts to decline. This may be due to the fact that the $\sqrt{\frac{\varepsilon}{H}}$ (or $\frac{\varepsilon}{H}$) term becomes very small and the H^2 term starts to dominate the error. The numerical results are shown in Figure A.47, A.48, A.49 and A.50.

Table 7.5.13: Fixed $H = \frac{1}{16}$ and decreasing ε

ε	N_{micro}	n	$\|u_\varepsilon - u_\varepsilon^H\|_{L^2(\Omega)}$	Rate	$\|u_\varepsilon - u_\varepsilon^H\|_\infty$	Rate
$\varepsilon = \frac{1}{16}$	108513	423	0.00210409	-	0.006357	-
$\varepsilon = \frac{1}{32}$	434730	1681	0.00132141	0.67	0.003952	0.69
$\varepsilon = \frac{1}{64}$	1750441	6829	0.000986151	0.42	0.002667	0.57
$\varepsilon = \frac{1}{128}$	7011255	27253	0.000900171	0.14	0.002103	0.34

- **Fixed $\varepsilon = \frac{1}{128}$ and decreasing H**

  We have a total of $128^2 = 16384$ holes in the whole domain with varying number of coarse grid blocks. From the results in Table 7.5.14 we see that first, when H is bigger, the error decreases, and then, when H becomes smaller, the error begins to increase with the improved theoretical convergence rate. This is probably due to the fact that, initially the H^2 term dominates the error, and then its influence diminishes as H becomes smaller. The microscale and the MsFEM solution are given in Figures A.51, A.52, A.53 and A.54.

Table 7.5.14: Fixed $\varepsilon = \frac{1}{128}$ and decreasing H

H	N_{micro}	n	$\|u_\varepsilon - u_\varepsilon^H\|_{L^2(\Omega)}$	Rate	$\|u_\varepsilon - u_\varepsilon^H\|_\infty$	Rate
$H = \frac{1}{16}$	7011255	27253	0.000900171	-	0.002103	-
$H = \frac{1}{32}$	7011255	6801	0.000374589	1.26	0.001014	1.05
$H = \frac{1}{64}$	7011255	1685	0.000494076	-0.4	0.0009249	0.13
$H = \frac{1}{128}$	7011255	423	0.00109031	-1.14	0.001979	-1.1

7.6 Systems of partial differential equations

This section is devoted to systems of parabolic PDEs in perforated domains with time-independent coefficients and nonlinear Neumann boundary conditions on the holes. The MsFEM is very efficient for such problems since the multiscale basis is also time-independent and consequently constructed only once, and then reused at each time step. This leads to solving a problem with very little number of unknowns at each time step. We demonstrate the computational algorithm with a numerical example. We calculate the L_2 norms of the difference between the reference microscale solution and the one computed via the MsFEM for perforated domains, and we obtain a convergence rate which coincides with either the theoretically predicted rate – (6.5.2) or the improved one – (6.5.3) for the standard MsFEM.

7.6.1 Setup of the problem

Let Ω_ε be a perforated domain, where $\Omega_\varepsilon = \Omega \backslash B_\varepsilon$ with $\Omega = [0,1] \times [0,1]$ and B_ε being the domain of the perforations with $\partial B_\varepsilon \cap \partial\Omega = \emptyset$. The perforated domain Ω_ε is given in blue in Figure 7.2. With ∂B_ε we denote the perforations' boundary. We solve the following

system of parabolic partial differential equations for $x \in \Omega_\varepsilon$ and $t \in [0,T]$

$$\frac{\partial u_\varepsilon}{\partial t} - \nabla \cdot (k_{11}^\varepsilon(x)\nabla u_\varepsilon + k_{12}^\varepsilon(x)\nabla v_\varepsilon) = f_1(x), \quad x \in \Omega_\varepsilon \tag{7.6.1a}$$

$$\frac{\partial v_\varepsilon}{\partial t} - \nabla \cdot (k_{21}^\varepsilon(x)\nabla u_\varepsilon + k_{22}^\varepsilon(x)\nabla v_\varepsilon) = f_2(x), \quad x \in \Omega_\varepsilon \tag{7.6.1b}$$

$$-(k_{11}^\varepsilon(x)\nabla u_\varepsilon + k_{12}^\varepsilon(x)\nabla v_\varepsilon)\cdot \mathbf{n} = \varepsilon g_1(u_\varepsilon, v_\varepsilon), \quad x \in \partial B_\varepsilon \tag{7.6.1c}$$

$$-(k_{21}^\varepsilon(x)\nabla u_\varepsilon + k_{22}^\varepsilon(x)\nabla v_\varepsilon)\cdot \mathbf{n} = \varepsilon g_2(u_\varepsilon, v_\varepsilon), \quad x \in \partial B_\varepsilon \tag{7.6.1d}$$

$$u_\varepsilon(x,0) = u_0(x), \quad x \in \Omega_\varepsilon \tag{7.6.1e}$$
$$v_\varepsilon(x,0) = v_0(x), \quad x \in \Omega_\varepsilon \tag{7.6.1f}$$
$$u_\varepsilon(x,t) = u_0(x), \quad x \in \partial\Omega, \forall t \in [0,T] \tag{7.6.1g}$$
$$v_\varepsilon(x,t) = v_0(x), \quad x \in \partial\Omega, \forall t \in [0,T] \tag{7.6.1h}$$

With ε we indicate the characteristic size of the small scale. We impose nonlinear Neumann boundary conditions on the holes (7.6.1c)-(7.6.1d), where $\mathbf{n}$ is the unit outward normal vector on the perforations' boundary ∂B_ε pointing in direction from the domain Ω_ε into the perforations B_ε. Again, by analogy with Chapter 4, we scale the fluxes on the boundary of the holes with ε, so that the total flux across the perforations' boundary does not blow up when $\varepsilon \to 0$. As in the case of a scalar linear elliptic PDE with nonzero Neumann boundary condition on the holes, that we considered earlier in this chapter, the idea for solving numerically problem (7.6.1) is to account naturally for the Neumann boundary conditions (7.6.1c) and (7.6.1d) in the global weak form of the problem, and then to construct the multiscale basis functions by imposing zero flux on the holes.

7.6.2 Weak form of the problem

The weak formulation of problem (7.6.1) is to find $u_\varepsilon \in H^1(\Omega_\varepsilon)$ and $v_\varepsilon \in H^1(\Omega_\varepsilon)$ such that the following integral equalities are true for all functions $w_1, w_2 \in H^1(\Omega_\varepsilon)$ (we formally test with two different functions w_1 and w_2, since they both belong to the same space

$H^1(\Omega_\varepsilon))$

$$\int\limits_{\Omega_\varepsilon} \frac{\partial u_\varepsilon}{\partial t} w_1\,dx + \int\limits_{\Omega_\varepsilon} k_{11}^\varepsilon(x)\nabla u_\varepsilon \cdot \nabla w_1\,dx + \int\limits_{\Omega_\varepsilon} k_{12}^\varepsilon(x)\nabla v_\varepsilon \cdot \nabla w_1\,dx +$$

$$+ \int\limits_{\partial B_\varepsilon} \varepsilon g_1(u_\varepsilon, v_\varepsilon) w_1\,ds = \int\limits_{\Omega_\varepsilon} f_1 w_1\,dx, \quad \forall w_1 \in H^1(\Omega_\varepsilon) \tag{7.6.2a}$$

$$\int\limits_{\Omega_\varepsilon} \frac{\partial v_\varepsilon}{\partial t} w_2\,dx + \int\limits_{\Omega_\varepsilon} k_{21}^\varepsilon(x)\nabla u_\varepsilon \cdot \nabla w_2\,dx + \int\limits_{\Omega_\varepsilon} k_{22}^\varepsilon(x)\nabla v_\varepsilon \cdot \nabla w_2\,dx +$$

$$+ \int\limits_{\partial B_\varepsilon} \varepsilon g_1(u_\varepsilon, v_\varepsilon) w_2\,ds = \int\limits_{\Omega_\varepsilon} f_2 w_2\,dx, \quad \forall w_2 \in H^1(\Omega_\varepsilon) \tag{7.6.2b}$$

Let $\Omega_\varepsilon = \bigcup\limits_{K\in\mathcal{T}_H} K$, where $\mathcal{T}_H$ is a partition of Ω_ε into perforated rectangular coarse finite elements K, as shown in Figure 7.3(b). A perforated coarse grid rectangular finite element K, with only one hole, is shown in Figure 7.3(a). Of course, each coarse element may contain a random number of holes. Let also $\{\mathbf{x}^i\}_{i=1}^N$ be the nodes of the mesh of finite elements. Since we have a system of equations, we need two sets of multiscale basis functions – $\{\phi_i^M(x)\}_{i=1}^N$ for the function u_ε and $\{\psi_i^M(x)\}_{i=1}^N$ for the function v_ε. Then we introduce the following finite-dimensional approximation spaces associated with $\mathcal{T}_H$:

- $V^H = span\{\varphi_i^L(x)\}_{i=1}^N \subset H^1(\Omega_\varepsilon)$, where $\{\varphi_i^L(x)\}_{i=1}^N$ is the standard piecewise linear basis
- $\mathcal{U}^H = span\{\phi_i^M(x)\}_{i=1}^N \subset H^1(\Omega_\varepsilon)$, where $\{\phi_i^M(x)\}_{i=1}^N$ is the multiscale basis associated with the function u_ε, i.e., $\mathcal{U}^H$ is the finite-dimensional approximation space for the function u_ε
- $\mathcal{V}^H = span\{\psi_i^M(x)\}_{i=1}^N \subset H^1(\Omega_\varepsilon)$, where $\{\psi_i^M(x)\}_{i=1}^N$ is the multiscale basis associated with the function v_ε, i.e., $\mathcal{V}^H$ is the finite-dimensional approximation space for the function v_ε

Therefore $u_\varepsilon^H(x) = \sum\limits_{i=1}^N U_i(t)\phi_i^M(x)$ and $v_\varepsilon^H(x) = \sum\limits_{i=1}^N V_i(t)\psi_i^M(x)$ are the approximate discretized solutions in the finite-dimensional approximation spaces $\mathcal{U}^H$ and $\mathcal{V}^H$, respectively. When we restrict the weak formulation (7.6.2) to the finite-dimensional spaces $\mathcal{U}^H$ and $\mathcal{V}^H$, we obtain: find $u_\varepsilon^H \in \mathcal{U}^H$ and $v_\varepsilon^H \in \mathcal{V}^H$ such that the following integral equalities are true for all functions $w_1^H \in V^H$ and $w_2^H \in V^H$ (or for all functions $w_1^H \in \mathcal{U}^H$ and all

functions $w_2^H \in \mathcal{V}^H$)

$$\int\limits_{\Omega_\varepsilon} \frac{\partial u_\varepsilon^H}{\partial t} w_1^H \, dx + \int\limits_{\Omega_\varepsilon} k_{11}^\varepsilon(x) \nabla u_\varepsilon^H \cdot \nabla w_1^H \, dx + \int\limits_{\Omega_\varepsilon} k_{12}^\varepsilon(x) \nabla v_\varepsilon^H \cdot \nabla w_1^H \, dx +$$

$$+ \int\limits_{\partial B_\varepsilon} \varepsilon g_1(u_\varepsilon^H, v_\varepsilon^H) w_1^H \, ds = \int\limits_{\Omega_\varepsilon} f_1(x) w_1^H(x) \, dx \tag{7.6.3a}$$

$$\int\limits_{\Omega_\varepsilon} \frac{\partial v_\varepsilon^H}{\partial t} w_2^H \, dx + \int\limits_{\Omega_\varepsilon} k_{21}^\varepsilon(x) \nabla u_\varepsilon^H \cdot \nabla w_2^H \, dx + \int\limits_{\Omega_\varepsilon} k_{22}^\varepsilon(x) \nabla v_\varepsilon^H \cdot \nabla w_2^H \, dx +$$

$$+ \int\limits_{\partial B_\varepsilon} \varepsilon g_1(u_\varepsilon^H, v_\varepsilon^H) w_2^H \, ds = \int\limits_{\Omega_\varepsilon} f_2(x) w_2^H(x) \, dx \tag{7.6.3b}$$

7.6.3 Construction of the multiscale basis functions

As we have already discussed it above, since we have a system of equations, we need two sets of multiscale basis functions – $\{\phi_i^M(x)\}_{i=1}^N$ and $\{\psi_i^M(x)\}_{i=1}^N$ for the functions u_ε and v_ε, respectively. It is clear that the two sets of basis functions have the same local supports, because they are built on the same partition $\mathcal{T}_H$ of the solution domain Ω_ε. We denote $\mathcal{S}_i = supp\{\phi_i^M(x)\} \equiv supp\{\psi_i^M(x)\}$. Since the coefficients $k_{ij}^\varepsilon(x)$, $i,j = 1,2$ are time-independent, we need to solve only once the following time-independent local problems in order to construct the multiscale basis functions $\left\{\phi_i^M(x)\right\}_{i=1}^N$ and $\left\{\psi_i^M(x)\right\}_{i=1}^N$ for $\forall K \in \mathcal{T}_H$, such that $K \in \mathcal{S}_i$

$$\left|\begin{array}{ll} -\nabla \cdot \left(k_{11}^\varepsilon(x)\nabla\phi_i^M + k_{12}^\varepsilon(x)\nabla\psi_i^M\right) = 0, & x \in K, \\ -\nabla \cdot \left(k_{21}^\varepsilon(x)\nabla\phi_i^M + k_{22}^\varepsilon(x)\nabla\psi_i^M\right) = 0, & x \in K, \\ -\left(k_{11}^\varepsilon(x)\nabla\phi_i^M + k_{12}^\varepsilon(x)\nabla\psi_i^M\right) \cdot \mathbf{n} = 0, & x \in \partial B \\ -\left(k_{21}^\varepsilon(x)\nabla\phi_i^M + k_{22}^\varepsilon(x)\nabla\psi_i^M\right) \cdot \mathbf{n} = 0, & x \in \partial B \\ \phi_i^M(x) = \psi_i^M(x) = \varphi_i^L(x), & x \in \partial K \backslash \partial B \end{array}\right. \tag{7.6.4}$$

Consequently, we can reuse the multiscale basis at each time step. This makes the numerical solving of the time-dependent problem (7.6.1) very efficient in terms of computational time, because at each time step we have to solve a problem with a very few degress of freedom.

7.6.4 Numerical results

We run the simulations for 4 time steps with time step $\Delta t = 1$ and we show numerical results for the function v_ε. For the time discretization we use the Backward Euler method and for the linearization of the problem - the Newton-Raphson method. For the microscale solution we apply the standard FEM with triangular elements and piecewise linear basis functions and as a linear solver we use SAMG (Algebraic Multigrid Methods for Systems) [64] developed by the Fraunhofer Institute for Algorithms and Scientific Computing (SCAI). In the MsFEM framework we apply the Galerkin formulation. Again, as in Section 7.5, H is the coarse grid size and the small parameter ε characterizes the size of the periodic microstructures. Consequently, $\left(\frac{1}{H}\right)^2$ is the number of coarse elements and $\left(\frac{1}{\varepsilon}\right)^2$ is the number of holes in the solution domain. As before, with N_{micro} we denote the number of finite elements in the microscale simulation, and with n we denote the number of finite elements per single coarse grid block in the MsFEM formulation of the problem. In the simulations we take $N_{micro} \approx n \left(\frac{1}{H}\right)^2$, i.e., the total number of fine mesh elements in all of the coarse elements to be equal to the number of finite elements in the microscale simulation. The coarse grid consists of finite elements which are perforated squares and we run numerical simulations with different number of holes per coarse element. We consider two test cases and we show numerically that the solution obtained with the MsFEM converges to the reference microscale solution. First we calculate the L_2 norm of the error for fixed H and decreasing ε, and then for fixed ε and varying H. We take the coefficients, the right-hand sides and the Neumann data to be respectively

$$\begin{aligned} &k_{11}^\varepsilon(x) = 5, && k_{22}^\varepsilon(x) = 7 \\ &k_{12}^\varepsilon(x) = 3, && k_{21}^\varepsilon(x) = 5 \\ &f_1(x) = x_1 x_2, && f_2(x) = 16 \\ &g_1(u_\varepsilon, v_\varepsilon) = u_\varepsilon^2 v_\varepsilon, && g_2(u_\varepsilon, v_\varepsilon) = 2u_\varepsilon v_\varepsilon \end{aligned} \tag{7.6.5}$$

For initial and boundary conditions we have

$$u_\varepsilon(x,0) = 0, \quad x \in \Omega_\varepsilon \tag{7.6.6}$$
$$v_\varepsilon(x,0) = 0, \quad x \in \Omega_\varepsilon \tag{7.6.7}$$
$$u_\varepsilon(x,t) = 0, \quad x \in \partial\Omega, \forall t \in [0,T] \tag{7.6.8}$$
$$v_\varepsilon(x,t) = 0, \quad x \in \partial\Omega, \forall t \in [0,T] \tag{7.6.9}$$

Fixed $H = \frac{1}{16}$ and decreasing ε

Here we have $16^2 = 256$ coarse grid blocks with varying number of holes per block. We start with 1 hole per macro element and we reach $8^2 = 64$ holes per block in the last experiment. The results from Table 7.6.1 show a convergence rate, which is even better

than the theoretical one (6.5.2) and approaching the improved one (6.5.3). We also observe that when ε becomes very small, which means that the $\sqrt{\frac{\varepsilon}{H}}$ term is getting very small, the convergence rate starts to decline. This behaviour is most likely due to the fact that the H^2 term becomes dominant for very small values of ε. In Figure 7.11 and Figure 7.12 we show the microscale and the MsFEM solution for $\varepsilon = \frac{1}{16}$ and $\varepsilon = \frac{1}{64}$, respectively.

Table 7.6.1: Fixed $H = \frac{1}{16}$ and decreasing ε

ε	N_{micro}	n	$\|v_\varepsilon - v_\varepsilon^H\|_{L^2(\Omega)}$	Rate	$\|v_\varepsilon - v_\varepsilon^H\|_\infty$	Rate
$\varepsilon = \frac{1}{16}$	65076	254	0.00718523	-	0.01507	-
$\varepsilon = \frac{1}{32}$	260959	1019	0.00362805	0.99	0.008224	0.87
$\varepsilon = \frac{1}{64}$	1051787	4195	0.00213326	0.77	0.005743	0.52
$\varepsilon = \frac{1}{128}$	4190481	15751	0.00208196	0.04	0.004590	0.32

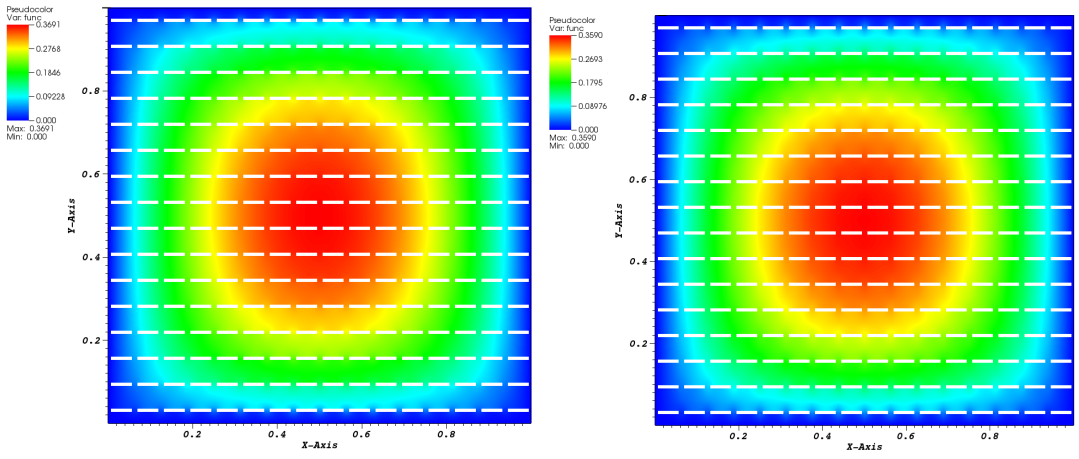

(a) Microscale solution with maximum=0.3691 (b) MsFEM solution with maximum=0.3590

Figure 7.11: Comparison between the microscale and the MsFEM solution for $\varepsilon = H = \frac{1}{16}$

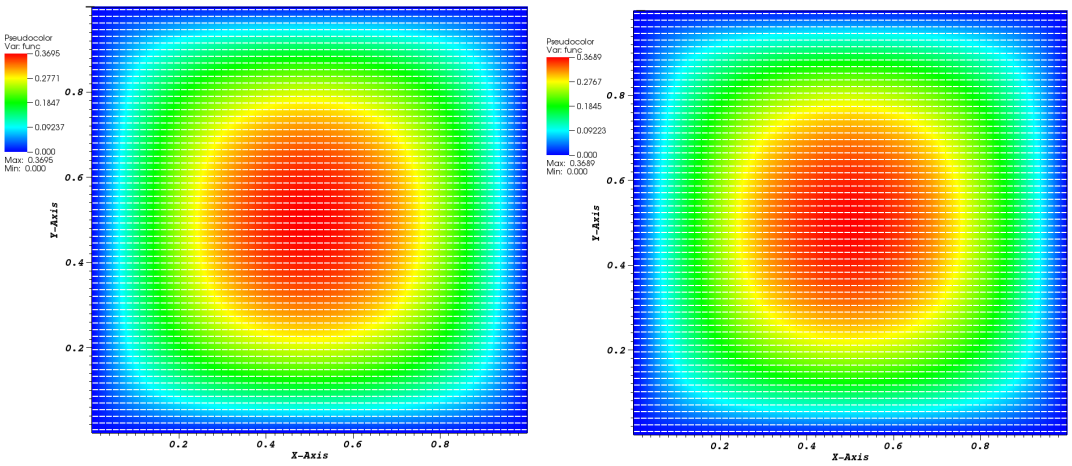

(a) Microscale solution with maximum=0.3695 (b) MsFEM solution with maximum=0.3689

Figure 7.12: Comparison between the microscale and the MsFEM solution for $\varepsilon = \frac{1}{64}$

Fixed $\varepsilon = \frac{1}{128}$ and decreasing H

In this experiment we have a total of $128^2 = 16384$ holes in the whole domain with varying number of coarse grid blocks. From the results in Table 7.6.2 we see that first, when H is relatively big, the error practically does not change, and then, when H becomes smaller, the error begins to increase with the improved convergence rate (6.5.3). This is probably due to the fact that, initially the H^2 term dominates the error, and then its influence diminishes as H becomes smaller. The microscale and the MsFEM solution for $H = \frac{1}{16}$ and $H = \frac{1}{32}$ are given in Figures 7.13 and 7.14, respectively.

Table 7.6.2: Fixed $\varepsilon = \frac{1}{128}$ and decreasing H

H	N_{micro}	n	$\|v_\varepsilon - v_\varepsilon^H\|_{L^2(\Omega)}$	Rate	$\|v_\varepsilon - v_\varepsilon^H\|_\infty$	Rate
$H = \frac{1}{16}$	4190481	15751	0.00208196	-	0.004590	-
$H = \frac{1}{32}$	4190481	4065	0.00198284	0.07	0.003545	0.37
$H = \frac{1}{64}$	4190481	1019	0.00331127	-0.74	0.005856	-0.72
$H = \frac{1}{128}$	4190481	271	0.00598942	-0.86	0.01047	-0.84

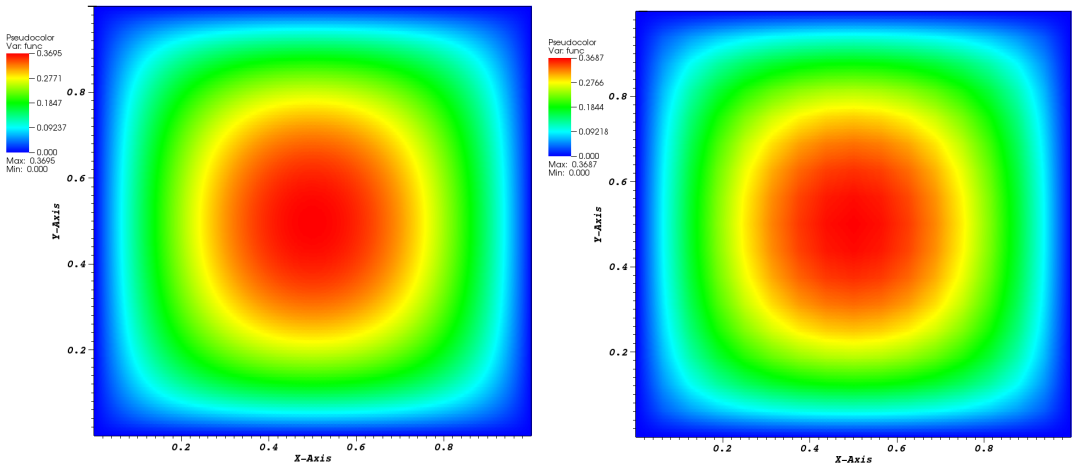

(a) Microscale solution with maximum=0.3695 (b) MsFEM solution with maximum=0.3687

Figure 7.13: Comparison between the microscale and the MsFEM solution for $H = \frac{1}{16}$

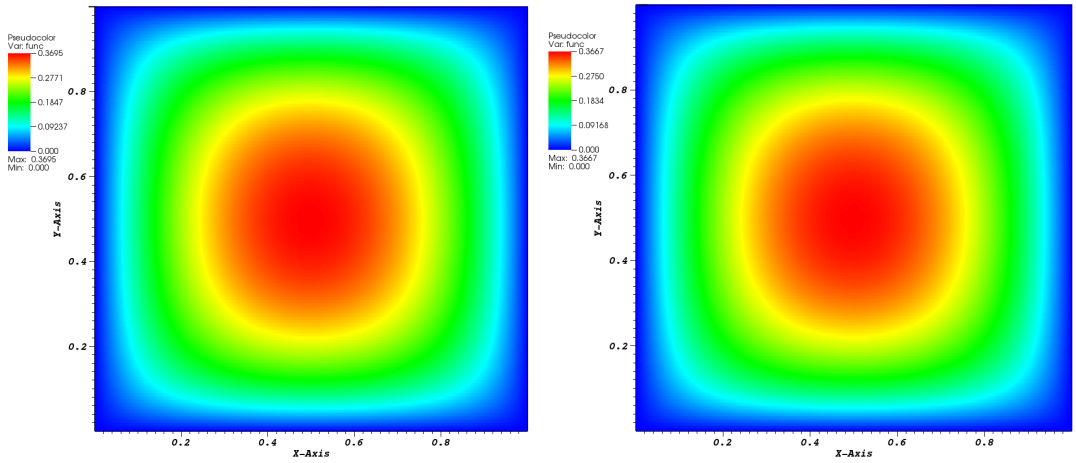

(a) Microscale solution with maximum=0.3695 (b) MsFEM solution with maximum=0.3667

Figure 7.14: Comparison between the microscale and the MsFEM solution for $H = \frac{1}{32}$

Chapter 8

Upscaling of a Simplified Two-Dimensional Li-ion Battery Problem via the MsFEM for Perforated Domains

8.1 Introduction

In this chapter we consider a simplified two-dimensional Li-ion battery problem, which we solve using the MsFEM for perforated domains with nonlinear Neumann boundary conditions on the holes. The results that we present in the chapter are an original contribution of the current work. We start with the formulation of the problem in Section 8.2. In the next Section 8.3 we give the weak formulation of the simplified battery model. We discuss the numerical methods that we use in Section 8.4 and in Section 8.5 we briefly summarize the advantages of the proposed numerical algorithm. Qualitative numerical results are given in Section 8.6.1, and in Section 8.6.2 we demonstrate numerical convergence of the considered upscaling method.

8.2 Setup of the problem

We consider a simplified 2D version of the Li-ion battery model from Chapter 2. The solution domain is shown in Figure 8.1 where the blue part is the "electrolyte phase" and the yellow inclusions form the "solid phase particles". This is a very basic representation of the battery cell, because in real 3D electrodes, the solid is a connected domain. Nevertheless, the concept for solving this simplified problem is the same as for solving the full Li-ion battery model. We denote with Ω_e^ε the electrolyte domain and with Ω_s^ε - the solid domain. Then, we have that $\Omega = \Omega_e^\varepsilon \cup \Omega_s^\varepsilon$, where $\Omega = [0,1] \times [0,1]$ is the unit square. In order to conduct a consistent numerical investigation, we consider a periodic arrangement of identical solid particles as illustrated in Figure 8.1. For $x \in \Omega$ and $t \in [0,T]$ we solve the following 2D Li-ion battery problem for the diffusion of Lithium ions in the electrolyte

and in the solid

$$\frac{\partial c_\varepsilon^e}{\partial t} - \nabla \cdot (k_e \nabla c_\varepsilon^e) = 0, \quad x \in \Omega_e^\varepsilon, \tag{8.2.1a}$$

$$\frac{\partial c_\varepsilon^s}{\partial t} - \nabla \cdot (k_s \nabla c_\varepsilon^s) = 0, \quad x \in \Omega_s^\varepsilon, \tag{8.2.1b}$$

$$-k_e \nabla c_\varepsilon^e \cdot \mathbf{n_s} = -k_s \nabla c_\varepsilon^s \cdot \mathbf{n_s} = \varepsilon g(c_\varepsilon^e, c_\varepsilon^s) = \varepsilon \exp\left(c_\varepsilon^e + c_\varepsilon^s\right), \quad x \in \Gamma_\varepsilon, \tag{8.2.1c}$$

$$c_\varepsilon^e(x,0) = c_0^e, \quad \forall x \in \Omega_e^\varepsilon, \tag{8.2.1d}$$

$$c_\varepsilon^e(x,t) = c_0^e, \quad x \in \partial\Omega_D, t \in [0,T] \tag{8.2.1e}$$

$$-k_e \nabla c_\varepsilon^e \cdot \mathbf{n} = C, \quad x \in \partial\Omega_N, t \in [0,T] \tag{8.2.1f}$$

$$c_\varepsilon^s(x,0) = c_0^s, \quad \forall x \in \Omega_s^\varepsilon \tag{8.2.1g}$$

where Γ_ε is the interface boundary between the electrolyte Ω_e^ε and the solid Ω_s^ε. With $\mathbf{n_s}$ we denote the unit normal vector pointing from the solid into the electrolyte domain, and $\mathbf{n}$ is the unit outward normal vector to the domain Ω. The simplified model consists of diffusion equations for the concentration c_ε^e of Li+ in the electrolyte and the concentration c^s of ions in the active material. The two phases are coupled with a highly nonlinear Butler-Volmer type of interface condition (8.2.1c). Therefore, just as in the full model [48], the concentration of Li+ is a discontinuous function across the solid-electrolyte interface, whereas the flux of ions is continuous. We assume that $k_s \ll k_e$, i.e., the diffusion of Lithium ions in the solid phase is much slower than the diffusion in the electrolyte phase. We also assume that we do not have scale separation for the concentration c_ε^s. This is the same setting that we have in the real Li-ion battery problem. We also consider constant diffusion coefficients k_e and k_s because, as mentioned before, we are interested only in oscillations coming from the perforations (solid inclusions).

The small parameter ε in (8.2.1) indicates the dependence of the solution on the number and size of solid phase inclusions and it characterizes the dimensions of the particles, with $\left(\frac{1}{\varepsilon}\right)^2$ being the total number of solid particles in Ω. At each time step we apply constant current on the outer boundary $\partial\Omega_N$ and constant Dirichlet boundary condition on $\partial\Omega_D$. Therefore, following the same argument as in the homogenization in perforated domains from Chapter 4, we scale the interface condition (8.2.1c) with the small parameter ε, so that the total electrolyte flux of ions across the solid-electrolyte interface does not blow up when $\varepsilon \to 0$. The numerical results also confirm that this scaling is necessary.

Our idea for solving numerically the 2D battery problem is the following:

1. To consider each phase - the electrolyte and the solid, as a separate perforated domain
2. To apply the MsFEM for perforated domains to the scale-separable concentration c_ε^e in the electrolyte
3. To leave on the microscale the equation (8.2.1b) for the concentration c_ε^s in the solid

4. To couple the macroscale electrolyte problem with the microscale solid phase problem via the interface conditions (8.2.1c)

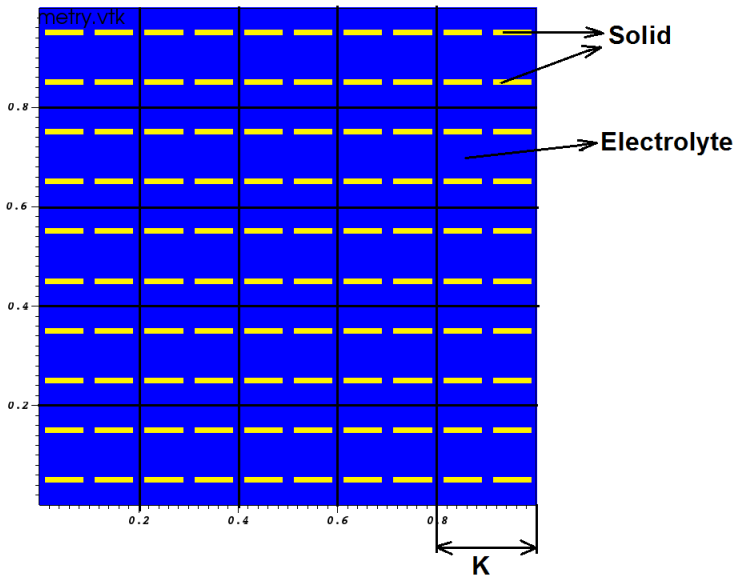

Figure 8.1: Discretized solution domain consisting of electrolyte and solid phase

Consequently, we have to solve a coupled macro-micro problem, where the macroscale electrolyte problem is given by

$$\frac{\partial c_\varepsilon^e}{\partial t} - \nabla \cdot (k_e \nabla c_\varepsilon^e) = 0, \quad x \in \Omega_e^\varepsilon, \tag{8.2.2a}$$

$$-k_e \nabla c_\varepsilon^e \cdot \mathbf{n_s} = \varepsilon g(c_\varepsilon^e, c_\varepsilon^s) = \varepsilon \exp\left(c_\varepsilon^e + c_\varepsilon^s\right), \quad x \in \Gamma_\varepsilon, \tag{8.2.2b}$$

$$c_\varepsilon^e(x,0) = c_0^e, \quad \forall x \in \Omega_e^\varepsilon, \tag{8.2.2c}$$
$$c_\varepsilon^e(x,t) = c_0^e, \quad x \in \partial\Omega_D, t \in [0,T] \tag{8.2.2d}$$
$$-k_e \nabla c_\varepsilon^e \cdot \mathbf{n} = C, \quad x \in \partial\Omega_N, t \in [0,T] \tag{8.2.2e}$$

and the microscale solid phase problem is

$$\frac{\partial c_\varepsilon^s}{\partial t} - \nabla \cdot (k_s \nabla c_\varepsilon^s) = 0, \quad x \in \Omega_s^\varepsilon, \tag{8.2.3a}$$

$$-k_s \nabla c_\varepsilon^s \cdot \mathbf{n_s} = \varepsilon g(c_\varepsilon^e, c_\varepsilon^s) = \varepsilon \exp\left(c_\varepsilon^e + c_\varepsilon^s\right), \quad x \in \Gamma_\varepsilon, \tag{8.2.3b}$$

$$c_\varepsilon^s(x,0) = c_0^s, \quad \forall x \in \Omega_s^\varepsilon \tag{8.2.3c}$$

8.3 Weak formulation of the problem

We consider the electrolyte phase as a perforated domain, where we think of the solid phase inclusions as of holes. Then, we apply the MsFEM for problems in perforated domains that we presented in Chapter 7. Our idea is to write the weak form of the electrolyte phase problem in the perforated domain Ω_e^ε and then to divide Ω_e^ε into perforated coarse finite elements K as shown in Figure 8.1. It is clear that each element K contains both electrolyte and solid medium, where the active material is viewed as holes when solving the macroscale electrolyte problem. We make the assumption that the solid particles are entirely included in the coarse finite elements K and do not intersect their edges. We apply a semi-implicit time-stepping scheme in order to solve the microscale solid problems independently of one another in each coarse grid finite element. This allows for a very efficient parallel implementation of the coupled macro-micro problem.
The weak formulation of the electrolyte problem, restricted to a finite dimensional approximation space $V^H \subset H^1(\Omega_e^\varepsilon)$ reads: find $(c_\varepsilon^e)^H \in V^H$ so that the following integral equality is true for all test functions $v^H \in V^H$:

$$\int\limits_{\Omega_e^\varepsilon} \frac{\partial (c_\varepsilon^e)^H}{\partial t} v^H \, dx + \int\limits_{\Omega_e^\varepsilon} k_e \nabla (c_\varepsilon^e)^H \cdot \nabla v^H \, dx + \int\limits_{\partial\Omega^N} C v^H \, dx - \int\limits_{\Gamma_\varepsilon} \varepsilon g((c_\varepsilon^e)^H, c_\varepsilon^s) v^H \, ds = 0 \tag{8.3.1}$$

Let $\Omega_e^\varepsilon = \bigcup\limits_{K \in \mathcal{T}_H} K$, where $\mathcal{T}_H$ is the partition of Ω_e^ε into perforated finite elements K as shown in Figure 8.1. We construct the multiscale basis functions $\left\{\phi_i^M(x)\right\}_{i=1}^N$ as in Chapter 7 by solving a problem equivalent to (7.3.9), namely, we compute the multiscale basis by considering only the elliptic part of the differential equation (8.2.1a). In the current case B is the domain of the solid inclusions inside the macro finite element K as shown in Figure 7.3(a). The local electrolyte problems are solved in all $K \in \mathcal{T}_H$ such that $K \in supp\left(\phi_i^M(x)\right)$, for $i = 1, 2, \ldots, N = dim(V^H)$ and they are given by

$$-\nabla \cdot \left(k_e \nabla \phi_i^M\right) = 0, \quad x \in K, \tag{8.3.2a}$$

$$-k_e \nabla \phi_i^M \cdot \mathbf{n} = 0, \quad x \in \partial B \tag{8.3.2b}$$

$$\phi_i^M(x) = \phi_i^L(x), \quad x \in \partial K \backslash \partial B \tag{8.3.2c}$$

Now, in (8.3.1) we use both as test and trial functions the multiscale basis functions $\{\phi_j^M(x)\}_{i=1}^N$. Then, the approximate discretized solution, expanded with respect to the multiscale basis, is

$$(c_\varepsilon^e)^H(x,t) = \sum_{i=1}^N C_i^e(t) \phi_i^M(x) \tag{8.3.3}$$

Since the diffusion coefficients k_e and k_s are constants and they do not depend on the time or the concentrations c_ε^e and c_ε^s, we can compute the multiscale basis functions only once and then reuse them at each time step and each Newton-Raphson iteration (which we need for the linearization of the problem).

In the solid inclusions, we write the weak form separately in each inclusion Ω_s^i, for $i = 1, 2, \ldots, P_\varepsilon$, where $P_\varepsilon \in \mathbb{N}$ is the number of solid particles. Then, the solid phase weak formulation, restricted to a finite dimensional approximation space $W_i^H \subset H^1(\Omega_s^i)$, is: find $(c_\varepsilon^s)^H \in W_i^H$ so that the following integral equality is true for all test functions $w^H \in W_i^H$:

$$\int\limits_{\Omega_s^i} \frac{\partial (c_\varepsilon^s)^H}{\partial t} w^H \, dx + \int\limits_{\Omega_s^i} k_s \nabla (c_\varepsilon^s)^H \cdot \nabla w^H \, dx + \int\limits_{\Gamma_\varepsilon^i} \varepsilon g(c_\varepsilon^e, (c_\varepsilon^s)^H) w^H \, ds = 0 \tag{8.3.4}$$

where with Γ_ε^i we denote the interface boundary in each solid inclusion Ω_s^i.
As we can see from (8.3.1) and (8.3.4), the coupling between the electrolyte and the solid phase is due to the interface integrals $\int\limits_{\Gamma_\varepsilon} \varepsilon g((c_\varepsilon^e)^H, c_\varepsilon^s) v^H \, ds$ and $\int\limits_{\Gamma_\varepsilon^i} \varepsilon g(c_\varepsilon^e, (c_\varepsilon^s)^H) w^H \, ds$.

8.4 Numerical methods

First we sum up the algorithm for the numerical solving of the coupled macro-micro problem and then we discuss the methods that we use.

Numerical Algorithm:

1. Compute the multiscale basis functions $\{\phi_i^M(x)\}_{i=1}^N$ by solving the local problems (8.3.2)

2. Start from given initial values for $c_\varepsilon^e \to c_0^e$ and $c_\varepsilon^s \to c_0^s$

3. Start time iterations

   (a) Start Newton-Raphson iterations for the electrolyte phase problem, where as an initial guess use c_ε^e and c_ε^s from the previous time step

      i. Assemble the Jacobian and the right-hand side using the values for c_ε^s from the previous time step

      ii. Stop the Newton-Raphson iterations when a desired predefined accuracy is reached

   (b) Solve the microscale solid phase problems in each coarse finite element K, using the already computed values for c_ε^e

4. Stop time iterations after a desired predefined number of discrete time steps

We start by solving numerically the local problems (8.3.2) in each coarse element K using the standard FEM with piecewise linear basis functions $\{\varphi_j^K(x)\}_{j=1}^{n^K}$. Then, the discretized

approximate solution to (8.3.2), restricted to the macro element $K: K \in supp\{\phi_i^M(x)\}$ has the form

$$\left(\phi_i^M\right)^h(x) = \sum_{j=1}^{n^K} \Phi_j^{i,K} \varphi_j^K(x) \tag{8.4.1}$$

Let $K = \bigcup_{e \in \tau_h^K} e$, where τ_h^K is the partition of the macro finite element K into triangular finite elements e. With $e_\Gamma \in \tau_h^K$ we denote the following set of elements

$$e_\Gamma = \{e \in \tau_h^K : e \quad has \quad an \quad edge \quad \mathcal{E}_\Gamma \in \partial B^K\} \tag{8.4.2}$$

where ∂B^K is the boundary of the perforations inside the coarse element K.
We solve the microscale solid phase problems with the standard FEM with linear Lagrange triangular elements. We use the Backward Euler method for the time discretization for both the solid and the electrolyte problems. For the linearization of the resulting systems of nonlinear algebraic equations we apply the Newton-Raphson method. As a result, for ***the electrolyte phase problem***, we obtain the following linear system of equations which we solve at each time step with the preconditioned Stabilized Biconjugate Gradient Method

$$\mathbf{J}\left(\mathbf{C_e}^{m,(k-1)}\right)\left(\mathbf{C_e}^{m,(k)} - \mathbf{C_e}^{m,(k-1)}\right) = -\mathbf{F}\left(\mathbf{C_e}^{m,(k-1)}\right) \tag{8.4.3}$$

where the superscript "m" indicates the current m-th time step, "(k-1)" - the solution from the previous Newton iteration, and "(k)" - the unknown solution at the current Newton iteration. With $\mathbf{C_e}^m = \left(C_1^{e,(m)}, C_2^{e,(m)}, \ldots, C_N^{e,(m)}\right)^T$ we denote the solution vector at the current m-th time step, and $\mathbf{F} = (F_1, F_2, \ldots, F_N)^T$ is the right-hand side. The elements of the Jacobian $\mathbf{J}$ are given by

$$\begin{aligned} J_{jl} = &\sum_{K \in \mathcal{T}_H} \left(\sum_{e \in \tau_h^K} \int_e \frac{1}{\Delta t} \left(\phi_l^M\right)^h \left(\phi_j^M\right)^h \, dx \right) + \\ &+ \sum_{K \in \mathcal{T}_H} \left(\sum_{e \in \tau_h^K} \int_e k_e \nabla \left(\phi_l^M\right)^h \cdot \nabla \left(\phi_j^M\right)^h \, dx \right) - \\ &- \sum_{K \in \mathcal{T}_H} \left(\sum_{e_\Gamma \in \tau_h^K} \int_{\mathcal{E}_\Gamma} \varepsilon \frac{\partial g}{\partial c_\varepsilon^e} \left(\left(c_\varepsilon^e\right)^H, c_\varepsilon^s \right) \left(\phi_l^M\right)^h \left(\phi_j^M\right)^h \, ds \right) \end{aligned} \tag{8.4.4}$$

where Δt is the time step and $j, l = 1, 2, \ldots, N$. The elements of the right-hand side are

$$F_j = \sum_{K\in\mathcal{T}_H}\left(\sum_{e\in\tau_h^K}\int_e \sum_{i=1}^{N}\frac{C_i^{e,(m)}-C_i^{e,(m-1)}}{\Delta t}\left(\phi_i^M\right)^h\left(\phi_j^M\right)^h\,dx\right)+$$

$$+\sum_{K\in\mathcal{T}_H}\left(\sum_{e\in\tau_h^K}\int_e k_e\sum_{i=1}^{N}C_i^{e,(m)}\nabla\left(\phi_i^M\right)^h\cdot\nabla\left(\phi_j^M\right)^h\,dx\right)-$$

$$-\sum_{K\in\mathcal{T}_H}\left(\sum_{e_\Gamma\in\tau_h^K}\int_{\mathcal{E}_\Gamma}\varepsilon g\left(\sum_{i=1}^{N}C_i^{e,(m)}\left(\phi_i^M\right)^h,c_\varepsilon^s\right)\left(\phi_j^M\right)^h\,ds\right)+$$

$$+\sum_{K\in\mathcal{T}_H}\left(\sum_{e\in\tau_h^K}\int_{\partial\Omega_N} C\left(\phi_j^M\right)^h\,ds\right) \tag{8.4.5}$$

We use the following notation for the interface integrals in (8.4.4) and (8.4.5)

$$\mathcal{I}_J=\int_{\Gamma_\varepsilon}\varepsilon\frac{\partial g}{\partial c_\varepsilon^e}\left(\left(c_\varepsilon^e\right)^H,c_\varepsilon^s\right)\phi_l^M\phi_j^M\,ds=\sum_{K\in\mathcal{T}_H}\left(\sum_{e_\Gamma\in\tau_h^K}\int_{\mathcal{E}_\Gamma}\varepsilon\frac{\partial g}{\partial c_\varepsilon^e}\left(\left(c_\varepsilon^e\right)^H,c_\varepsilon^s\right)\left(\phi_l^M\right)^h\left(\phi_j^M\right)^h\,ds\right) \tag{8.4.6}$$

$$\mathcal{I}_F=\int_{\Gamma_\varepsilon}\varepsilon g\left(\left(c_\varepsilon^e\right)^H,c_\varepsilon^s\right)\phi_j^M\,ds=\sum_{K\in\mathcal{T}_H}\left(\sum_{e_\Gamma\in\tau_h^K}\int_{\mathcal{E}_\Gamma}\varepsilon g\left(\left(c_\varepsilon^e\right)^H,c_\varepsilon^s\right)\left(\phi_j^M\right)^h\,ds\right) \tag{8.4.7}$$

We assemble element-wise the Jacobian matrix $\mathbf{J}$ and the right-hand side $\mathbf{F}$. This is typical for the FEM because the basis functions have local supports. We also have to integrate on the fine mesh due to the multiscale basis functions which we compute numerically. Therefore, as we can see from (8.4.4) and (8.4.5), calculating the microscale interface integrals $\mathcal{I}_J$ and $\mathcal{I}_F$ does not require additional computational effort. We only need to identify the fine mesh finite elements which have an interface edge. We compute these interface integrals taking c_ε^s from the previous time step. We do this by matching the discretization nodes on the interface in the local electrolyte problems (8.3.2) and in the microscale solid problem (8.2.3). We also take advantage of the matching meshes when we compute the interface integrals over Γ_ε^i in the microscale solid phase problems, because there we need the values of $\left(c_\varepsilon^e\right)^H$ on the interface.

For the microscale reference solution of problem (8.2.1) we apply the standard FEM with linear Lagrange finite elements. For the time discretization we use again the Backward Euler method and we apply Newton-Raphson method for the linearization. The specifics for solving the microscale reference problem are explained in [70]. The linear solver is the preconditioned Stabilized Biconjugate Gradient Method.

8.5 Advantages of the proposed numerical algorithm

Here we summarize the advantages of the proposed numerical upscaling scheme for solving the simplified battery problem (8.2.1):

- The (electrolyte phase) equation coefficients are time-independent and consequently we construct the multiscale basis only once and reuse it at all time steps and all Newton-Raphson iterations
- At each time iteration for the elctrolyte phase we solve a problem with small number of unknowns
- We solve semi-implicit in time the coupled macro-micro problem, which allows the microscale solid phase problems to be solved very efficiently in parallel

Remark: Solving the problem for realistic 3D geometries, where both the electrolyte and the solid are connected domains, introduces additional difficulties. Since we do not have scale separation for the concentration in the solid, one also needs to employ some kind of domain decomposition for the diffusion equation in the solid in order to keep the efficiency of the proposed method.

8.6 Numerical results

We show numerical results for the reference microscale solution and the MsFEM solution to the coupled macro-micro problem after 10 time steps. The size of the time step is $\Delta t = 1$. In Section 8.6.1 we give only qualitative results and in Section 8.6.2 we demonstrate numerical convergence of the method. The diffusion coefficients that we use are

$$k_e = 5, \quad k_s = 0.1 \tag{8.6.1}$$

and the boundary and initial conditions are given by

$$c_0^e = 0.1, \quad c_0^s = -4, \quad C = 20 \tag{8.6.2}$$

Even though we suppose that we do not have scale separation for the concentration c^s in the solid, we can see from the numerical experiments that c^s is actually scale-separable for the considered diffusion coefficients and boundary conditions. However, we solve problem (8.2.1) as if we did not have scale separation for c^s in order to demonstrate the proposed numerical approach.

8.6.1 Qualitative analysis

In Figure 8.2 and Figure 8.3 we give results for the concentration of ions c_ε^e in the electrolyte phase. In the microscale simulation we use approximately 300000 degrees of freedom. In the MsFEM framework we have 25 coarse finite elements K with 9 solid inclusions per element, and with circa 800 degrees of freedom in each perforated coarse grid element. We show the solid phase concentration c_ε^s in Figure 8.4.

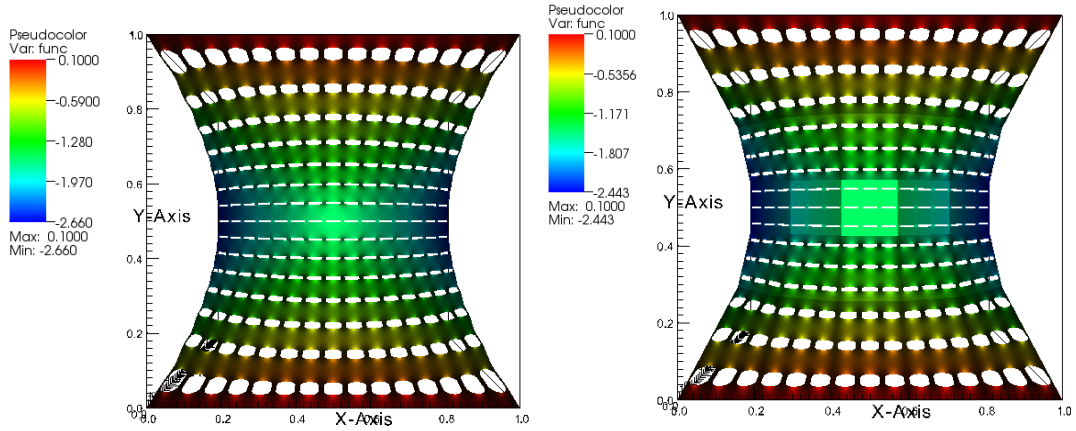

(a) Microscale reference electrolyte solution with minimum value=-2.660

(b) MsFEM electrolyte solution with minimum value=-2.443

Figure 8.2: Electrolyte phase solution

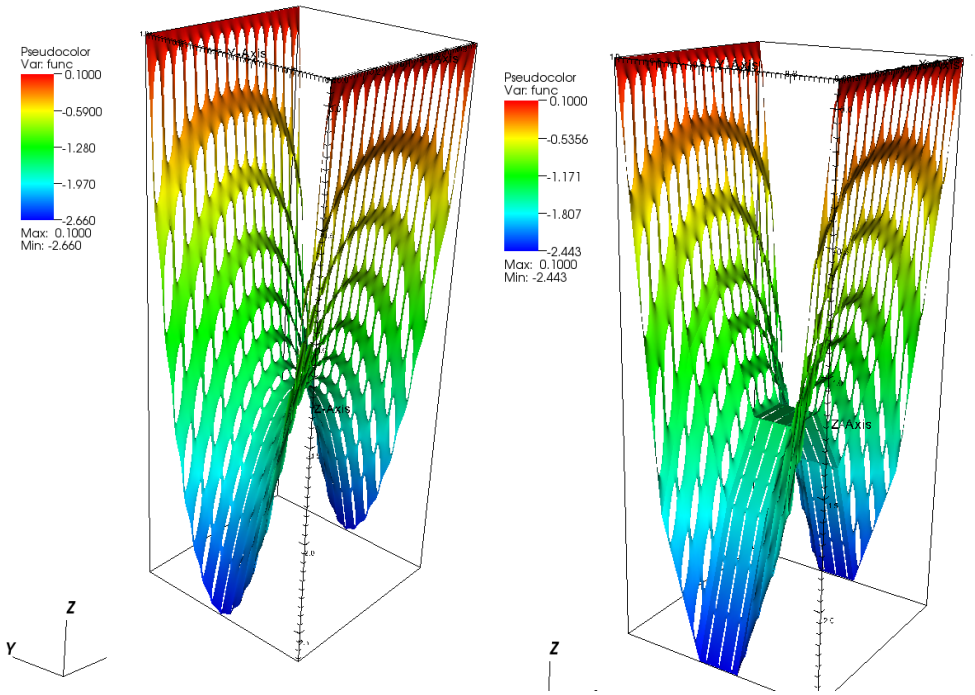

(a) Microscale reference electrolyte solution with minimum value=-2.660

(b) MsFEM electrolyte solution with minimum value=-2.443

Figure 8.3: Electrolyte phase solution: side view

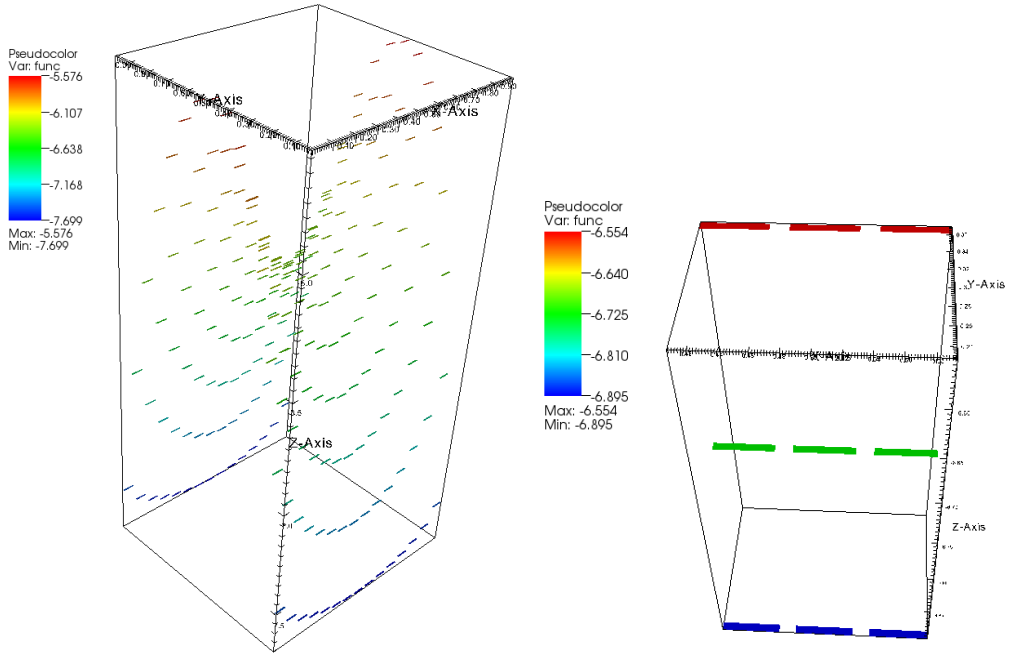

(a) Microscale reference solid solution

(b) MsFEM solid solution in a selected coarse finite element

Figure 8.4: Solid phase solution

8.6.2 Numerical convergence

We calculate the L^2 norms of the difference between the microscale reference electrolyte solution and the MsFEM one. The numerical results show that the electrolyte phase solution obtained with the MsFEM converges to the microscale one with a convergence rate which coincides with the convergence rate from the improved error estimate (6.5.3). In Tables 8.6.1 and 8.6.2 with N_{micro} we denote the number of unknowns that we have for the microscale solution and with n we denote the number of unknowns in a single coarse grid element K.

Fixed $H = \dfrac{1}{16}$ and decreasing ε

As we can see from the results in Table 8.6.1, when we decrease ε, the convergence rate is approximately equal to 1, which is exactly the improved error estimate (6.5.3). The microscale reference solution and the MsFEM one are shown in Figures 8.5, 8.6 and 8.7.

Table 8.6.1: Fixed $H = \dfrac{1}{16}$ and decreasing ε

ε	N_{micro}	n	$\|c_\varepsilon^e - (c_\varepsilon^e)^H\|_{L^2(\Omega)}$	Rate	$\|c_\varepsilon^e - (c_\varepsilon^e)^H\|_\infty$	Rate
$\varepsilon = 1/16$	104358	401	0.4411	-	0.8147	-
$\varepsilon = 1/32$	423336	1625	0.226885	0.96	0.4178	0.96
$\varepsilon = 1/64$	1693147	6574	0.108464	1.06	0.2035	1.04

- $H = \varepsilon = \dfrac{1}{16}$

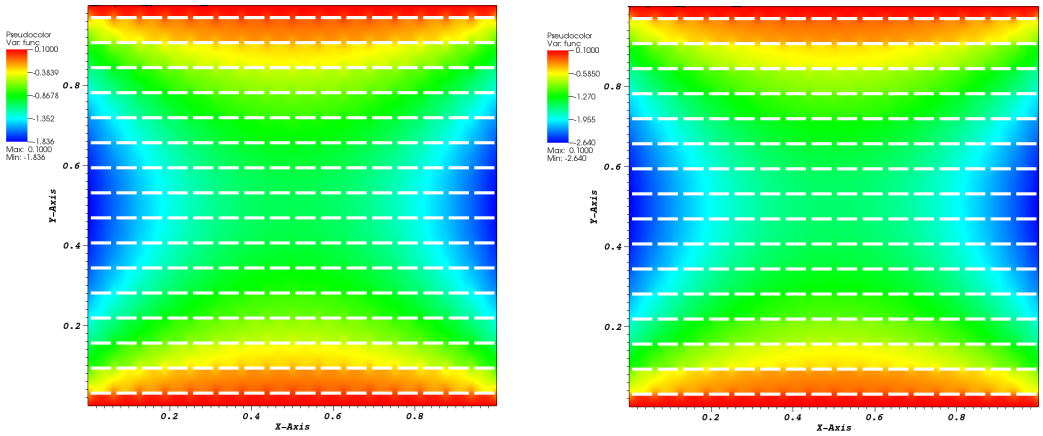

(a) MsFEM electrolyte solution with minimum value=-1.836

(b) Microscale electrolyte solution with minimum value=-2.640

Figure 8.5: Comparison between the microscale reference solution and the MsFEM solution

- $\varepsilon = \dfrac{1}{32}$

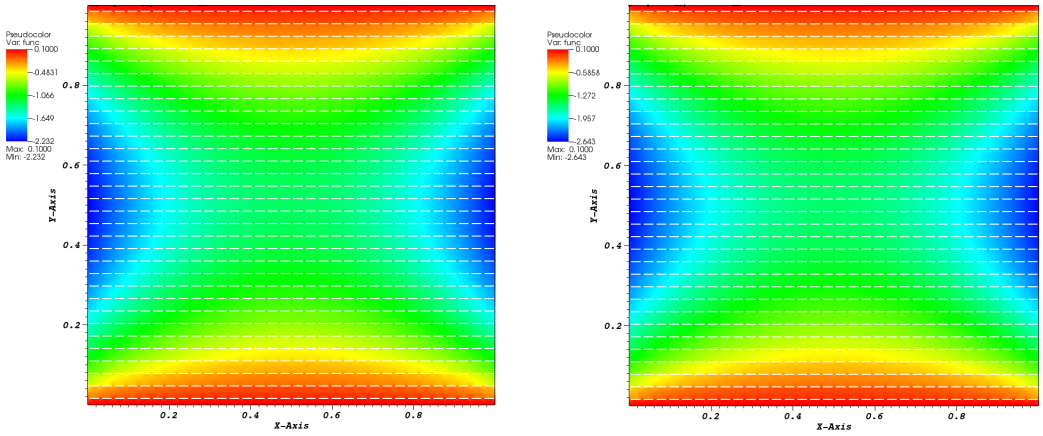

(a) MsFEM electrolyte solution with minimum value=-2.232

(b) Microscale electrolyte solution with minimum value=-2.643

Figure 8.6: Comparison between the microscale reference solution and the MsFEM solution

- $\varepsilon = \dfrac{1}{64}$

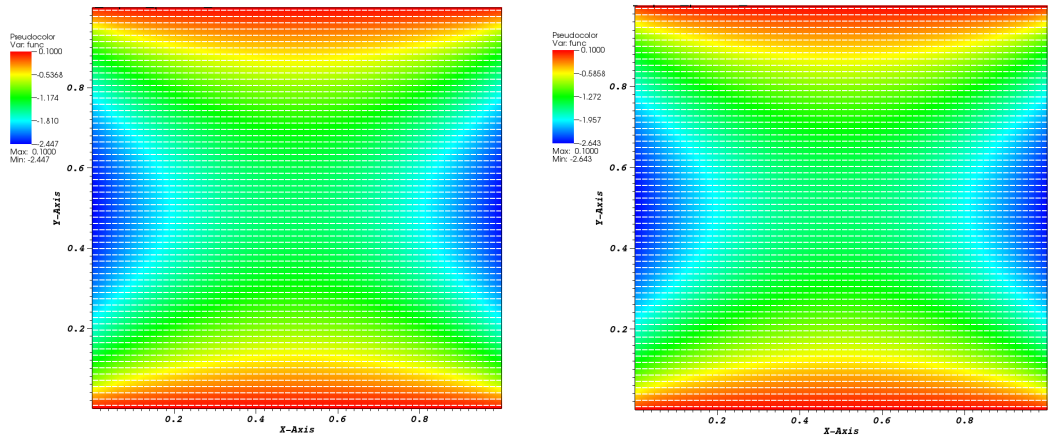

(a) MsFEM electrolyte solution with minimum value=-2.447

(b) Microscale electrolyte solution with minimum value=-2.643

Figure 8.7: Comparison between the microscale reference solution and the MsFEM solution

Fixed $\varepsilon = \dfrac{1}{64}$ and decreasing H

The L^2 norm of the error is given in Table 8.6.2. The convergence rate is around -1 and is in agreement with the improved error estimate (6.5.3). The microscale reference solution and the MsFEM one are shown in Figures 8.8, 8.9, 8.10 and 8.11. As we can see in Figure 8.8, in the case of $H = \dfrac{1}{8}$, i.e., for ε small enough and H sufficiently bigger than ε, with the MsFEM we obtain a very good approximation of the reference microscale solution.

Table 8.6.2: Fixed $\varepsilon = \dfrac{1}{64}$ and decreasing H

ε	N_{micro}	n	$\|c_\varepsilon^e - (c_\varepsilon^e)^H\|_{L^2(\Omega)}$	Rate	$\|c_\varepsilon^e - (c_\varepsilon^e)^H\|_\infty$	Rate
$H = 1/8$	1693147	26426	0.057927	-	0.1985	-
$H = 1/16$	1693147	6574	0.108464	-0.9	0.2035	-0.04
$H = 1/32$	1693147	1627	0.182082	-0.75	0.3294	-0.69
$H = 1/64$	1693147	398	0.439247	-1.27	0.8068	-1.29

- $H = \dfrac{1}{8}$

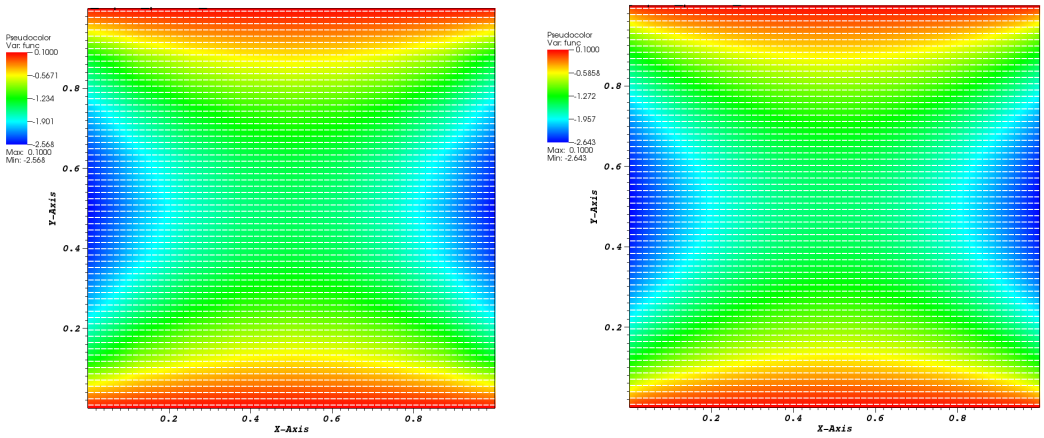

(a) MsFEM electrolyte solution with minimum value=-2.568

(b) Microscale electrolyte solution with minimum value=-2.643

Figure 8.8: Comparison between the microscale reference solution and the MsFEM solution

- $H = \varepsilon = \dfrac{1}{16}$

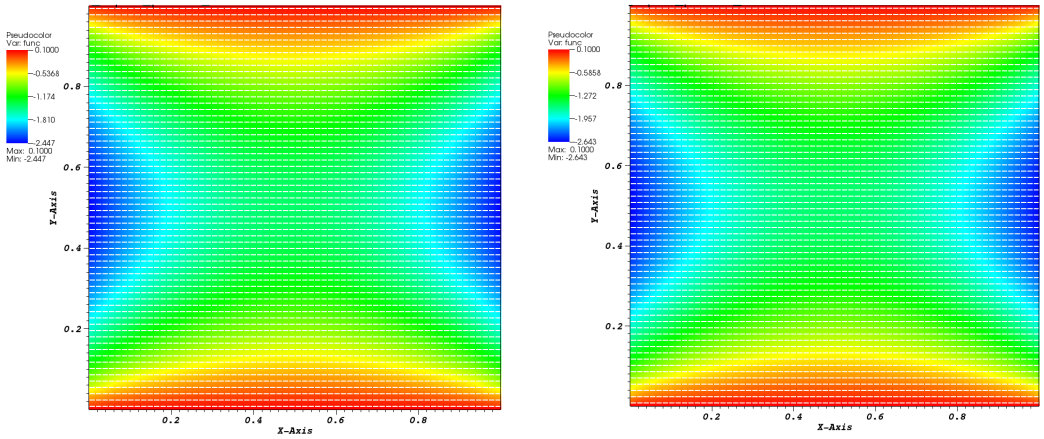

(a) MsFEM electrolyte solution with minimum value=-2.447

(b) Microscale electrolyte solution with minimum value=-2.643

Figure 8.9: Comparison between the microscale reference solution and the MsFEM solution

- $H = \dfrac{1}{32}$

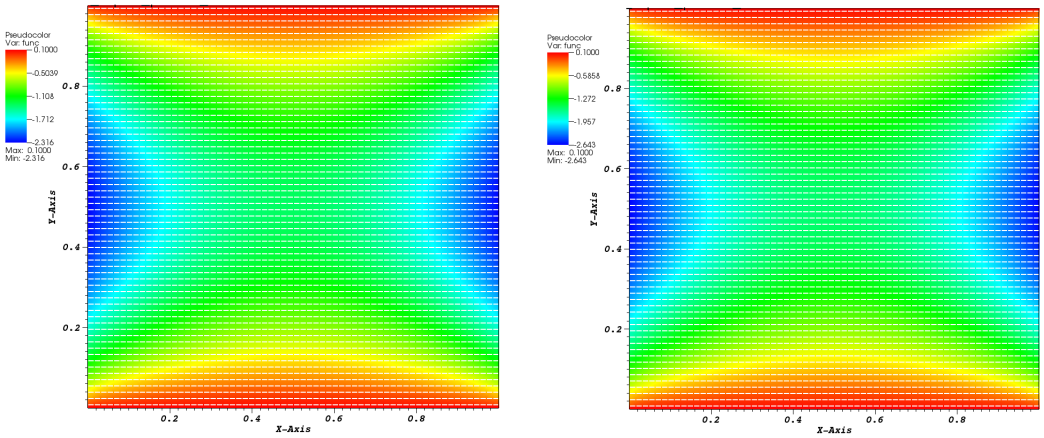

(a) MsFEM electrolyte solution with minimum value=-2.316

(b) Microscale electrolyte solution with minimum value=-2.643

Figure 8.10: Comparison between the microscale reference solution and the MsFEM solution

- $H = \dfrac{1}{64}$

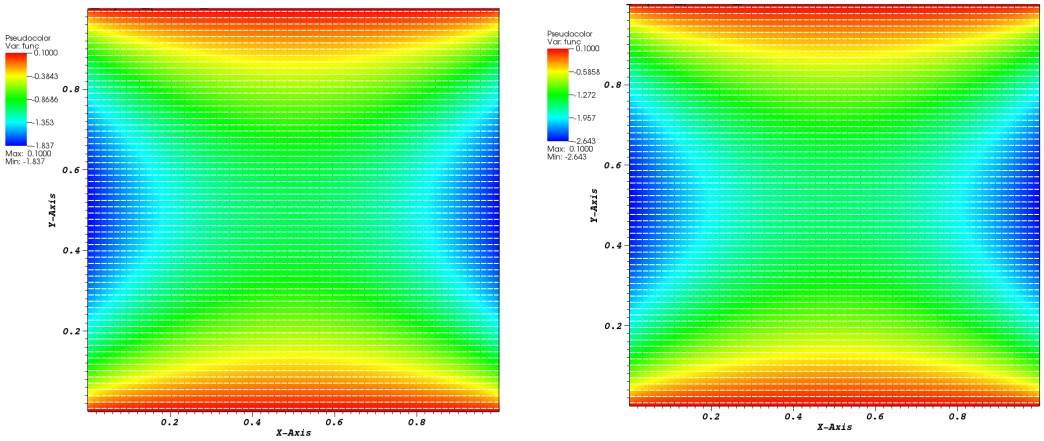

(a) MsFEM electrolyte solution with minimum value=-1.837

(b) Microscale electrolyte solution with minimum value=-2.643

Figure 8.11: Comparison between the microscale reference solution and the MsFEM solution

Chapter 9

Summary

In the current work we considered two upscaling approaches in the context of microscale Lithium-ion battery models - the asymptotic homogenization method and the multiscale finite element method. The two methods are very different in nature and when applying them one should take into account their advantages and disadvantages. Both methods deal with highly oscillating coefficients, with the main difference between them being that the first one handles only periodically oscillating coefficients, whereas the second one can be applied to problems with randomly oscillating coefficients. While the homogenization method is restricted only to periodic media, its main advantage is that it yields to macroscopic partial differential equations with explicit analytical formulas for effective transport coefficients. This makes the method very efficient and fast in terms of memory and computational time. Nevertheless, a serious drawback of the asymptotic homogenization is the rather complicated derivation of the effective macroscale PDEs, especially for more sophisticated problems, such as the considered battery model, where we have two phases coupled by complex and highly nonlinear interface conditions. On the other hand, the multiscale finite element method is based on the finite element method framework, which makes the method flexible and easy applicable to a broad range of problems. Another plus of the method is that it is very suitable for parallel implementations. However, the main disadvantage is that the method requires a lot of computer memory. This is due to the fact that the multiscale basis functions are calculated numerically by solving local boundary value problems and for the numerical integration and the visualization we need to store the solutions of these local problems.

With the help of the asymptotic homogenization method for perforated domains, in the first part of the thesis we derived a coupled macro-micro Li-ion battery model starting from the microscale model in [48]. We conducted a comprehensive numerical study and we showed that the developed upscaled model correctly captures the macroscopic properties of the battery cell electrodes. A major cornerstone in the homogenization procedure was establishing the asymptotic order of the interface exchange current densities, which we managed to rigorously determine. The homogenized battery model allows for fast and efficient numerical simulations, whilst providing a consistent and accurate macroscopic description of the electrochemical processes inside the battery cell. To the best of our knowledge, there are no other numerically investigated and validated upscaled Li-ion battery models, derived for random geometries of the active material in the periodicity

cell and not depending on the applied currents.
The second part of the thesis was devoted to the upscaling of the considered Li-ion battery model via the MsFEM. In order to apply the MsFEM to the battery problem we had to design a new MsFEM for perforated domains with Neumann boundary condition on the holes. We started from the simplest case of zero Neumann data, continued with nonzero Neumann and finally we considered nonlinear Neumann boundary conditions equivalent to the interface conditions (2.5.2) from the microscale Li-ion battery model. We showed numerical convergence of the proposed upscaling algorithm for different test cases. Finally, we solved a simplified two-dimensional Li-ion battery problem with the already developed MsFEM for perforated domains. The next step will be to extend the designed upscaling approach for solving the real three-dimensional Li-ion battery model. The main framework will be the same as in the case of the 2D simplified battery problem, except for the domain decomposition of the microscale problem for the concentration c^s of ions in the solid phase. Since in 3D the active material is a connected domain, a special care must be taken regarding what boundary conditions to be imposed for c^s on the faces of the coarse finite elements.
The developed MsFEM framework for perforated domains with Neuamann boundary condition on the holes is not restricted to Li-ion battery models and can be applied to different physical problems arising in domains with holes.

Appendix A

Numerical Results for MsFEM in Perforated Domains

A.1 Zero Neumann boundary condition on the holes

A.1.1 Numerical results for holes entirely included in the coarse grid finite elements

Fixed $H = \frac{1}{4}$ and decreasing ε

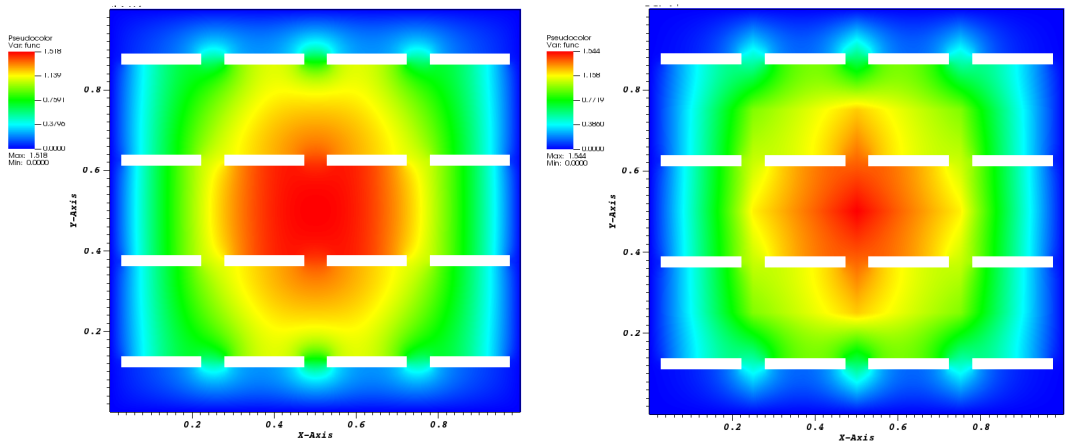

(a) Microscale solution with maximum=1.518 (b) MsFEM solution with maximum=1.544

Figure A.1: Comparison between the microscale and the MsFEM solution for $\varepsilon = H = \frac{1}{4}$

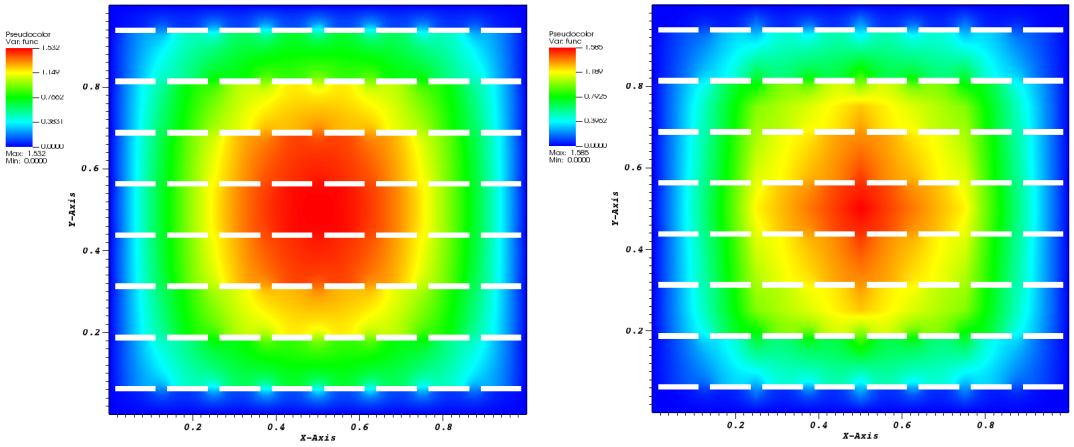

(a) Microscale solution with maximum=1.532 (b) MsFEM solution with maximum=1.585

Figure A.2: Comparison between the microscale and the MsFEM solution for $\varepsilon = \frac{1}{8}$

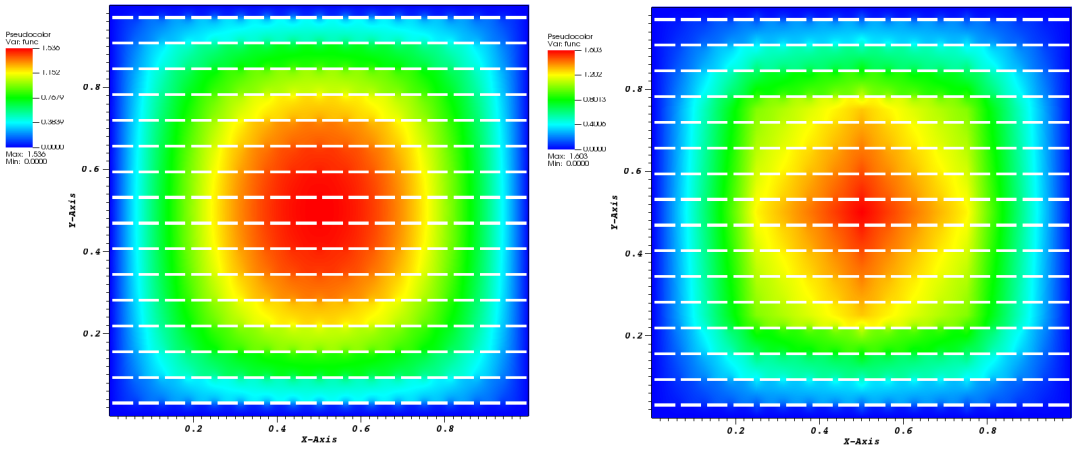

(a) Microscale solution with maximum=1.536 (b) MsFEM solution with maximum=1.603

Figure A.3: Comparison between the microscale and the MsFEM solution for $\varepsilon = \frac{1}{16}$

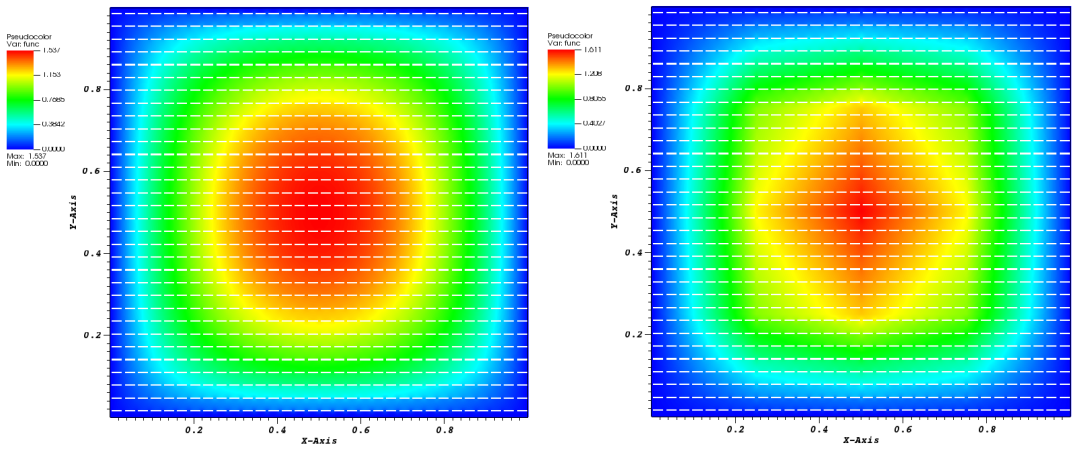

(a) Microscale solution with maximum=1.537 (b) MsFEM solution with maximum=1.611

Figure A.4: Comparison between the microscale and the MsFEM solution for $\varepsilon = \dfrac{1}{32}$

Fixed $H = \dfrac{1}{8}$ and decreasing ε

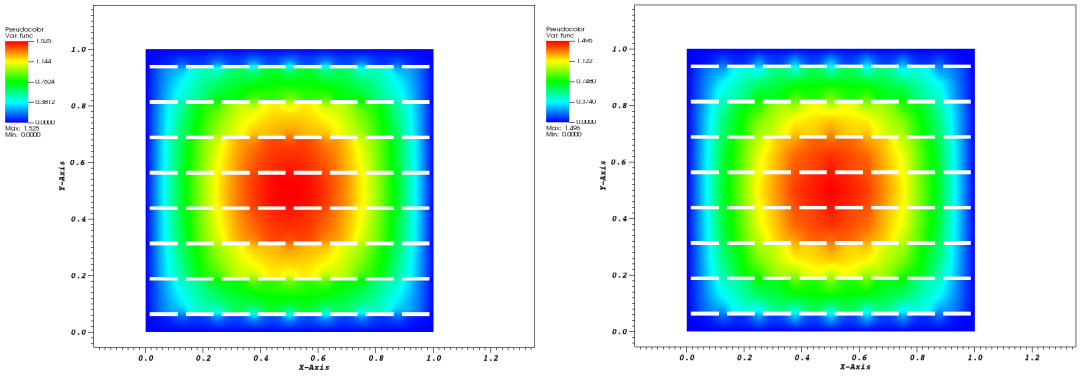

(a) Microscale solution with maximum=1.525 (b) MsFEM solution with maximum=1.496

Figure A.5: Comparison between the microscale and the MsFEM solution for $\varepsilon = H = \dfrac{1}{8}$

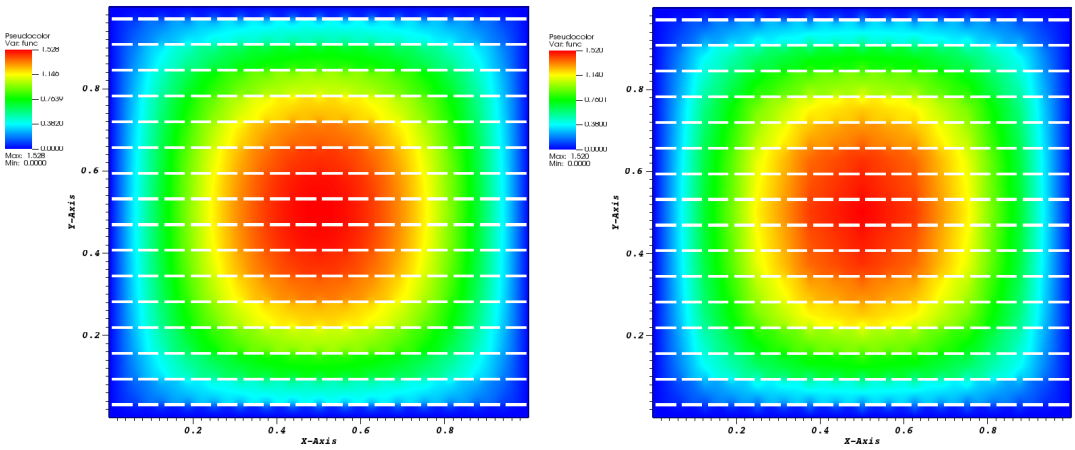

(a) Microscale solution with maximum=1.528 (b) MsFEM solution with maximum=1.520

Figure A.6: Comparison between the microscale and the MsFEM solution for $\varepsilon = \frac{1}{16}$

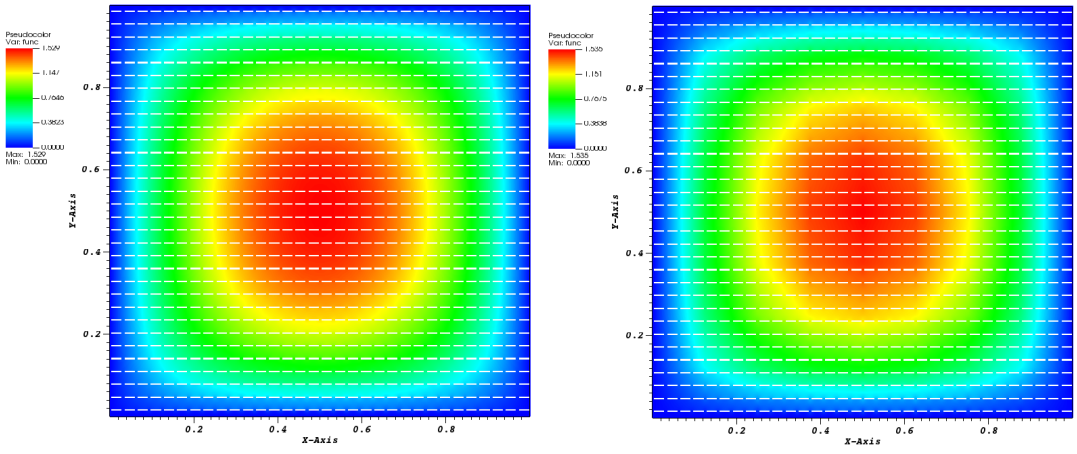

(a) Microscale solution with maximum=1.529 (b) MsFEM solution with maximum=1.535

Figure A.7: Comparison between the microscale and the MsFEM solution for $\varepsilon = \frac{1}{32}$

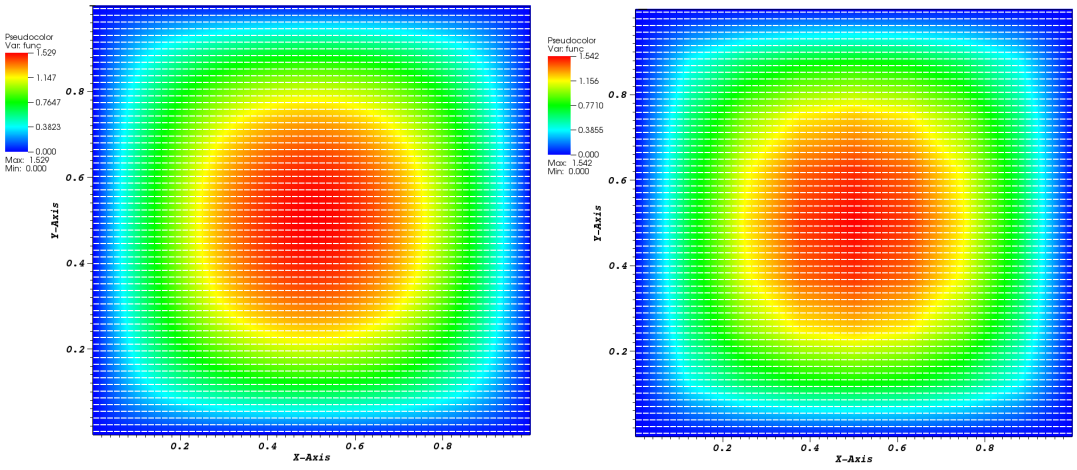

(a) Microscale solution with maximum=1.529 (b) MsFEM solution with maximum=1.542

Figure A.8: Comparison between the microscale and the MsFEM solution for $\varepsilon = \frac{1}{64}$

Fixed $H = \frac{1}{16}$ and decreasing ε

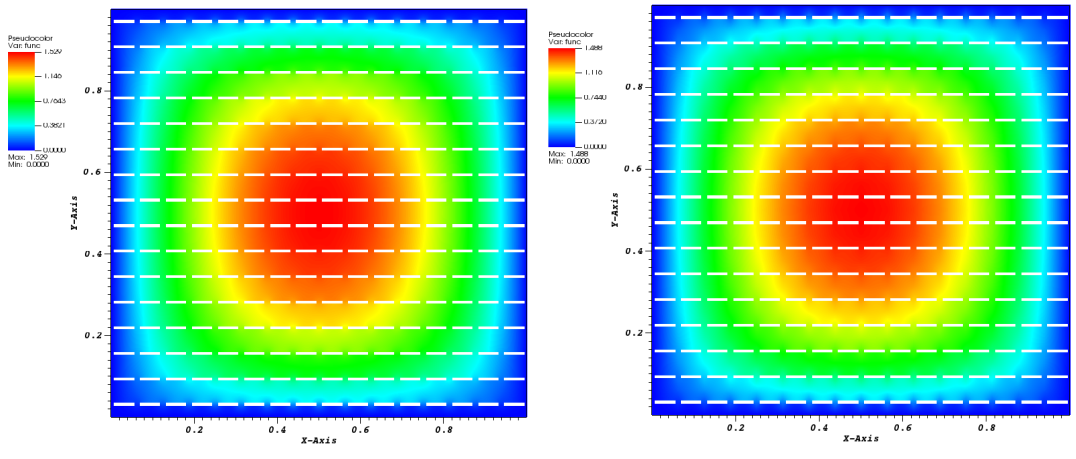

(a) Microscale solution with maximum=1.529 (b) MsFEM solution with maximum=1.488

Figure A.9: Comparison between the microscale and the MsFEM solution for $\varepsilon = H = \frac{1}{16}$

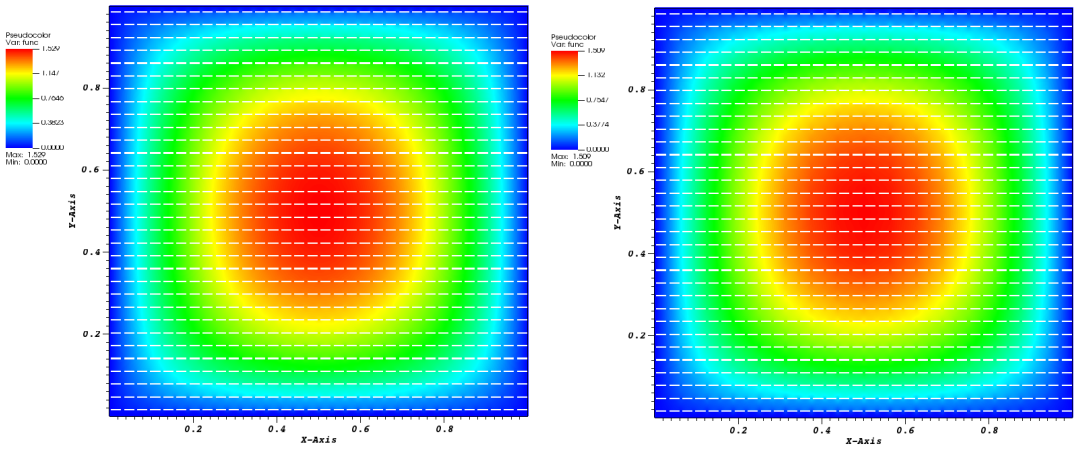

(a) Microscale solution with maximum=1.529 (b) MsFEM solution with maximum=1.509

Figure A.10: Comparison between the microscale and the MsFEM solution for $\varepsilon = \frac{1}{32}$

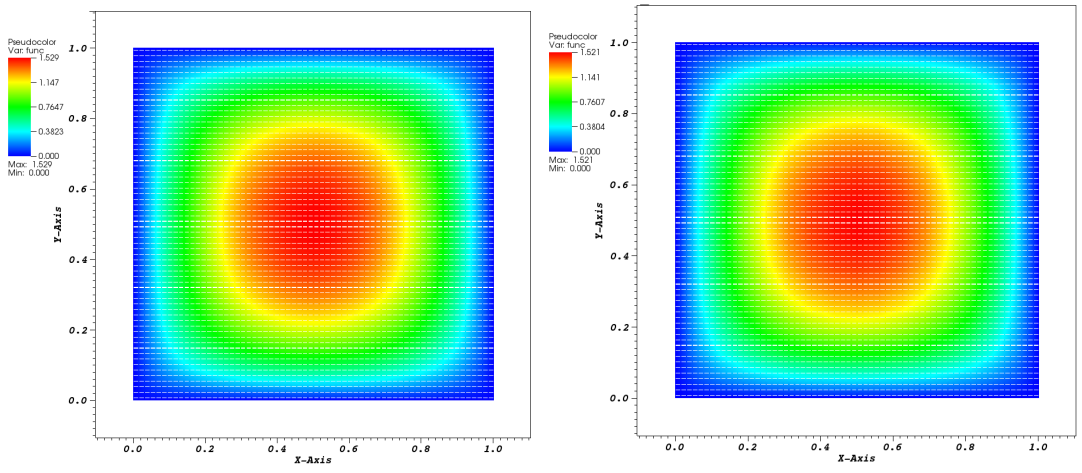

(a) Microscale solution with maximum=1.529 (b) MsFEM solution with maximum=1.521

Figure A.11: Comparison between the microscale and the MsFEM solution for $\varepsilon = \frac{1}{64}$

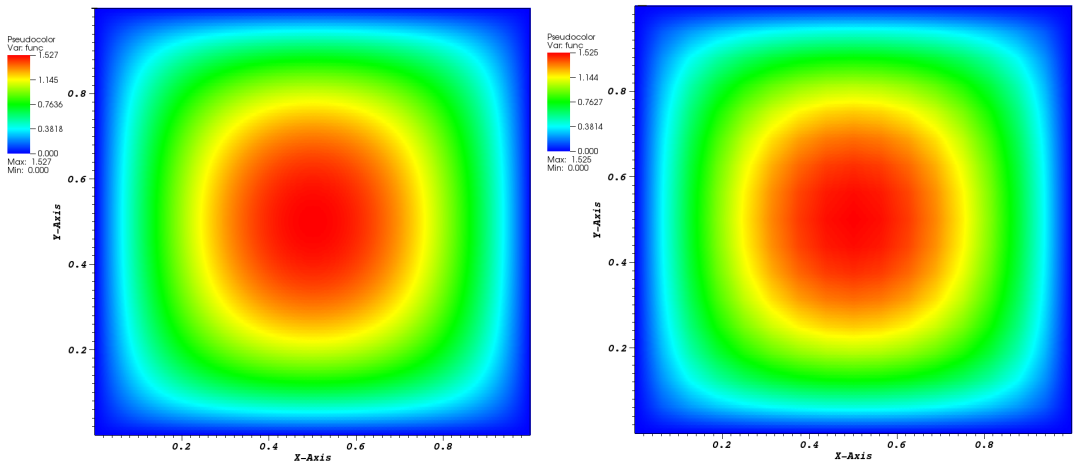

(a) Microscale solution with maximum=1.527 (b) MsFEM solution with maximum=1.525

Figure A.12: Comparison between the microscale and the MsFEM solution for $\varepsilon = \frac{1}{128}$

Fixed $\varepsilon = \frac{1}{64}$ and decreasing H

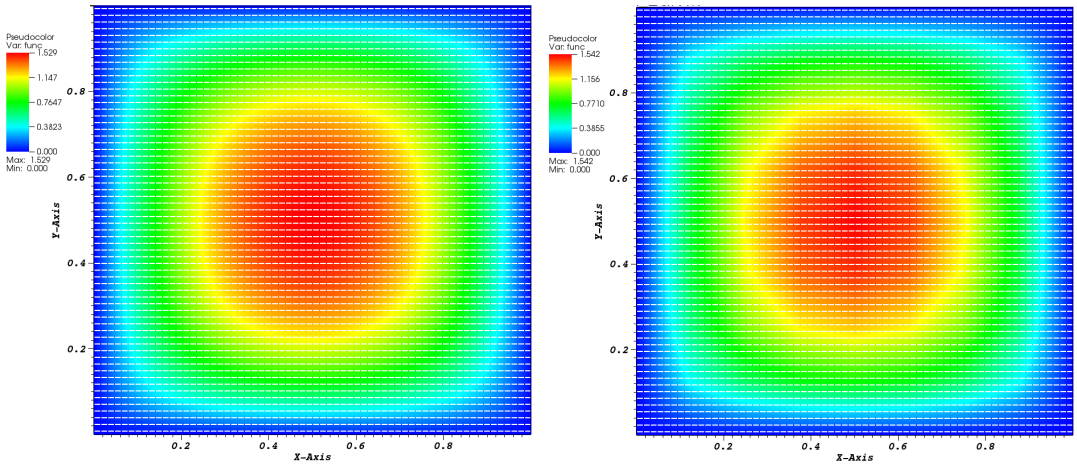

(a) Microscale solution with maximum=1.529 (b) MsFEM solution with maximum=1.542

Figure A.13: Comparison between the microscale and the MsFEM solution for $H = \frac{1}{8}$

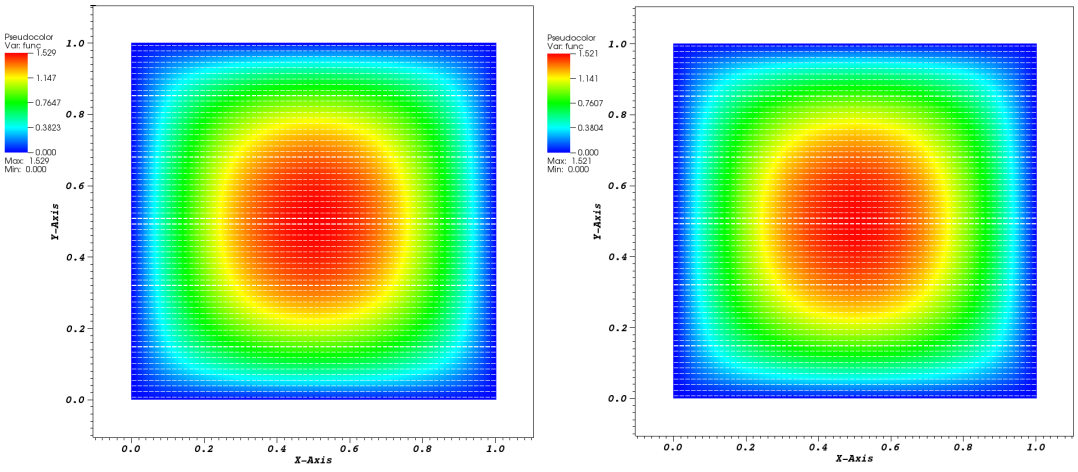

(a) Microscale solution with maximum=1.529 (b) MsFEM solution with maximum=1.521

Figure A.14: Comparison between the microscale and the MsFEM solution for $H = \frac{1}{16}$

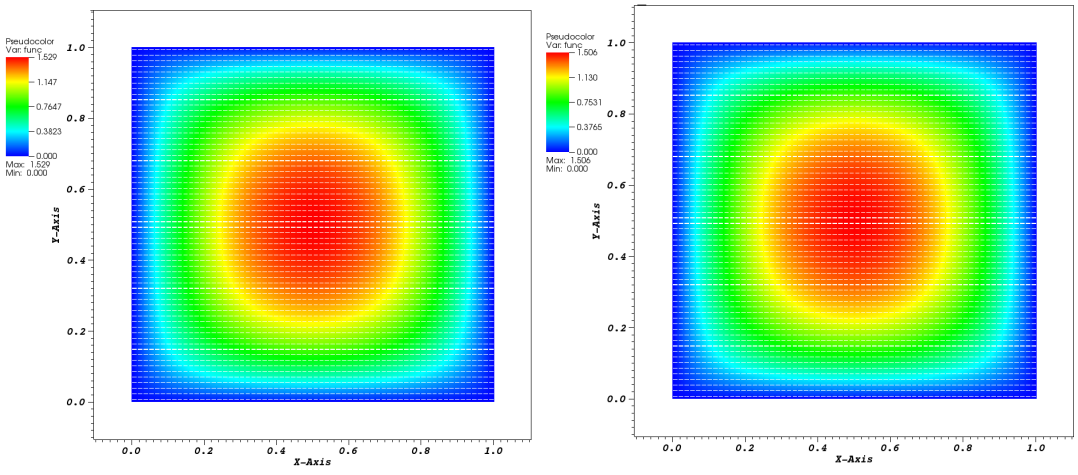

(a) Microscale solution with maximum=1.529 (b) MsFEM solution with maximum=1.506

Figure A.15: Comparison between the microscale and the MsFEM solution for $H = \frac{1}{32}$

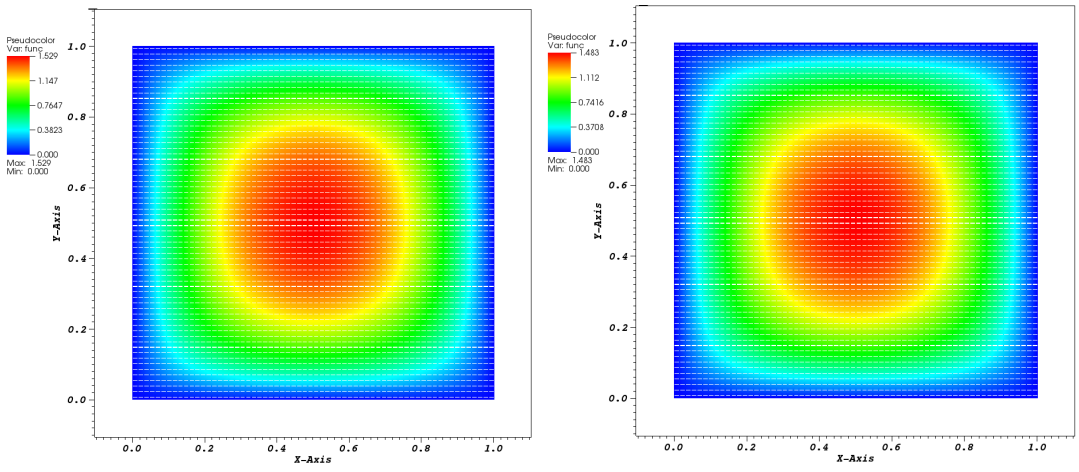

(a) Microscale solution with maximum=1.529 (b) MsFEM solution with maximum=1.483

Figure A.16: Comparison between the microscale and the MsFEM solution for $H = \frac{1}{64}$

Fixed $\varepsilon = \frac{1}{128}$ and decreasing H

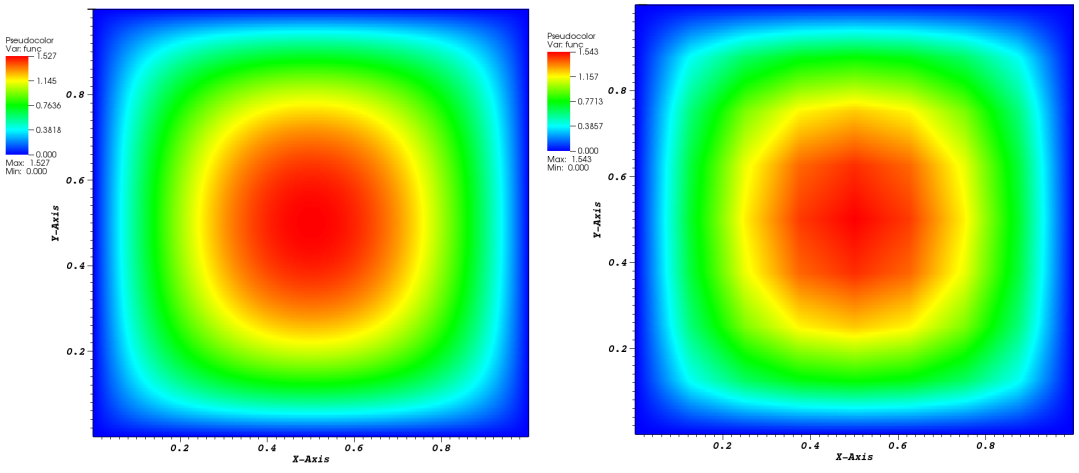

(a) Microscale solution with maximum=1.527 (b) MsFEM solution with maximum=1.543

Figure A.17: Comparison between the microscale and the MsFEM solution for $H = \frac{1}{8}$

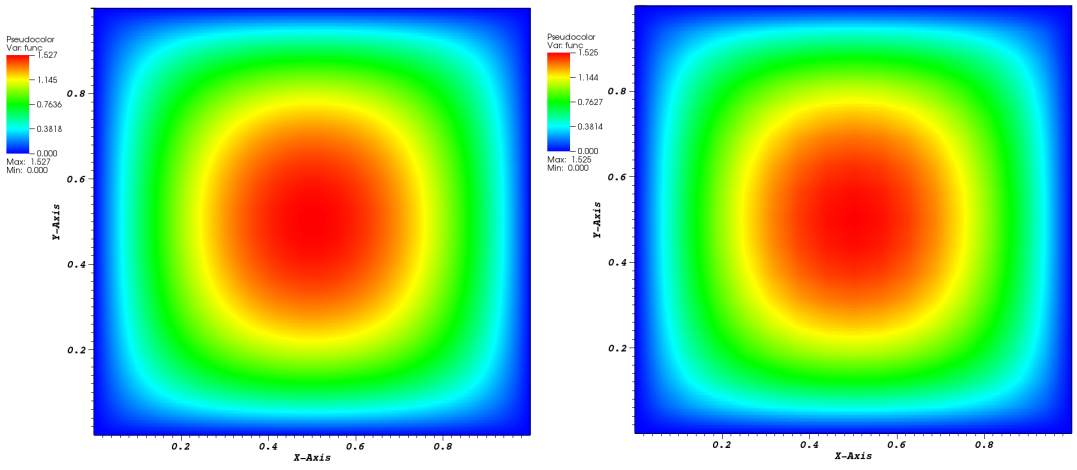

(a) Microscale solution with maximum=1.527 (b) MsFEM solution with maximum=1.525

Figure A.18: Comparison between the microscale and the MsFEM solution for $H = \frac{1}{16}$

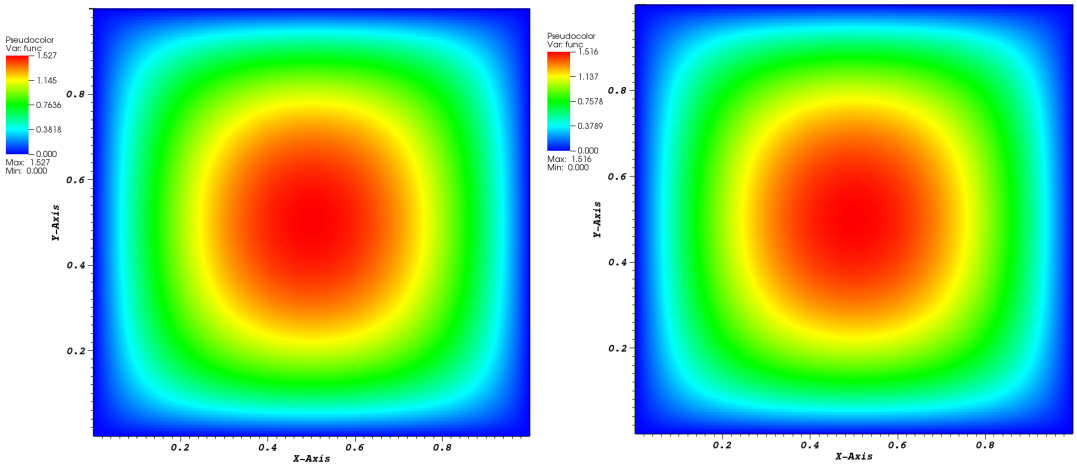

(a) Microscale solution with maximum=1.527 (b) MsFEM solution with maximum=1.516

Figure A.19: Comparison between the microscale and the MsFEM solution for $H = \frac{1}{32}$

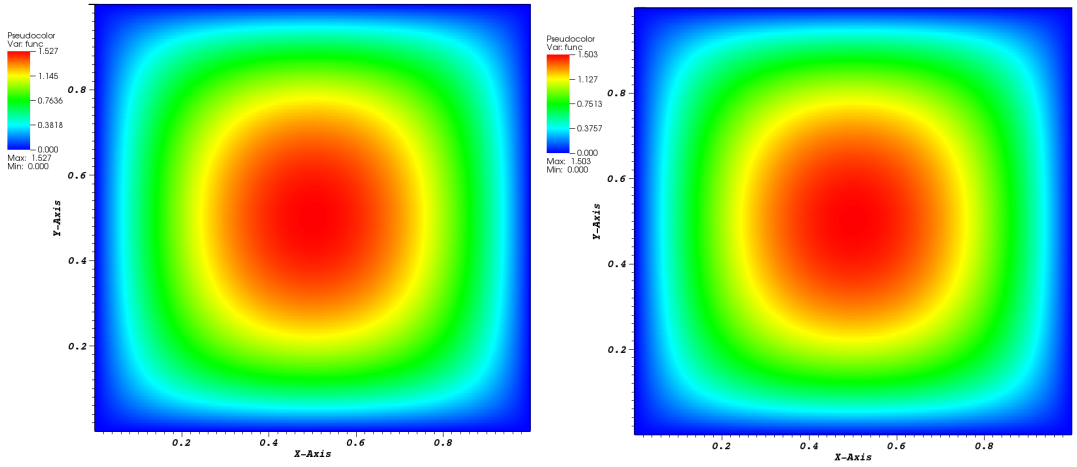

(a) Microscale solution with maximum=1.527 (b) MsFEM solution with maximum=1.503

Figure A.20: Comparison between the microscale and the MsFEM solution for $H = \frac{1}{64}$

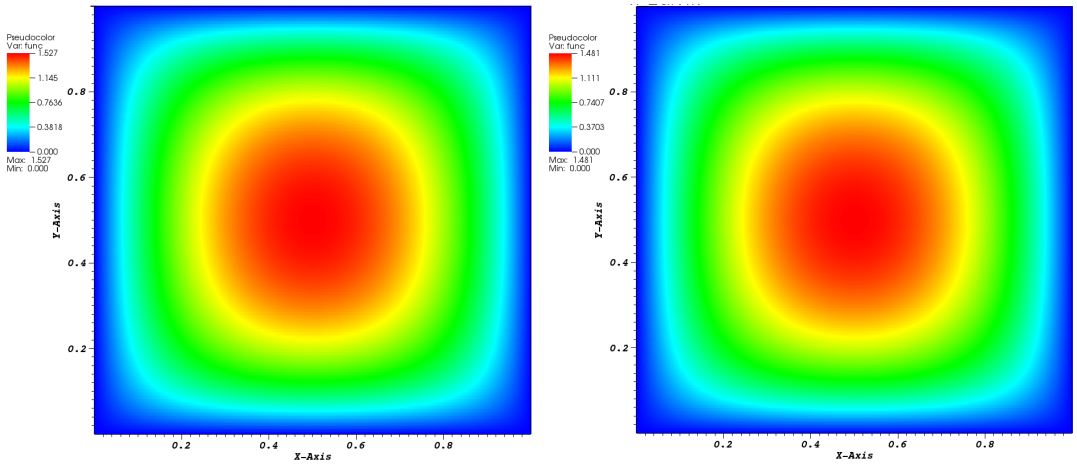

(a) Microscale solution with maximum=1.527 (b) MsFEM solution with maximum=1.481

Figure A.21: Comparison between the microscale and the MsFEM solution for $H = \frac{1}{128}$

A.1.2 Numerical results for holes on the vertices and intersecting the edges of the coarse grid finite elements

Fixed $H = \frac{1}{16}$ and decreasing ε

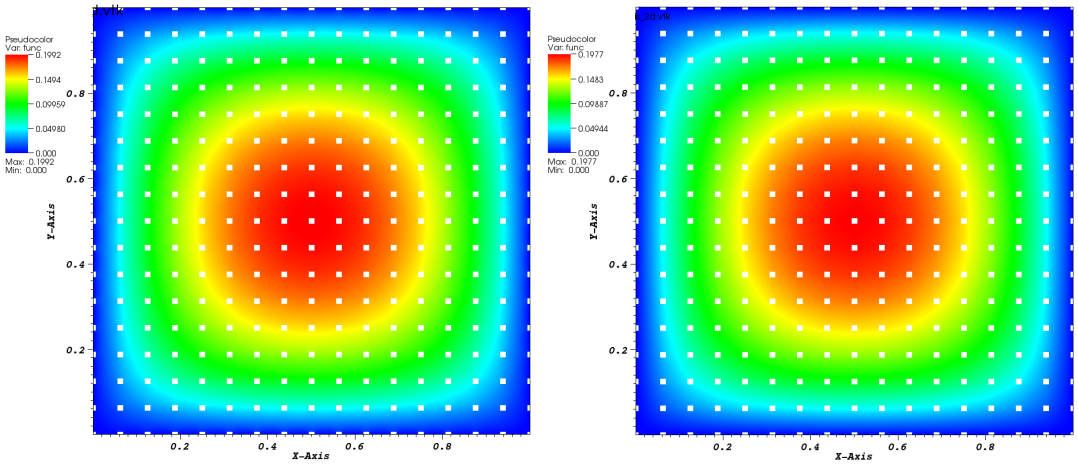

(a) Microscale solution with maximum=0.1992 (b) MsFEM solution with maximum=0.1977

Figure A.22: Comparison between the microscale and the MsFEM solution for $\varepsilon = H = \frac{1}{16}$

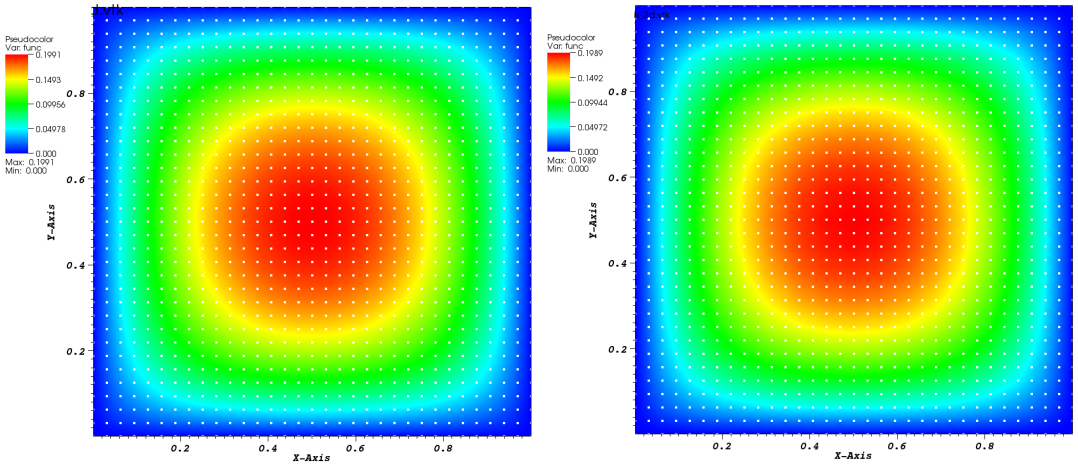

(a) Microscale solution with maximum=0.1991 (b) MsFEM solution with maximum=0.1989

Figure A.23: Comparison between the microscale and the MsFEM solution for $\varepsilon = \frac{1}{32}$

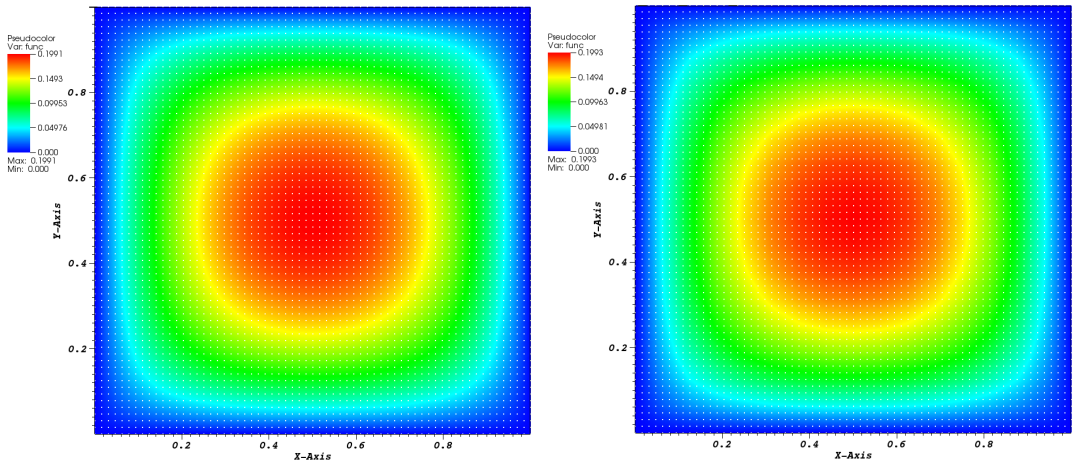

(a) Microscale solution with maximum=0.1991 (b) MsFEM solution with maximum=0.1993

Figure A.24: Comparison between the microscale and the MsFEM solution for $\varepsilon = \frac{1}{64}$

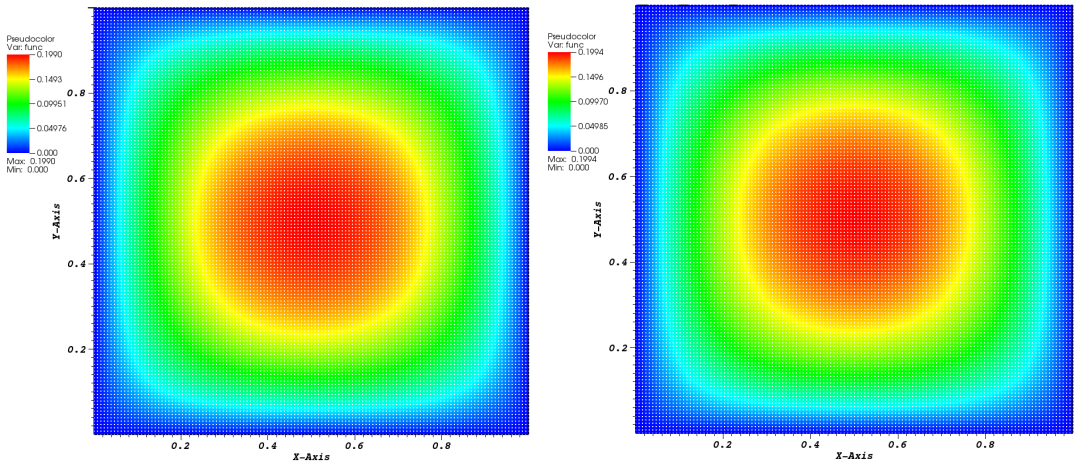

(a) Microscale solution with maximum=0.1990 (b) MsFEM solution with maximum=0.1994

Figure A.25: Comparison between the microscale and the MsFEM solution for $\varepsilon = \frac{1}{128}$

Fixed $\varepsilon = \dfrac{1}{128}$ and decreasing H

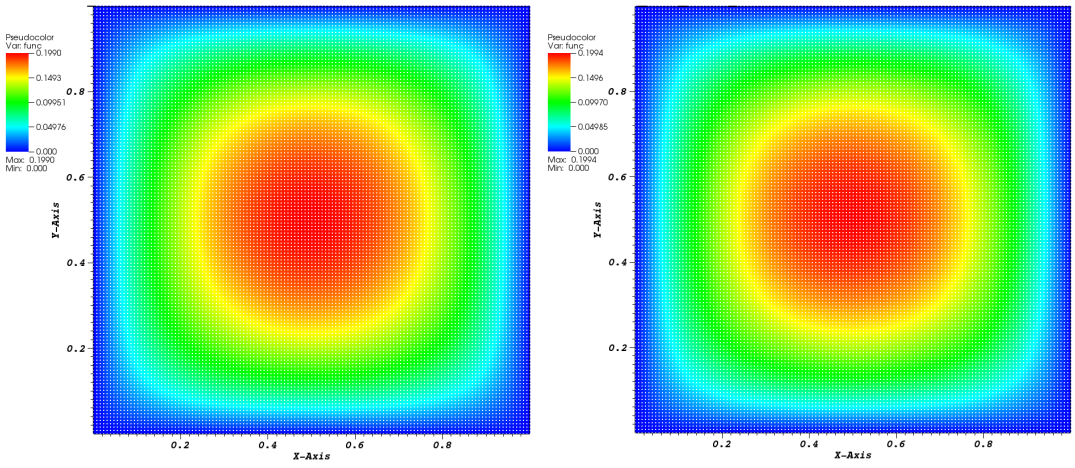

(a) Microscale solution with maximum=0.1990 (b) MsFEM solution with maximum=0.1994

Figure A.26: Comparison between the microscale and the MsFEM solution for $H = \dfrac{1}{16}$

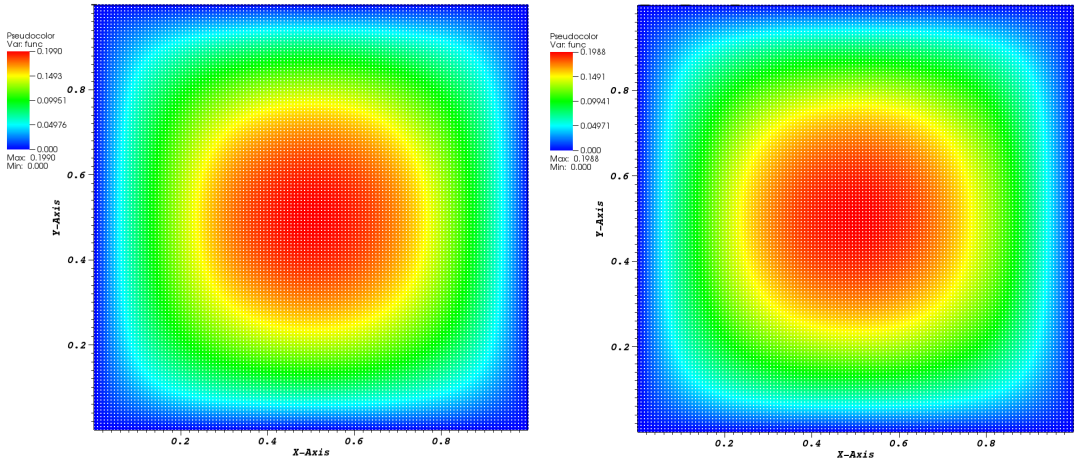

(a) Microscale solution with maximum=0.1990 (b) MsFEM solution with maximum=0.1988

Figure A.27: Comparison between the microscale and the MsFEM solution for $H = \dfrac{1}{32}$

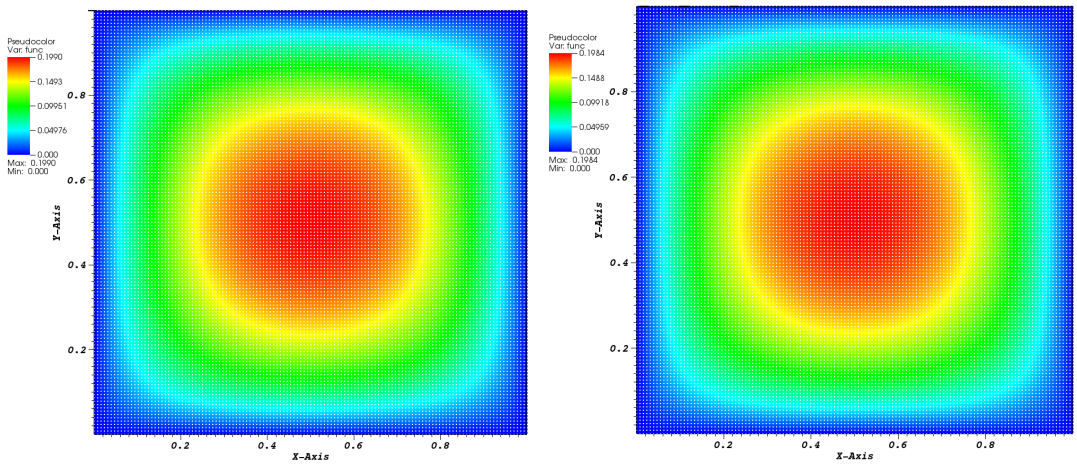

(a) Microscale solution with maximum=0.1990 (b) MsFEM solution with maximum=0.1984

Figure A.28: Comparison between the microscale and the MsFEM solution for $H = \dfrac{1}{64}$

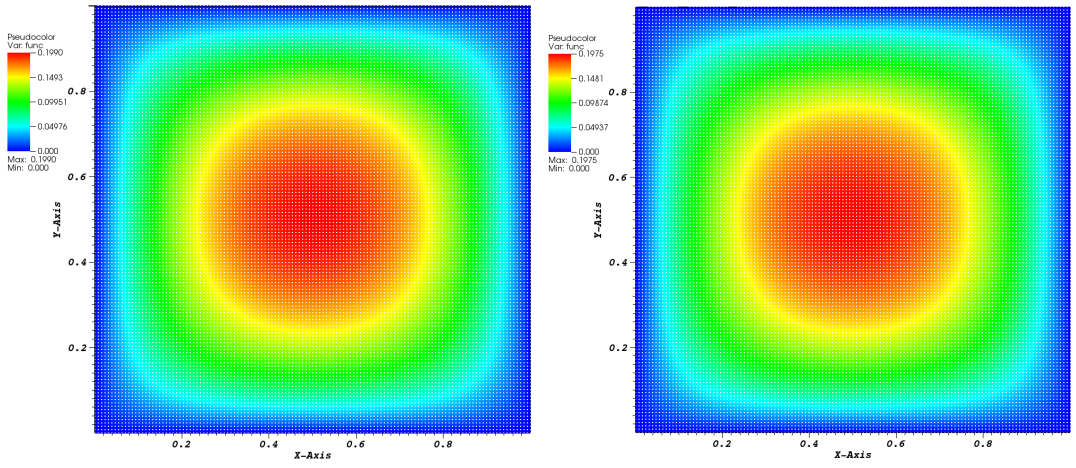

(a) Microscale solution with maximum=0.1990 (b) MsFEM solution with maximum=0.1975

Figure A.29: Comparison between the microscale and the MsFEM solution for $H = \varepsilon = \dfrac{1}{128}$

A.1.3 Numerical results for bigger holes on the vertices and edges of the coarse finite elements

Fixed $H = \frac{1}{16}$ and decreasing ε

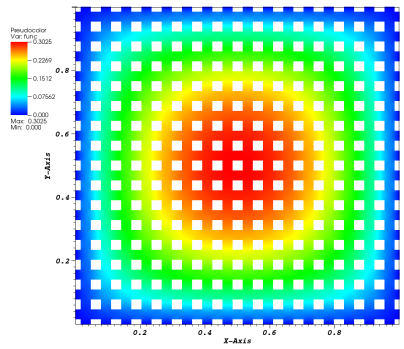

(a) Microscale solution with maximum=0.3025

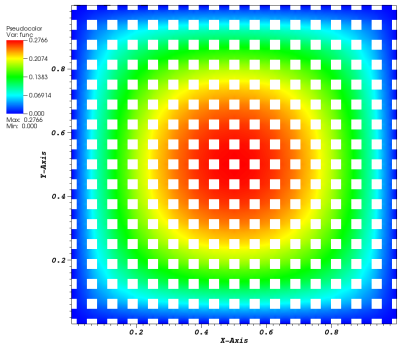

(b) MsFEM solution with maximum=0.2766

Figure A.30: Comparison between the microscale and the MsFEM solution for $H = \varepsilon = \frac{1}{16}$

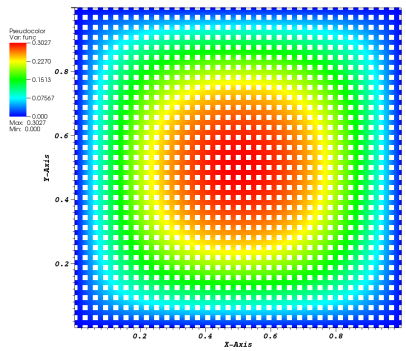

(a) Microscale solution with maximum=0.3027

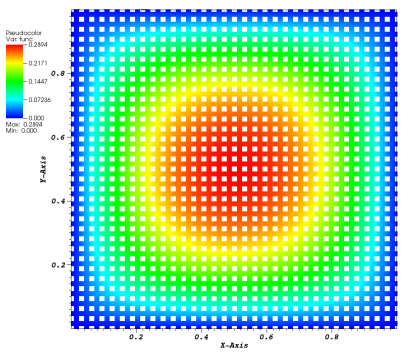

(b) MsFEM solution with maximum=0.2894

Figure A.31: Comparison between the microscale and the MsFEM solution for $H = \frac{1}{16}$ and $\varepsilon = \frac{1}{32}$

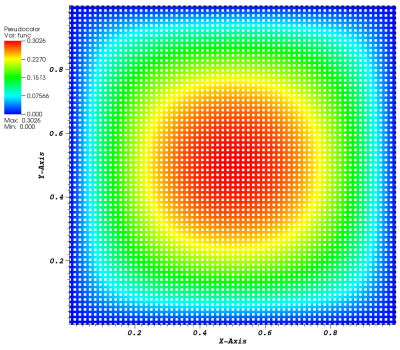

(a) Microscale solution with maximum=0.3026

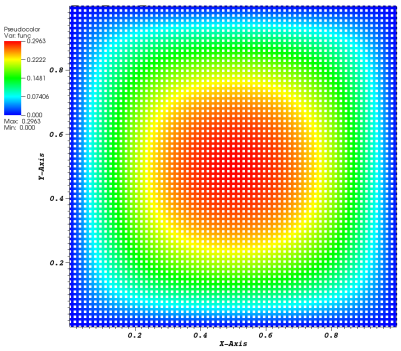

(b) MsFEM solution with maximum=0.2963

Figure A.32: Comparison between the microscale and the MsFEM solution for $H = \frac{1}{16}$ and $\varepsilon = \frac{1}{64}$

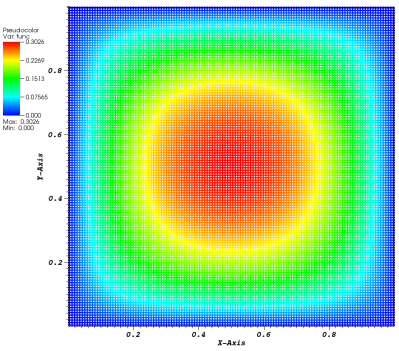

(a) Microscale solution with maximum=0.3026

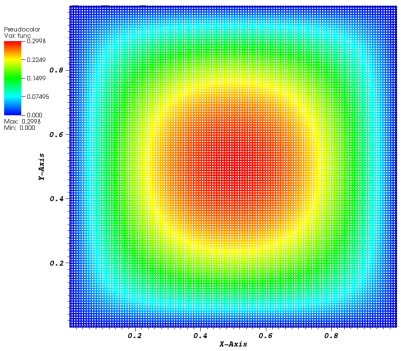

(b) MsFEM solution with maximum=0.2998

Figure A.33: Comparison between the microscale and the MsFEM solution for $H = \frac{1}{16}$ and $\varepsilon = \frac{1}{128}$

Fixed $\varepsilon = \frac{1}{128}$ and decreasing H

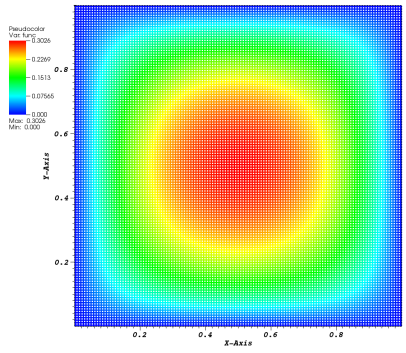

(a) Microscale solution with maximum=0.3026

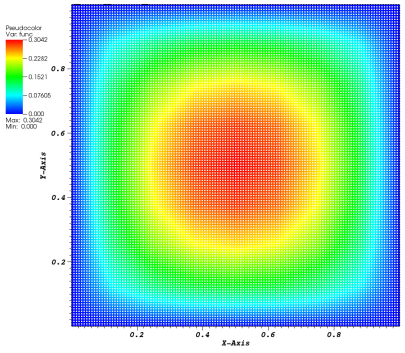

(b) MsFEM solution with maximum=0.3042

Figure A.34: Comparison between the microscale and the MsFEM solution for $H = \frac{1}{8}$

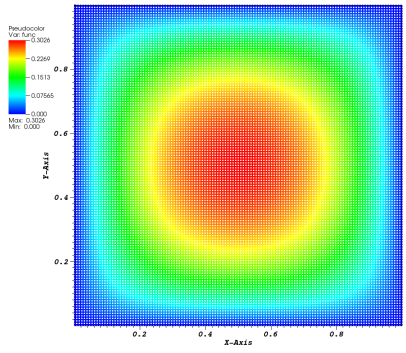

(a) Microscale solution with maximum=0.3026

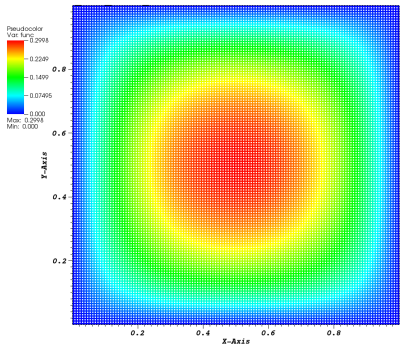

(b) MsFEM solution with maximum=0.2998

Figure A.35: Comparison between the microscale and the MsFEM solution for $H = \frac{1}{16}$

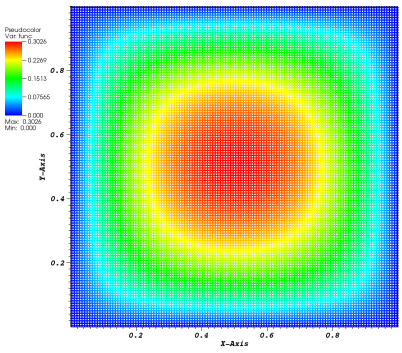

(a) Microscale solution with maximum=0.3026

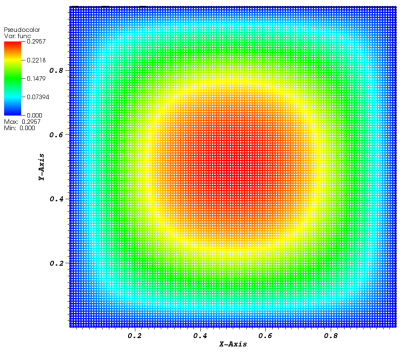

(b) MsFEM solution with maximum=0.2957

Figure A.36: Comparison between the microscale and the MsFEM solution for $H = \frac{1}{32}$

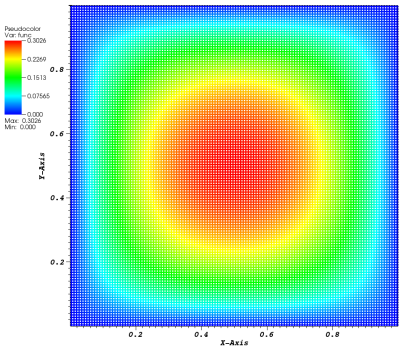

(a) Microscale solution with maximum=0.3026

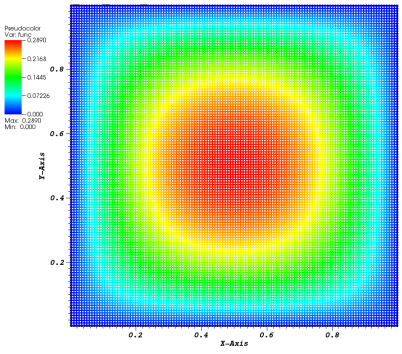

(b) MsFEM solution with maximum=0.2890

Figure A.37: Comparison between the microscale and the MsFEM solution for $H = \frac{1}{64}$

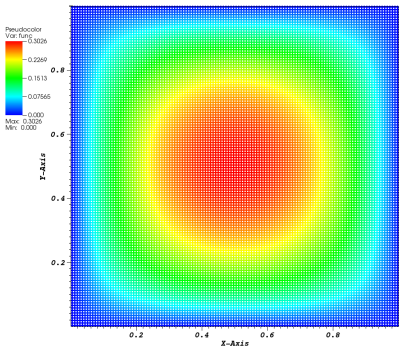

(a) Microscale solution with maximum=0.3026

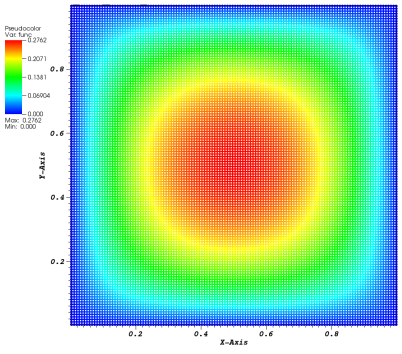

(b) MsFEM solution with maximum=0.2762

Figure A.38: Comparison between the microscale and the MsFEM solution for $H = \frac{1}{128}$

A.2 Nonzero Neumann boundary condition on the holes

A.2.1 Numerical results for perforations entirely included in the coarse grid finite elements

Fixed $H = \frac{1}{16}$ and decreasing ε

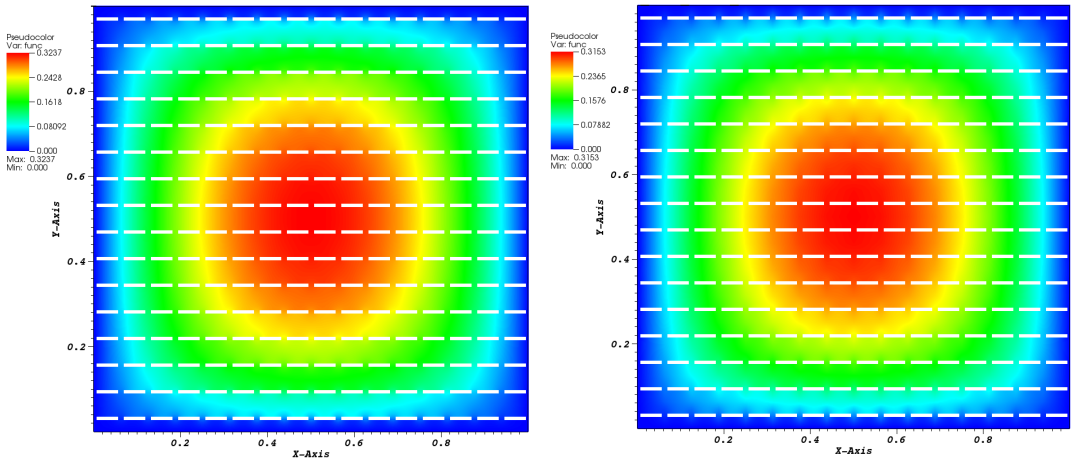

(a) Microscale solution with maximum=0.3237 (b) MsFEM solution with maximum=0.3153

Figure A.39: Comparison between the microscale and the MsFEM solution for $\varepsilon = H = \frac{1}{16}$

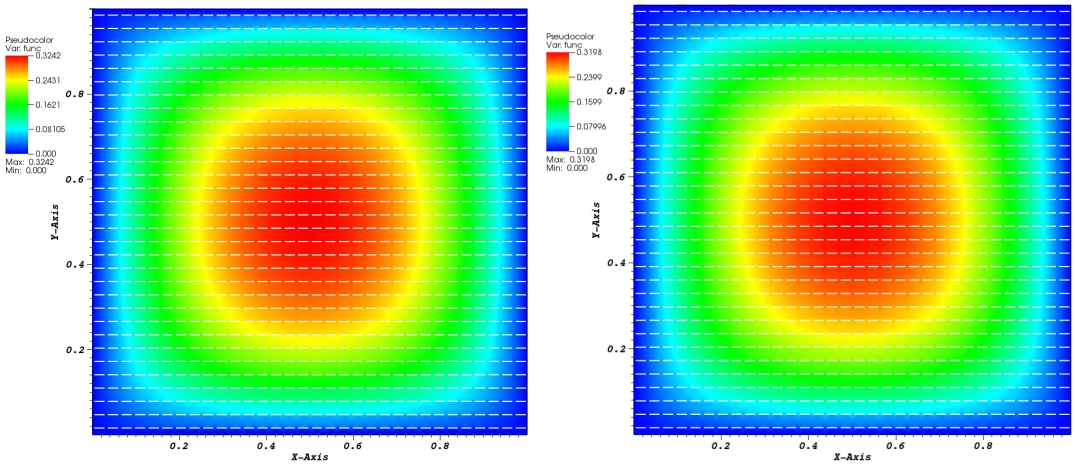

(a) Microscale solution with maximum=0.3242 (b) MsFEM solution with maximum=0.3198

Figure A.40: Comparison between the microscale and the MsFEM solution for $\varepsilon = \frac{1}{32}$

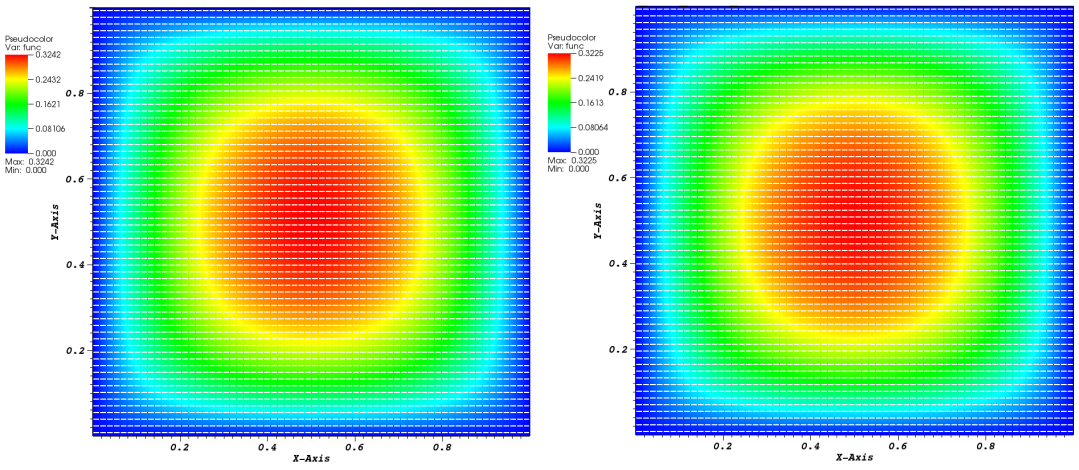

(a) Microscale solution with maximum=0.3242 (b) MsFEM solution with maximum=0.3225

Figure A.41: Comparison between the microscale and the MsFEM solution for $\varepsilon = \frac{1}{64}$

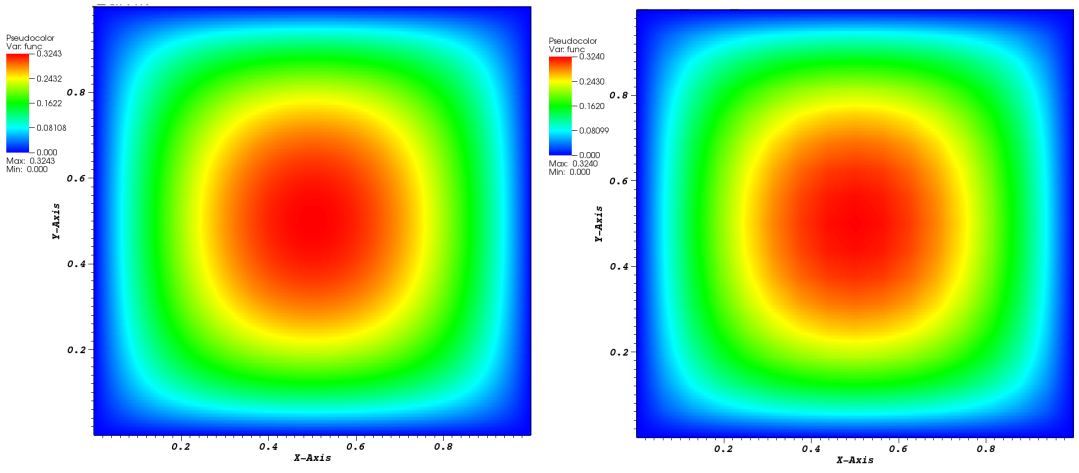

(a) Microscale solution with maximum=0.3243 (b) MsFEM solution with maximum=0.3240

Figure A.42: Comparison between the microscale and the MsFEM solution for $\varepsilon = \frac{1}{128}$

Fixed $\varepsilon = \dfrac{1}{128}$ and decreasing H

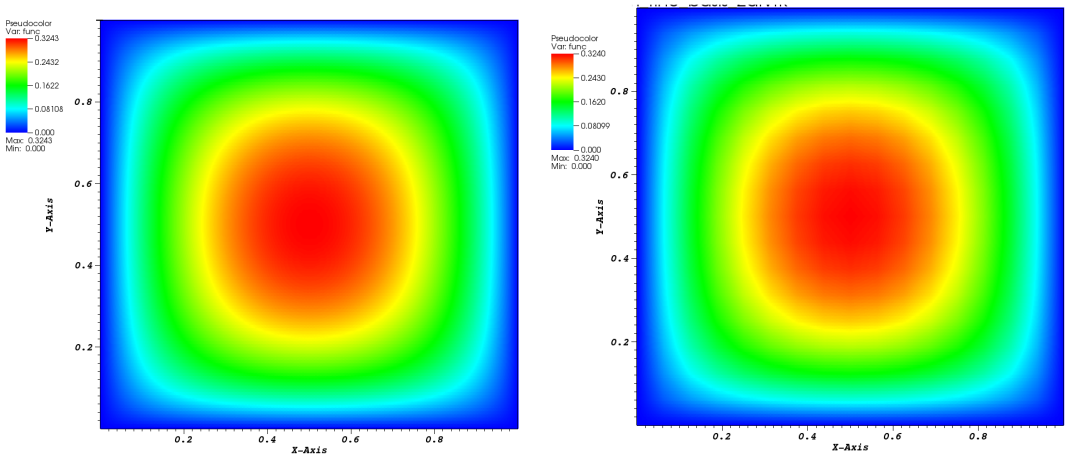

(a) Microscale solution with maximum=0.3243 (b) MsFEM solution with maximum=0.3240

Figure A.43: Comparison between the microscale and the MsFEM solution for $H = \dfrac{1}{16}$

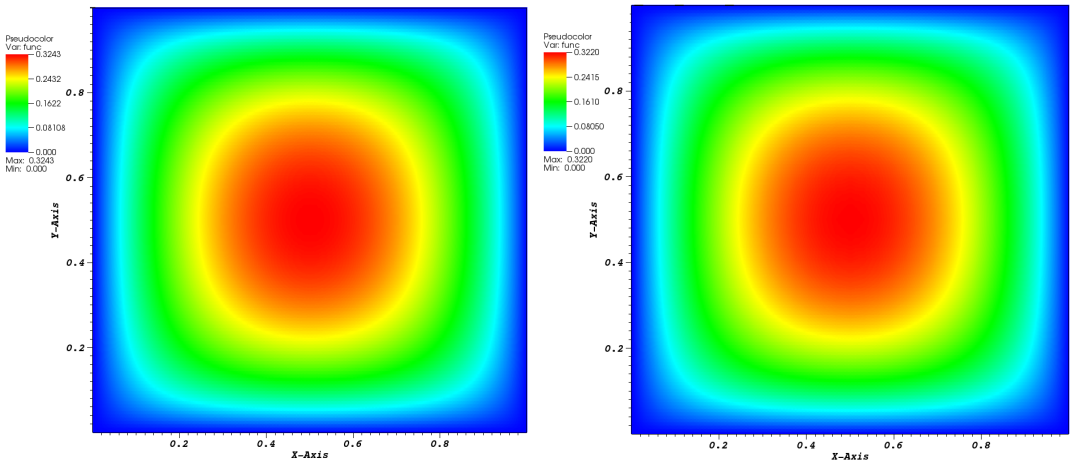

(a) Microscale solution with maximum=0.3243 (b) MsFEM solution with maximum=0.3220

Figure A.44: Comparison between the microscale and the MsFEM solution for $H = \dfrac{1}{32}$

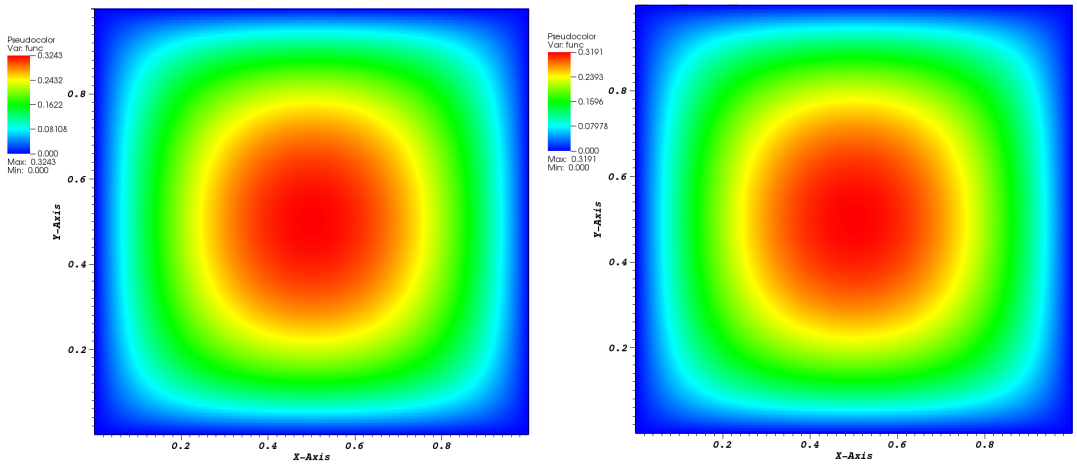

(a) Microscale solution with maximum=0.3243 (b) MsFEM solution with maximum=0.3191

Figure A.45: Comparison between the microscale and the MsFEM solution for $H = \frac{1}{64}$

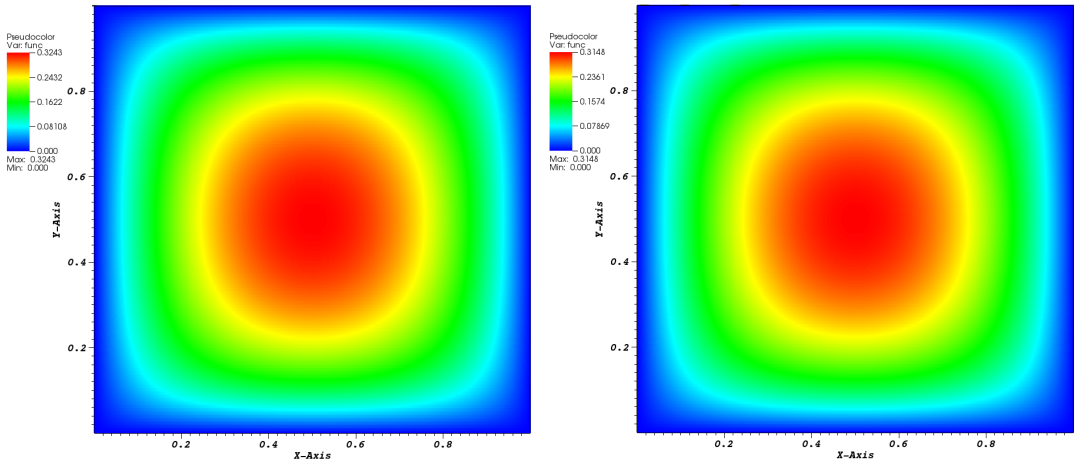

(a) Microscale solution with maximum=0.3243 (b) MsFEM solution with maximum=0.3148

Figure A.46: Comparison between the microscale and the MsFEM solution for $H = \frac{1}{128}$

A.2.2 Numerical results for perforations on the vertices and edges of the coarse grid finite elements

Fixed $H = \frac{1}{16}$ and decreasing ε

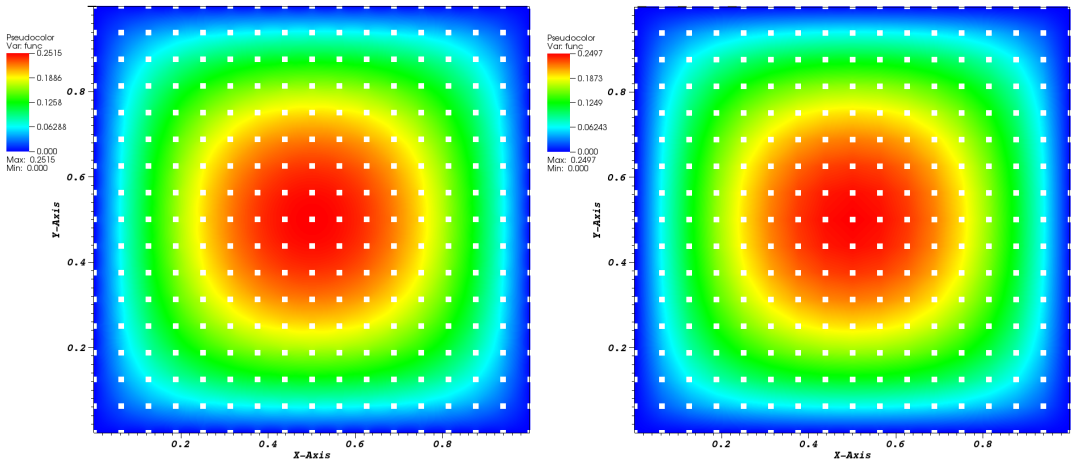

(a) Microscale solution with maximum=0.2515 (b) MsFEM solution with maximum=0.2497

Figure A.47: Comparison between the microscale and the MsFEM solution for $\varepsilon = H = \frac{1}{16}$

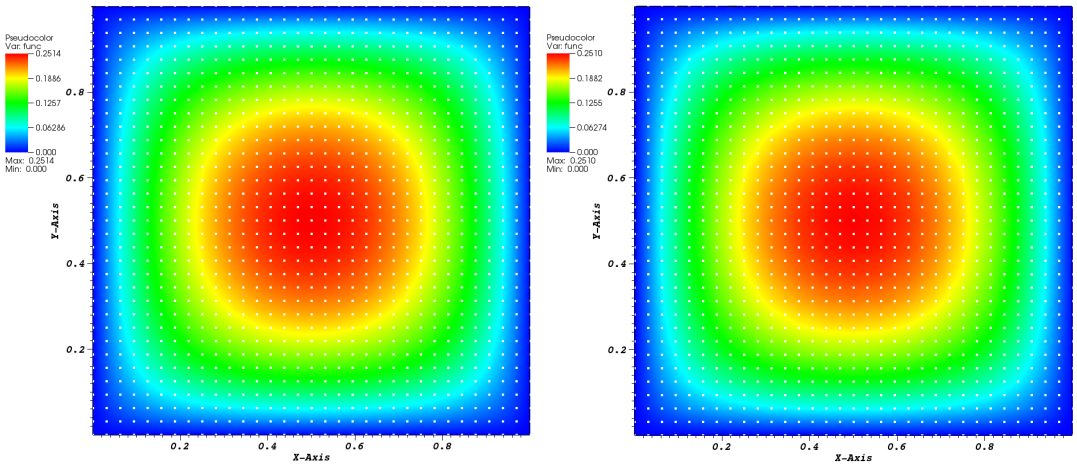

(a) Microscale solution with maximum=0.2514 (b) MsFEM solution with maximum=0.2510

Figure A.48: Comparison between the microscale and the MsFEM solution for $\varepsilon = \frac{1}{32}$

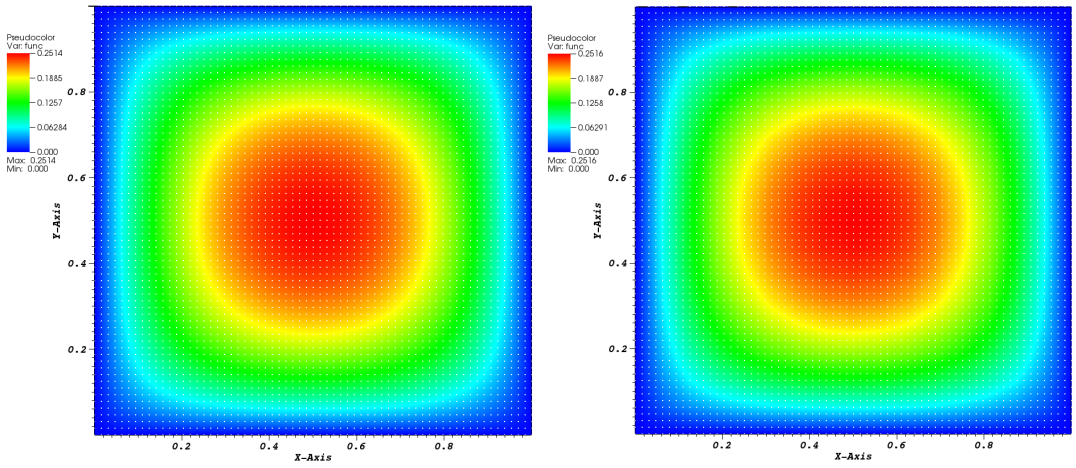

(a) Microscale solution with maximum=0.2514 (b) MsFEM solution with maximum=0.2516

Figure A.49: Comparison between the microscale and the MsFEM solution for $\varepsilon = \frac{1}{64}$

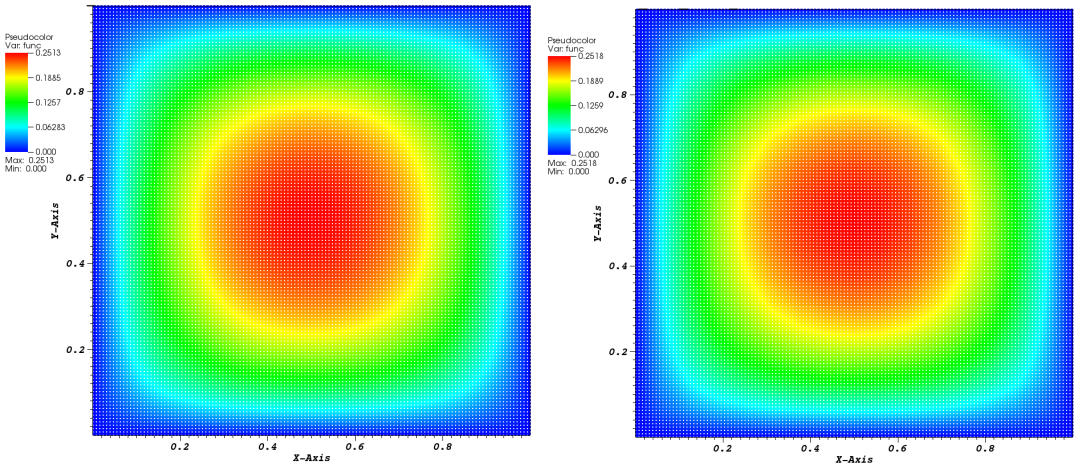

(a) Microscale solution with maximum=0.2513 (b) MsFEM solution with maximum=0.2518

Figure A.50: Comparison between the microscale and the MsFEM solution for $\varepsilon = \frac{1}{128}$

Fixed $\varepsilon = \dfrac{1}{128}$ and decreasing H

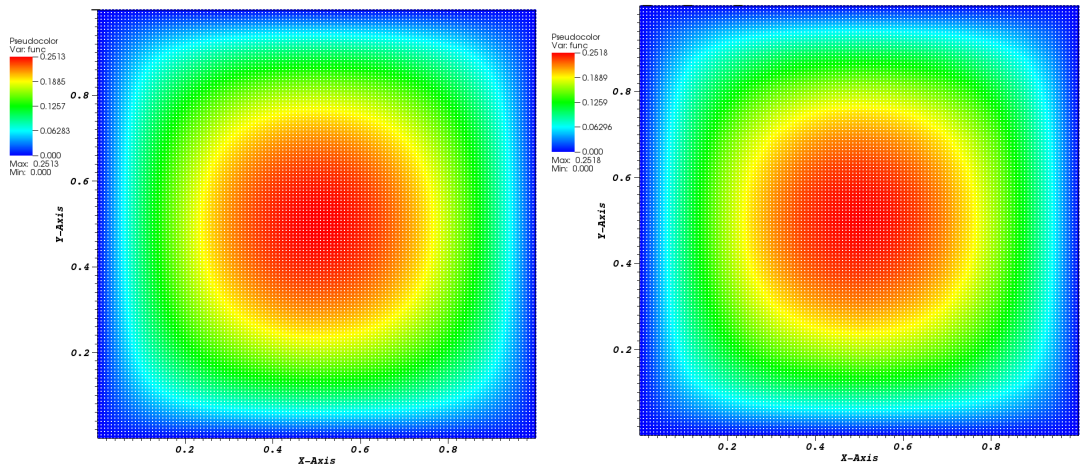

(a) Microscale solution with maximum=0.2513 (b) MsFEM solution with maximum=0.2518

Figure A.51: Comparison between the microscale and the MsFEM solution for $H = \dfrac{1}{16}$

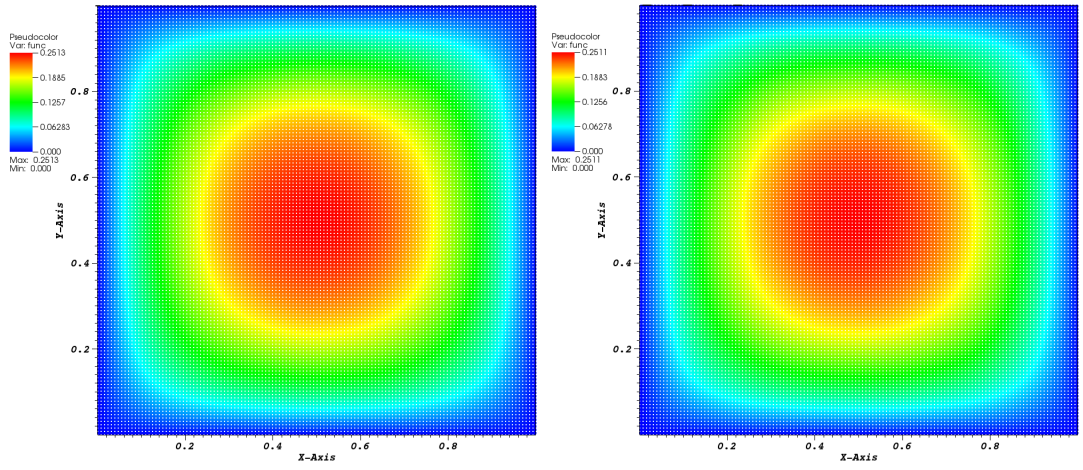

(a) Microscale solution with maximum=0.2513 (b) MsFEM solution with maximum=0.2511

Figure A.52: Comparison between the microscale and the MsFEM solution for $H = \dfrac{1}{32}$

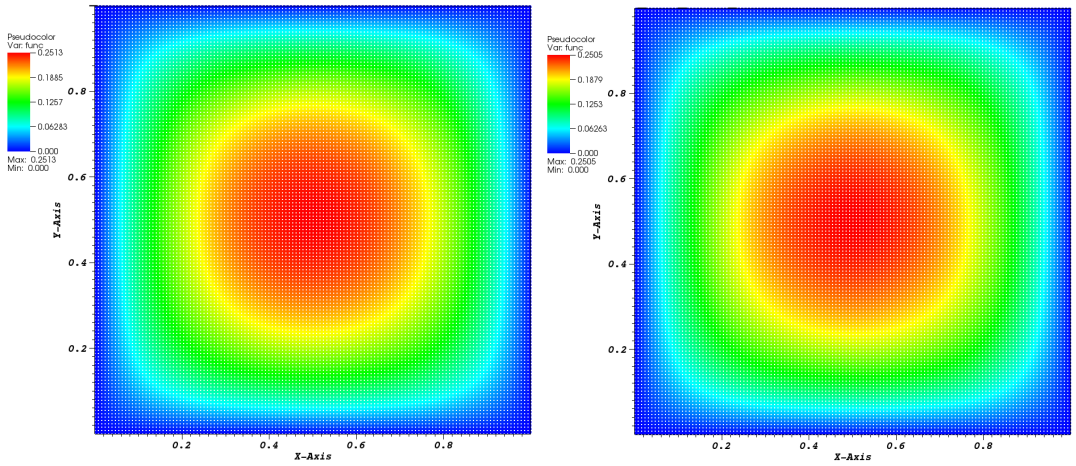

(a) Microscale solution with maximum=0.2513 (b) MsFEM solution with maximum=0.2505

Figure A.53: Comparison between the microscale and the MsFEM solution for $H = \dfrac{1}{64}$

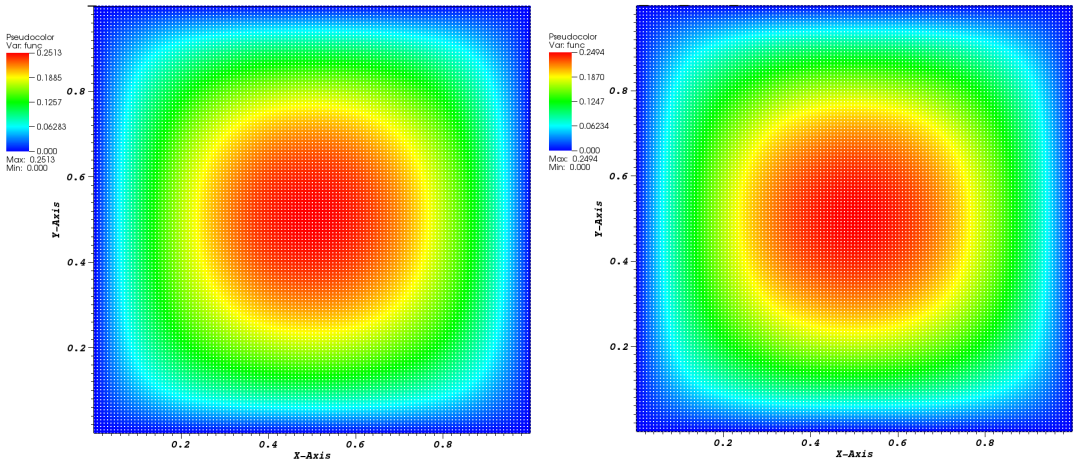

(a) Microscale solution with maximum=0.2513 (b) MsFEM solution with maximum=0.2494

Figure A.54: Comparison between the microscale and the MsFEM solution for $H = \varepsilon = \dfrac{1}{128}$

Bibliography

[1] Physical Analysis of Lithium-ion Battery Electrodes in Non-air Atmosphere. `http://www.kobelcokaken.co.jp/en/example/f/index.html`.

[2] E. Acerbi, G. Dal Maso, D. Percivale, and V. Chiadò Piat. An extension theorem from connected sets, and homogenization in general periodic domains. *Nonlinear Analysis: Theory, Methods and Applications*, 18(5):481–496, March 1992.

[3] G. Allaire. Homogenization and two-scale convergence. *SIAM Journal of Mathematical Analysis*, 23(6):1482–1518, 1992.

[4] G. Allaire and F. Murat. Homogenization of the Neumann problem with nonisolated holes. *Asymptotic Analysis*, 7(2):81–95, 1993.

[5] T. Arbogast, J. Douglas Jr., and U. Hornung. Derivation of the Double Porosity Model of Single Phase Flow via Homogenization Theory. *SIAM Journal of Mathematical Analysis*, 21(4):823–836, 1990.

[6] T. Arbogast, J. Douglas Jr., and U. Hornung. Modeling of Naturally Fractured Reservoirs by Formal Homogenization Techniques. *Frontiers in Pure and Applied Mathematics*, pages 1–19, 1991.

[7] Timothy Barth and Mario Ohlberger. Finite Volume Methods: Foundation and Analysis. In *ENCYCLOPEDIA OF COMPUTATIONAL MECHANICS, VOLUME 1, FUNDAMENTALS*, pages 439–474. John Wiley and Sons Ltd, 2004.

[8] A. Bensoussan, J. L. Lions, and G. Papanicolaou. *Asymptotic Analysis for Periodic Structures*. North-Holland Publishing Company, 1978.

[9] Susanne C. Brenner and L. Ridgway Scott. *The Mathematical Theory of Finite Element Methods*. Springer, 3rd edition, 2008.

[10] C. C. Chu and I. G. Graham and T. Hou. Multiscale Finite Element Method for High-Contrast Elliptic Interface Problems. *Mathematics of Computation*, 79(272):1915–1955, 2010.

[11] C. Le Bris and F. Legoll and A. Lozinski. MsFEM a la Crouzeix-Raviart for Highly Oscillatory Elliptic Problems. *Chinese Annals of Mathematics, Series B*, 34B(1):113–138, 2013.

[12] C. Le Bris and F.Legoll and A.Lozinski. An MsFEM Type Approach for Perforated Domains. *Multiscale Modeling and Simulation*, 12:1046–1077, 2014.

[13] Zhangxin Chen. *Finite Element Methods and Their Applications*. Springer, 2005.

[14] Hank Childs, Eric Brugger, Brad Whitlock, Jeremy Meredith, Sean Ahern, David Pugmire, Kathleen Biagas, Mark Miller, Cyrus Harrison, Gunther H. Weber, Hari Krishnan, Thomas Fogal, Allen Sanderson, Christoph Garth, E. Wes Bethel, David Camp, Oliver Rübel, Marc Durant, Jean M. Favre, and Paul Navrátil. VisIt: An End-User Tool For Visualizing and Analyzing Very Large Data. In *High Performance Visualization–Enabling Extreme-Scale Scientific Insight*, pages 357–372. Chapman and Hall/CRC, Oct 2012.

[15] D. Cioranescu, A. Damlamian, P. Donato, G. Griso, and R. Zaki. The periodic unfolding method in domains with holes. *SIAM Journal of Mathematical Analysis*, 44(2):718–760, 2012.

[16] D. Cioranescu, A. Damlamian, and G. Griso. The Periodic Unfolding Method in Homogenization. *SIAM Journal on Mathematical Analysis*, 40(4):1585–1620, 2008.

[17] D. Cioranescu and P. Donato. *An Introduction to Homogenization*. Oxford University Press, 1999.

[18] D. Cioranescu, P. Donato, and R. Zaki. Periodic unfolding and Robin problems in perforated domains. *Comptes Rendus Mathmatique*, 342(7):469–474, 2006.

[19] D. Cioranescu, P. Donato, and R. Zaki. Asymptotic behaviour of elliptic problems in perforated domains with nonlinear boundary conditions. *Asymptotic Analysis*, 53(4):209–235, 2007.

[20] D. Cioranescu, J. Saint, and J. Paulin. Homogenization in open sets with holes. *Journal of Mathematical Analysis and Applications*, 71:590–607, 1979.

[21] D. E. Stephenson and B. C. Walker and C. B. Skelton and E. P. Gorzkowski and D. J. Rowenhorst and D. R. Wheeler. Modeling 3D Microstructure and Ion Transport in Porous Li-Ion Battery Electrodes. *Journal of the Electrochemical Society*, 158:A781–A789, 2011.

[22] M. Doyle, T.F. Fuller, and J. Newman. Modeling of Galvanostatic Charge and Discharge of the Lithium/Polymer/Insertion Cell. *Journal of The Electrochemical Society*, 140(6):1526–1533, 1993.

[23] E. Weinan and B. Engquist. The heterogeneous multiscale methods. *Communications in Mathematical Sciences*, 1(1):87–133, 2003.

[24] E. Weinan and B. Engquist and X. Li and W. Ren and E. Vanden-Eijnden. Heterogeneous Multiscale Methods: A Review. *Communications in Computational Physics*, 2(3):367–450, 2007.

[25] Y. Efendiev and T. Hou. *Multiscale Finite Element Methods. Theory and Applications, Surveys and Tutorials in the Applied Mathematical Sciences*. Springer, 3rd edition, 2009.

[26] Y. Efendiev and A. Pankov. Numerical Homogenization of monotone elliptic operators. *Multiscale Modeling and Simulation*, 2:62–79, 2003.

[27] Y. Efendiev and A. Pankov. Numerical homogenization and correctors for nonlinear elliptic equations. *SIAM Journal of Apllied Mathematics*, 65(1):43–68, 2004.

[28] Y. Efendiev and A. Pankov. Numerical Homogenization of Nonlinear Random Parabolic Operators. *Multiscale Modeling and Simulation*, 2:237–268, 2004.

[29] L.C. Evans. *Partial Differential Equations*. American Mathematical Society, 1998.

[30] R. Eymard, T. Gallout, and R. Herbin. *The Finite Volume Method (Handbook for Numerical Analysis)*. North Holland, 2000.

[31] Fuller, Thomas F., Doyle, Marc, and John Newman. Simulation and Optimization of the Dual Lithium Ion Insertion Cell. *Journal of The Electrochemical Society*, 141(1):1–10, 1994.

[32] M. Gahn, P. Knabner, and M. Neuss-Radu. Homogenization of reaction-diffusion processes in a two-component porous medium with a nonlinear flux condition at the interface, and application to metabolic processes in cells. *Preprint-Reihe Angewandte Mathematik des Departments Mathematik, Friedrich-Alexander-Universitaet Erlangen-Nuernberg*, 2014.

[33] William C. Gear. *Numerical Initial Value Problems in Ordinary Differential Equations*. Prentice-Hall Inc., 1971.

[34] P. Henning and M. Ohlberger. The Heterogeneous Multiscale Finite Element Method for Elliptic Homogenization Problems in Perforated Domains. *Numerische Mathematik*, 113, Issue 4 (2009):601 – 629, october 2009.

[35] P. Henning and M. Ohlberger. On the implementation of a heterogeneous multiscale finite element method for nonlinear elliptic problems. In *Advances in DUNE. Proceedings of the DUNE User Meeting, Held 6.-8.10.2010, in Stuttgart, Germany.*, pages 143–155. Springer, may 2012.

[36] P. Henning and M. Ohlberger. Error control and adaptivity for heterogeneous multiscale approximations of nonlinear monotone problems. *Discrete and Continuous Dynamical Systems - Series S*, 8(1):119–150, july 2014.

[37] P. Henning, M. Ohlberger, and B. Schweizer. An Adaptive Multiscale Finite Element Method. *SIAM Multiscale Mod. Simul.*, 12(3):1078–1107, july 2014.

[38] U. Hornung. *Homogenization and Porous Media, Interdisciplinary Applied Mathematics 6*. Springer-Verlag, 1997.

[39] I. Babuška and G. Caloz and J. E. Osborn. Finite Element Methods for the Solution of Problems with Rough Input Data. *Singularities and Constructive Methods for Their Treatment, Lecture Notes in Mathematics*, 1121:1–18, 1985.

[40] I. Babuška and G. Caloz and J. E. Osborn. Special Finite Element Methods for a Class of Second Order Elliptic Problems with Rough Coefficients. *SIAM Journal on Numerical Analysis*, 31(4):945–981, 1994.

[41] I. Babuška and J. E. Osborn. Generalized Finite Element Methods: Their Performance and Their Relation to Mixed Methods. *SIAM Journal on Numerical Analysis*, 20(3):510–536, 1983.

[42] Vasilena Taralova (joint with Yalchin Efendiev and Oleg Iliev). Upscaling Approaches for Nonlinear Processes in Li-ion Batteries. *Oberwolfach Reports: Mini-Workshop: Numerical Upscaling for Media with Deterministic and Stochastic Heterogeneity, Report No. 07/2013*, 72:416–419, 2013.

[43] C.T. Kelley. *Solving Nonlinear Equations with Newton's Method*. SIAM, 2003.

[44] S.M. Kozlov, O.A. Oleinik, and V.V. Zhikov. *Homogenization of differential operators and integral functionals*. Springer-Verlag, 1994.

[45] W. Lai and F. Ciucci. Derivation of Micro/Macro Lithium Battery Models from Homogenization. *Transport in Porous Media*, 88:249–270, 2011.

[46] W. Lai and F. Ciucci. Mathematical modeling of porous battery electrodes–Revisit of Newman's model. *Electrochimica Acta*, 56(11):4369–4377, April 2011.

[47] A. Latz and J. Zausch. Thermodynamic consistent transport theory of Li-ion batteries. *Journal of Power Sources*, 196:3296–3302, 2011.

[48] Arnulf Latz, Jochen Zausch, and Oleg Iliev. Modeling of species and charge transport in Li-Ion batteries based on non-equilibrium thermodynamics. In *Proceedings of the 7th international conference on Numerical methods and applications*, NMA'10, pages 329–337, Berlin, Heidelberg, 2011. Springer-Verlag.

[49] Randall J. LeVeque. *Finite Volume Methods for Hyperbolic Problems (Cambridge Texts in Applied Mathematics)*. Cambridge University Press, 1st edition, 2002.

[50] LLNL. VisIt. `https://wci.llnl.gov/simulation/computer-codes/visit/`.

[51] M. Barraulta and Y. Maday and N. C. Nguyen and A. T. Patera. An empirical interpolation method: application to efficient reduced-basis discretization of partial differential equations. *Comptes Rendus Mathematique*, 339:667672, 2004.

[52] K. W. Morton and D. F. Mayers. *Numerical Solution of Partial Differential Equations: An Introduction*. Cambridge University Press, 2nd edition, 2005.

[53] N. C. Nguyen. A multiscale reduced-basis method for parametrized elliptic partial differential equations with multiple scales. *Journal of Computational Physics*, 227:98079822, 2008.

[54] G. Nguetseng. A general convergence result for a functional related to the theory of homogenization. *SIAM Journal of Mathematical Analysis*, 20(3):608–623, 1989.

[55] M. Ohlberger. A posterior error estimates for the heterogenoeous mulitscale finite element method for elliptic homogenization problems. *SIAM Multiscale Mod. Simul.*, 4(1):88 – 114, 2005.

[56] Tsutomu Ohzuku, Masaki Kitagawa, and Taketsugu Hirai. Electrochemistry of Manganese Dioxide in Lithium Nonaqueous Cell: III . XRay Diffractional Study on the Reduction of SpinelRelated Manganese Dioxide. *Journal of The Electrochemical Society*, 137:769–775, 1990.

[57] P. Degond and A. Lozinski and B. P. Muljadi and J. Narski. Crouzeix-Raviart MsFEM with Bubble Functions for Diffusion and Advection-Diffusion in Perforated Media. *arXiv:1310.8639 [math.NA]*, 2013.

[58] G. Pavliotis and A. Stuart. *Multiscale Methods. Averaging and Homogenization (Texts in Applied Mathematics)*. Springer, 2008.

[59] J. Pikul, H. G. Zhang, J. Cho, P. V. Braun, and W. P. King. High-power lithium ion microbatteries from interdigitated three-dimensional bicontinuous nanoporous electrodes. *Nature Communications*, 2013.

[60] J.N. Reddy. *An Introduction to the Finite Element Method*. McGraw-Hill, Inc., 2nd edition, 1993.

[61] Michael Renardy and Robert Rogers. *An Introduction to Partial Differential Equations*. Springer, 2nd edition, 2004.

[62] G. Richardson, G. Denuault, and C.P. Please. Multiscale modelling and analysis of lithium-ion battery charge and discharge. *Journal of Engineering Mathematics*, 72:41–72, 2012.

[63] E. Sanchez-Palencia. *Non-Homogeneous Media and Vibration Theory*. Springer-Verlag, 1980.

[64] Fraunhofer SCAI. SAMG. `http://www.scai.fraunhofer.de/en/business-research-areas/numerical-software/products/samg.html`.

[65] J. Schöberl. Netgen Mesh Generator. `http://sourceforge.net/projects/netgen-mesher/`.

[66] J. Schöberl. NETGEN - An advancing front 2D/3D-mesh generator based on abstract rules. *Comput.Visual.Sci*, 1:41–52, 1997.

[67] Jonathan Richard Shewchuk. Triangle: Engineering a 2D Quality Mesh Generator and Delaunay Triangulator. In Ming C. Lin and Dinesh Manocha, editors, *Applied Computational Geometry: Towards Geometric Engineering*, volume 1148 of *Lecture Notes in Computer Science*, pages 203–222. Springer-Verlag, May 1996. From the First ACM Workshop on Applied Computational Geometry.

[68] T. Hou and X. H. Wu. A Multiscale Finite Element Method for Elliptic Problems in Composite Materials and Porous Media. *Journal of Computational Physics*, 134:169–189, 1997.

[69] T. Hou and X. Wu and Z. Cai. Convergence of a Multiscale Finite Element Method for Elliptic Problems with Rapidly Oscillating Coefficients. *Mathematics of Computation*, 68(227):913–943, 1999.

[70] M. Taralov, V. Taralova, P. Popov, O. Iliev, A. Latz, and J. Zausch. Report on Finite Elements Simulations of Electrochemical Processes in Li-ion Batteries with Thermic Effects. *Berichte des Fraunhofer ITWM, Nr. 221*, 2012.

[71] M. Taralov, V. Taralova, P. Popov, O. Iliev, A. Latz, and J. Zausch. On 2D Finite Element Simulation of a Thermodynamically Consistent Li-ion Battery Microscale Model. In *Mathematics in Industry (Proceedings of the 8th Annual Meeting of BGSIAM)*, pages 148–161. Cambridge Scholars Publishing, 2014.

[72] Y. Efendiev and J. Galvis and X. H. Wu. Multiscale finite element methods for high-contrast problems using local spectral basis functions. *Journal of Computational Physics*, 230:937–955, 2011.

[73] Y. Efendiev and T. Hou. Multiscale finite element methods for porous media flows and their applications. *Applied Numerical Mathematics*, 57:577–596, 2007.

[74] Y. Efendiev and T. Hou and V. Ginting. Multiscale Finite Element Methods for Nonlinear Problems and Their Applications. *Communications in Mathematical Sciences*, 2(4):553–589, 2004.

[75] Y. Efendiev and T. Hou and X. H. Wu. Convergence of a Nonconforming Multiscale Finite Element Method. *SIAM Journal on Numerical Analysis*, 37(3):888–910, 2000.

[76] Y. Maday and E. Rønquist. A Reduced-Basis Element Method. *Journal of Scientific Computing*, 17:447–459, 2002.

Academic Career

Since 10/2011–05/2015	PhD student at Fraunhofer Institute for Industrial Mathematics (ITWM), Department Flow and Material Simulation, and Technical University of Kaiserslautern, Department of Mathematics, Kaiserslautern, Germany
04/2013	Visiting researcher at the Institute for Scientific Computation (ISC) at Texas A&M University, College Station, USA
07/2011–10/2011	Researcher at Fraunhofer Institute for Industrial Mathematics (ITWM) with scholarship awarded by the German Academic Exchange Service (Deutscher Akademischer Austauschdienst, DAAD), Kaiserslautern, Germany
03/2011–07/2011	Mathematician, working on the international project "IterUpscale - FSI", Bulgarian Academy of Sciences, Institute for Information and Communication Technologies
08/2010–10/2010	Internship at Fraunhofer Institute for Industrial Mathematics (ITWM), Kaiserslautern, Germany
01/2010–06/2010	Mathematician, working on the international project "IterUpscale - FSI", Bulgarian Academy of Sciences, Institute for Information and Communication Technologies
11/2009–06/2011	Master's degree in Computational Mathematics and Mathematical Modelling, University of Sofia "St. Kliment Ohridski", Faculty of Mathematics and Informatics, Sofia, Bulgaria
10/2005–09/2009	Bachelor's degree in Applied Mathematics, University of Sofia "St. Kliment Ohridski", Faculty of Mathematics and Informatics, Sofia, Bulgaria
2000–2005	High school degree, High School of Mathematics and Natural Sciences, Veliko Tarnovo, Bulgaria

Akademischer Werdegang

10/2011–05/2015	Promotion am Fraunhofer-Institut für Techno- und Wirtschaftsmathematik (ITWM), Abteilung Strömungs- und Materialsimulation, und Technische Universität Kaiserslautern, Fachbereich Mathematik, Kaiserslautern, Deutschland
04/2013	Gastwissenschaftler am Institute for Scientific Computation (ISC) at Texas A&M University, College Station, USA
07/2011–10/2011	DAAD-Stipendiat am Fraunhofer-Institut für Techno- und Wirtschaftsmathematik (ITWM) Kaiserslautern, Deutschland
03/2011–07/2011	Mathematiker, Bulgarische Akademie der Wissenschaften, Institute for Information and Communication Technologies
08/2010–10/2010	Forschungsaufenthalt am Fraunhofer-Institut für Techno- und Wirtschaftsmathematik (ITWM), Kaiserslautern, Deutschland
01/2010–06/2010	Mathematiker, Bulgarische Akademie der Wissenschaften, Institute for Information and Communication Technologies
11/2009–06/2011	Master in Numerische Mathematik und Mathematische Modellierung, Universität zu Sofia "St. Kliment Ohridski", Fachbereich Mathematik und Informatik, Sofia, Bulgarien
10/2005–09/2009	Bachelor in Angewandte Mathematik, Universität zu Sofia "St. Kliment Ohridski", Fachbereich Mathematik und Informatik, Sofia, Bulgarien
2000–2005	Mathematisch-naturwissenschaftliches Gymnasium, Veliko Tarnovo, Bulgarien